EFFECT ON PROCESSING CONDITION

ON GRAIN BOUNDARY CHARACTER DISTRIBUTION AND

MOBILITY IN OXIDE NUCLEAR FUELS

by

Karin Rudman Prieto

A Dissertation Presented in Partial Fulfillment
of the Requirements for the Degree
Doctor of Philosophy

Approved January 2014 by the
Graduate Supervisory Committee:

Pedro Peralta
Fernando Ponce
Karl Sieradzki

ARIZONA STATE UNIVERSITY

MAY 2014

ABSTRACT

The initial microstructure of oxide fuel pellets can play a key role in their performance. At low burnups, the transport of fission products has a strong dependence on oxygen content, grain size distribution, porosity and grain boundary (GB) characteristics (crystallography, geometry and topology), all of which, in turn depend on processing conditions. These microstructural features can also affect the fuel densification, thermal conductivity and microstructure evolution inside the reactor. Understanding these effects can provide insight into microstructure evolution of fuels in-pile.

In this work, mechanical and ion beam serial sectioning techniques were developed to obtain Electron Backscatter Diffraction (EBSD) data, both in 2-D and 3-D, for depleted UO_{2+X} pellets manufactured under different conditions. The EBSD maps were used to relate processing conditions to microstructural features, with emphasis on special GBs according to the Coincident Site Lattice (CSL) model, as well as correlations between pore size and location in the microstructure.

Furthermore, larger grains (at least 2.5 times the average grain size) were observed in all the samples and studied. Results indicate that larger grains, in samples manufactured under different conditions, dominate the overall crystallographic texture and have a fairly strong GB texture. Moreover, it seems that the preferential misorientation axis for these GBs, regardless of the O/M, is {001}. These results might be related to GB energy and structure and, suggest that the mechanism that controls grain growth seems to be independent of both processing conditions and stoichiometry.

Additionally, a sample was heat treated to relate grain growth and crystallography. The results indicate that at least two mechanisms were involved. Lengthening of GBs was

observed for larger grains. Another mechanism of grain growth was observed, in this case, grains rotate to match a neighboring grain forming a larger grain. In the new grain, the misorientation between the two neighboring grains decreases to less than 5°, forming a new larger grain.

The results presented in this work indicate that detailed studies of the initial microstructure of the fuel, with emphasis on the crystallography of grains and GBs could help to give insights on the in-pile microstructural evolution of the fuel.

ACKNOWLEDGMENTS

I would like to thank my advisor for all his help and wisdom, my co-workers at the lab for always keeping me laughing. To my family, friends and Ash for always being there, for their support and understanding.

This project is a part of the Advanced Fuel Cycle Initiative (AFCI) and the Fuel Cycle Research and Development (FCRD). This project was funded by Los Alamos National Laboratory (LANL), Award # DE-FC07-05ID14654.

TABLE OF CONTENTS

Page

Page

CHAPTER

Page

CHAPTER

LIST OF FIGURES

Figure Page

Figure Page

Figure Page

CHAPTER 1

MOTIVATION

Nuclear power represents a reliable source of electricity for many countries in the world; in 2010, 13% of the world's electricity was provided by nuclear power. A total of 441 units were operating in 29 countries. Currently in the United States, a total of 104 nuclear power plants generate approximately 20% of the country's electricity, being the second largest source of electricity after coal. Additionally, it remains as the largest contributor (more than 70%) of the non-green-house-gas-emitting electric power generation in the United States [1-3].

The vast majority of these plants are water reactors that use uranium oxide (UO_2), with uranium enrichment up to 5%, or a mixture of UO_2 and PUO_2 (MOX) as a fuel. The design and materials used in these plants have not changed in the last 50 years, Figure 1.1 shows a generic light water reactor fuel element that consists of: a zirconium-tin alloy tube for cladding, a stack of fuel pellets and an open volume above the fuel stack (called plenum) to accommodate fission gases released from the fuel without over-pressurizing the cladding [4].

There is a need in the industry for reactors that can achieve higher burnups[1] and generate more electricity. The fuel life is limited by fretting wear, cladding corrosion, hydrogen embrittlement, pellet-cladding interaction and/or excessive internal pressure due to fission gas release. The maximum burnup of current fuel designs is ~60 MWd/kgU. At larger

[1] Burnup is a measure of the total amount of fissile material used. It is typically measured as the fraction of initial metal atoms (FIMA), in percent, consumed or as the total energy generated per kilogram of the fissile element, e.g., Watts.day/kgU.

burnups there is significant increase of the cladding failure, becoming a safety issue [4]. Therefore, more efficient fuels and reactor designs are needed.

In order to design more efficient fuels a more a detailed characterization of the microstructure of the fuel is needed. These results can be used as inputs in more complex multi-physics models to predict in-pile fuel behavior and evolution. The models are extremely complex since so many variables are involved during the fission process. However, the more details we have on the initial fuel microstructure, the more accurate the model will be. For instance, the initial microstructure plays a key role on the fuel's in-pile behavior. As an example, the initial grain size and distribution can be directly related to the release or retention of the fission products as well as the pellet swelling [5, 6]. Large grains, produced usually under extended sintering at high temperatures [6, 7] or under oxidative sintering atmospheres [8, 9], can retain larger amounts of fission gases, but tend to swell and generate cracks that will decrease the fuel's thermal efficiency [4].

Empirical studies of the fuel behavior are extremely expensive due the complexity of the problem and the classical approach to do experiments to determine empirical data can no longer be pursued. Therefore, key experiments that can provide data on different steps of the evolution of the microstructure can be used to understand the physics of each step to build predictive models of the in-pile fuel evolution and to validate these models. These data and models can in turn help to establish structure-property-processing relationships. For instance, a consequence of burnup is the dilution of uranium on the cation sublattice, as the uranium ion concentration is reduced from 1 to ~0.94 [4]. Studies in samples with different stoichiometries and densities can show snapshots of the microstructure at different burnup stages. The further the oxygen to metal (O/M) ratio is from 2, the higher the burnup.

Similar phenomena can be expected with density: initially the fuel has a higher density, that decreases as the burnup increases, as fission products generate bubbles and eventually leave the fuel [10]. Experiments of interrupted sintering can be used to study the microstructural evolution of the fuel, as the reverse process occurs during the initial stages of fission.

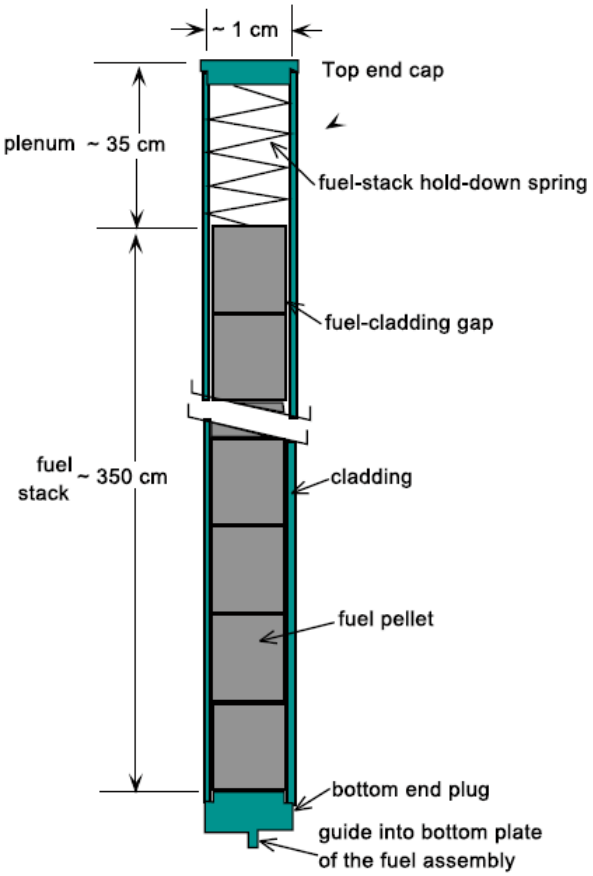

Figure 1.1 Fuel assembly [4]

Moreover, fractography images from an irradiated fuel, as shown in Figure 1.2, suggest that the grain boundary (GB) character has a strong influence on the shape and connectivity of the fission bubbles. Some of the grain facets are decorated with isolated round bubbles,

while others have elongated interconnected bubbles. Once the bubbles are connected and reach other GBs, the gaseous fission products can be released from the fuel, affecting its efficiency for heat transfer. As the GB energy can depend on the GB misorientation [11-14], pores and bubbles will migrate to high energy GBs to minimize the system energy. Variations on the GB character distribution and location should affect the percolation paths whereby the fission gases are released. Yet, there is almost no information in the literature on how the processing conditions affect the grain texture, grain boundary character and distribution. Therefore, the initial microstructure of the fuel needs to be fully characterized, as it can affect the overall behavior of the fuel as well as its efficiency. This information can in turn be used as inputs for finite models of the fuels as well as to create more efficient fuels using GB engineering.

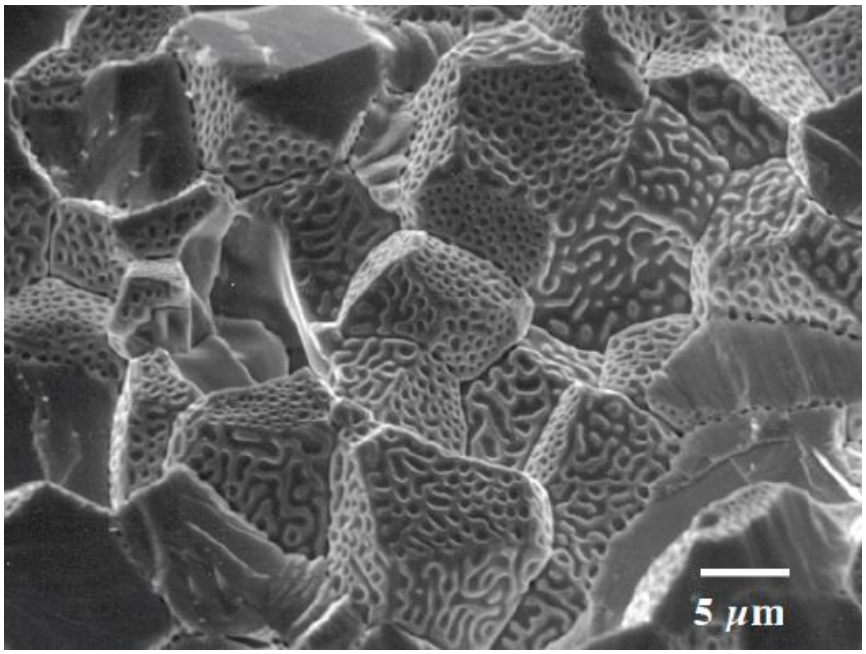

Figure 1.2. Fractography image of an irradiated fuel pellet after annealing during 5h at 1400^0C [15].

The brief summary given above indicates that there are still many questions that need to be answered regarding the connection between fuel's microstructure and processing conditions: How the GB misorientation distribution is affected depending on the sintering conditions? Are some GBs special? How is GB mobility, a key aspect of grain growth, affected by oxygen stoichiometry? Is there any relevant texture generated under certain sintering conditions? How are the porosity location, shape and distribution affected? How does the oxygen excess affect the kinetics of the sintering and grain growth processes?

The process for most of the existing nuclear power plants to renew the licenses is ongoing so they can continue to operate another 20 years, answers to these questions are needed. Sixty one reactors have already extensions on their licenses and another twenty two have pending applications [1-3]. In order to prove that the plants can operate for longer periods of time without having any structural damage, several national laboratories as well as universities are working together to simulate, at different levels, the behavior of all the different components and materials in the reactors. Details of the fuel microstructure such as porosity distribution and location as well as GB character, distribution and location are needed to create more accurate models to predict the fuel's evolution in-pile, as well as to design more efficient fuels that can last longer cycles.

CHAPTER 2

LITERATURE REVIEW

2.1. Uranium dioxide ($UO_{2\pm x}$)

Uranium dioxide is a stable compound, with a large partial free energy of formation, as seen in Figure 2.1. Most of the fission products, such as oxides of rare earth metals, fall below UO_2 and, therefore, a large fraction of the fission products form stable oxides that are retained in the fuel [16]. Additionally, there is an excellent compatibility between UO_2 and water [12, 16], which makes it compatible for use in water reactors, under normal operating temperature and pressure conditions.

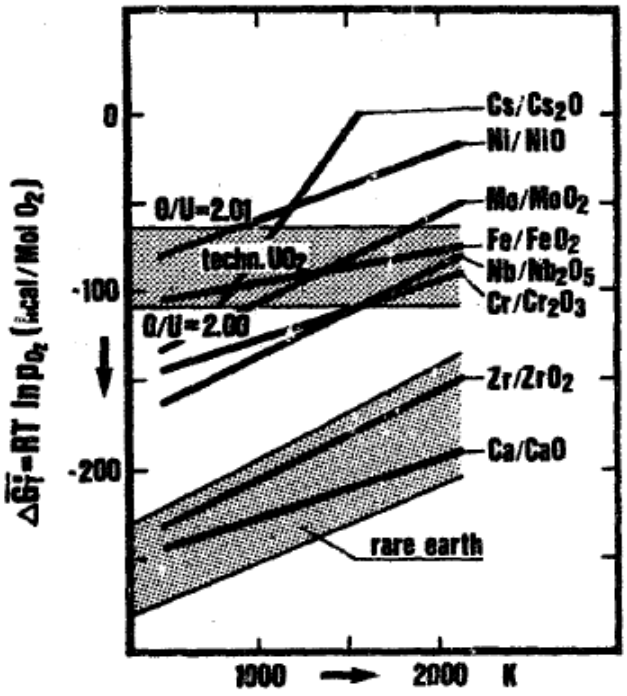

Figure 2.1. Partial free energy of formation of multiple oxides of fission products. [16]

Uranium dioxide (UO_2) has a flourite structure, shown in Figure 2.2, with a highly symmetric face-centered cubic lattice structure and a space group $Fm\bar{3}m$. The cations are

arranged at the face centered cubic lattice (a_0 = 5.470 Å) and the anions are arranged at the corners of an inner cube with cell edges (2.73 Å). The uranium atoms have eight-fold coordination and the oxygen atoms are four fold coordinated. At higher oxygen contents (U_4O_9), the symmetry of the uranium oxide is reduced to I43d [17].

The isometric fluorite structure can accommodate extra oxygen atoms to form hyperstoichiometric UO_{2+x} with $x \leq 0.25$. In order to accommodate the extra oxygen atoms, an increase in the ratio of U(V) or U(VI) relative to U(IV) is required to maintain the charge balance. There is also a change in the lattice parameter. Moreover, the U_4O_9 lattice is characterized by long-range ordering of oxygen defects and interstitials, creating a unit-cell dimension almost four times larger than the original UO_2 cell. While the UO_{2+x} lattice is characterized by short-range defects [18].

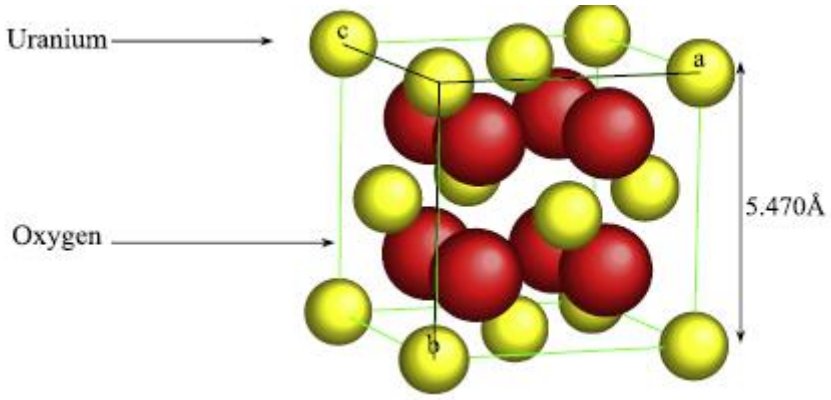

Figure 2.2. Fluorite structure [12].

The UO_2 phase is a stable line compound at room temperature, and can accept more oxygen at temperatures above 575 K forming $UO_{2\pm x}$, where x can reach a maximum of 0.28 at 1930

K. The extra oxygen enters at interstitial sites and O atoms are displaced from their original positions forming vacancies and generating distortion in the lattice (Figure 2.3) [12, 16, 19, 20]. The charge balance is maintained by the presence of some U^{3+} ions in the uranium sublattice. Experimental data suggest that there are two types of interstitial oxygen atoms O_i^a and O_i^b in positions that do not correspond to the classical interstitial sites of the fluorite structure. A third oxygen sublattice is added to the two normal oxygen sublattices of the fluorite and some U^{6+} cations are introduced in the uranium sublattice to accommodate the oxygen excess [21].

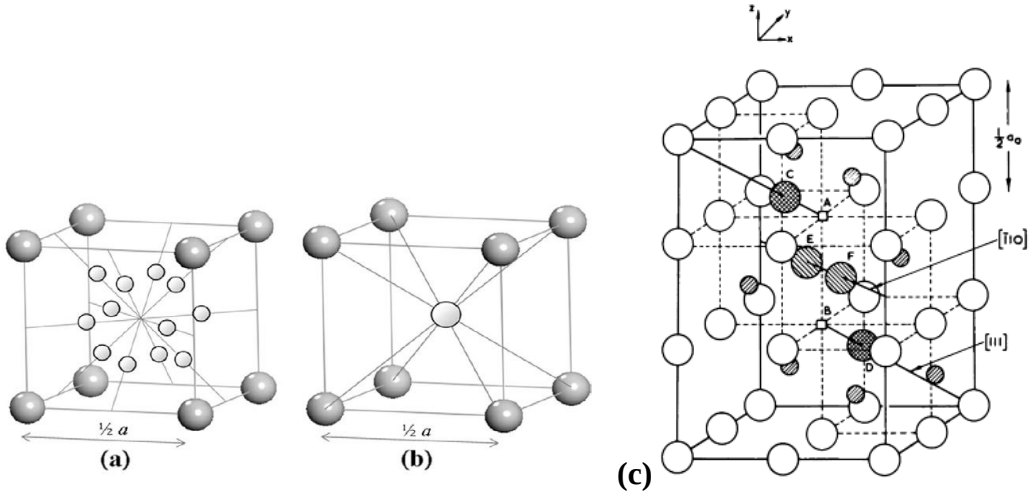

Figure 2.3. Models illustrating two possible sites for interstitial oxygen in the unoccupied cubic sites created by the oxygen sublattice in UO_2 ($a=1/2a_o$). Larger spheres are lattice oxygen atoms; smaller spheres represent 12 possible perpendicular bisector sites (a), or the body center site (b) for interstitial oxygen in UO_2 [18] and (c) the 2:2:2 defect cluster (small circles are the uranium atoms and large hatched circles are the interstitial oxygen atoms) [22].

Willis [23] studied the oxygen positions in $U_{2.13}$, proposing a more complete expression for the non-stoichiometric oxide as:

$$U_{1.00}O_{1.82}O^{a}_{0.08}O^{b}_{0.23} \quad (2.1)$$

His results show that the uranium atoms fully occupy the face-centered positions. While the O atoms are close to the fluorite positions (¼ ¼ ¼), but slightly shifted along <111> towards the interstitial holes at (½ ½ ½), 9 out of 10 oxygen atoms are located in these positions. The rest of the oxygen atoms are located at the O^a or O^b positions (Figure 2.3(b)). These interstitial positions are not located at the large interstitial holes at (½ ½ ½), but about 1 Å away [23]. Moreover, as the oxygen atoms are displaced from its original positions, oxygen vacancies are created. The distance between the new interstitial positions and the regular oxygen atoms is ~1.5 Å, compared to ~2.6 Å of the normal interatomic distance for O-O [24]. Thus, defect clusters are needed to locally maintain the electroneutrality.

Therefore, the $UO_{2\pm x}$ defect model consists of oxygen vacancies (Vo) at the normal lattice sites and two different interstitial oxygen sites are required in order to maintain electroneutrality, as seen in Figure 2.3. Using the Kröger-Vink notation, the formation of the complex defect is described by [25]:

$$2V_i^a + 2V_i^b + 2O_o + O_2(g) = \left\{2(O_i^a O_i^b V_o)\right\}^{m\prime} + mh^{\circ} \quad (2.2)$$

Where h° is a hole and m' is the charge of the complex defect.

However, near stoichiometry, the complex defects are described by [25]:

$$2V_i^a + 2V_i^b + 2O_o + 1/2O_2(g) = \left\{2O_i^a O_i^b V_o\right\}^{m\prime} + mh^{\circ} \quad (2.3)$$

These defects can play a key role in the release of fission gases as fission gas atoms diffuse via vacancy clusters of one uranium vacancy and two oxygen vacancies [26].

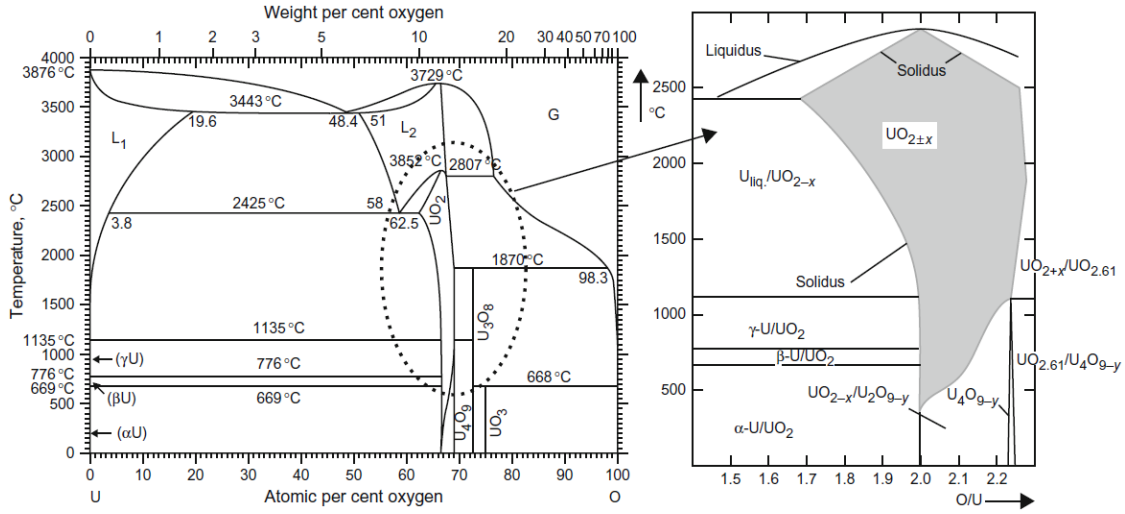

Figure 2.4. Phase diagram of the O-U system [27].

One of the reasons why urania is used as fuel is its chemical stability. The phase diagram for the U-O system is shown in Figure 2.4; no phase transformation occurs up to its melting point, which makes it stable under operational reactor conditions (up to 1500 K) [16, 28]. Nevertheless, there is an extended range of compositions that, starting at 575 K, depart from the exact UO_2 stoichiometry. These deviations from the stoichiometry can affect the fuel's properties, in particular the ones that depends on atomic defects and atomic mobility, as well as the oxygen partial pressure of the fission products [16, 28, 29]. Therefore, it is very important to determine the initial fuel's stoichiometry and how it is affected by the processing conditions, as it will be affected by variables such as the sintering atmosphere,

temperature and initial stoichiometry and composition. More details on how the sintering conditions can affect the fuel's microstructure will be described on the next section.

2.2. Processing of fuel pellets

The fuel pelletsfor light water reactors (LWRs) are typically made by cold pressing UO_{2+x} powder to obtain "green" pellets and sintering them in a reducing atmosphere at about 1600-1700 ^{0}C, to obtain highly dense ($\geq$ 95% theoretical density) and nearly stoichiometric pellets [16, 30, 31]. As a "green" powder compact is sintered, it typically goes through three stages: initial, intermediate and final [32]. The initial stage is characterized by the formation of necks and extremely curved GBs, and it finalizes with the formation of continuous GBs and initial grain growth. During the intermediate stage, grains start growing and pores form continuous channels at triple and quadruple junctions. During the final stage, pores become spherical and grain coarsening starts [5, 32, 33].

2.2.1 Powder compaction

Power compaction is a process that can be described as pressing of a free-flowing powder, with or without binders. Uniaxial pressing begins with a prepared granulated feed that is compressed at a relative high pressure under a rigid die. This forming technique is a mature and well understood technology that can be applied for mass production of simple shapes [34]. In the case of the nuclear fuel, the powder is compacted in a metal die by pressure that is applied in a single direction.

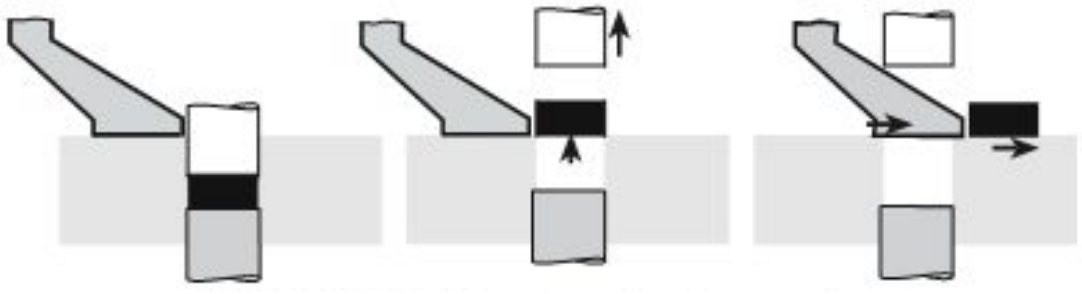

Figure 2.5. The three stages of dry pressing [35].

Dry pressing consist mainly in three steps: (1) filling the die, (2) compaction and shaping, and ejection, as seen in Figure 2.5. The free flowing granules/powder is fed into the die using a sliding feed shoe. Once the cavity is filled, the top punch descends and compresses the powder to a fix size or pressure. A particle size distribution between 20 and 200 μm is often used for dry pressing. Pressing rates range from a fraction of a second to several minutes, depending on the sample size, with pressing pressures ranging between 20-300 MPa. In some cases, lubricants are used to reduce die wear and improve density uniformity [34, 35].

The pressure, produced by moving the punches, compacts the powder into a cohesive piece. The rate of densification is initially high and decreases rapidly. The particles slide and rearrange during pressing, reducing the intergranular porosity. The air compressed in the pores migrates and partially exhausts between the punch and the die [34, 35].

A portion of the applied load during pressing is transferred to the die wall during compaction. The latter produces pressure and density gradients in the compact, shown in Figure 2.6. The shear stress at the wall increases with the pressing pressure, but it can be reduced by using lubricants. In general, relative axial displacement of particles is greater

in the center than near the die wall. Therefore, the minimum pressure occurs near the top corner of the compact and diminishes in depth toward the central axis. This in turn results in pressure and density gradients that may lead to dimensional distortions during sintering [34, 35].

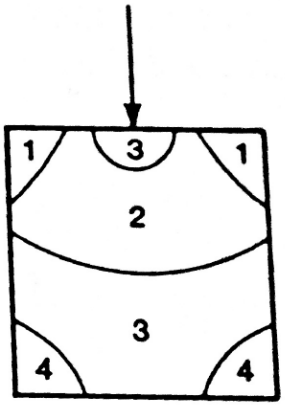

Figure 2.6 Pressure profiles for pressing from the top, $P_1>P_2>P_3>P_4$. Note the low pressure region near the top surface below the center of the punch, produced by friction [34].

Moreover, pressure gradients, non-uniform powder filling, trapped compressed air, frictional restraints and differential springback during unloading are the most common sources of defects for the compacts. The differential springback within the compact or between the compact and the die creates cracks and laminations (Figure 2.7). The most common pressing defects are laminations, end capping, ring capping, vertical cracks in the exterior region, shape distortions on sintering, and surface defects. Examples of some of these defects are shown in Figure 2.7.

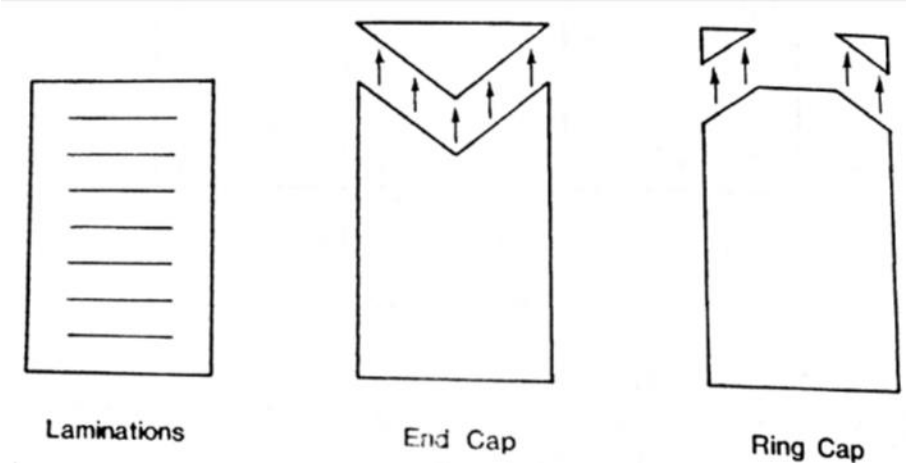

Figure 2.7. Common defects in pressed compacts [34].

Laminations are circumferential cracks on the frictional surface and are oriented perpendicular to the pressing directions. Lamination can be avoided by using die-wall lubrication and/or lowering the pressing pressure to reduce the springback [34].

Another common defect is end capping. An end cap is a shallow wedge-shaped section that separates at an angle of 10°-20° from the end of the compact on ejection. This defect is observed when the springback is high and the compact strength is relatively low. Control of the powder shape/size distribution to obtain denser compacts at lower pressures helps to reduce the appearance of this defect. Also, the use of lubricants and/or a highly smooth wall surface will reduce the springback effect, eliminating this type of defect [34].

Ring capping occurs by a high differential springback at the corner of the compact. The escape of air on compression tends to draw granules into the gap between the die and the punch, creating a high springback. Therefore, the greater the wear on the tool, the more frequently this defect will appear [34].

Vertical cracks in the exterior region are created by differential springback from compressed air. Consequently a combination of high pressure, fast punch velocity, accompanied by large compact thickness and low gas permeability will promote this defect [34].

An additional defect that can occur during compaction is shape distortion during sintering. This is caused by density gradients causing non-uniform shrinkage during sintering. This can be controlled by reducing the wall friction to reduce the density gradients [34].

Extremely large pores can be a common defect in solid sintering, where no glassy phase is present. This can be reduced by decreasing the size of the granules and increasing the granule's compressibility [34].

Finally, surface defects can also be present. The quality of the compact surface is directly related to the friction and the smoothness of the wall of the die and the punch; the size and deformation of the granules and the pressing pressure. Larger pores on the surface are usually observed between large granules which resist deformation and are poorly joined [34].

In the case of the pellets described in this study, no granulated powders were used. The starting powders usually are made into compacts that are sintered, grinded and sieved, to obtain a particular stoichiometry. Therefore, the powders consist on sharp particles that do not easily flow to fill the die and do not fill all the space to create dense green compacts. Some of the defects that can appear as a consequence of this processing choice were observed on the samples and will be discussed in Chapter 5.

Once the compacts are formed, the green bodies are dried and then sintered to develop certain microstructure and properties. Details on the sintering process will be described next.

2.2.2. Sintering

During processing, crystalline or non-crystalline powders are compacted and heated at a temperature sufficient to develop useful properties, usually in the range of $0.5 < Sintering\ Temperature/Melting\ Point < 0.95$ [32]. The "green" pellets are usually composed of individual powder particles separated by 25 to 60 vol% porosity, depending on the material and the processing conditions. The compacts are heat treated to maximize properties such as strength, translucency, and thermal conductivity. The latter is accomplished by decreasing the porosity by mass transport in the structure [32]; this processing step is usually referred as sintering.

Therefore, sintering can be described as a thermal treatment for bonding particles into a coherent, predominantly solid structure via diffusion or other mass transport processes that occur at the atomic scale. The bonding leads to improved strength and a reduction of the system energy. Sintering occurs when packed particles are heated to a temperature where there is sufficient atomic motion to grow bonds between particles [36], and is associated with changes in pore shape and size as well as grain growth during heating [37]. Usually during sintering a dimensional change occurs, typically shrinking, accompanied by densification of the powder compacts and strengthening [36].

The driving force for densification is a change in the free-energy due the decrease in surface area and the elimination of solid-vapor interfaces. This usually occurs by the formation of new lower-energy solid-solid interfaces. There are several possible mechanisms of mass

transfer: evaporation-condensation, viscous flow, surface diffusion, grain boundary or lattice diffusion, and plastic deformation are some of the most common ones (Figure 2.8) [37].

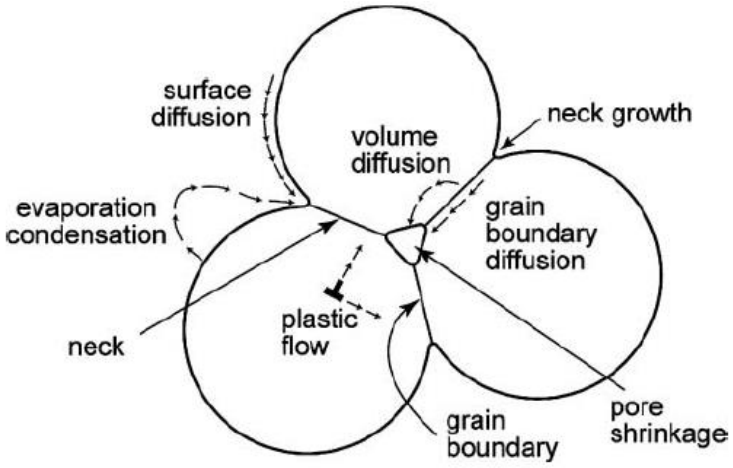

Figure 2.8. Various mass transport paths for neck growth and pore shrinkage [36].

The sintering process can be divided in three stages (initial, intermediate and final). These stages can be described as intervals of geometric change of the pore shape or an interval of time where the pore's shape remains constant while its size decreases [37]. Figure 2.9, represents an actual 3-D reconstruction of the evolution of a microstructure (composed by glass spheres) using X-ray microtomography [38].

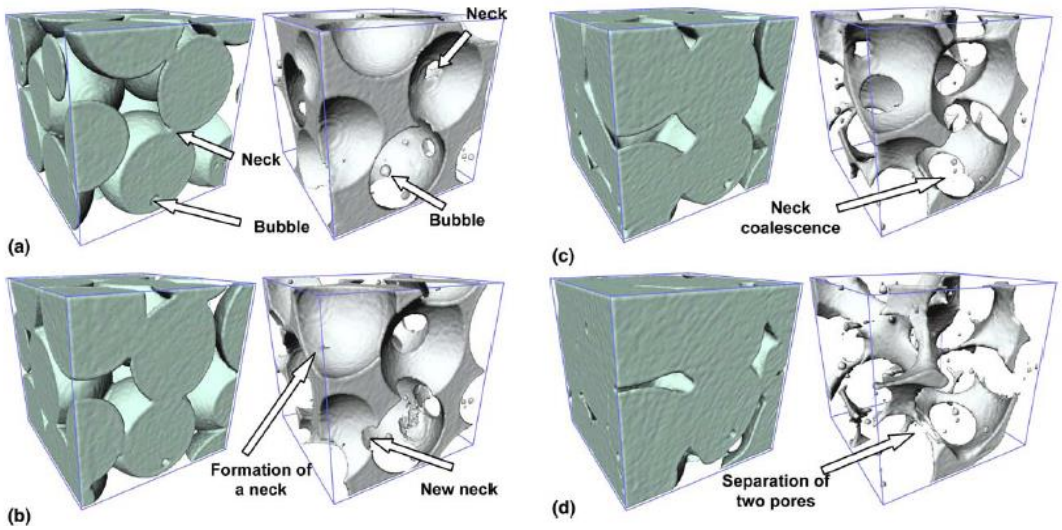

Figure 2.9. Local morphological evolution of a glass powder sample (left: solid phase, right: void space) as a function of sintering time: (a) 20, (b) 120, (c) 180 and (d) 270 min. [38].

The initial sintering stage is characterized by neck growth and inter-particle shrinkage of several percent, with an increase in relative density. At this point the sinter bond, or neck (Figure 2.8 and 2.9(a)) is formed between contacting particles intersected by a GB and sintering is driven by the curvature gradient from the particle surface to the top of the neck [36, 37]. During the initial sintering stage, the grain boundary is initially confined to the neck area (Figure 2.9(a)). After the neck surface has become blunted by neck growth, the inhibition to boundary motion decreases until grain growth is possible. The point at which grain growth first occurs is considered to terminate the initial stage of sintering (Figures 2.9(b) and (c)) [36].

The intermediate stage begins after grain growth and pore shape change causes transition to a pore and grain boundary matrix consisting of equilibrium dihedral angles formed on

the solid-vapor (pore) surface at the intersections of GB surfaces [36]. At this stage, the pores are rounded and form a tubular network located on GBs, as seen in Figure 2.9(c). Coarsening becomes most evident in the intermediate stage of sintering as pores shrinkages due vacancy flow from the pores to annihilation sites on the GBs or free surfaces [36, 39]. At the final stage, the residual pores collapse into closed spheres mostly located on triple junctions or inside the grains (see Figure 2.9(d)); densification takes place based on the vacancy diffusion from the pores to the GBs (Figure 2.8), and decreases as the GB area decreases due to coarsening [36].

During the final stage of sintering, discontinuous grain growth can occur before all the porosity is removed. An interesting example of this behavior is shown in Figure 2.10. Some of the grains have a higher population of isolated round pores inside than others. Why the porosity is not evenly distributed? According to Cobble, the fact that pores are observed adjacent to one side of the boundaries and absent from the other side is attributed to the migration of GBs toward their centers of curvature [37], which leads to the following questions: Why some GBs are more mobile than others? Why some GBs are curved and others are straight? Why not all GBs are curved or straight?

Moreover, discontinuous grain growth has been reported in sintered UO_2 pellets where organic additives were added [20] or oxygen-rich sintering atmospheres were used [40]. There are several papers in the literature that present experimental procedures and data for abnormal grain growth and lower temperature sintering [8, 9, 40-45]. Again, why are some grains growing more than others? The intermediate and final stages are characterized by the shape and connectivity of the pores and is also related to the GB energy. If some grains

are growing more than others, is because some anisotropy in the GB energy? Is it related to the grain and GB crystallography?

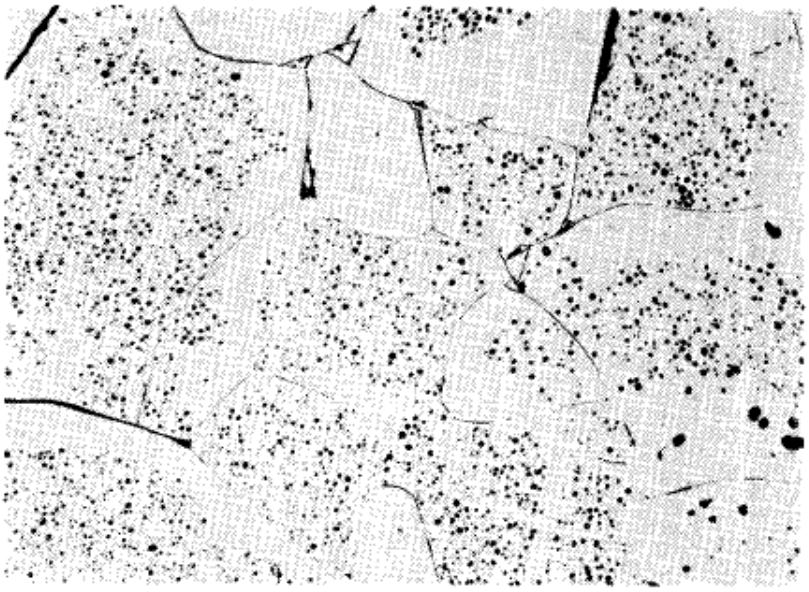

Figure 2.10. Final sintering stage after discontinuous grain growth. Photomicrograph at 60X; α alumina, 1950^{0}C, 2hrs [37].

During sintering, the reduction of the total interfacial energy occurs via densification and grain growth, which are competing mechanisms. When GBs and pores undergo simultaneous displacement, the grain growth is controlled either by the GB or by the pores. If the grain growth is controlled by the GBs, the pore dragging effect is negligible. If pores control the grain growth, the displacement rate of pore/GB ensembles is fixed by the rate of displacement of the pore [36, 46]. Details on how the porosity as well as grain coarsening evolves during the intermediate and final stages of sintering will be described next.

2.2.3. Grain Boundary-Porosity interactions

Another important aspect to study during sintering is the porosity evolution and their interaction with GBs, as pores play a key role during densification and can greatly affect grain growth. When the grain growth is controlled by GBs, the matter displacement occurs via atomic migration from one grain toward another grain through the separating GB. In the case of the grain growth controlled by pores, matter displacement proceeds by surface diffusion at the pore surface, gas-phase transport in the pore or bulk diffusion in the grains [46].

In order to obtain a dense pellet, the sample porosity needs to be eliminated. As seen in Figures 2.9 and 2.10, pores are initially located at triple junctions and are interconnected. Then, the morphology evolves from cylindrical connected pores located at three-grain junctions during the intermediate sintering stage, to isolated pores located at two-grain junctions (GBs) at the final stage of sintering [39].

It has been shown that the aspect ratio (pore length (L)/pore diameter (D)), could be used to predict the evolution in the shape of the pore. Cylindrical pores with $L/D > N$ (where N is a constant number) will become oval shaped pores and if $L/D < N$ they will become spheres. Therefore, the pore location (three- or four-grain junctions) and pore volume would have an important modifying effect on the mechanisms and conditions of the transport of pores located at three-grain junctions onto two-grain interfaces. For uniform, fine-grained microstructures, the pore motion will be influenced by the configuration of the microstructures. Figure 2.11 shows a model proposed by Fang [39] for pore relocation during sintering due grain growth. The model starts with a pore, located at a triple junction (Figure 2.11(a)) and associated with a larger grain and two smaller grains that will

eventually disappear, as the larger grain grows (Figure 2.11(c)). In an intermediate step, shown in Figure 2.11(b), the pore is now located at a GB and has a lenticular shape. Finally, the pore becomes spherical and is trapped in the grain, as the grain boundary moves away.

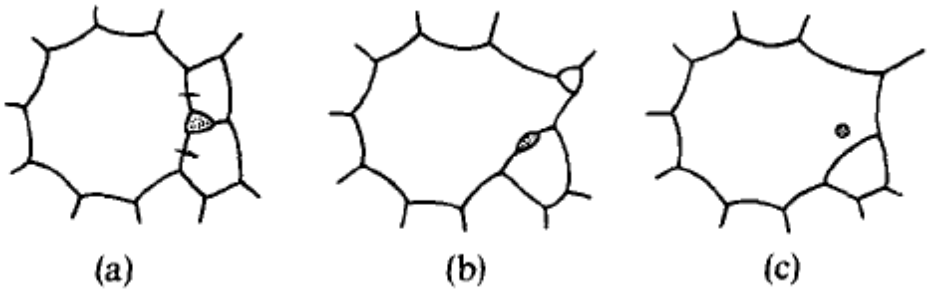

Figure 2.11. Pore motion due grain coarsening. (a) The initial pore, colored in gray, is located at a triple junction. (b) The larger grain grows, ripening one of the smaller neighboring grains. (c) The larger grain continues growing and the pore is left behind by the moving GB [39].

Pores can be left behind by the moving GB, or migrate with it, gradually agglomerating at grain corners [32]. In the case of solid-state sintering, porosity acts as a pinning phase and the interactions between GBs and porosity play an important role during grain growth and densification [47].

Several authors [33, 39] have proposed models for GB-pore interactions to determine when the pore is going to be dragged, stay behind or pin the boundary, especially at intermediate sintering stages, where pores are still open and connected forming channels at triple junctions. In general, pores slow down the GB motion as they pin the GBs. The attached pore reduces the total GB energy and can control grain growth kinetics of the sintering process. The interaction between the porosity and the moving GBs can be described as

retarding pressure on the GBs and a pulling pressure for the pores during GB migration. The tension will reach a maximum value, when the pores are immobile and will drop to zero if the GB breaks free [39].

Figure 2.12 shows some sequences of possible GB-pore interactions, proposed by Svoboda et al. [48]. In their research, different scenarios of GB-pore interactions were simulated changing variables such as dihedral angles, drag angle, pore size and pore and GB mobility. Their results indicated that three-dimensional pores, that are highly mobile and located at the GB, will follow the GB (Figure 2.12 (a)); while pores with low mobility will detach from it (Figure 2.12(b)). However, if the pore reaches a critical value, the pore is not able to follow the GB and separates from the GB. After separation, the pore gradually assumes its equilibrium spherical shape within the grain. Another possibility, as shown in Figure 2.12(c), for low dihedral angles and high GB mobility, is that the pore dissociates in two parts: one is left behind and one travels with the GB. Moreover, the results for the simulations of GB-pore interaction of two dimensional pores indicates that the pores will not detach and can reduce the grain coarsening rate if the pore mobility is low [48].

(a)

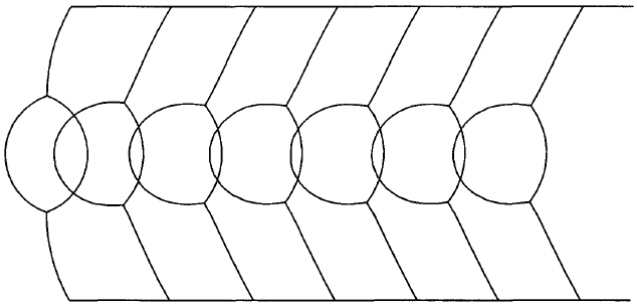

(b)

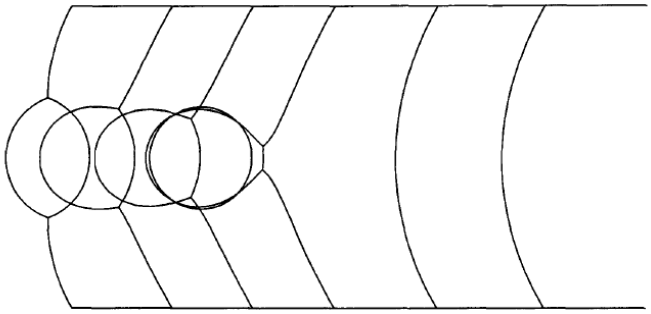

(c)

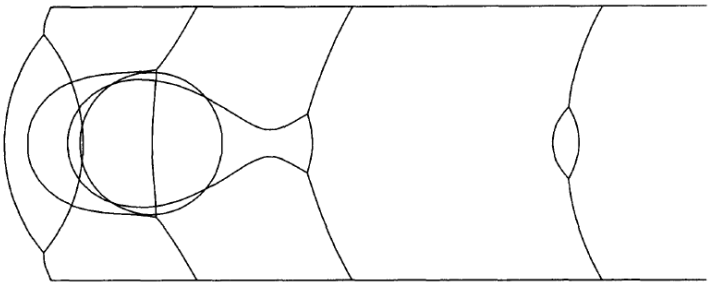

Figure 2.12. Possible GB-pore interactions: (a) the pore stays attached to the moving GB; (b) the pore is left behind by the moving GB and; (c) the pore is decomposed in two parts as the GB moves [48].

As the GBs moves grains start to grow and grain coarsening occur. Pores can decrease the GB mobility as they can be dragged by the GBs, pores also can pin the GBs and inhibit or decrease the grain growth. Coarsening is inherent in all systems consisting of grains of varying size; during heating the grains coalesce and coarsen by diffusion, such that the

smaller grains are consumed by the larger grains as the system moves toward a lower interfacial energy [36].

Moreover, grain growth and coarsening can be affected by the distribution and location of the pores. Figure 2.13 shows the evolution of a simulated microstructure with a non-uniform porosity distribution. The results suggest that if the microstructure includes areas with non-uniform distribution, the grains located at the pore-free region will grow faster than the grains located in the porous region, creating abnormal grain growth. [49]

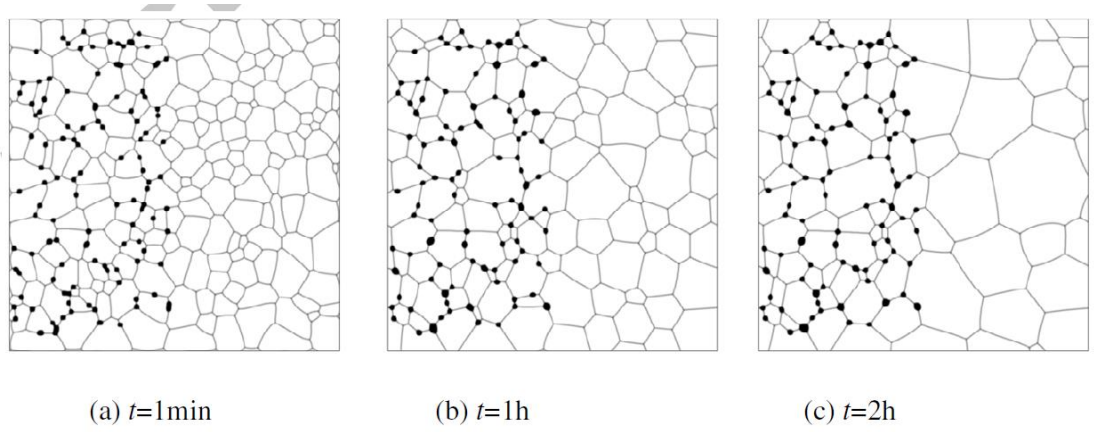

Figure 2.13. Snapshots of the microstructure evolution of porous UO_2 at 1727°C with non-uniform pore distribution.[49]

During coarsening, the grain structure converges to a self-similar character in grain shape and size distributions. The grain size increases while the number of grains decreases. Sintering densification is dominated by transport along the GB, while simultaneously transport across the GB and pore drag occurs in order to give grain growth [36, 46].

Coarsening is driven by an energy difference across an interface, where the interface might be a GB, liquid film, second phase, or pore. Grain growth occurs by both diffusion and

coalescence events. Coalescence occurs when two grains come into contact with a low degree of crystallographic misorientation and fuse to form a single grain, as seen in Figure 2.10(b). In general, coalescence is favored when the misorientation angle between adjacent grains is less than 10^0. Coalescence is also favored by large grain size differences, where the larger grains absorb the smaller grains. Grain coarsening can also be driven by differences in composition, strain, and crystal structure [36]. Therefore, grain coarsening can be affected by the GB crystallography, which could explain why some grains grow more than others, but how exactly? Is it just the GB crystallography or is there something more that differentiates one GB from another? And, how do the sintering conditions affect the different GBs?

Dillon et al.[50] studied the mechanism for the development of anisotropic GB character distributions (GBCD) during normal grain growth of magnesia-doped alumina and yttrium aluminum. Figure 2.14, shows the configuration of the different triple junctions used in his simulations. Their results indicate that, on average, the GBs with lower energies tend to grow, while the GBs with high energies tend to shrink. These findings suggest the development of an anisotropic GBCD due the disappearance of higher energy GBs as well as an increase of the length and population of lower energy GBs during grain growth. However the proposed mechanism only applies for normal grain growth. Although microstructures with abnormal grain growth or recrystallization due plastic deformation due tent to have anisotropic GBCDs is not obvious that GB energy is the only deciding factor in which GB will grow or shrink.[50]

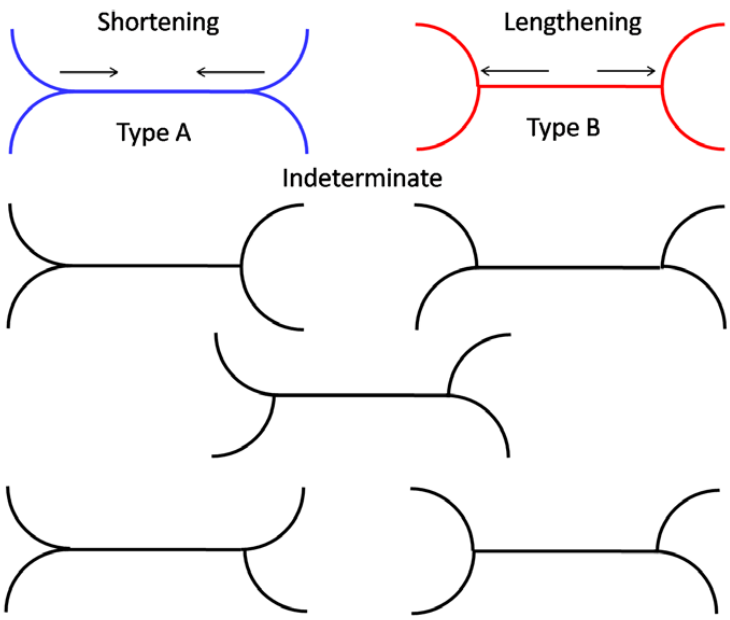

Figure 2.14. Schematic of seven different GB topologies based on the curvature of the adjacent GBs studied by Dillon et al. When all 4 GBs are concave (Type A) the central GB will decrease in length (shortening), if all 4 GBs are convex (Type B), the central GB will increase in length (lengthening), in all the other cases is uncertain how the GB will evolve. **[50]**

Furthermore, the current trend in the literature indicates that energy anisotropy has a measurable effect on the misorientation texture development while GB mobility anisotropy does not [51-54]. Most of the proposed models for anisotropic GBCD are based on the model developed by Holm et al. [55] where low angle GB increase by lengthening (Figure 2.13) not proliferating and; microstructures with strong texture and highly curved GB tend to shift to low angle GBs. In the model, the increase of the length on the low energy GBs is driven by certain requirements of interfacial equilibrium at triple junctions. Based on this model, Gruber et al. [52] developed a model for the evolution of the misorientation

distribution during grain growth. The model proposes a critical event mechanism based on triple junction dynamics. The amount of GB with a specific GBCD changes only by discrete topological events in the GB network, and is related to the geometry and configuration of the triple junctions. Therefore, a full characterization of the GBs of the fuel is needed as the initial fuel microstructure can affect its evolution during fission, as grain growth seems to be affected by its GBCD.

General details on the microscopic scale of sintering have already been described. However, the next section will describe some of the sintering parameters during processing of fuel pellets such as atmosphere and temperature. Variations on these variables can affect the microstructure of the final product and modify the fuel's performance.

2.2.4. Fuel pellets sintering

Fuel pellets for light water reactors are usually sintered in a reducing atmosphere at temperatures of > 1750 ^{0}C [56]. Several attempts to lower the sintering temperatures and increase the fuel density have been made [8, 9, 28, 42, 44, 57, 58]. Deviations from stoichiometry favor faster sintering kinetics, i.e., the higher the oxygen content, the lower the temperature required to obtain certain density [44]. The sintering process is controlled by the diffusion rate of the uranium atoms, as $D^o/D^u > 10^7$, for any value of x or temperature [59]. Additionally, the lattice diffusion coefficient of U in UO_{2+x} increases proportional to x^2 [9]. Consequently, the rate of the uranium ion diffusion will control the sintering process. Assmann et al [9] studied several sintering paths, as shown in Figure 2.15. The excess oxygen can come from an initial addition of powders from an oxygen rich phase (U_3O_8 or U_4O_9) and a reducing atmosphere during cooling can be used to control the final pellet

stoichiometry. The addition of the second phase can also create a bimodal distribution of grain size, as the oxygen rich grains will grow larger due the enhanced U diffusivity. A bimodal distribution of grains has the advantage of a mixture of larger grains that can retain the fission gases, and smaller grains, with better structural properties. This type of microstructure could increase the fuel's life and lead to lower sintering temperatures, decreasing the costs.

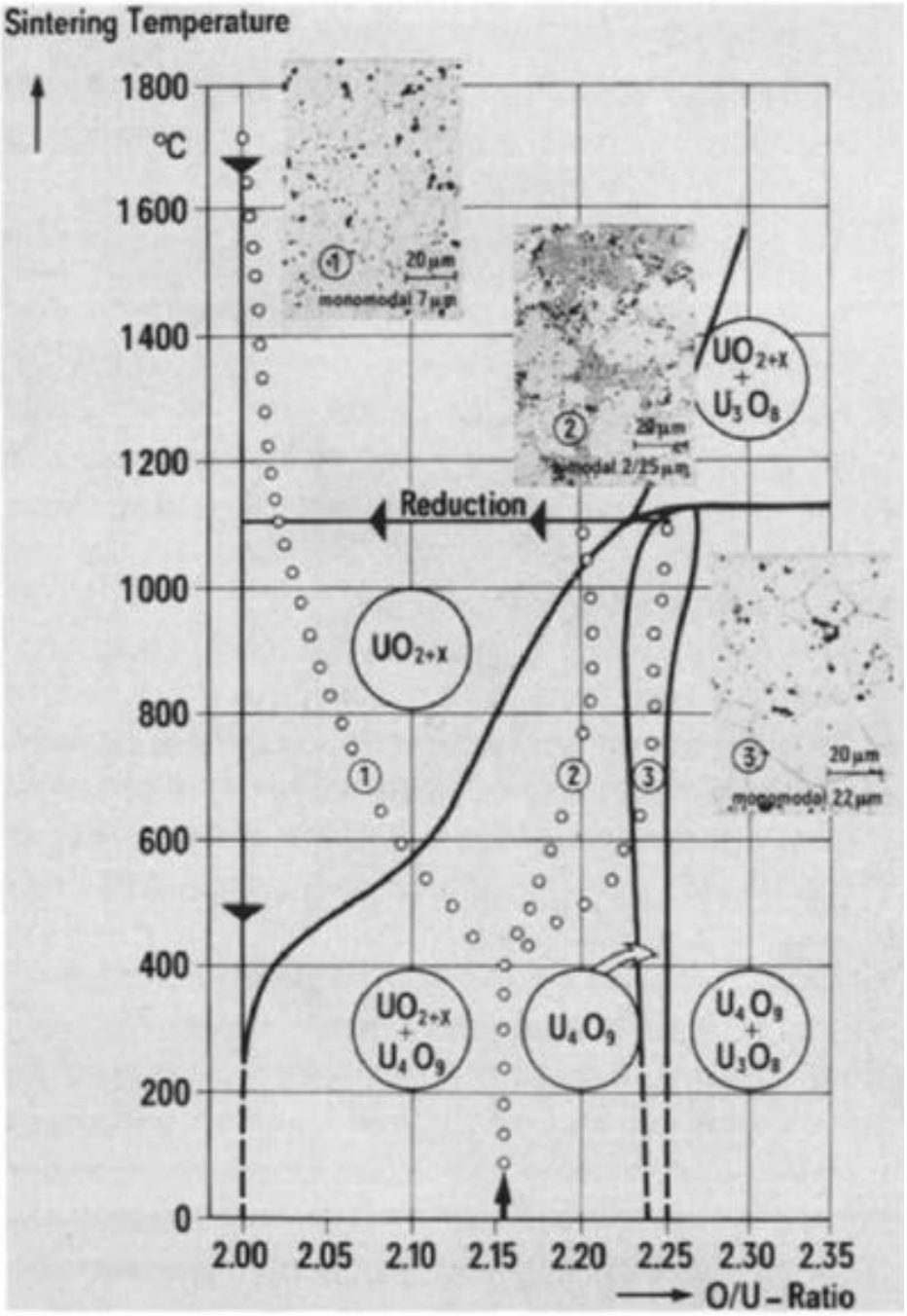

Figure 2.15. Sintering paths and microstructures in the U-O phase diagram studied by Assmann et al [9]. Microstructural changes are observed depending on the initial stoichiometry and phases present on the sample. All the samples were reduced during the cooling stage to obtain nearly stoichiometric samples.

Another method to reduce the sintering time is to introduce oxygen in the sintering atmosphere to create an oxygen-rich environment and promote densification enhancing the uranium diffusivity. An example of this approach is shown in Figure 2.16: pellets were sintering under a reducing atmosphere (hydrogen) and under two neutral atmospheres (nitrogen and argon), with small traces of oxygen; with an initial O/U of 2.18. Densification at 1300 ^{0}C was clearly higher at the neutral atmospheres, compared to the reducing atmosphere. There was some reduction of the pellet sintered under a reducing atmosphere, decreasing the uranium atom mobility. Therefore, the sintering atmosphere also plays a key role during sintering [44].

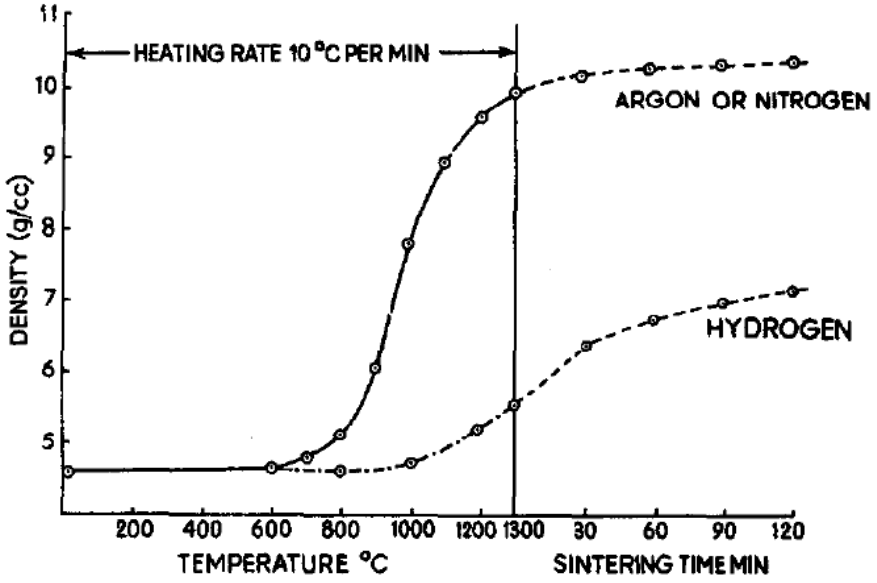

Figure 2.16. Plot of density vs. temperature and sintering time for $U_{2.18}$ pellets, sintered in argon, nitrogen and hydrogen atmospheres [44].

Recent data show that sintering under more aggressive atmospheres and using different gases during sintering, including dry air at the sintering temperature and a reduction to stoichiometric UO_2 in hydrogen, can enhance the grain growth and reduce the sintering temperatures [33], as shown in Figure 2.17.

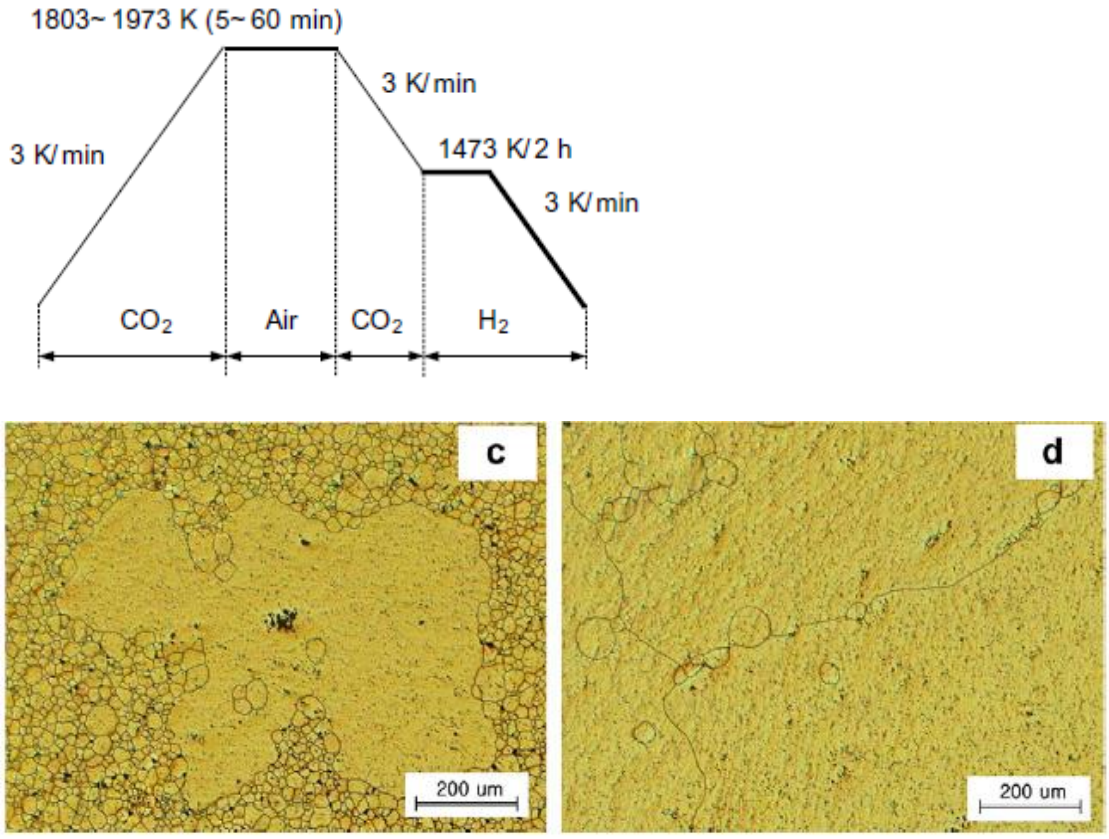

Figure 2.17. Sintering curve proposed by Joung et al. to obtain single or large sized UO_2 grains. The microstructure shown in (c) was sintered for 6 min in air and (d) for 8 min in air [40].

Working at temperatures just below the UO_2+U_3O_8 region and using an oxygen rich atmosphere, the grain growth is enhanced and microstructures with larger grains, even

single grains, can be obtained. Even though some grains are evidentially growing more than others, grain and GB crystallography are not discussed in any of the papers reviewed above; only the experimental procedures and results are described, on how to manufacture pellets with certain grain size distribution. If grain coarsening depends on the GB crystallography: Are some GB then moving faster than others, therefore creating larger grains? If so, which ones and why?

The enhanced densification and grain growth can be explained from the kinetics point of view. However, there is contradiction in the literature regarding the mechanism during the initial stages of sintering. Some authors' results indicate that the controlling sintering mechanism is volume diffusion of the uranium ion [60], while others suggest that is GB diffusion [61]. Therefore, a wide range of activation energies for the initial sintering stages (84 kJ/mol-420 kJ/mol) are reported in the literature [20, 41, 62]. An explanation for the large scatter on the data could be a result of the difficulty on the measurements and control of the stoichiometry. Reduction on pellets sintered under neutral atmospheres has been reported and, for most of these papers, only the initial O/U was reported, which could explain in part the variability on the data. Also, as previously described, the defect model for the hyper-stoichiometric urania lattice includes slightly displaced interstitial oxygen and uranium atoms. The sudden jumps on the activation energies, shown in Figure 2.18, could be explained due the defect model and how the atoms accommodate in the lattice, depending on the oxygen content and the type of oxygen defect that is active.

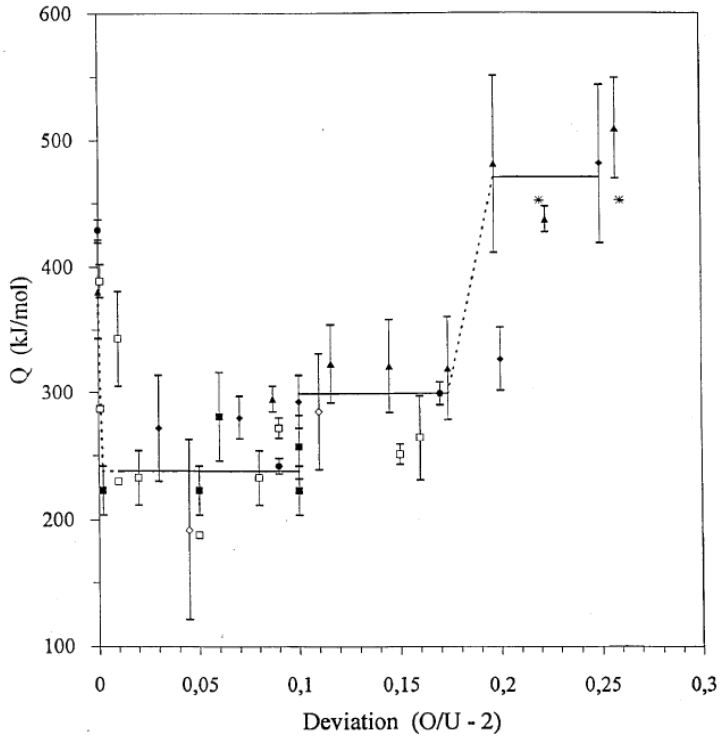

Figure 2.18. Activation energy data for various stoichiometries. The plot is a compilation of values reported in the literature using different methods by various authors [63].

Regarding the final stages of sintering, there is not much information available on the activation energy for grain growth that relates the stoichiometry with the grain growth kinetics and the values range from 40 to 107 kcal/mol depending on the stoichiometry range [43]. These data are of critical importance to model in-pile behavior, since the fuel increases its density during the initial stages of fission and data are needed to simulate this behavior as a function of O/U.

Moreover, once the fuel is introduced in the reactor and fission starts, the initial microstructure of the fuel continuously changes due the fission induced densification, resintering and formation/evolution of bubbles. This, in turn, affects the fuel's thermal

conductivity among other properties [64]. Hence, the in-pile pellet densification will depend on the initial porosity content, grain size as well as the fission rate. The grain size and porosity distribution can be controlled by variations on the processing conditions such as initial powder stoichiometry, atmosphere [65] and sintering temperature [66]; while the fission rate will depend on the reactor operation conditions. Microstructures with different grain sizes and stoichiometries can be studied to understand how the fuel will behave inside the reactor and evaluate properties at different stages during fission.

More details on the in-pile microstructural evolution will be described in the next section.

2.3 Restructuring and grain growth in-pile

Once the fission process starts, the pellet experiences a large thermal gradient due to its low thermal conductivity (3000 ^{0}C/cm is a common value [67]). Characteristic microstructural changes then occur by thermally driven processes. The immediate effect of the steep thermal gradient is that the pellet cracks radially under thermal expansion stress, increasing the total exposed surface area [67]. Additionally, further sintering and significant grain growth has been observed above 1500 ^{0}C. Equiaxed grain growth is expected up to around 1800 ^{0}C and at higher temperatures radially aligned columnar grains are formed[16, 67]. The extent of these changes will depend on the temperature and duration of the irradiation process; Figure 2.19 shows an example of a temperature profile for a fuel pellet.

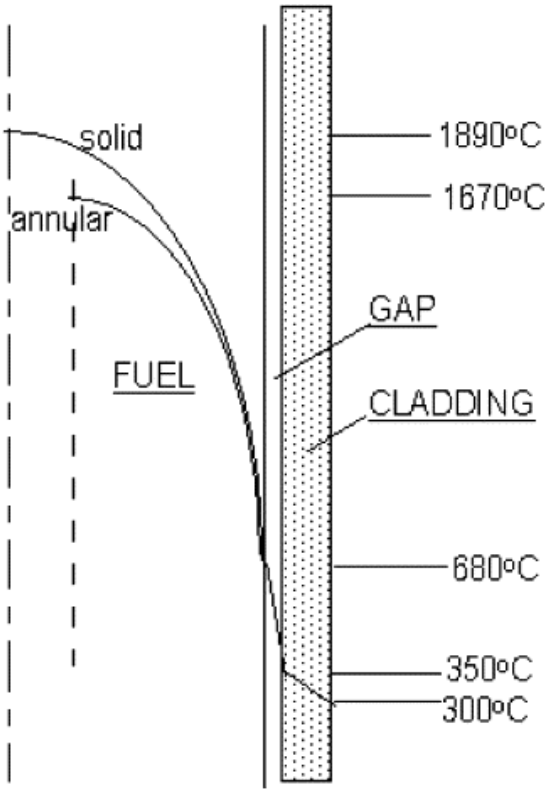

Figure 2.19. Radial Temperature distributions in solid and annular fuel pellets. Linear power: 350 W/cm; gap thickness: 50 microns; fuel diameter: 10 mm; central hole diameter in annular pellet: 2 mm; gap gas: 20% xenon, 80% helium [68].

The initial porosity in the pellet plays a key role during this process, e.g., the equiaxed grain growth can be hindered by GB pinning, especially at triple juntions. This is a diffusion-controlled process where columnar grains are formed by an evaporation-condensation mechanism within pores or gas bubbles. Due the temperature gradient along the pellet's radial direction, UO_2 is evaporated on the hot side and condensed on the cold side. The pores are moving up the temperature gradient and leaving behind columnar grains. During this process, the pore changes in size and shape, becoming lenticular, 10-

150 μm in diameter and about 20 μm thick in the radial direction. The average density and grain size of this columnar grain region is appreciably greater than the initial grain size [67] and a void is formed in the center of the pellet as a result of this process, as seen in Figures 2.20(a) and (b) [16].

Initial microstructural parameters such as pore size, shape, distribution, connectivity as well as the location of the pores, grain size and distribution, as well as the GB character and how the GB are connected will in turn affect the in-pile evolution of the fuel. Current fuel performance codes, for instance MARMOT and BISON multi-scale models (implemented at Idaho National Laboratory), are slowly taking into account microstructural features such as porosity and grain size distribution [70-72]. However, the models only use either mono-modal or bi-modal porosities (based on experimental data) that are randomly located in the microstructure. This approach is not entirely accurate as pores with different size and shape, tend to locate at preferential sites [6]. As mentioned before, pores can pin GBs affecting the grain growth, also in-pile recrystallization starts at GBs and large pores [73].Therefore, statistical data are needed to relate porosity shape, size and location on the un-irradiated fuel as initial inputs for more precise models; as the in-pile evolution of the microstructure and the fuel's properties will be affected by these parameters.

(a)

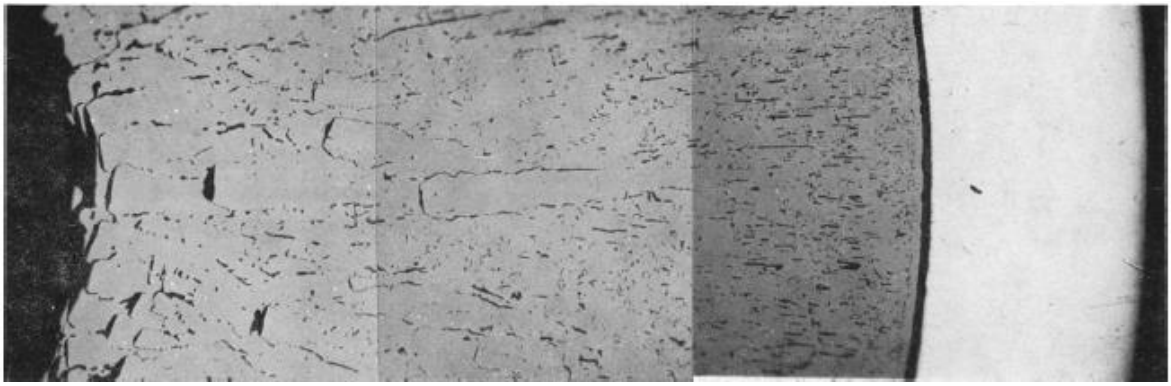

(b)

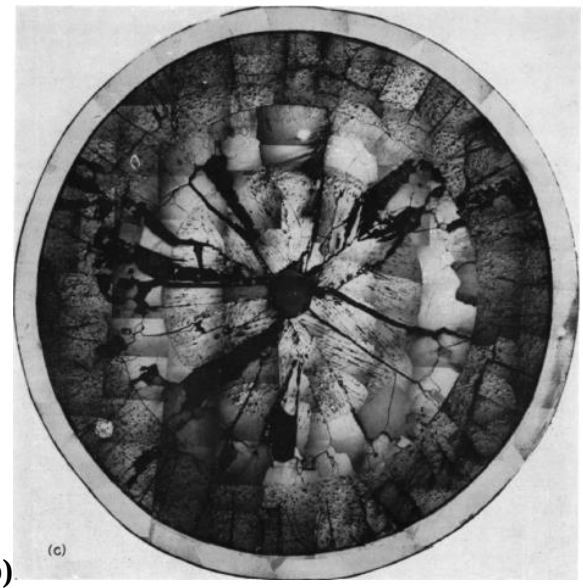

Figure 2.20 (a) Cross-section of a UO_2 sample (80X) irradiated at high temperatures, note the pore migration to the center of the pellet [69]; and (b) polished and etched pellet showing central void, porous core, columnar grain annulus and outer unchanged region [67] .

Furthermore, the way the GBs are connected in a network will affect how the pores, gas bubbles and GBs will move. The literature suggests that pores of certain size and shape tend to locate at certain preferential sites (Triple junctions, GBs, grains) and that pores

migrate to high energy GBs to minimize its surface energy. But there is not much information on how these parameters are related. These data can be used again as inputs for fuel models.

So far, we have mentioned that abnormal grain growth could be related to the GB crystallography, but we have not explained why. The next section explains what is a GB and how some GBs can be classified as special. These concepts are very important as GBs and pores play a key role on the precipitation and release of the fission gases, as it will be described in section 2.4.

2.4 Grain Boundaries (GBs)

A GB refers to an interface where the long-range translational symmetry of a crystal abruptly changes [74]. Essentially, a GB is a bi-dimensional medium that separates two adjacent crystals [75]. The two adjacent grains are related by a rotation axis and meet on a 2-D surface, which may be plane or curved. Even though the rotation axis is fixed for a given boundary, there are different ways to obtain the same GB. If we consider two identical grains; fix one and rotate the other about any axis. Cut each crystal parallel to a particular flat plane in space and join the grain at this plane, the plane is the GB. Then allow the atoms to relax to a low energy configuration, which might not be the minimum energy [35]. As different symmetry operations (tilt, twist, twin and mixed) can be used to obtain the same GB, a more specific description of the GB is needed to describe it.

Therefore, to fully describe a GB, 8 degrees of freedom (DOF) should be specified. These DOF include 5 macroscopic ones and 3 microscopic or translational ones. The macroscopic DOF consist on two crystallographic vectors and one rotation angle, i.e., the normal to the

symmetry dividing plane and the rotation axis-angle pair that describes the GB misorientation. The remaining three DOF are necessary to describe the atomistic level geometry of the GBs, and are given by a translational vector [14, 74].

As the GBs are structural discontinuities, the disorderliness of the structure increases as the misorientation between the neighboring increases. The Read and Shockley model[74] is used to describe the low angle GBs, an example of low-angle GBs is shown in Figure 2.21. This is a theoretical model that quantifies the disorderliness due the mismatch of the atomic bonds at the GBs. Low angle GBs can be interpreted as planar defects that consist of a periodic array of dislocations. If the dislocations are parallel arrays of edge dislocations, then the GB is called a "tilt" boundary. While, hexagonal or square networks of screw dislocations are called a twist GB [74]. In general, the GB energy increases monotonically with misorientation and levels off at a maximum value at around ~40^0 as seen in Figure 2.22.

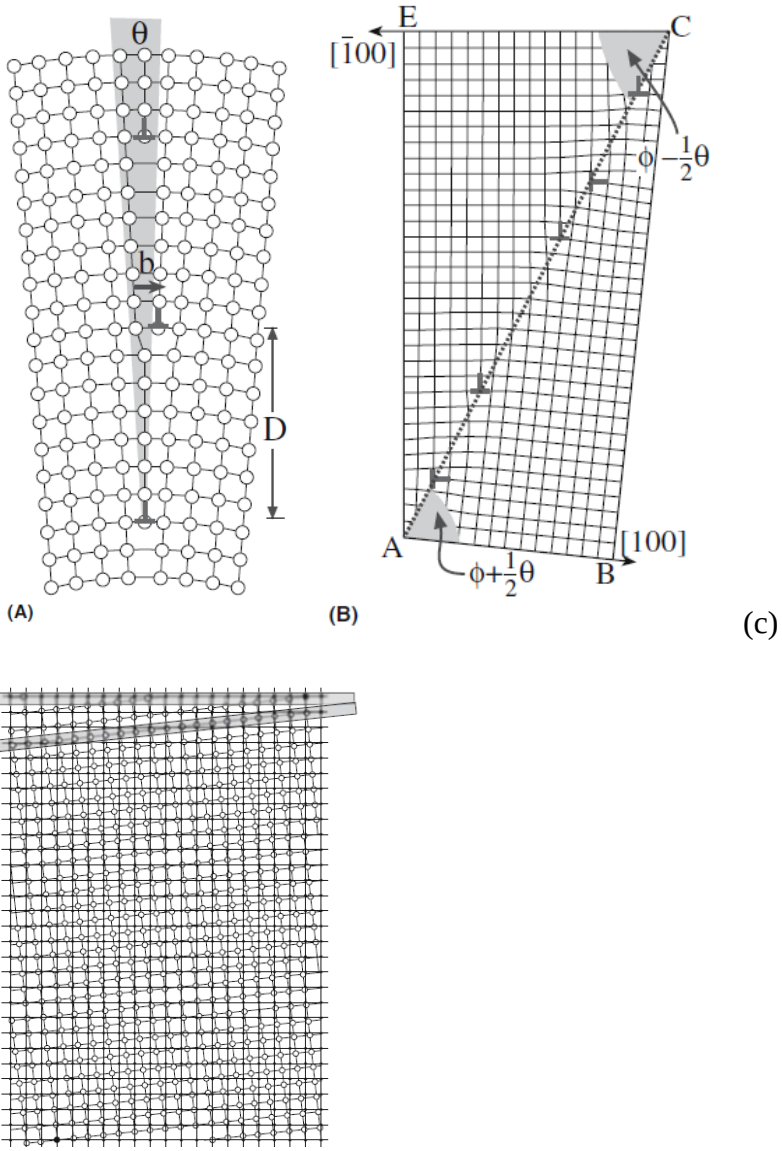

Figure 2.21 Schematics of low-angle GBs: (a) Tilt symmetric, (b) Tilt asymmetric and (c) twist [35].

[14].

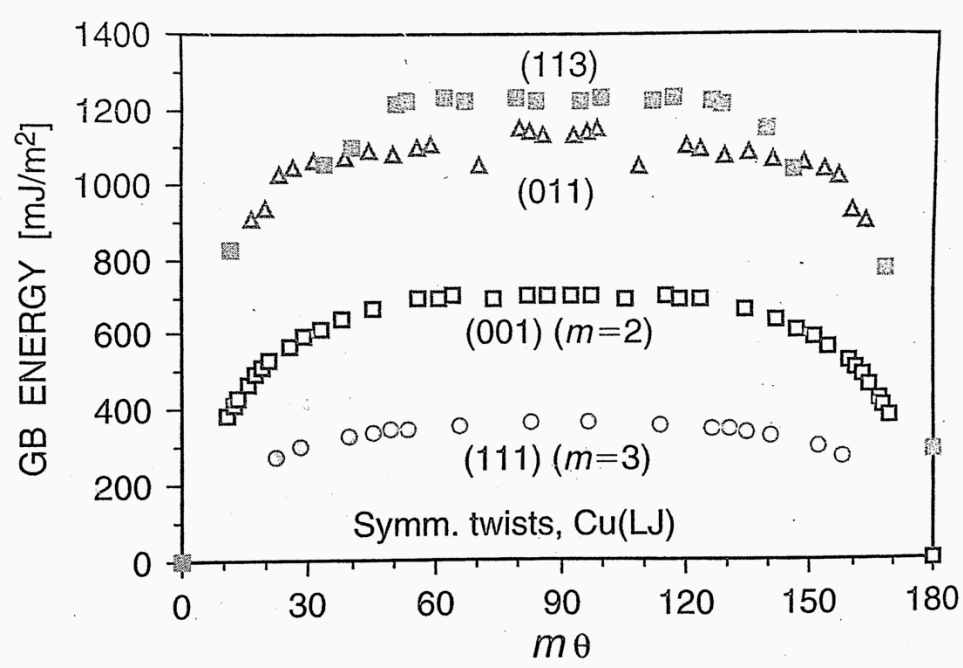

Figure 2.22. Simulated energies of twist boundaries on the four densest planes of the FCC lattice[14]

As the GB misorientation angle increases, there is an overlap of the dislocation cores when the misorientation exceeds the 10^0-15^0 range, and GBs with misorientation angles higher than this are called "high angle." There are also models to describe specific GBs, such as the coincidence site lattice (CSL) model. The CSL model determines the basic periodicity of the atomic structure of the GB core region. The coincident lattice can be constructed by translating two adjoining perfect crystal lattices with respect to each other (without any rotation) so their atoms coincide at one point. The space at which the atoms coincide is the CSL. These GBs have an appreciable amount of order or crystallinity, as seen in Figure 2.23 [76]. The reciprocal density of the CSL sites is denoted by the coincidence index, $\sum$, and is often used as geometric parameter characterizing the structure/property relationships

at the GB. The coincidence index is an odd integer equal to the ratio of the volume of the CSL to the lattice cell volume [74].

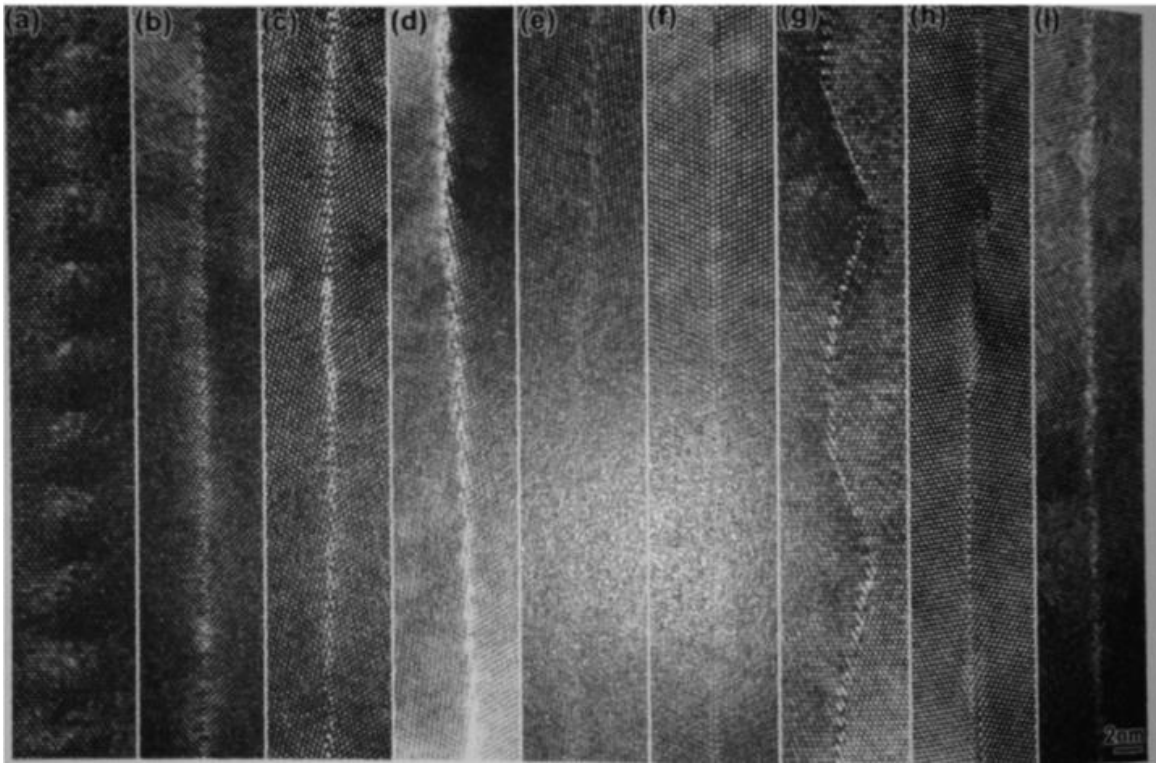

Figure 2.23 HRTEM images of symmetrical tilt CSL boundaries in yttria-stabilized zirconia. Misorientation angle is between {100} surfaces and the common axis {110}: (a) 5.0°, (b) 20.0° (c) 39.0° (Σ9, {221}), (d) 50.4°(Σ11, {332}), (e) 60.0°, (f) 70.6° (Σ3, {111}), (g) 109.4° (Σ3, [6]), (h) 129.6° (Σ11, {113}), (i) 141.0° (Σ9, {114}) [74],

Additionally, some GBs are called “special” and involve the densest lattice planes and the smallest planar unit cells, these characteristics are usually associated with energy cusps in the phase space, as seen in Figure 2.23. Most of these “special” GBs are associated with special misorientations including lower values of ∑. However, not all the low ∑ GBs are

special, Figure 2.24, shows the experimentally determined energies of <110> symmetrical-tilt GBs in Al near its melting point. As seen in the figure, the GB energies for the same ∑ boundaries change depending on the GB crystallography. For instance, the energy for ∑3 boundaries at 70.53^0 is smaller than the one at 109.47^0. The first ∑3 corresponds to a {111} boundary plane and is the densest in pure metallic FCC crystals, while the latter is [6] ∑3, which is a more open structure.

These results indicate that CSL denomination alone is not enough to describe and characterize a GB, as the CSL model does not include information on the GB crystallographic planes.

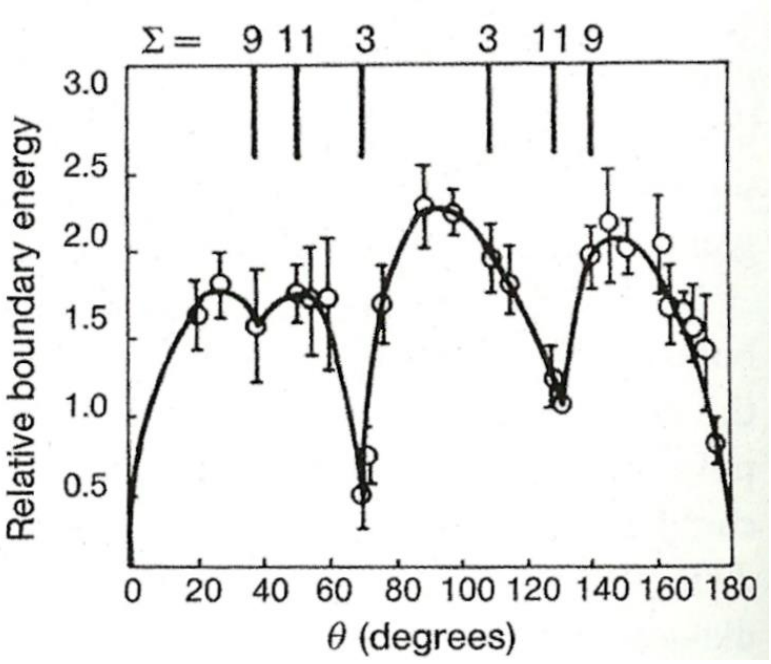

Figure 2.24. Experimentally determined GB energies of aluminum as a function of misorientation.[74]

The difference on the GB energies can be explained schematically by Figure 2.23 and 2.25. In the case of Σ3 GBs (Figure 2.25), although in both cases the coincidence site occurs in every three lattice points, therefore having the same ∑, the size and configuration for each case is different. The ∑3 {111} (70.53°) boundary (Figure 2.25(a)), is the densest for pure FCC crystals, while the ∑3[6] 109.47°) boundary (Figure 2.25(b)) has a more open structure [74]. Therefore, the plane normal is also needed to fully characterize the GBs. Nonetheless, CSL boundaries in general are usually associated with anisotropy in the interfacial energy [74], as seen in Figure 2.24 and are worth to take in account as a preliminary step of the GB characterization.

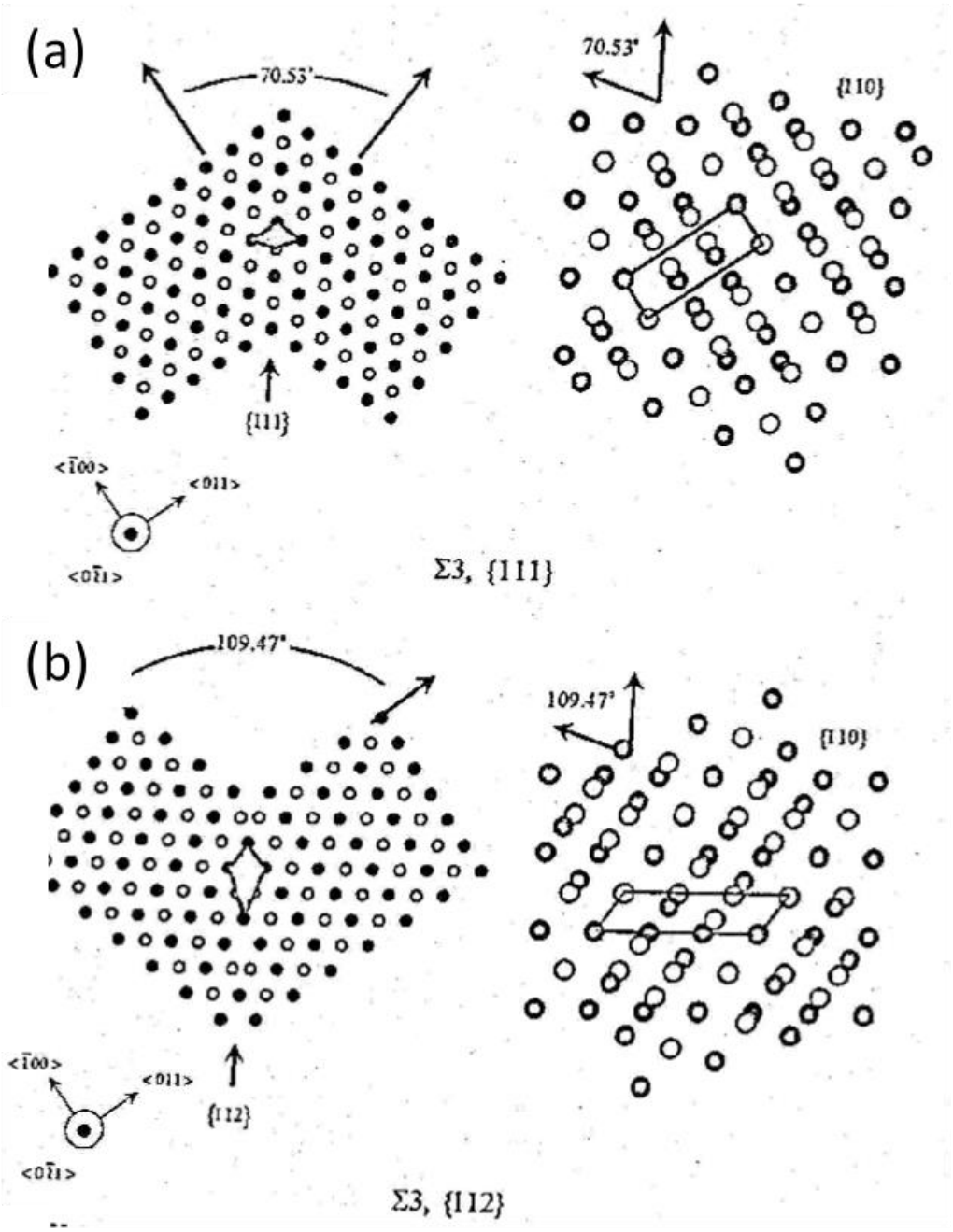

Figure 2.25. Schematic illustrations of (a) ∑3, {111} (70.53°) and (b) ∑3, [6] (109.47°) CSL boundaries occurring in the <110> symmetrical tilt (left side) and twist (right side) boundaries. The demarked region represents the repeating unit of each boundary [74].

Moreover, the GB structure and physical behavior controls many of the thermal, mechanical and electrical properties of polycrystalline solids. The evolution of the microstructures under the driving forces of temperature and stress is controlled by the dynamical behavior of the GBs. A polycrystalline structure usually includes a combination of high angle, low angle and special GBs [14]. In general, the atomic structure of high angle GBs is characterized by a complete overlap of the GB dislocation cores, creating a mostly continuously distributed type of structural disorder along the interface and a GB energy that is entirely independent of the GB misorientation. However, for high angle GBs that have the lowest plane-density of a given lattice, i.e., {111} in FCC crystals, where there is relatively little structural disorder, there is a rather low GB energy, as seen in Figure 2.25. High-angle and high-energy GBs have very high mobility and diffusivity, making them play a possible rate controlling role in many high temperature properties.

Furthermore, molecular dynamics studies in yttria-stabilized zirconia conducted by Fisher et al. [77] concluded that the tilt $\sum 5$ (310)/[001] and $\sum 13$ (320)/[001] GBs reduce the overall ionic conductivity, while the $\sum 5$ (111) 60^0 twist boundary is able to support rapid diffusion and increase the total conductivity. Additionally, Nerikar et al. [78], performed atomistic calculations for different UO_2 GB structures and reported significant variations on each studied structure; and concluded that $\sum 3$ tilt boundaries have the lowest GB energy among all the GBs considered in his study, as seen in Figure 2.26. The GB structure will affect how GBs interact with each other and with fission gases.

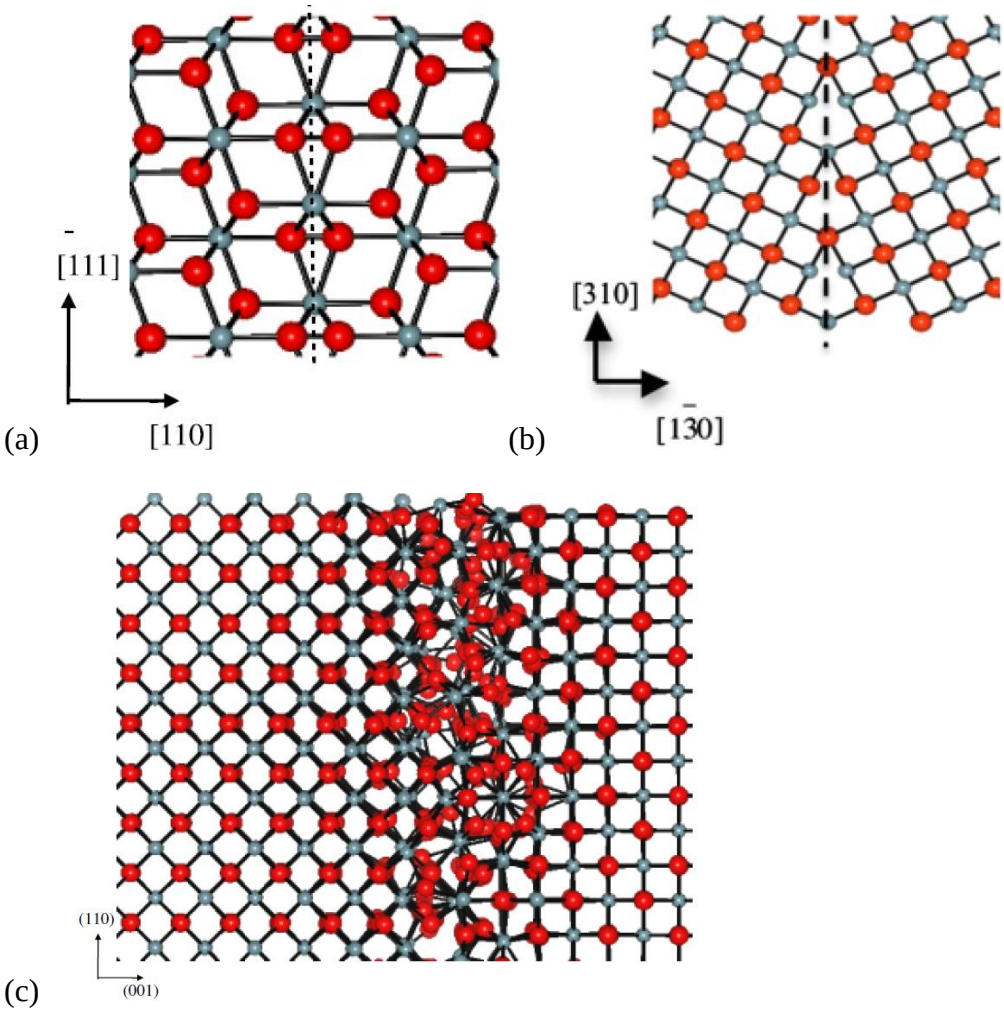

Boundary type	Grain boundary energy (J/m^2)
Σ3 tilt	1.04
Σ5 twist	1.17
Σ5 tilt	1.58
Asymmetric	1.86

Figure 2.26. Structure of (a) Σ3 tilt, (b) Σ5 tilt GBs and (c) relaxed structure of an asymmetric (011)(100)/[100] tilt highly disoriented GB. In addition, GB energies of four GB calculated using the Basak Potential [78] are also shown.

Additionally, GBs are often fast diffusion paths in polycrystalline materials, with diffusivities several order of magnitude greater than that in the lattice [79]. Mass transport along the GBs often controls the evolution of the microstructure and properties of engineering materials at elevated temperatures, as diffusional transport along individual GBs can play an important role [79, 80]. The mass transport of the fission products in a polycrystalline fuel will depend on the whole GB ensemble, as the GB network comprises a spectrum of local boundary diffusivities [79]. In general, increased structural disorder in high-angle boundaries accelerates mass transport, and lower diffusivities have been associated with low CSL boundaries [79] [14].

Moreover, results from microstructurally-explicit finite element simulations of the initial fuel microstructure, indicate that the GB type and location can alter the diffusion paths for fission products [81]. Therefore, a good understanding on the GB type, location and connectivity is needed as the GB network configuration will change depending on how the GBs are linked, changing how the fission products will move along the GB network. Grain boundary data can be very useful to model and manufacture more efficient fuels. For instance, variations on the sintering conditions, such as the fuel's stoichiometry, can affect the GB character, as the oxygen content can affect the GB mobility, which in turn affects the evolution of the microstructure. A preliminary study of the GB character of two depleted urania (d-UO_{2+x}) samples manufactured under identical conditions, but with different stoichiometries (d-$UO_{2.0}$ and d-$UO_{2.14}$) indicates that even though the samples had similar CSL fraction the distribution of the $\sum$ GBs (~20% fraction) as well as the distribution of GB crystallographic normals had significant variations. For example, the sample with lower oxygen content presented a large fraction of GB planes close to the $\sum 3$

twinning planes, compared to the oxygen rich sample. These results suggest that lower energy interfaces might be used to minimize energy in the fuel, potentially due to lower overall GB mobility for the stoichiometric sample [82]. However, more data that include other O/U ratios as well as a larger data set are needed to establish correlations between GB character and manufacturing conditions, such as oxygen content. Understanding how the manufacturing conditions affect the GB character as well as the GB connectivity can help to design more efficient fuels, as the release of fission gases decreases the overall fuel's thermal conductivity, decreasing its efficiency. The experimental data can be used, for instance, as inputs for models to determine how the GB network configuration affects the percolation of fission gases, i.e. as shown by Lim et al [81] (Figure 2.27). Therefore, more efficient fuels that can stand longer burn-ups can be designed.

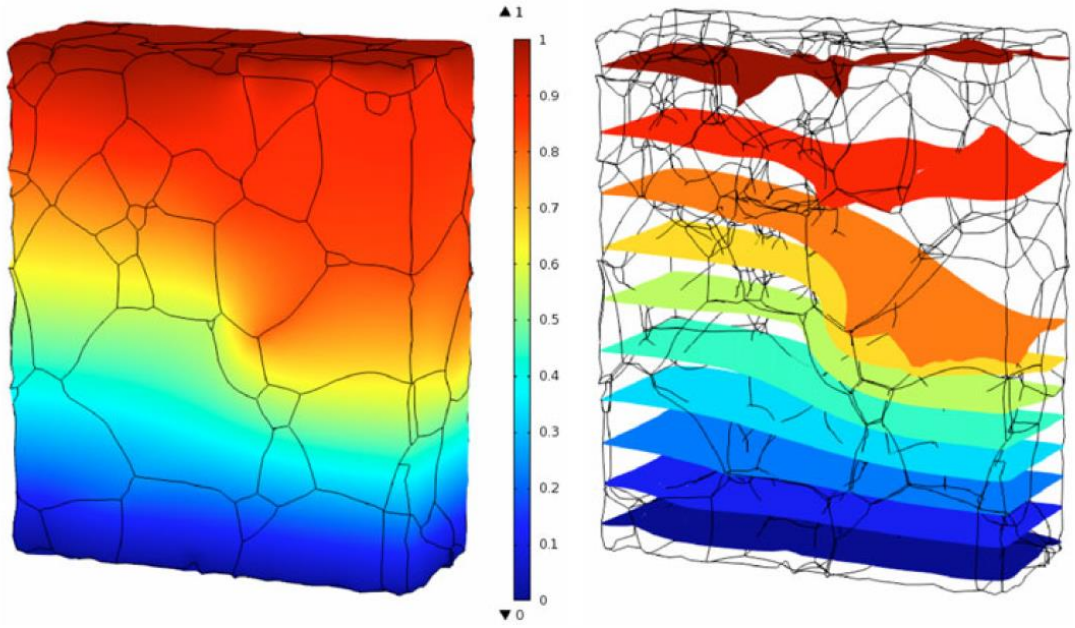

Figure 2.27. Concentration profile under the effect of GB percolation paths and its isosurface plot. Based on the geometry of an actual d-UO_{2+x} microstructure [81].

Once the fuel is introduced in the reactor and fission starts, the microstructure starts to evolve as previously described. The ^{235}U isotopes splits and multiple fission products are generated. Fission products can be solid precipitates and gases. Fission gases play a key role in the evolution of the microstructure as they precipitate as bubbles that are generated inside the grains and segregate to the GBs. The fission bubbles can form interconnected channels where the fission gases can eventually escape, affecting the fuel performance. A more detailed description of some of the fission products will be provided in the next section.

2.5 Fission Products

About 30 stable inert gas atoms are produced per 100 fissions of ^{235}U. Early in life, the fission gases consist of mixture 86 at % xenon and 14 at % krypton. At higher burn-ups, the composition shifts to a higher percentage of xenon due to an increasing amount of ^{239}Pu fissions [16, 83]. Other fission products are: gases and volatile elements (Br, Kr, Rb, I, Cs and Te); metallic precipitates (Mo, Tc, Ru, Rh, Pd, Ag, Cd, In, Sn, Sb, Se and Te), oxide precipitates (Rb, Sr, Zr, Nb, Mo, Se, Te, Cs, Ba) and fission products dissolved as oxides in the fuel matrix (Rb, Sr, Zr, Nb, Ce, Pr, Nd, Pm, Sm, Eu), as seen in Figure 2.28 [84].

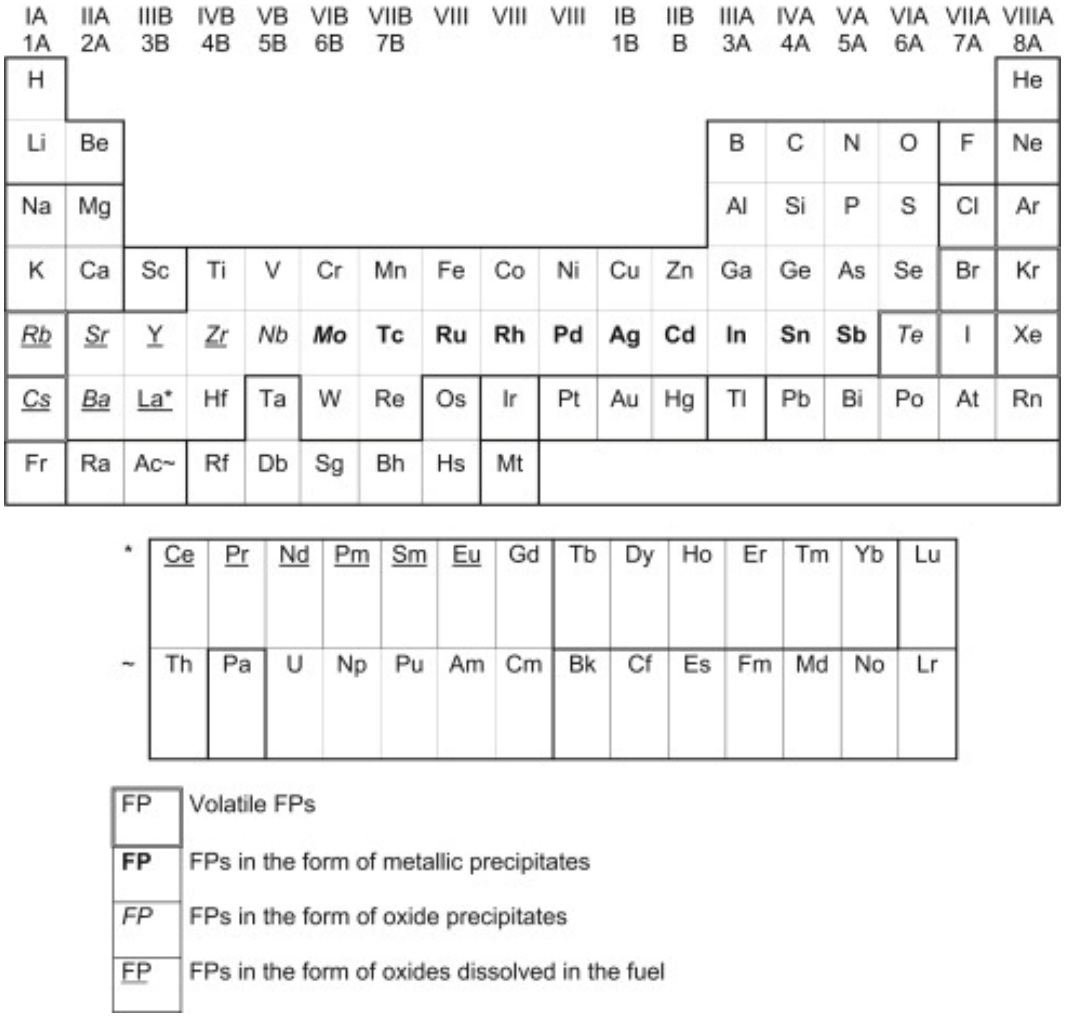

Figure 2.28. Possible fission products [85].

In general, during the incubation period, all gas that arrives to the GBs is trapped locally as seen in Figure 2.29. The intergranular gas concentration increases with burn-up until bubbles are nucleated. These bubbles eventually are interconnected triggering the gas release process [86].

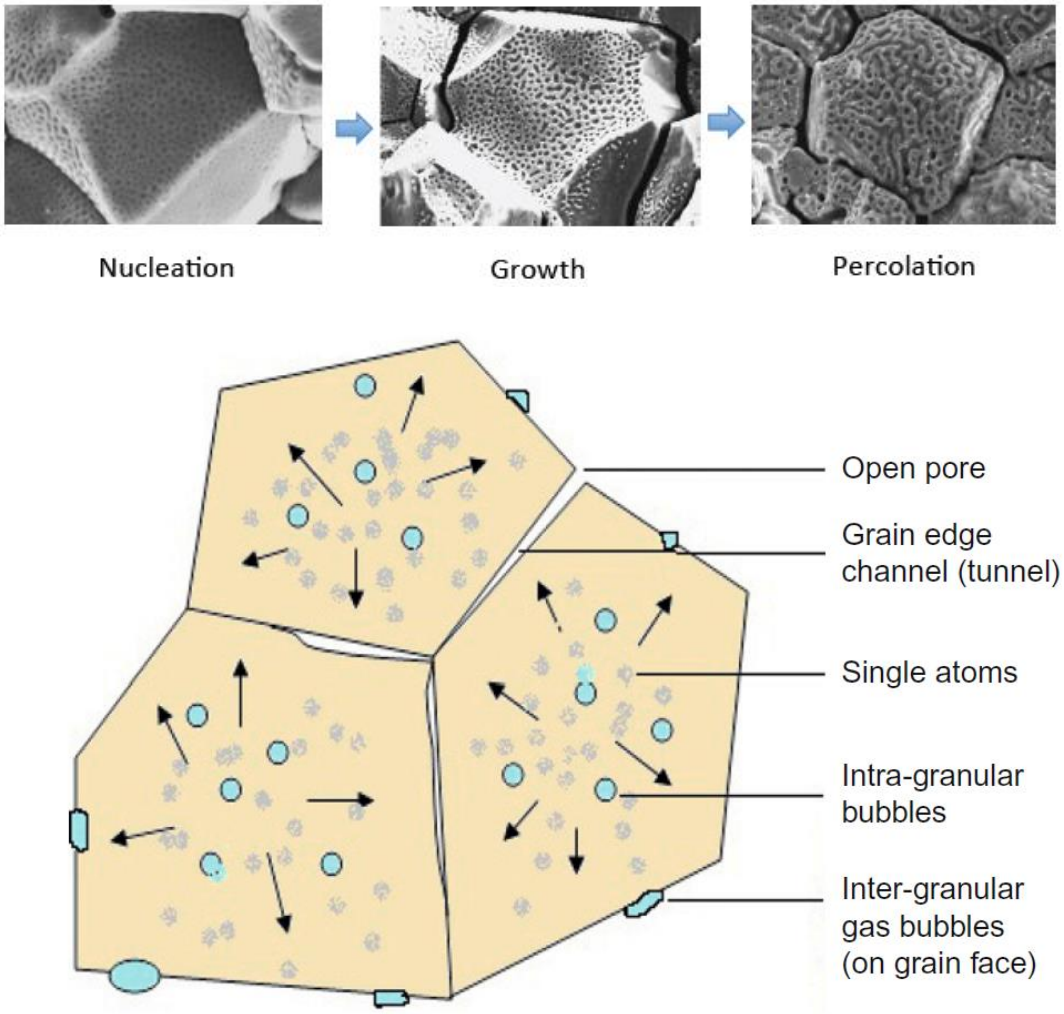

Figure 2.29. Evolution and location of gas bubbles in the irradiated fuel [27, 87].

Fission gas atoms are considered to diffuse via vacancy cluster defects, which consist of one uranium vacancy and two oxygen vacancies. In general, the diffusion coefficients of fission gases are a very pronounced function of damage concentration and the trivacancy effect is less important at higher burnups [25]. The fission gases precipitate forming bubbles that can grow by collecting vacancies from the solid crystal and collecting new gas atoms. The gas bubbles located on GBs or near free surfaces would grow faster than others

due the rapid access to vacancies and the lack of constraint [88, 89]. Bubble diffusivity along a vacancy gradient near GBs has been the basis of a model for fission gas release in transient annealing [90].

As the burn-up increases, more fission products are generated. At low burn-ups, these products migrate to the GBs and all the locally generated fission gases are retained in the inter-granular porosity [84]. Moreover, when a burn-up of ~4.5% is reached, which is the typical peak burn-up target in LWR fuel rods, 1 cm^3 of UO_2 has produced about 16 cm^3 of fission gases [16] and 5-10 at % of fission gases are released [84]. However, microstructural changes such as larger grains, due to different sintering conditions or the addition of dopants such as TiO_2, MgO and Nb_2O_5, can reduce the gas release to up one half [66], increasing the fuel efficiency at lower burnups. Olander et al. [86] examined Xe released from trace-irradiated UO_2 at low burnups, their results indicate that the gas release includes GB diffusion to nucleate and grow at GBs as bubbles. Additionally, atomistic calculations made by Nerikar et al. [78], for different GBs, indicate that some GBs favored segregation more than others. Therefore, a deeper understanding on how sintering conditions affect the initial fuel microstructure is needed as the distribution of GBs in the fuel is then likely to play a role on the tendency for fission gases to segregate to them.

For instance, excessive internal pressurization of the fuel rod (due gas retention) could lead to a reduction of the thermal contact between the fuel and the cladding, increasing the internal temperature and affecting the fuel performance [84], but if the fission gas is released too early, the overall thermal conductivity of the fuel is decreased, decreasing the fuel efficiency. As previously stated, the migration of the gas is related to the GB crystallography; therefore, it can control the fission gas release/retention. Understanding

how the processing conditions can affect the GB character distribution can help develop more efficient fuels where a balance between gas retention/release and swelling can be achieved.

2.6 Role of stoichiometry

Although, there are multiple publications dedicated on how to manufacture samples with certain grain size distribution and composition,there is no experimental data available on how changes on the different manufacturing parameters affect (or not) the crystallography of the pellet. The literature indicates that some of the GBs can have special properties, but there is no data available on how to fabricate samples with these special GBs (if there is a way?).

Section 2.2.4 described some of the "sintering recipes" to obtain nearly stoichiometric pellets. There is a fundamental reason why the pellets need to be stoichiometric, as fission starts the amount of uranium atoms decreases increasing the sample stoichiometry. Therefore, the starting O/M needs to be as low as possible.

The oxidation state in the pellet can affect its chemical properties, as diffusion controlled properties such as grain growth, creep, fission gas release and the behavior of the fission products, as described in section 2.5. The initially near stoichiometric pellet becomes oxygen rich during fission. The extra oxygen atoms can go into a solid solution or react with fission product to produce solid precipitates, with and estimated rate of increase of the average stoichiometry of $\Delta(O/M)=0.0013$ per 1 at.% burn-up [91].

Moreover, local changes on the O/M can affect the concentration of available point defects and therefore affecting the diffusivity of the fission products. Figure 2.30 shows the results

published by Yakub et al. of calculated diffusion coefficients of helium in solid $UO_{2\pm x}$ [26]. From the figure it can be seen that there is a clear relationship between the O/M and the diffusivity of He in the fuel.

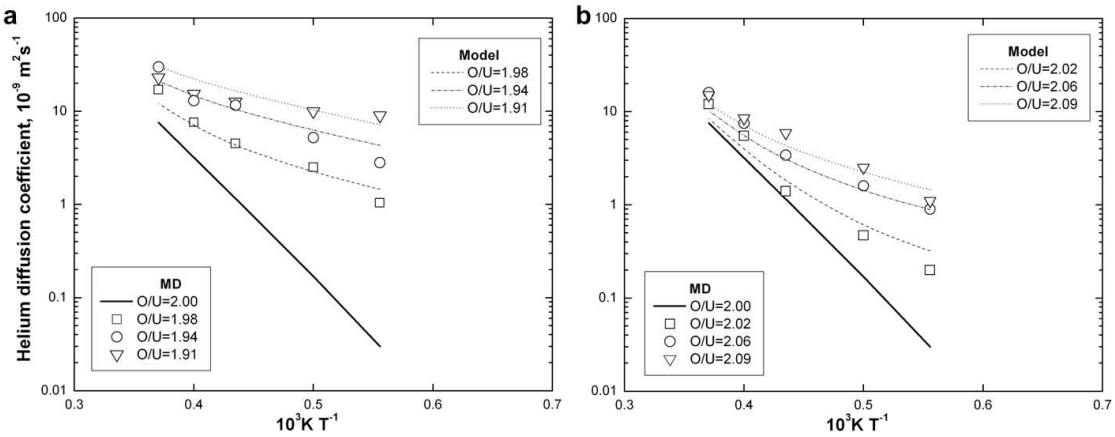

Figure 2.30. He diffusion coefficients computed at high concentration of He atoms for (a) hypo-stoichiometric and (b) hyper-stoichiometric uranium dioxide [26].

Furthermore, the fuel stoichiometry is also affected by the large temperature gradients within the pellet during normal operations, as previously described. The thermal gradients result in a major redistribution of the oxygen atoms by thermal diffusion and local differences in the oxygen and chemical potentials of the fission products in the pellet, as seen in Figures 2.31-2.32 [91].

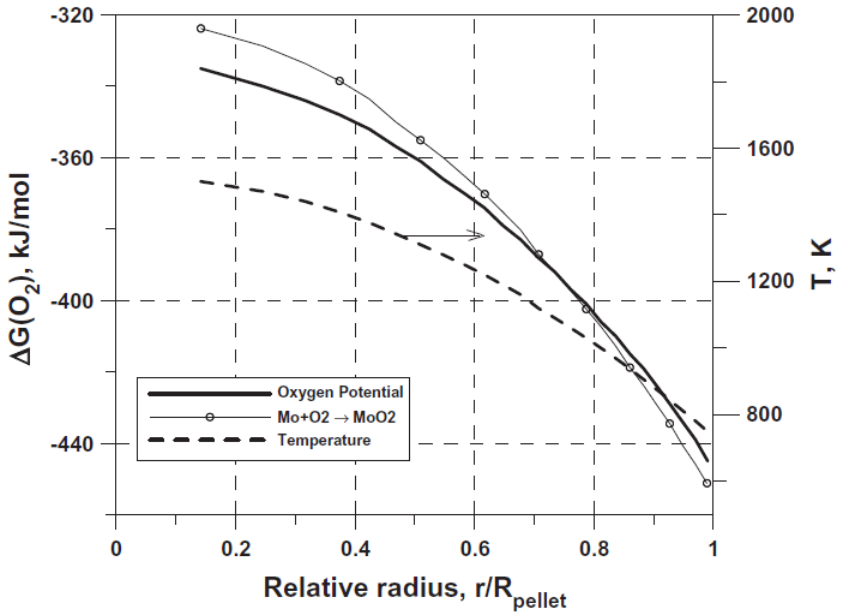

Figure 2.31. Temperature profile and calculated oxygen potential as a function of the radial position in the high burnup region (from 2% to 10%) [91].

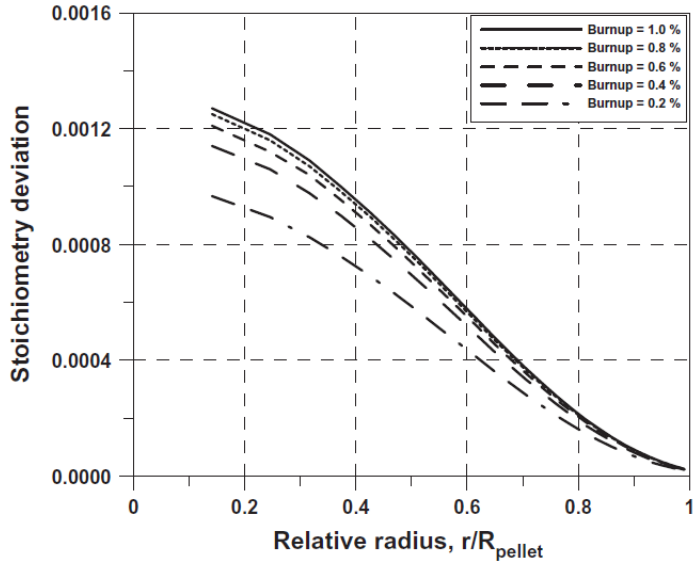

Figure 2.32. Fuel stoichiometry as a function of the radial position at different burnup levels in the low burn-up region [91].

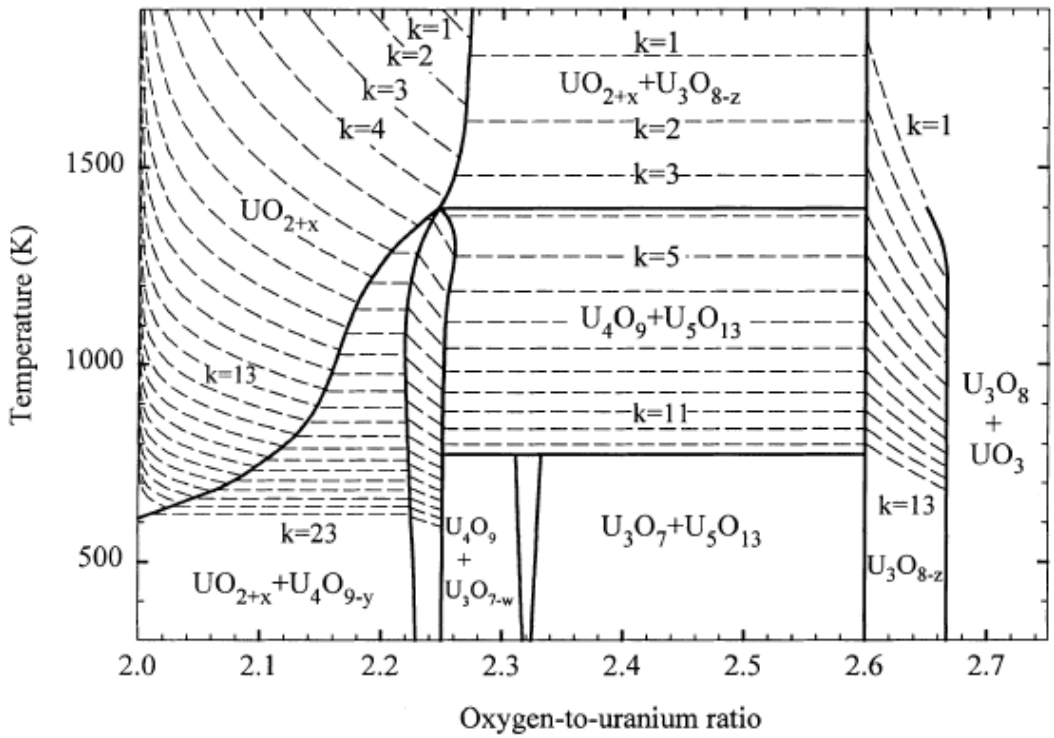

Figure 2.33 Revised phase diagram of the U-O system with oxygen pressure isobars superimposed. The isobars are indicated by the index k in $p=10^{-k}$ where p is in atm. [91].

As shown in Figure 2.33, change in the oxygen partial pressure of the sintering atmosphere can help to control the stoichiometry of the pellet. Therefore, a study that includes samples with different stoichiometries can help to develop more comprehensive models of the fuel as they can represent different radial positions in the fuel. These samples can be used to determine if there are differences in the GB character. Are some GBs more mobile than others? Are these GBs the same regardless of the oxygen content? Part of the next chapters will help us to answer these questions.

2.6 Summary

Uranium dioxide is a line compound at room temperature but starting at 575 °F can form solid solutions with U and O atoms, depending on the temperature and the O/U ratio. Therefore, the initial stoichiometry of the fuel will depend on the sintering conditions (initial powder composition and size, sintering temperature and atmosphere, etc.). Variations on the sintering parameters, for instance sintering atmosphere, can affect the sintering kinetics as the diffusion of the uranium atom is the limiting parameter for grain growth. Increasing the oxygen content can increase the uranium atom mobility by x^2. Consequently oxygen-rich sintering atmospheres will accelerate the sintering process and decrease the sintering temperature. There are several papers that describe how variations on the sintering atmospheres (air, CO/CO_2, H_2/H_2O, Ar/O_2 mixes) can decrease the sintering temperature and increase the grain size. However, none of these papers describe the crystallographic and GB textures of the obtained microstructure. Are some grains growing more than others? Why? Which ones? Are some GBs more mobile than others? Why? All the reviewed literature seems to point out that the crystallography plays a key role on the microstructure evolution both during sintering and in-pile, but there are not enough data to corroborate this statement. Determining correlations between microstructural features and processing conditions can help to determine how the fuel will evolve during fission, and the data can be used as initial inputs for multi-scale models. These correlations can also be used to design more efficient fuels that can work at higher burn-ups using GB engineering and modeling. Details on the research objectives, characterization techniques and some preliminary results as well as the proposed research work will be described in the next chapters.

CHAPTER 3

OBJECTIVES

- Establish how the processing conditions, in general, and oxygen content, in particular, can affect microstructural features such as: grain size, shape, CSL fraction and distribution, porosity in both 2-D and 3-D, with special emphasis on the GB character.
    - Determine the minimum area size that statistically represents the microstructure using the parameter that has the largest variability in 2-D.
        - Compare several microstructural parameters such as grain size, GB misorientation, CSL fraction and distribution to determine their variability in different samples.
        - Establish a procedure that can be applied to samples manufactured under different conditions.
    - Determine the 5 parameters need to characterize GBs of samples manufactured under similar conditions but with different stoichiometry, to establish relationships between the oxygen content and the GB crystallography.
        - Obtain 3-D models of the microstructures to evaluate the grain and porosity size and shape.
        - Using serial sectioning techniques obtain 3-D models to determine the physical normals of GB boundaries.
        - Determine if there is microstructural variability as a function of position in the samples.

        - Study at least three areas between the center and the edge of the pellet.
        - Study grain size and shape as well as GB character.
    - Determine if and how the oxygen content affects:
        - Microstructural parameters such as: GB misorientation, GB texture, porosity, grain shape and grain size.
        - Grain boundary pinning and mobility.
        - Grain boundary plane distribution.

- Perform heat treatment of a sample that have been fully characterized to establish how the microstructure crystallography evolves during grain growth.
    - Study grain growth kinetics during the final sintering stages at a fixed temperature and stoichiometry.
    - Determine if there are specific GBs textures and grain textures that are preferentially developed during grain growth.

CHAPTER 4

EXPERIMENTAL PROCEDURES

As previously stated the main objective of this work is to determine how and if changes on the manufacturing conditions can affect the pellet's microstructure, with emphasis on the GB character. In order to accomplish this objective several samples, manufactured under different conditions, were studied.

The initial set of samples, consisted on samples manufactured under diverse conditions and with different densities. These samples were used to develop polishing techniques for microstructure characterization, in general, and serial sectioning, in particular.

A second set of samples, where the only processing variable that was changed was the sintering ramp, were studied. These samples were characterized to study how and if this processing parameter can affect the final microstructure.

Additionally, a set of 3 samples with variations on the stoichiometry (oxygen content) were thoroughly examined using both mechanical polishing and focused ion beam (FIB) micromachining to obtain both 2-D and 3-D data. The serial sectioning data, obtained using FIB, were used to create 3-D reconstructions of the microstructure and fully characterize the GBs.

Finally, a sample with > 95 % theoretical density (TD) was fully characterized and heat treated, under a controlled atmosphere, to study GB mobility. Details on the experimental procedures are described next.

4.1 Description of the studied samples

In general, all the samples were manufactured the same manner: the powders were milled, pressed and sintered. However, variations were present on the manufacturing conditions such as powder source, compacting pressure, sintering atmosphere, sintering heating/cooling ramps, and sintering temperature, among others. These variations are shown in Table 4.1.

Table 4.1. Description of the processing conditions of the different samples

Sample	TD (%)	Powder	Compacting Pressure (MPa)	O/M	Sintering T (^{0}C)	Dwell time (hrs)	Heating ramp (^{0}C/min)	Sintering Atmosphere	Polishing
1	86	ABB	40	-	1750	10	-	UHP Ar	M
3	92	Sigma	160	-	1750	3	-	O_2 trap	M
2	95	Sigma	160	-	1680	No hold	20	O_2 trap	M
8	97	Areva	160	-	1350	4	10	O_2 trap	M
10	97	Areva	160	-	1350	4	20	O_2 trap	M
9	97	Areva	160	-	1350	4	5	O_2 trap	M
4	91	Areva	40	2.00	1350	2	5	Gas mixture	FIB M
5	94	Areva	40	2.06	1350	2	5	Gas mixture	FIB M
6	92	Areva	40	2.14	1350	2	5	Gas Mixture	FIB M
38	98	Areva	200	-	1600	4	-	O_2 trap	M

M stands for mechanical polishing and **FIB** ion beam milling using the focused ion beam. **Color code:** initial characterization set, variation on sintering ramp, variations on oxygen content and sample for heat treatment.

Moreover, the depleted UO_2 pellets were fabricated with feedstock powder. Pellets were produced using approximately 0.95 g of the powder and pressed using a 6 mm die set at different pressures with a 60 second dwell. The green pellets were sintered under different conditions as described in Table 4.1. The final product consisted in a 3-5 mm diameter pellet, 4-20 mm tall, which was cut in smaller discs (2-3mm) or in quarters (first cut in the longitudinal direction and then in half parallel to the radial direction).

The samples were polished using various techniques and characterized to determine grain size and shape distributions and well as GB character among other microstructural features. Details on the characterization procedures are described below.

4.2 General sample characterization

The microstructure of the samples described above was studied using mainly Electron Backscatter Diffraction (EBSD) and Scanning Electron Microscopy (SEM). The samples were polished using either mechanical polishing or ion milling. A preliminary study of a larger area was conducted to understand the minimum area that must be characterized to obtain reliable statistical data on microstructure and its variability, and also to determine how the selection of smaller areas can affect the results. Additionally, in some cases, serial sectioning was performed for samples manufactured under different conditions. The data were used to obtain 3-D models of the microstructure. These models were used to fully characterize the GBs as well as to study some 3-D microstructural features such as grain size and shape. The details on the experimental procedures are described below.

4.2.1 Mechanical Polishing

Some of the samples, as described in Table 4.1, were polished using a Buhler Minimet inside a glovebox that has a controlled atmosphere. Oxygen filters (20-200ppm) as well as moisture (5-200 ppm) filters were included to minimize the sample oxidation of the samples. Nuclear filters at the glovebox gas purging outlets as well as an ionizer were included. A procedure with details on how to manipulate the samples and the waste was developed to minimize the contamination during polishing.

Most of the sintered pellets were mounted in epoxy and sectioned in the transversal direction. The samples were first ground with SiC paper (320 to 1200 grit), using water as lubricant. Then, rough polishing was performed using the following sequence: 15 minutes with 3 μm diamond paste, 15 minutes with 1 μm diamond and 20 minutes with 0.25 diamond and colloidal silica; polypropylene glycol was used as a lubricant in all these steps. Then, the samples were polished using 0.04 μm colloidal silica for 1 hour. Finally, the samples were polished using a fresh solution of five parts of colloidal silica (0.04 μm) and one part of hydrogen peroxide (30%) for 20 min. This step was repeated, as necessary, to remove 0.5 μm of material for serial sectioning, while 60 minutes of polishing removed 1.6 microns, for the case of sample 2 (95 %TD) Some changes on the polishing steps were made depending on the sample. For instance, the final step was skipped for very porous samples as it was too aggressive for some of them. After polishing, the samples were rinsed in water, cleaned with micro-organic soap and ultrasonically cleaned in water, acetone, ethanol and isopropanol (15 min each step).

In the case of sample 2, fiducial marks were made using a Vickers indenter for depth measurements and for image alignment during serial sectioning. The indentation was done

following the ASTM C1327-08 standard. The Vickers indents were examined using optical microscopy and later on with SEM as seen in Figure 4.1. Optical microscopy images were used to determine the amount of material removed over a specific area. The indents were also used as reference to locate the area of interest for EBSD scans for serial sectioning, as well as reference marks for alignment during the 3-D reconstruction of the microstructure.

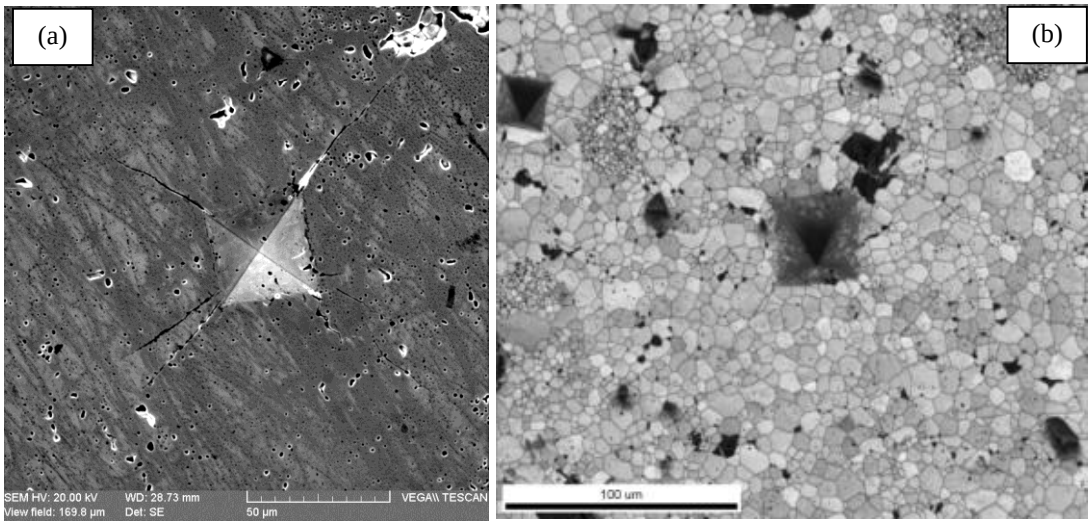

Figure 4.1. Vickers indents on sample 2: (a) Secondary electron image and, (b) Image quality map obtained from the EBSD scan.

4.2.2. Focused Ion Beam

The samples were rough polished using 600 grit SiC paper to obtain a flat surface running parallel to the axis of the cylindrical pellets to create a flat edge for ion milling. The sample was then serial sectioned using a FEI Helios NanoLab 600 Dual Beam SEM and FIB with an EBSD detector attached. An area of 30 μm by 40 μm was studied, and to avoid charging the adjacent region was coated with platinum. The serial sectioning was carried out using 30 keV and 21 nA in the FIB, while secondary electron images and EBSD maps were

obtained for each slice, with the SEM operating at 20 keV and 2.7 nA. The slices were spaced 0.33 μm and a total of over 80 slices were collected for each sample. The slices were taken from the outer edge of the pellet and the removal of the material was done in the radial direction, as seen in Figures 4.2(a) and (b). Fiducial marks, as seen in Figure 4.2(b), were placed near the sectioned area in order to facilitate alignment of the images and it was required to run the automated serial sectioning script.

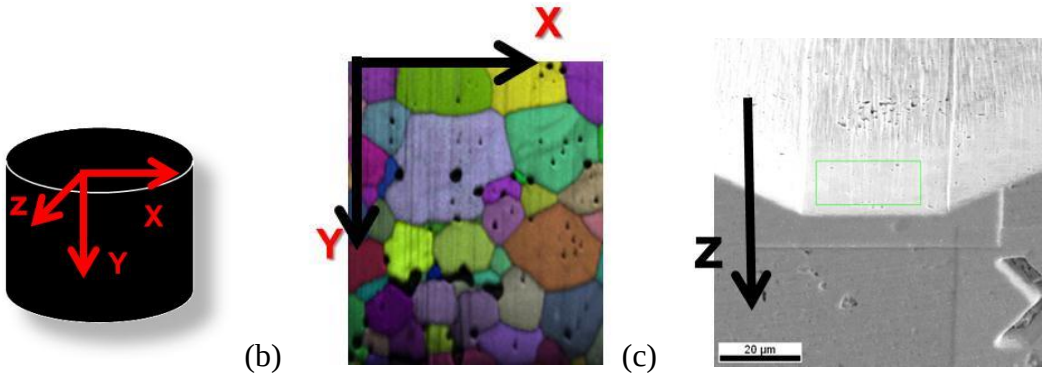

(a) (b) (c)

Figure 4.2. Configuration of the ion milled area (a) and (b). Note that the z direction is the radial direction of the pellet. (c) Secondary electron image of the ion milled area (top view) including the fiducial mark.

4.2.3. Microstructure Characterization

The microstructure characterization of the mechanically-polished samples was performed using a scanning electron microscope (VEGA TESCAN Microscope), equipped with an EDAX-TSL OIM^{TM} attachment, and OIM^{TM} 6.2 analysis software. Secondary electron images of the sample were first obtained to select a region of interest. Electron Backscatter Diffraction data were collected from a selected region with a step size of 0.5 μm or 0.7 μm to determine local crystallographic orientations. The best results were obtained at 20 kV, 100 nA and 0.015 s exposure time. Data points used for the analysis were chosen such that they all had more than 95% probability of being indexed correctly, as estimated by the EDAX-TSL OIM^{TM} analysis software. Furthermore, a minimum grain size of 10 pixels was used in the reconstruction of the microstructure from the crystallographic data to ensure that poorly indexed points at pores were not taken as individual grains by the data analysis software. Direct comparisons were made with optical and secondary electron images of the same region to ensure that the EBSD data resulted in maps that represented the actual microstructure. For serial sectioning, all the scans were performed under the same conditions and the same clean up methodology for the data was used on every slice.

The EBSD analysis software was also used to obtain general microstructural and crystallographic data, for all the samples, such as grain size distribution and GB misorientations. The misorientation data, obtained from the EBSD maps, was used to determine the number fraction of special boundaries, as defined by the Brandon criterion ($\Delta\theta=\theta_0/\Sigma^n$, $\theta_0=15°$, n=0.5) [92]. The analysis was conducted for CSLs up to Σ49. The data were also used to establish relationships between porosity distribution (geometry, location) and GB misorientation for sample 2. In order to do so, porosity data were collected using

SEM images, optical microscopy images and EBSD maps. For the general porosity size and shape distribution an area of 400 μm by 400 μm was selected and threshold using image analysis software. These data were compared with EBSD maps to correlate pore size and geometry with its location, over a smaller area (400 μm by 200 μm).

The EBSD data were also used to determine GB character, as the OIM™ software data outputs includes GB misorientation angles and axis, GB texture and reconstructed GBs which allow us to determine the GB normal and fully characterize the GBs from 2-D data. The advantage of using 2-D data set to determine GB normal distributions is that large data sets, that include thousands of GBs, can be evaluated simultaneously. Therefore the data can be statistically more representative of the overall population.

However, the output is an overall distribution and there is no specific information on the GB misorientation distribution

The reconstructed GBs are obtained using the OIM software™. The idea was to reconstruct a boundary trace from the GB segments that are superimposed to the original GB grid to match the actual boundary angle as closely as possible, as seen in Figure 4.3. The more curved the GB is, the larger the number of segments that are required to fit the GB, but the larger the data set will be. The obtained reconstructed grain boundaries were used to calculate GB traces and determine the distribution of the GB normals, using the method proposed by Saylor et al. based on 2-D data sets [93].

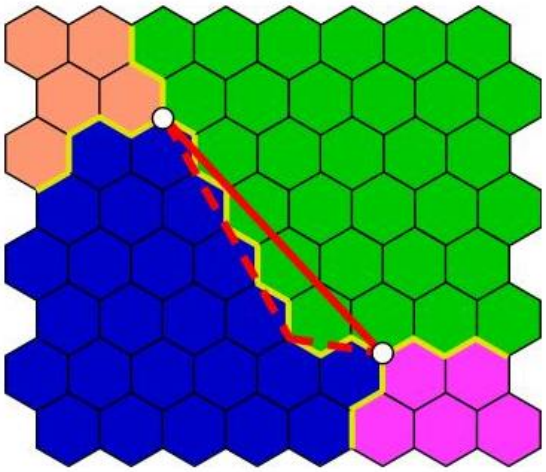

Figure 4.3 Reconstructed GB.

Finally, a partition that included only grains that were 2.5 times the average size was studied to study grain and GB texture. The partition was done after observing that most of the studied samples had abnormally large grains. Moreover, preliminary results showed that these grains dominate the overall crystallographic texture. Initially the study was done for the samples with different sintering ramp velocities and a more complete study was done for the samples with known stoichiometry. In the latter case, GB texture was evaluated to determine if the oxygen content was affecting the crystallography of the GBs associated with abnormally large grains. The idea was to study the crystallography of the GBs of these grains to determine why these grains were growing faster than the rest of the grains.

4.2.4. Reconstruction of the microstructure

The 2-D crystallographic data from each slice of the serial sectioning were used to obtain statistical information on variables such as grain size and GB misorientations. The fiducial marks, located in the samples, allowed alignment of the SEM images and EBSD maps used to reconstruct the microstructure in 3-D with AVIZO™ 6.3, as shown in Figure 4.4.

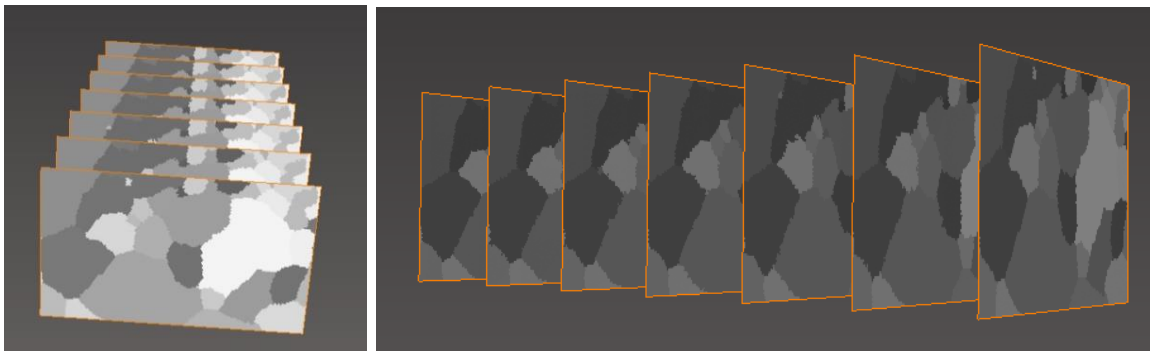

Figure 4.4 Stack of images aligned in AVIZO™ 6.3.

The fiducials marks were a key feature in the reconstruction of the microstructures as charging, shifting and drifting occurred during some of the scans and a reference was needed. Both, secondary electron images and image quality maps were used for alignment. This step was very important as the GB physical normals were measured from the reconstructed model.

Once the images were aligned, the software was used to interpolate images in between slices and finally reconstruct the microstructure. The final product can be a surface or volume mesh, as seen in Figure 4.5, which includes individual labels for each grain that can be associated with the EBSD crystallographic data. The reconstructed model can be used to determine statistical microstructural data, such as grain volume, shape, GB area,

among others. It can also be used to produce meshes for input to finite element models, where crystallographic information can be included.

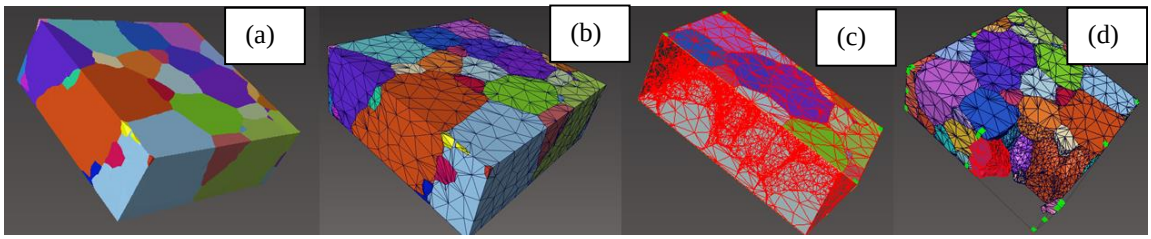

Figure 4.5. (a) Reconstructed model of the microstructure, (b) surface mesh, (c) surface cut (note that the grains have no elements inside), and (d) volumetric mesh.

For this study, the reconstructed microstructure was used to determine the equivalent 3-D grain diameters and compared to the 2-D results. Additionally, the 3-D images were used to evaluate the grain and pores shape and distribution. In particular, the effect of pores in grain pinning for samples manufactured under conditions that produce fixed stoichiometry. Samples with a density lower than 95 %TD can be at the intermediate stage of sintering, where the microstructure is still in flux and can be used to study microstructure evolution. At this point pores can be interconnected and pinning some of the GBs. The 3-D reconstruction can be used to evaluate the pore connectivity, pore size and distribution as well as to establish relationships between GB misorientation, curvature and pore location, size and shape.

The 3-D reconstruction was also used to obtain physical directions normal to the GB planes for each grain and then used to calculate the crystallographic GB planes. The physical normals were obtained by performing perpendicular cuts to the GB. Then, the physical

normals were rotated using the crystallographic rotation matrix that relates physical and lattice coordinate systems for each grain to obtain the two GB normals (one for each grain across the GB). With this method, the GBs were fully characterized. The 3-D results were compared to 2-D data to determine the accuracy of the results in both cases.

Once the samples were characterized and relationships were established between the manufacturing conditions and microstructural features, such as GBs, a final experiment was design to study the GB mobility.

4.3 Heat treatment

As a final experiment a heat treatment was conducted to establish relationships between GB crystallography and GB mobility. The objective of this experiment is to determine if there are some GB moving preferentially allowing abnormal grain growth for certain grains.

The heat-treated sample was initially polished and fully characterized, using the techniques previously described. Indents were placed as landmarks to compare the EBSD maps before and after the heat treatment. The EBSD maps were compared to identify, if possible, the grains that are growing and their crystallography. The scans can also were used to study GB pinning.

For the heat treatment, the fully characterized sample was placed in an alumina foam, inside an alumina tube in a vertical tube furnace. The tube was evacuated before the heat treatment to avoid introducing oxygen to the system. A scheme of the gas train is shown in Figure 4.6. The setup included: (1) silica gel to absorb moisture; (2) molecular sieve to adsorb hydrocarbons, CO/CO_2 and traces of moisture; (3) oxygen trap, that consist on a quartz tube filled with copper wire that can be heated up to 600°C to obtain $P_{O2}<10^{-17}$; (4)

flowmeter to control small gas flow (can be bypassed if necessary); (4) and (8) oxygen detectors, to determine the P_{O2} before and after the alumina tube; (7) nuclear filter and (8) bubbler.

The experiment was conducted at 1250 ^{0}C and an oxygen partial pressure of ~10^{-8} atm, as according to the phase diagram at that temperature the stoichiometry should be around 2.04, as seen in Figure 4.7. The sample was treated in a dry ultra-high purity argon atmosphere during the heat treatment.

The sample stoichiometry was determined according to {Soo Kim, 2000, A thermodynamic evaluation of the U‑O system from UO2 to U3O8}:

$$ln_{P_{O_2}}(UO_{2+x}) = 4.3 + \frac{31(C-2)}{3-C} - \frac{3.30\times10^4}{T} \quad (4.1)$$

Where P_{O2} is the oxygen partial pressure, C is the O/M and T is the temperature in Kelvin. A partial pressure of 10^{-8} would give a sample stoichiometry around ~2.035 at 1250°C.

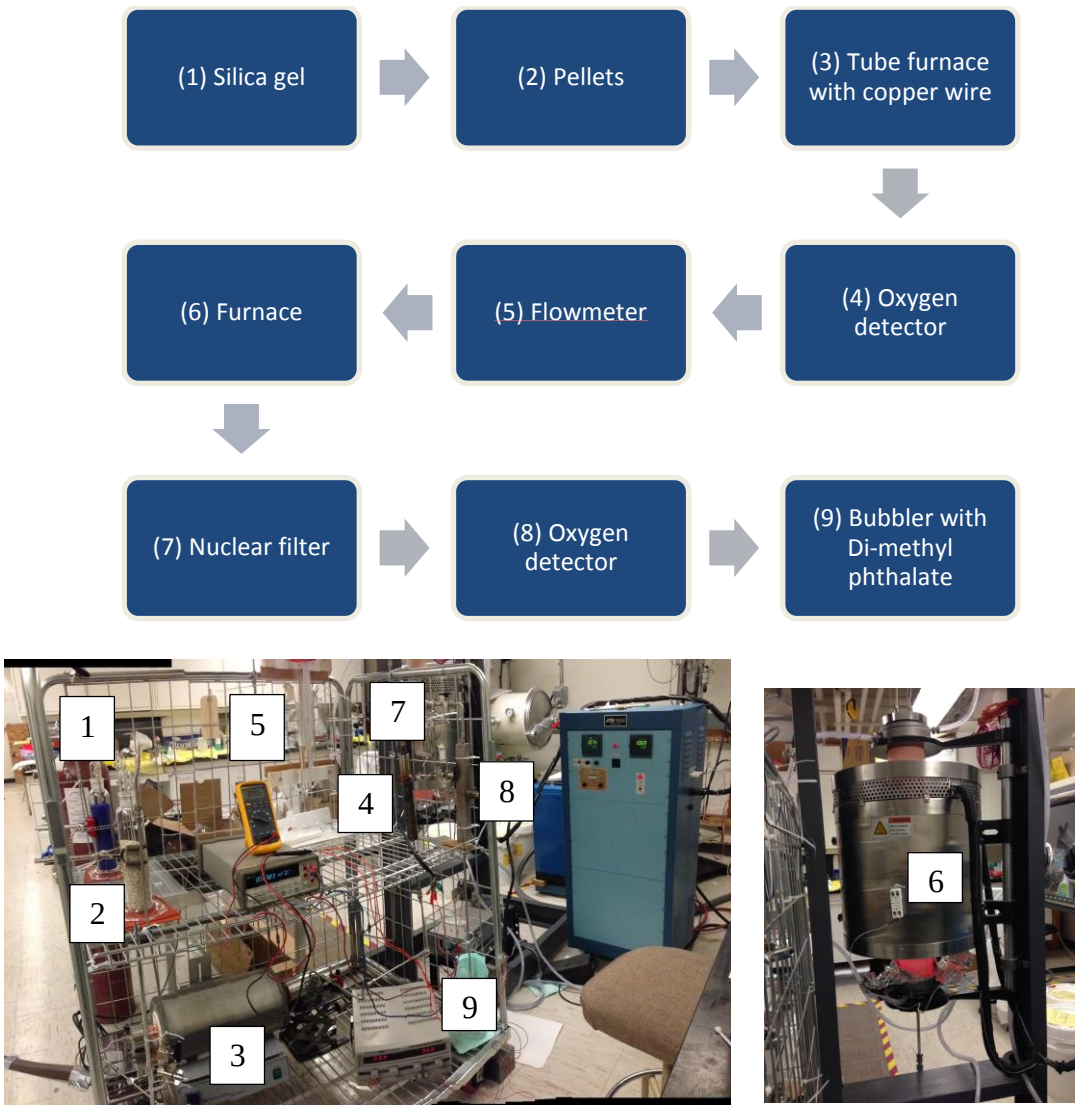

Figure 4.6 Gas train components.

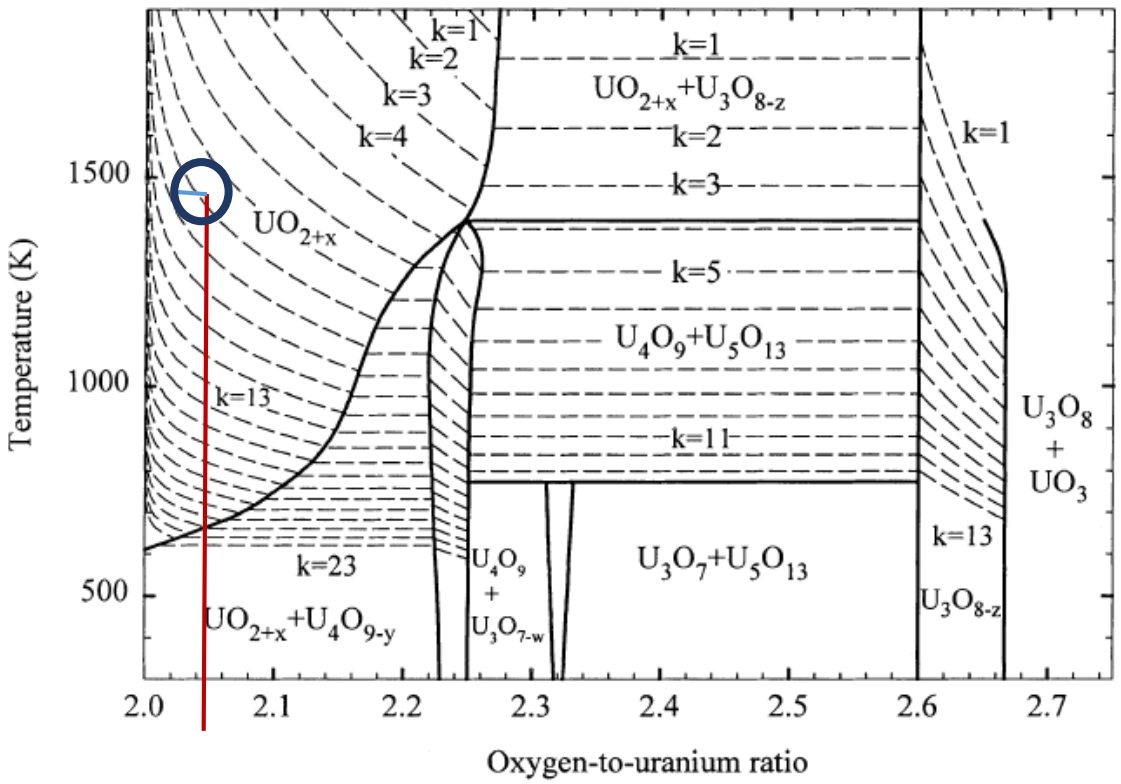

Figure 4.7 Phase diagram of the U-O system with oxygen pressure isobars superimposed. The isobars are indicated by the index k in $p=10^{-k}$, with p in atmospheres [23].

The sample was treated in a dry ultra-high purity (UHP) during the heat treatment and cooled down in a low-oxygen UHP argon atmosphere (around ~10^{-16} atm). The heating cycle is described in table 4.2. The target time for the dwell temperature was 2 hrs, the extra 30 min at the dwell temperature were used to reduce the sample to a lower O/M to "quench" the microstructure. At that point, the oxygen getter was switched on at 600°C and the oxygen partial pressure was dropped to around ~10^{-16} atm. As the heat treatment was done in an alumina tube, the system was slowly cooled down to avoid cracking from thermal shock.

Table 4.2 Heating cycle for the heat treatment

Step	Temperature [°C]	Time [hr]	Atmosphere [atm]
Heating ramp 1	0-900	1	Dry UHP Ar
Heating ramp 2	900-1250	4	Dry UHP Ar
Dwell 1	1250	2	Dry UHP Ar
Dwell 2	1250	0.5	Gettered dry UHP Ar
Cooling	1250-600 (switched the furnace off)	4	Gettered dry UHP Ar
Cooling	600-25	2.5	Gettered dry UHP Ar

The sample was characterized to determine if there were microstructural changes after the heat treatment. Sample 38, as seen in Table 4.1, has a density that is higher than 95%TD; therefore; is at the final stage of sintering. Heat treating the sample allowed to continue the sintering process during the final sintering stage. The porosity, grain size and crystallography were evaluated using optical microscopy images as well as SEM images and EBSD maps, according to the procedures previously described.

Additionally, the evolution of the grain size was studied using the average grain size obtained from EBSD maps after the heat treatment.

These results will help us understand the sintering mechanism during the late stage of sintering as well as increase the data set available on the literature, as there are not enough data in the literature that relates the kinetics of grain growth with the sample's crystallography.

Moreover, all the experiments described above will help increase our understating on how the processing conditions will affect overall different microstructural parameters that will, in turn, affect the fuel performance. These results will help to engineer more efficient fuels, as GB engineering can be applied with a combination of experimental data on manufacturing conditions and models. Different sintering conditions, for instance O/M, will generate different CSL distributions as well as different GB networks that will affect the percolation of fission gases. Understanding how the processing conditions affect the GB character, as well as the overall microstructure, will not only help to build more detailed models to predict the fuel life and evolution, but also to eventually create fuels that will withstand higher burnups.

The results obtained with the procedures described above will be presented and discussed in the following chapters.

CHAPTER 5

MICROSTRUCTURAL CHARACTERIZATION OF SAMPLES IN 2-D AND 3-D

Several samples fabricated under diverse conditions were characterized to study how processing parameters affect the overall microstructure of the samples, as well as some specific microstructural features such as GB character.

We start the analysis with two samples with different densities (85% TD and 95% TD) to determine which, if any, microstructural features are more sensitive to changes in density. Out of these two samples, the sample with 95% TD was further characterized to determine the minimum area size to accurately represent the overall microstructure. Also, relationships among pore size, shape and location (including GB misorientation) were determined.

A second set of samples were analyzed to determine how the heating rate of the sintering ramp can affect the overall microstructure. These samples were made with the same powder, pressed under the same conditions and sintered using the same sintering cycle only varying the sintering ramp rate.

An additional set of samples consist of three samples that were manufactured under the same pressing and sintering conditions but with variations on the oxygen content in the sintering atmosphere in order to obtain different stoichiometries. These set of samples were characterized both in 2-D and 3-D to determine how the oxygen content can affect the microstructure; in particular, how and if the oxygen content affects the GB character. The analysis includes a comparison between smaller data sets in 3-D vs larger 2-D data sets.

Finally, a sample was heat treated under a controlled oxygen partial pressure to relate the microstructure crystallography and grain growth.

The results of the characterization of all the previously described samples will be presented and discussed next.

5.1 Initial assessment of the microstructure of a depleted uranium sample

The first sample that we analyzed was an insulator pellet, with 86% TD. This type of pellet is placed on top of the fuel pin and has large pores. The sample was cut longitudinally and mounted in epoxy. Additionally, the sample was carbon coated to avoid charging during the EBSD scan. Because the sample was carbon coated and due to the large pores, the EBSD signal was weak and a large exposure time (4 secs for this sample, versus 0.015-0.030 secs in most conductive samples) was required. The porosity also limited the area that could be studied as the sample surface consisted mostly of large pores. Only an area of 60 μm by 100 μm was found good enough to scan.

The microstructure in the region of interest for the depleted UO_2 sample examined is shown in Figure 5.1.1, which displays an inverse pole figure (IPF) map, superimposed over a SEM image of the microstructure. In the IPF map, the color for each grain corresponds to the crystallographic orientation in the grain parallel to the out-of-plane direction, as given by the standard stereographic triangle in the inset. Special GBs are highlighted with different colors depending on their Σ value. The sample had equiaxed grains with an average size of 6 ± 2 μm and porosity with an area fraction of approximately 14%, which is consistent with the large porosity expected in an insulator pellet. Large pores were located mostly near GBs and triple points, while small pores were present mainly inside large grains.

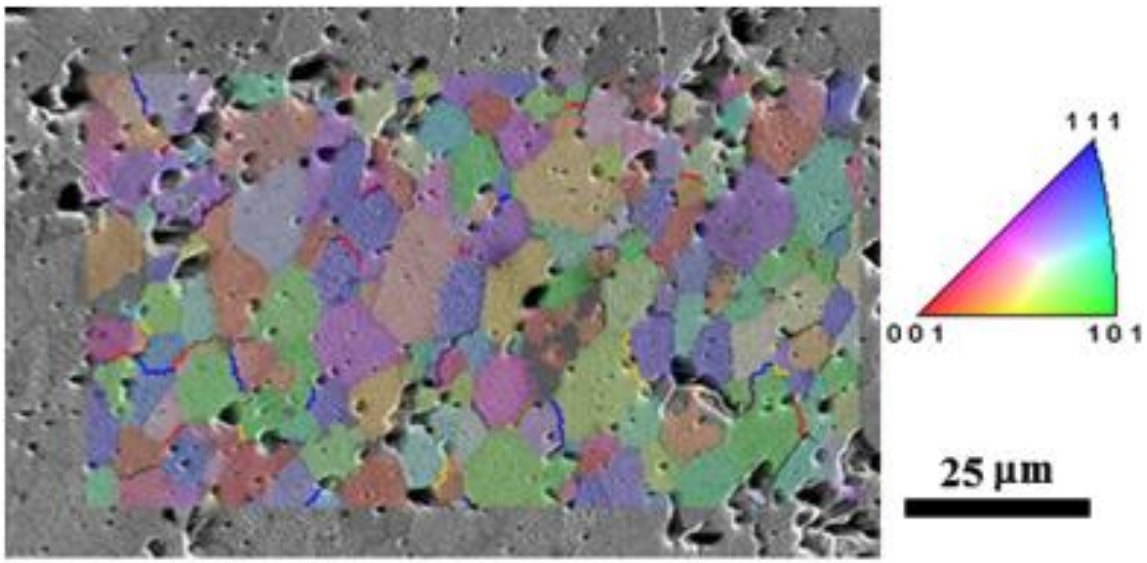

Figure 5.1 SEM and EBSD images from the studied area of the depleted uranium oxide sample. The CSL GBs are highlighted in red (∑3), yellow (Σ5), green (Σ7), blue (Σ9), purple (Σ11), and black (other special GBs).

The number fraction of individual CSL GBs obtained from the misorientation data collected manually was compared with the length fraction statistics provided by the EDAX-TSL OIM™ software. There were some differences between the two sets of results, especially regarding the fraction of Σ3 and Σ5 GBs. We note from Fig. 5.1 that, in general, the total number of Σ5 GBs is lower than for Σ3 GBs; however, the Σ5 GBs tend to have longer lengths than Σ3 GBs, which would result in differences between number and length fractions for these GBs that are consistent with the results obtained in this study. That is, the number fraction overestimates the abundance of Σ3 GBs and underestimates the fraction of Σ5 GBs when compared with their length fractions. Hence, collecting data on just the number of GBs does not truly reflect their actual ‘‘abundance’’ in the

microstructure, even in this case where grains are fairly equiaxed. Therefore, the statistics of GB characteristics presented here corresponds to length fraction and not the number fraction, because the former is a more appropriate metric to represent GB statistics than the latter, as suggested by Randle [92].

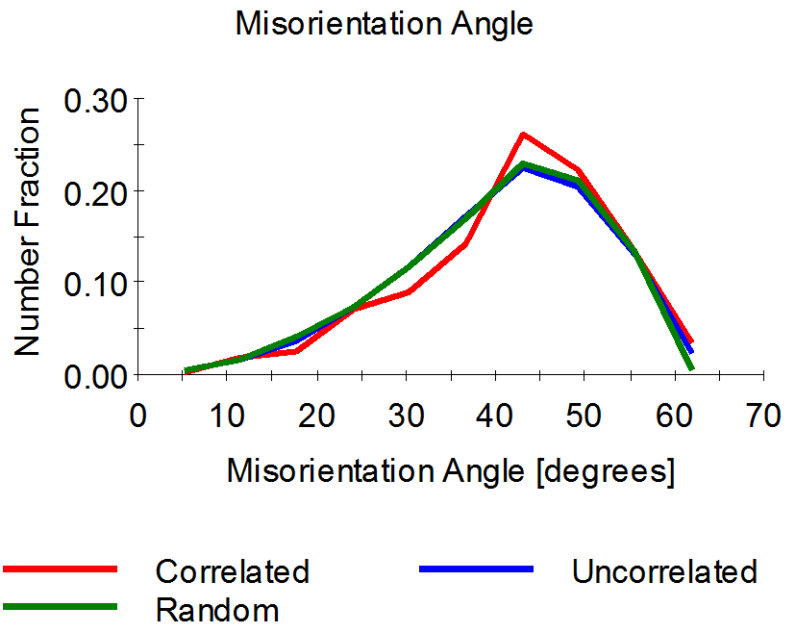

Figure 5.2 Misorientation angle distribution for sample 1 (insulator pellet).

The distribution of specific misorientation angles obtained is shown in Figure 5.2. Three different measures are shown: a correlated distribution, calculated from grains that share a common boundary; an uncorrelated distribution, calculated from the overall grain orientation distribution; and a random distribution, which represents the Mackenzie distribution for a cubic crystal [93]. The correlated distribution is the actual distribution present in the sample as it is obtained from grains that share a GB. The uncorrelated distribution is calculated from the texture and in that sense is purely ‘‘geometric’’ in nature,

i.e., grain orientations from the measured texture are sampled and placed adjacent to each other which in turn results in a potential GB misorientation distribution. The difference between the two measures points to the effects influencing the microstructure. If the correlated and uncorrelated distributions are similar, then the GBs themselves, say, their energies, do not play a significant role on the final misorientation distribution.

The correlated distribution presented a maximum at about 42.1°, which agrees with the maximum for the uncorrelated distribution, but the amplitude of the peak was higher for the former, indicating that there is a tendency for boundaries with misorientations close to this angle to be present in the material with a frequency higher than that expected from just random pairing of the existing grains in the area chosen for examination. Note that the uncorrelated distribution resembles the random distribution, which indicates that the sample had either a random or a fairly weak crystallographic texture.

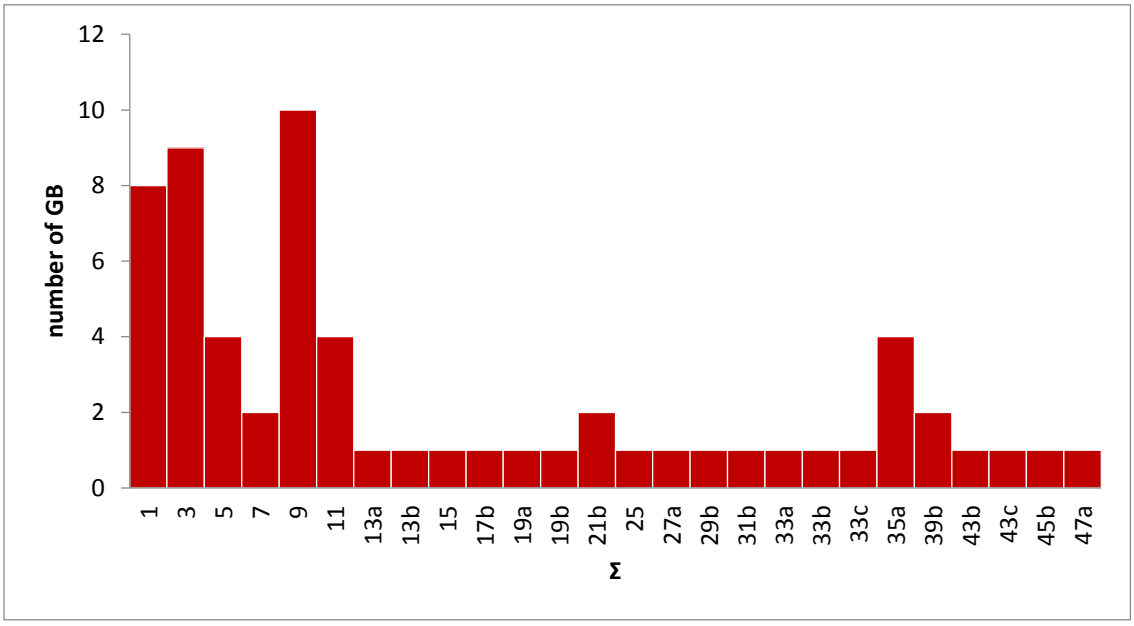

Figure 5.3 CSL distribution of sample 1 (insulator pellet)

Regarding of the CSL distribution, the total fraction of CSL boundaries was determined to be 15.7%, which is comparable to 17.8%, reported by Vonlanthen [94] for YSZ, an oxide with the fluorite structure. The length fraction of individual CSL boundaries, with the respect to the overall CSL population, is shown in Fig. 5.3. As can be observed, the largest fraction of CSL boundary type was Σ9, followed by Σ3 with smaller fractions of Σ5 and Σ11. The general CSL distribution is similar to the one presented by Vonlanthen and colleagues [94] for YSZ, but with a significantly larger fraction of Σ9 and a smaller fraction of Σ3, Σ5, and Σ11. This result indicates that sintered YSZ has a similar, but not identical CSL distribution to conventionally sintered UO_2. This comparison suggests that not all fluorite-structured compounds exhibit exactly the same GB misorientation distribution and/or that the final GB misorientation distribution depends to a significant degree on the processing conditions.

Moreover, as seen in Figure 5.1, the microstructure of the pellet with 86% TD is consistent with the intermediate sintering stage, where pore size distribution has large variability [95]. Grain agglomerates and occasional large pores can be observed. The larger porosity fraction as well as the large pores can affect and in some cases inhibit grain growth [95]. The latter can affect the CSL distribution as GBs cannot move freely, as GB motion can be restricted by the surrounded porosity, in contrast to Vonlanthen's [94] results for a dense pellet.

Finally, grains that formed selected low-Σ boundaries (3, 5 and 9) were analyzed using the EDAX-TSL software to obtain the crystallographic directions in each grain parallel to the average GB trace, for boundaries with fairly straight traces, or the directions parallel to long straight segments for those boundaries where the traces kinked (or curved) at one or

more locations. Once traces were obtained, they were used to find out how many of them were consistent with the standard GB planes for symmetric CSL boundaries, either tilt or twist, by taking the dot product of the trace with the normals to the twinning planes and with the rotation axes listed in the literature for each of these CSL grain boundaries [96]. As described in the literature review, 5 parameters are needed to fully characterize a GB. The EBSD data provide 3 out of the 5 parameters, as the GB normals cannot be directly obtained from 2-D data. The trace analysis was done as a first step to quantify the crystallography of the boundary planes and the nature of the boundary itself, i.e., tilt, twist or mixed. If the GB trace vectors and the normals of the selected GB planes were not orthogonal for both grains, then they were considered mixed GBs [97]. The results are shown in Table 5.1.

Table 5.1. Percentage of boundaries examined with traces consistent with high symmetry planes for a subset of Σ3, Σ5 and Σ9 GBs for sample 1 (86%TD).

Sigma	**Potential Planes [5]**	**Percentage of GBs with consistent traces**
3	{111}	91
	{211}	9
	mixed	0
5	{100}	14
	{301}	57
	mixed	29
9	{221}	33.3
	{411}	33.3
	{110}	33.3
	mixed	0

Regarding the analysis of the GB traces, there were cases where the GB traces in both grains were close to being perpendicular to more than one of the potential planes chosen, in that case, the GB plane that was closest to being 90° from the measured traces in the two grains was chosen. Traces and GB normal were typically within < 2° from being perpendicular to each other, well within the angular tolerance used to determine the CSL, i.e., Brandon criterion [98], and also within the experimental error for the misorientation

measurement, i.e., about 1°. Most of the traces were consistent with either a twinning plane or a rotation axis except for the Σ5 GBs, which presented some mixed GBs. However, a full characterization to determine if the actual boundaries are pure twist or tilt requires five macroscopic degrees of freedom and cannot be achieved with 2D planar sections [99].

From the initial characterization of the insulator sample we were able to learn that the CSL total fraction seems to be consistent with the data available in the literature. However, the distribution of the CSL GBs seems to be sensitive to the material, since UO_2 has significant variations compared to a cubic zirconia sample.

Also, low Σ GBs represent a significant fraction of the overall CSL distribution, about 44%. This is consistent with work published by Randle [92] who established that for many materials and conditions, only a few types of special GBs dominate the Σ distribution.

After analyzing the data some questions rise: Was the area analyzed large enough to be representative of the microstructure? How sensitive is the CSL fraction to processing conditions or the material? How can we fully characterize the GBs? Do these results represent a typical fuel pellet? In the next sections we will try to answer some of these questions.

5.2 Characterization of the 95% TD sample

As previously mentioned, several samples were studied; however, the sample with the 95% TD (sample 2) was the most widely characterized. General microstructural data (grain size distribution, GB misorientation, CSL distribution, texture, porosity) as well as relationships among these features were obtained. This sample was also used to obtain the first 3-D

model, as the reconstructed area could be selected from a larger area and easily localized using fiducials.

Some of the results were compared with data obtained for samples manufactured under different conditions, including sample 1. General trends were obtained. However, due the large amount of variables that could cause variability in the results, no specific trends could be established.

The microstructure in the region of interest of the d-UO_2 95% TD pellet is shown in Figure 5.4, which displays a SEM image and an image quality (IQ) map. The IQ maps are related to the quality of the EBSD data and local defects as GBs and pores will have low IQ, and, since the sample is not etched, IQ maps can be used to visualize the actual microstructure. One of the initial concerns from the characterization of sample 1 was how representative the analyzed area is of the whole microstructure. As sample 2 had a higher density, larger EBSD scans were obtained and divided into smaller scans to determine the minimum area that was representative of the overall microstructure within an acceptable error.

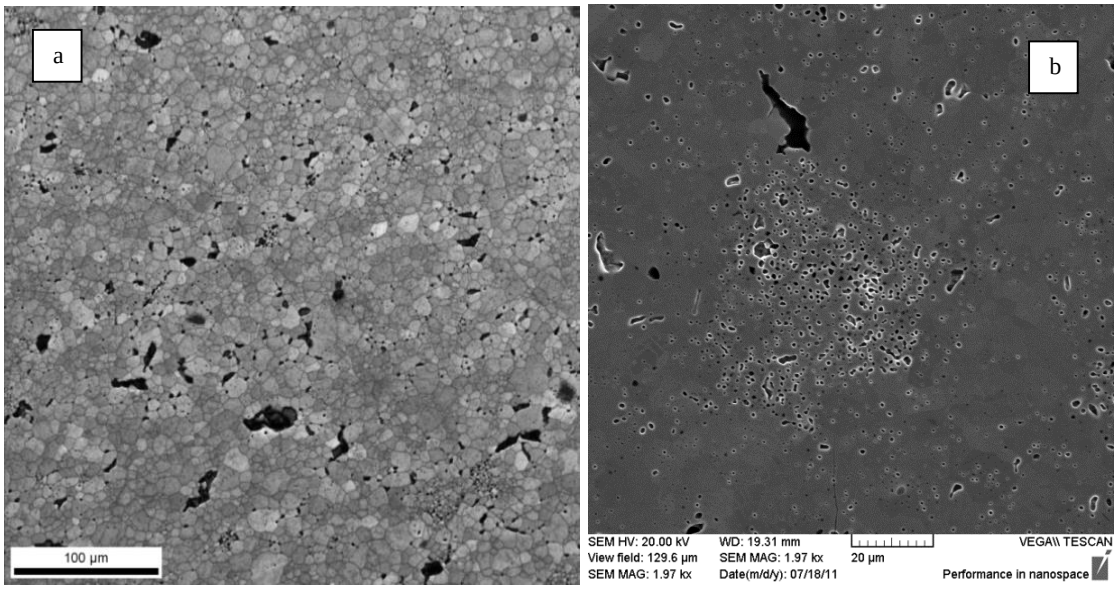

Figure 5.4. Image Quality map of the micrsotructure (a) and SEM image detail of a cluster of pores (b) for the 95%TD Pellet (sample 2)

5.2.1 Coincident Site Lattice (CSL) GB distribution variability and determination of the minimum representative area

A scan over an area of 400 µm by 400 µm was performed, as shown in Figure 5.5. This area was sectioned in smaller areas (400 µm x 200 µm, 200 µm x 200 µm) and the CSL distribution of these areas were compared. The procedure was used to determine the minimum area that exhibited the same distribution as that of the largest scan within an acceptable deviation, less than 5% in this case. The CSL distributions for the different areas are shown in Figure 5.6.

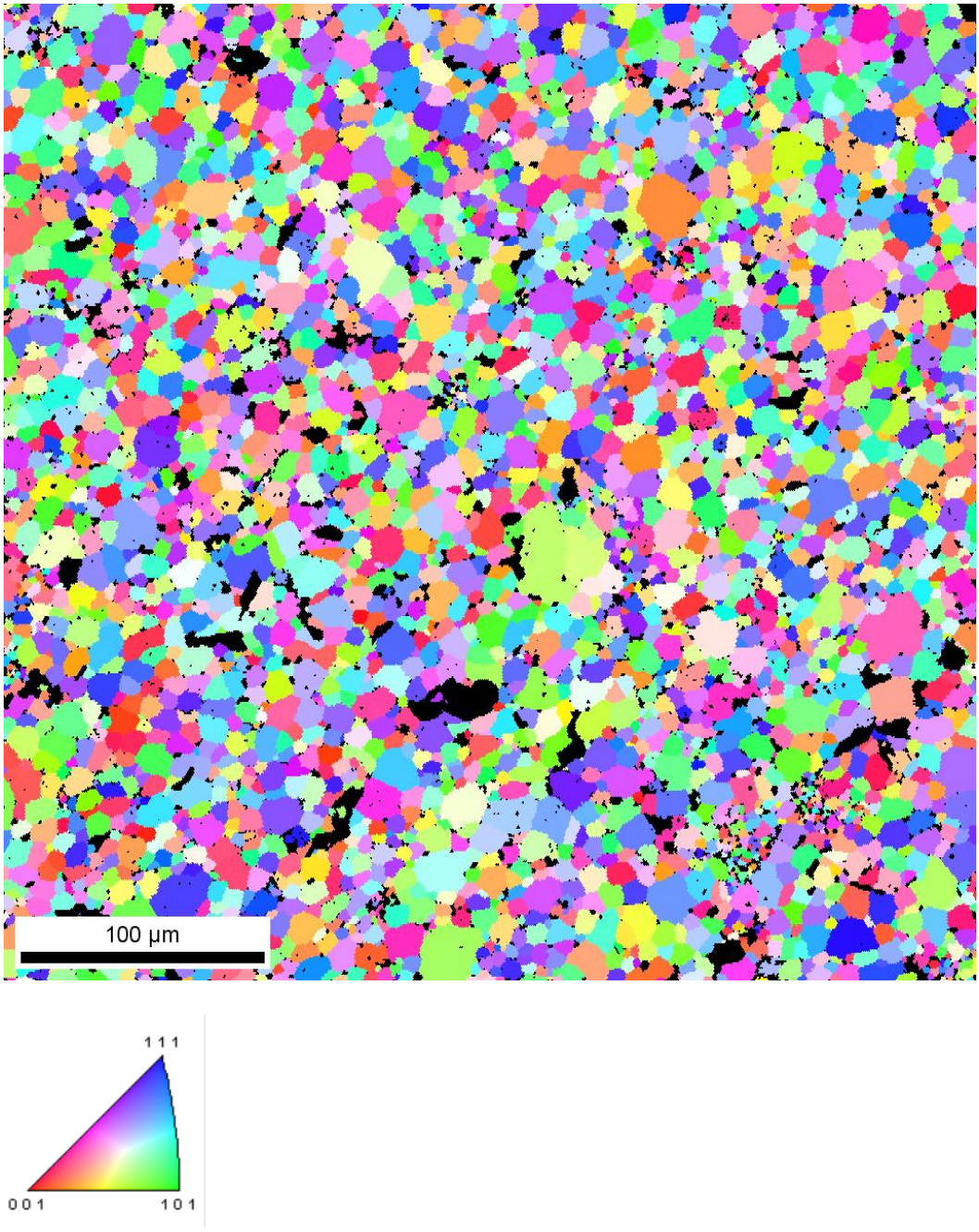

Figure 5.5. EBDS map for a 400 µm x 400 µm area.

(a)

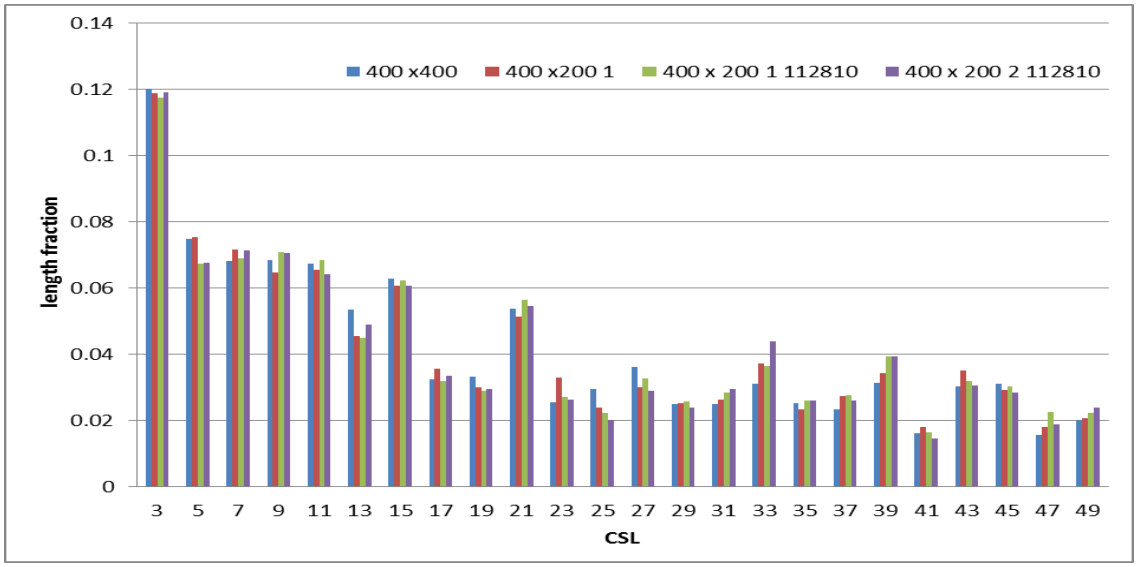

(b)

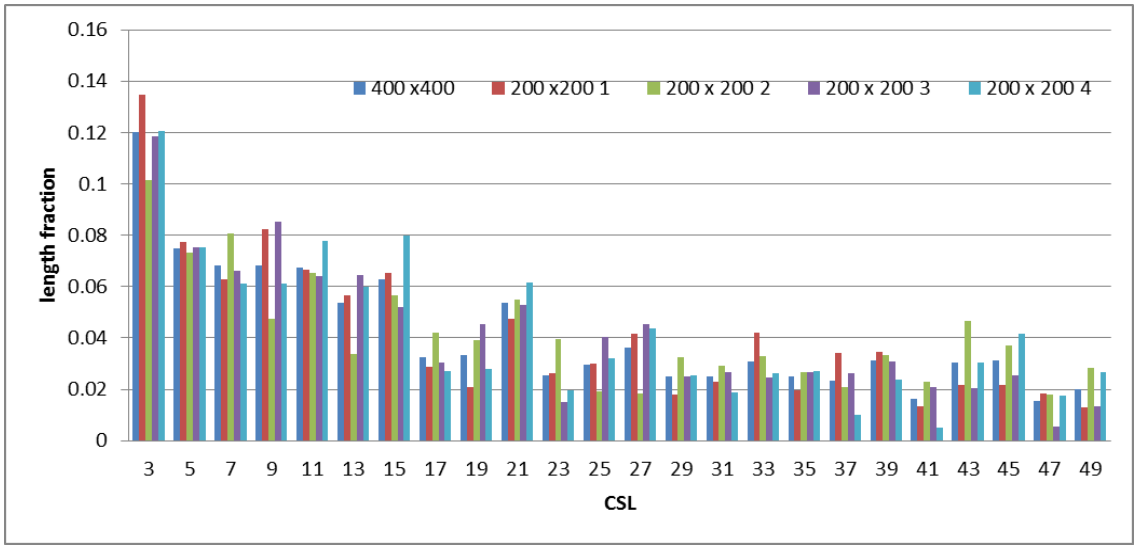

Figure 5.6. CSL distribution for: (a) : 400 µm x 400 µm (blue), 400 µm x 200 µm (green) cropped top of the 400 µm x 400 µm scan, 400 µm x 200 µm (purple) and red is an additional scan over the same area. (b): 200 µm x 200 µm scans: (1) top right, (2) top left, (3) lower right and (4) lower left.

Even though the average grain size and the total fraction of CSL boundaries were similar for the smaller areas (200 μm x 200 μm), the CSL distribution presented more scatter on the data, with deviation up to 13% for some CSL boundaries, while the largest variation for the 200μm x 400 μm area was 5%. It is important to notice that the sample presented large pores, which, in some cases, were larger than the grains. Small areas could contain a larger amount of these large pores and small pores clusters, resulting in a CSL distribution that differs from the distribution of the larger scan, assumed here to be representative of the whole sample. These observations also suggest that if a smaller area is selected with lower porosity, no pore clusters and no large pores, then the representative area size can be reduced and be consistent with results for larger areas.

Additionally, in order to determine the reproducibility of the results, the top area of this scan was scanned twice, under the same conditions, as seen in Figure 5.5 (a). This was done to determine the variability of the CSL distribution over a particular area due to the data collection procedure. The results indicated that the CSL distribution for the 400μm x 200μm scans presented less scatter, particularly for low CSL. Therefore, a 400μm x 200μm area was selected as the smallest area that represented the overall CSL distribution on the d-UO_2 sample. Additionally, this general trend for the CSL distribution is the same for every scan, so that the measurement procedure as well as the cleanup of the data set led to acceptable reproducibility. Smaller areas can be used to study variations on specific microstructural features such as GB character and porosity.

Once that the minimum area size was determined, additional information was collected to fully characterize the sample. A general description of the microstructure is described next.

5.2.2 General microstructure description

Sample 2 (95%TD) presented equiaxed grains with an average grain size of 10 ± 3 µm with a monomodal distribution, and a porosity area fraction of approximately 5%. Regions with clusters of small grains and pores, and extremely large pores were observed, as shown in Figure 5.4(b). These clusters could be generated during the initial sintering stages as the lubricant used in the die set evaporated and left the pellet. Also, it could be a result of agglomerates of fine particles and pores, as well as uneven original particle packing during die pressing [95]. These regions were randomly located along the cross section and are not representative of the overall microstructure. However, as these grains are smaller than expected, they affect the representative element size required to obtain a general CSL GBs distribution, as previously discussed.

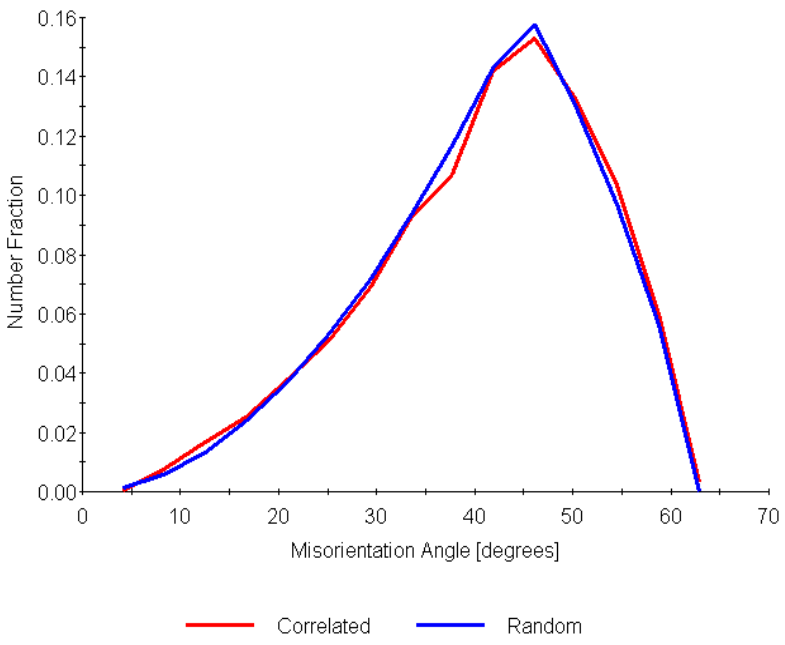

Figure 5.7. Misorientation angle distribution for sample 2

The distribution of misorientation angles obtained for the sample is shown in Figure 5.7. Two different measures are shown: a correlated distribution, calculated from grains that

share a common boundary and a random distribution, which represents the misorientation distribution for grains in the sample when paired at random. For the latter, if the sample has little to no crystallographic texture, the resulting misorientation distribution should be equal to the Mackenzie distribution for a cubic crystal [93]. The correlated distribution presented a maximum at about 46°, which is close to the maximum for the random distribution of 45^0. The amplitude of the peak was lower for the former, indicating that there is a tendency for boundaries with misorientations close to this angle to be present in the material with a frequency slightly lower than that expected from just random pairing of the existing grains.

Furthermore, misorientations distribution function (MDF) plots are shown in Figure 5.8. These plots consist on inverse pole figures (IPF) of the rotation axes of the GBs for different ranges of rotation angles (θ) and can be associated with the GB texture for a specific misorientation angle.

From the plot it can be seen that at low angles the GBs tend to have more random rotation axes, while at larger misorientation angles most of the GBs are produced by rotations about <111> and <101> axes. Additionally, some of the peaks can be related to CSL boundaries. For instance, there is a higher density of GBs with rotation axes close to <111> around the 60° misorientation angle, which is consistent with the presence of $\Sigma 3$ boundaries, as well as the peaks at 50° around <101>, which can be related to $\Sigma 11$ GBs.

However, even the peak values shown in Figure 5.8, are fairly weak in intensity, as shown by the legend in the inset, and in agreement with the results for the overall misorientation angle distribution. No significant texture was seen; as the correlated and random distributions plots have a fairly good match.

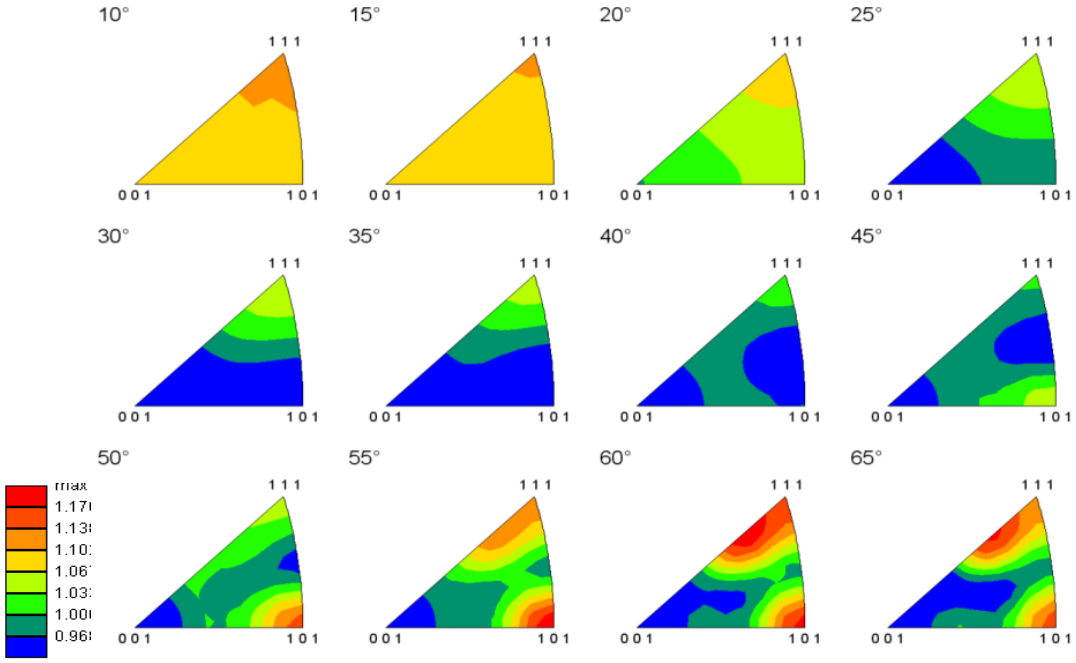

Figure 5.8. Misorientation distribution function plots.

Additionally, the CSL distributions for an insulator d-UO_2 pellet (86% TD density, sample 1), a "regular" d-UO_2 pellet (sample 2, 95%TD) and a conventionally sintered yttria stabilized zirconia (YSZ) sample were compared, and the results are shown in Figure 5.9, to determine CSL distribution variability in samples with fluorite structure (YSZ), as well as two samples manufactured under different conditions.

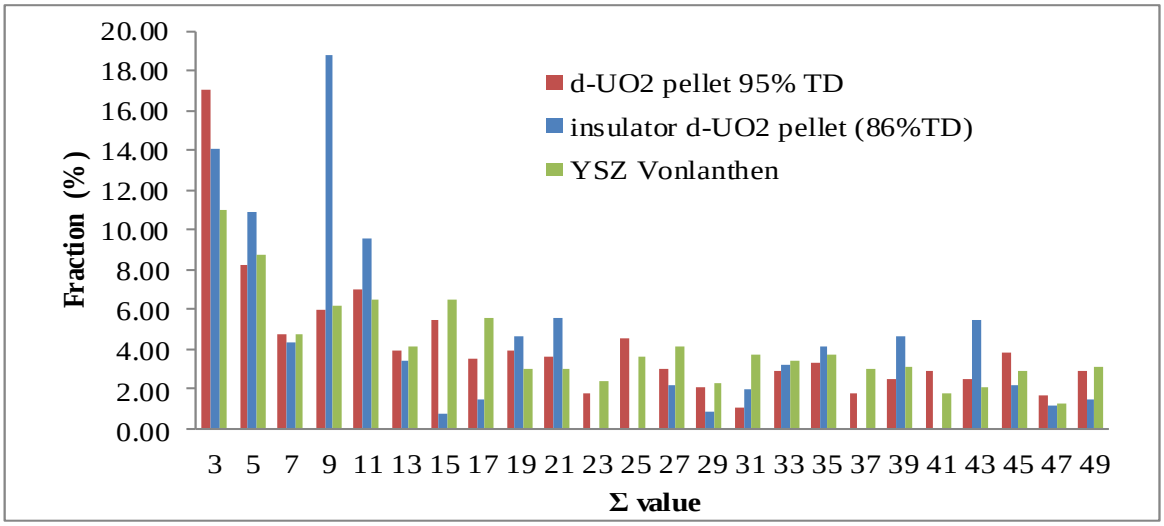

Figure 5.9 CSL distribution of sample 1 (insulator) d-UO_2 pellet (blue), sample 2 (95%TD) d-UO_2 pellet (red) and a conventionally sintered YSZ sample [94].

From Figure 5.9, it can be seen that the CSL distribution differs for each sample. Although their overall CSL fractions are similar (~15-20%), the amount and distribution of the CSL boundaries presented some variations, especially in the case of sample 1 (insulator, 86%TD). The most significant difference between the insulator pellet (86%TD) and the other samples is the larger fraction of ∑ 9 GBs, in contrast to a larger fraction of ∑3 GBs for sample 2 (95%TD) and the YSZ sample. There is also a difference on the distribution for ∑5 and ∑7 GBs. These results indicate that there seems to be a strong dependence on the processing conditions on the CSL distribution for UO_2. These differences can be also attributed to the fact that the results represent the total length fraction and not the total number of CSL. In the particular case of the insulator pellet, ∑9 GBs were longer than other CSL GBs, but not as frequent as, for instance, ∑3 GBs, which were actually shorter, therefore representing a smaller length fraction. This fact is important as not only the CSL,

but also the boundary length and location may affect the formation of percolation paths for mass transport of fission products [92, 100-110].

The difference on the distribution can be also attributed to the studied area in each case, as previously discussed microstructural anomalies (such as pore clusters and large pores) can locally affect the CSL distribution. In case of sample 1, the scanned area was the largest area that was possible to scan as the sample had a fairly large amount of large pores, limiting the areas available for good EBSD scanning. Also, the difference in the distribution could be attributed to variability in the "maturity" of the microstructure, as the insulator pellet had a lower density that was consistent with the intermediate stages of sintering (< 95% TD).

Another important microstructural feature is the porosity. Details on the porosity distribution, spatial location and correlations with the GB crystallography will be discussed below.

5.2.3 Porosity distribution and correlations

A region of 400 μm x 400 μm (Figures 5.2.4, 5.5, 5.10) was studied to obtain statistical data on the porosity, from sample 2 (95%TD). The selected area was larger than the representative area described above to study a larger pore population. Over 2000 pores were analyzed to obtain pore geometry, area distribution and location (inside the grains, at GBs, and at Triple Junction (TJs)) to establish correlations among these parameters. To the authors knowledge there are no data in the literature based on experimental observations that correlates this microstructural features for this material.

(a) 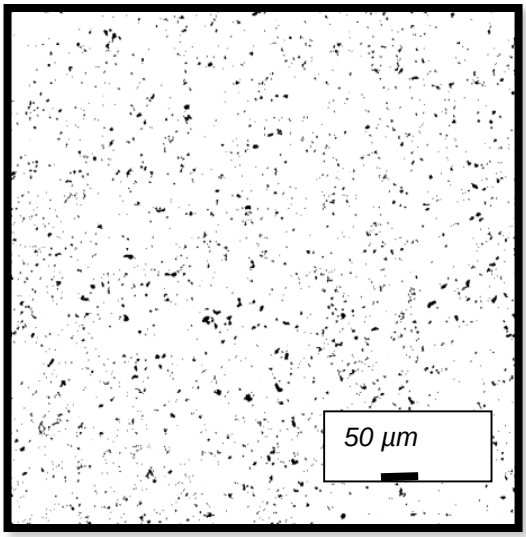

(b) 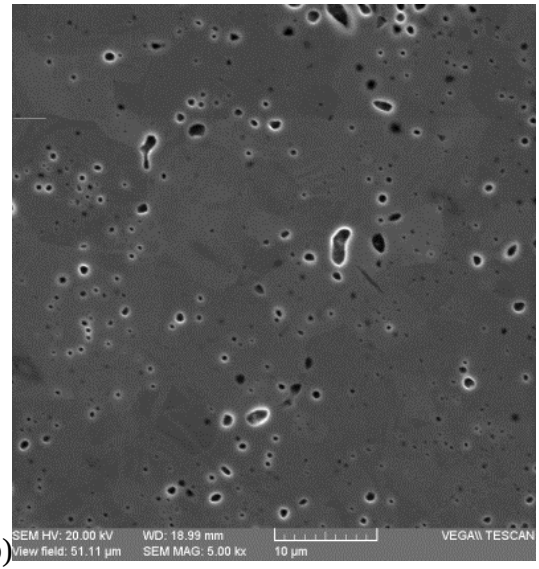

Figure 5.10. (a)Threshold SEM image used to determine porosity statistics and (b) SEM image with details of the porosity of sample 2.

The pore size distribution is shown in Figure 5.11, where the pore size was expressed in terms of pore area, as not all pores presented a round shape, as seen in Figure 5.10(b). The largest fraction of pores consists in pores with an area less than 3 μm^2, most of these pores present an elliptical shape. These results are consistent with data published in other studies of UO_2 samples [103-106].

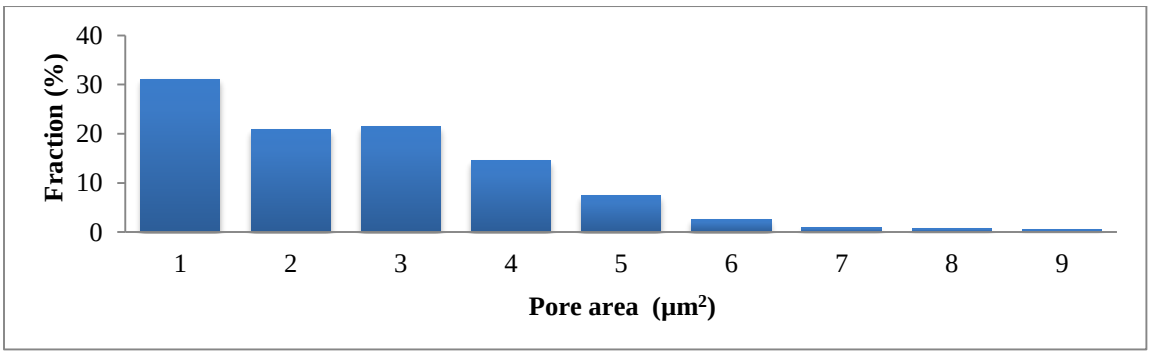

Figure 5.11. Pore size distribution for the studied area of sample 2.

The aforementioned data are not enough to fully describe the porosity as the pore location is not specified. The location of the pores is related to the manufacturing conditions (powder characteristics, pressing, sintering) and plays an important role in the fuel performance, as the in-pile microstructure is continuously evolving due the large thermal gradients, generation of fission products, induced densification and resintering [107]. Intergranular porosity, for instance, can retain fission gases [108] can also pin the GBs and impede the GB motion affecting the kinetics of the grain growth [105, 109]. Moreover, pores can act as pinning agents for GBs due to energy minimization of the GB energy. If the pores are relatedly immobile, the GB will only move if the driving pressure is large enough to create the missing GB area occupied by the pore [110]. During sintering, as the porosity declines the pores attached to the GB can move with the GB and shrink. The GB motion can also sweep pores and induce pore coalescence and growth [111]. Relationships between pore location, size and distribution can help to create more robust models that can predict the in-pile fuel evolution.

A general correlation between the pore size and the location is shown in Figure 5.12. There are no large pores situated inside the grains and most of them are located at triple points. Most of the small pores are located inside the grains or at GBs. These results are consistent with the models presented in the literature that indicates that pores can get trapped at triple junctions [95].

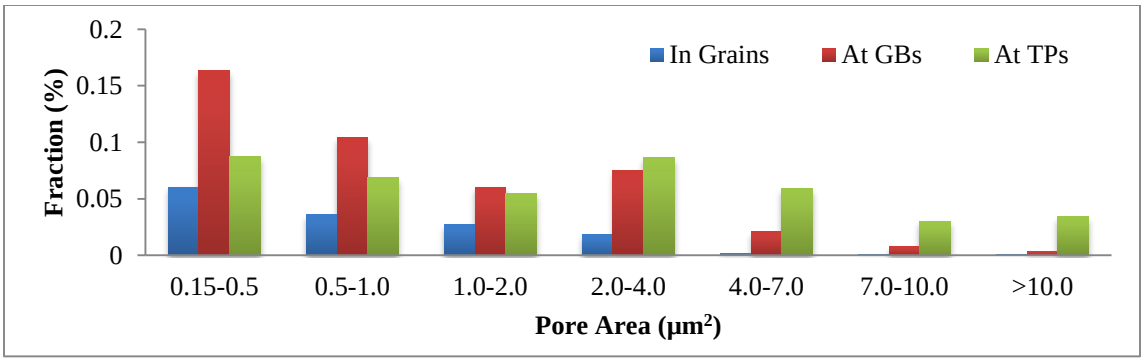

Figure 5.12. Overall porosity distribution at different microstructural sites for sample 2 (95% TD).

Furthermore, a smaller area over the same region, 400μm x 200μm, was analyzed to determine relationships between pore location, size and GB misorientation. A total of 408 pores were studied and classified according to size: as small (< 3 μm^2), medium (3-6 μm^2) and large (> 6 μm^2) and, the misorientations of the GB where the pores are located: low angle (0-15°), mid angle (15°-30°, 55°-70°), high angle (30°-55°) and sigma (CSL boundaries). The general results are shown in Figure 5.13.

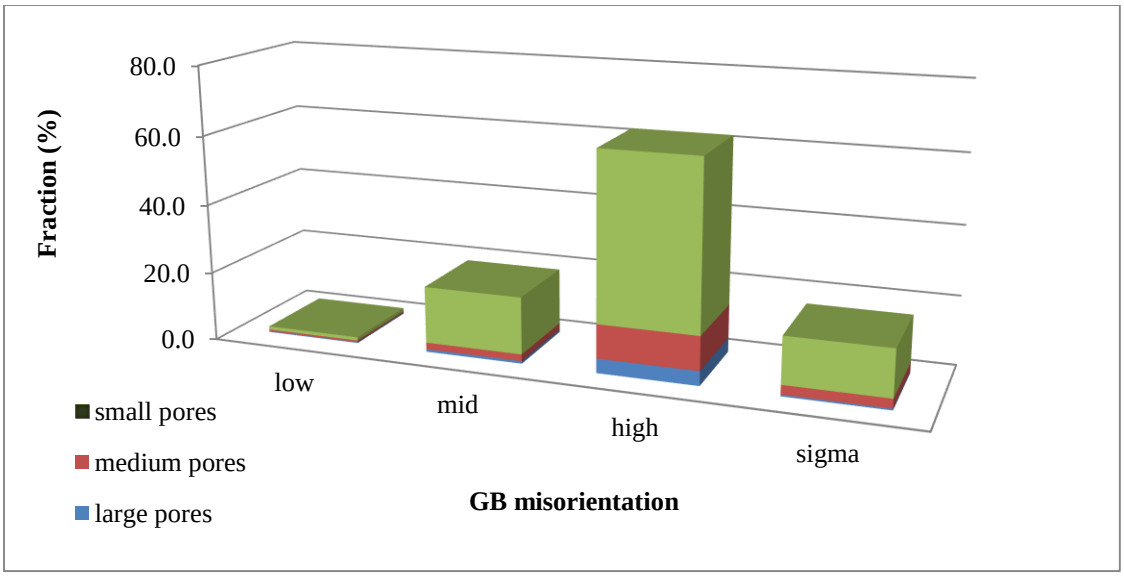

Figure 5.13. Overall distribution of pores located at different GB misorientations for sample 2. Notation: small pores (< 3 μm^2), medium pores (3-6 μm^2) and large pores (> 6 μm^2), high angle (30°-55°), mid angle (15°-30, 55°-70°), and low angle (0-15°).

Small pores exert a minimal dragging force in migrating GB surfaces while large pores can have a strong dragging effect [112]. Therefore, small pores can migrate and attach to both small and high angle GBs, as seen in Figure 5.13. However, low angle GBs tend to have lower GB energies than high angle GBs, as described in Chapter 2. Consequently, seems that large pores migrate to high angle GBs to reduce their GB energy.

As seen in Figure 5.13, the fraction of pores located at mid angle (15°-30, 55°-70°) GBs and CSL GBs are similar (~15%) and presented similar trends on size distribution. These results are comparable to the total fraction of CSL GBs (16%). However, the distribution of pores at different CSL boundaries (Figure 5.14), differs from the general CSL GBs distribution shown in Figure 5.9. There is a larger fraction of pores located at Σ9 and Σ11 and similar total amount of pores located at Σ3, Σ5, Σ7, Σ19 and Σ21, this result could be

related to the GB energy, as briefly discussed in Chapter 1. There is only a small amount of medium pores and an almost negligible fraction of large pores at CSL GBs. Most of the large pores are located at high angle boundaries.

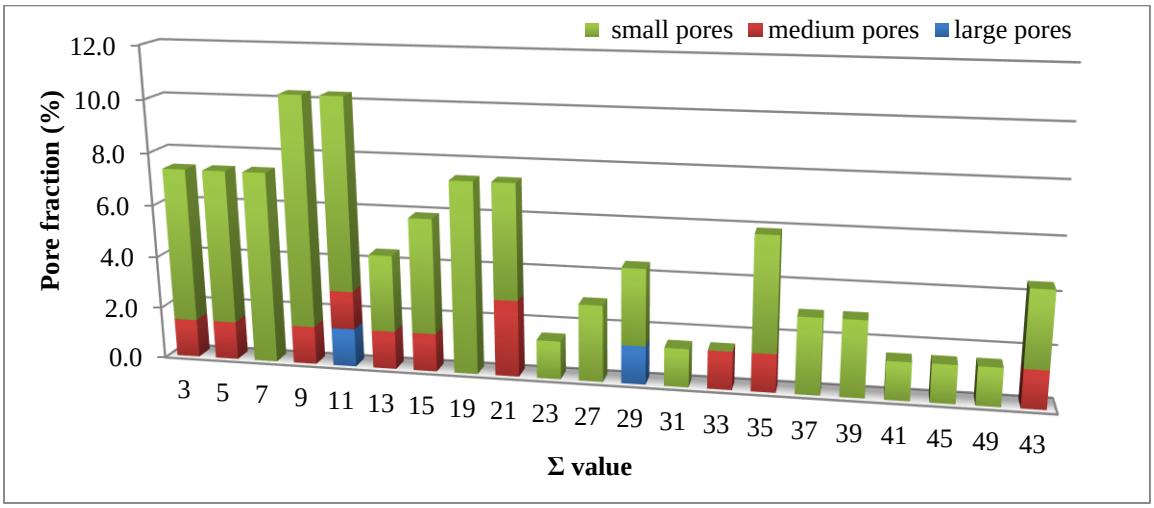

Figure 5.14. Pore distribution along CSL boundaries for sample 2.

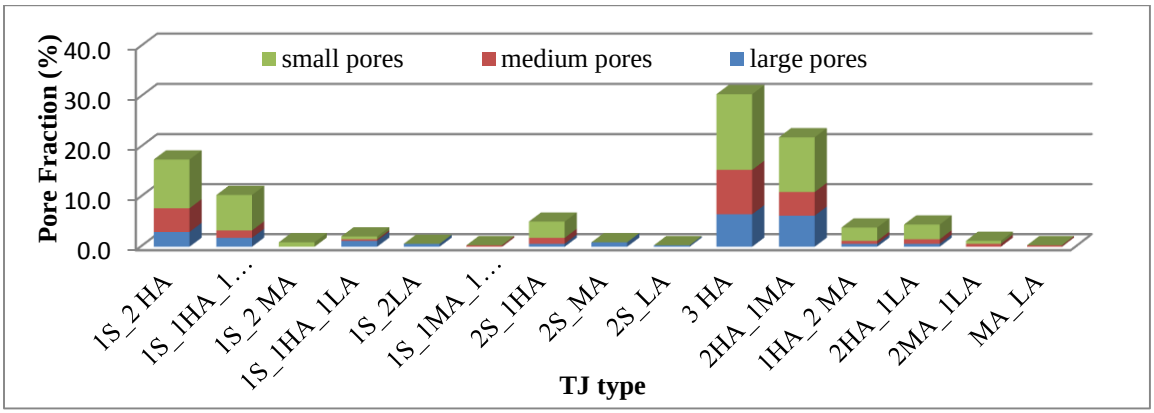

Figure 5.15. Pore location at different TJ of sample 2. The number before the letter stands for the number of GB of that particular misorientation. Notation: S sigma GBs, HA high angle (30°-55°), MA mid angle (15°-30, 55°-70°), LA low angle (0-15°).

The majority of the large pores located at the GBs were only at high angle boundaries. Pores were also located at TJs (Figures 5.12 and 5.15): out of 2788 TJs sampled only 17% had pores inside. The majority of these TJs (96%) contained one or more high angle GB (30°- 55°), 74% of had two high angle GBs and 38% of the TJ consisted of at least one CSL GB.

Furthermore, about half of the pores located at TJs were small pores (< 3 μm^2), the rest consisted in a nearly equal fraction of medium (3-6 μm^2) and large pores (> 6 μm^2). Most of the large pores were positioned at TJs with at least two high angle GBs, and a similar trend can be observed for mid-size pores. These results suggest that pores tend migrate to high-energy sites to minimize the total energy. The latter could also explain the lack of pores situated at low angle GBs.

Concerning the distribution of pores located at TJs with one CSL GB, the largest amount of pores were positioned at TJs that contained a Σ5 GB followed by Σ3 and Σ9 GBs, as seen in Figure 5.16. In this case, there were large pores at TJs with at least one CSL GBs, contrary to the case of the pores located at special GBs, where a negligible fraction of large pores was observed. Pores tend to associate with high energy GBs to minimize the its energy [113]. Moreover, pores located at TJs usually are trapped at the TJs can slow the grain growth [95]. During grain growth, pores can be dragged with the GB during GB motion. As the grains grow and GB shrink and disappear as other GBs grow, porosity attached to the disappearing GB coalesce and pores located at TJs will grow during the grain growth process [112]. One hypothesis that could explain these observations is that these pores are a results from low energy GB lengthening and the shrinkage of high energy GBs that leave behind porosity that migrates to the TJs.

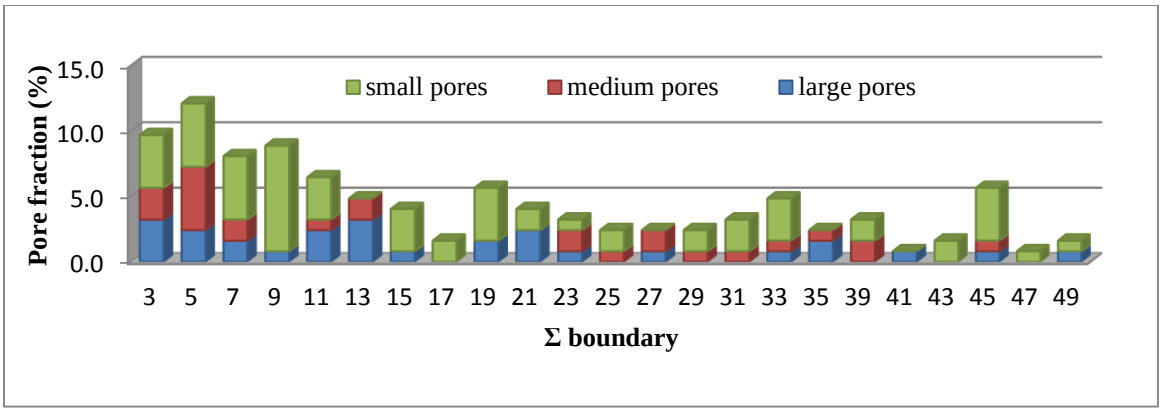

Figure 5.16. Pore distribution at TJs with one CSL GB.

Besides the 2-D microstructural characterization, EBSD maps from serial sections can be used to develop a 3D model of the microstructure that, in turn, can used to characterize the GBs as well as the general microstructure. The results of the study on the variation of the microstructure through the thickness of the sample are described below.

5.2.4 Preliminary 3-D model using mechanical polishing

Indents were used as fiducials, to measure the amount of material removed during mechanical polishing through optical and electron microscopy images. The indents were also used to locate the exact area of study to collect the Electron Backscattering Diffraction (EBSD) patterns. Figure 5.17 shows micrographs of the indents used as a reference for the serial sectioning. There is a clear reduction on the size of the indents as the sample was polished.

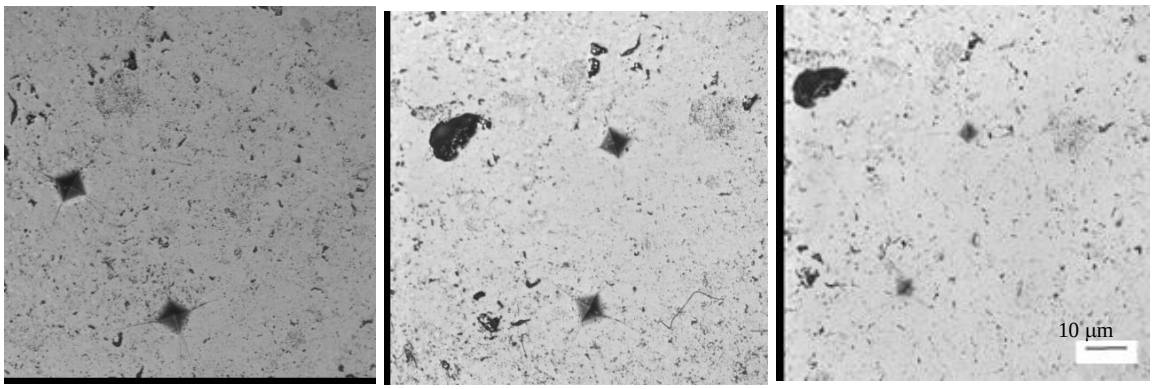

Slice 1 Slice 2 (0.5 μm removed) Slice 3 (2.1 μm removed)

Figure 5.17. Optical microscopy images for the Vickers indents for three serial sectioning slices (sample 2).

For serial sectioning, the last two polishing steps mentioned in the experimental procedures were used. In both cases, the sample was polished for an hour with 0.04 μm colloidal silica. However, the 5:1 suspension seems to be the most effective on removing material. Therefore, variations on the duration of the last polishing step were used to control the amount of material removed. Twenty minutes was sufficient to remove 0.5 μm, while 60 minutes of polishing removed 1.6 μm. An EBSD map for the area of interest is shown in Figure 5.18.

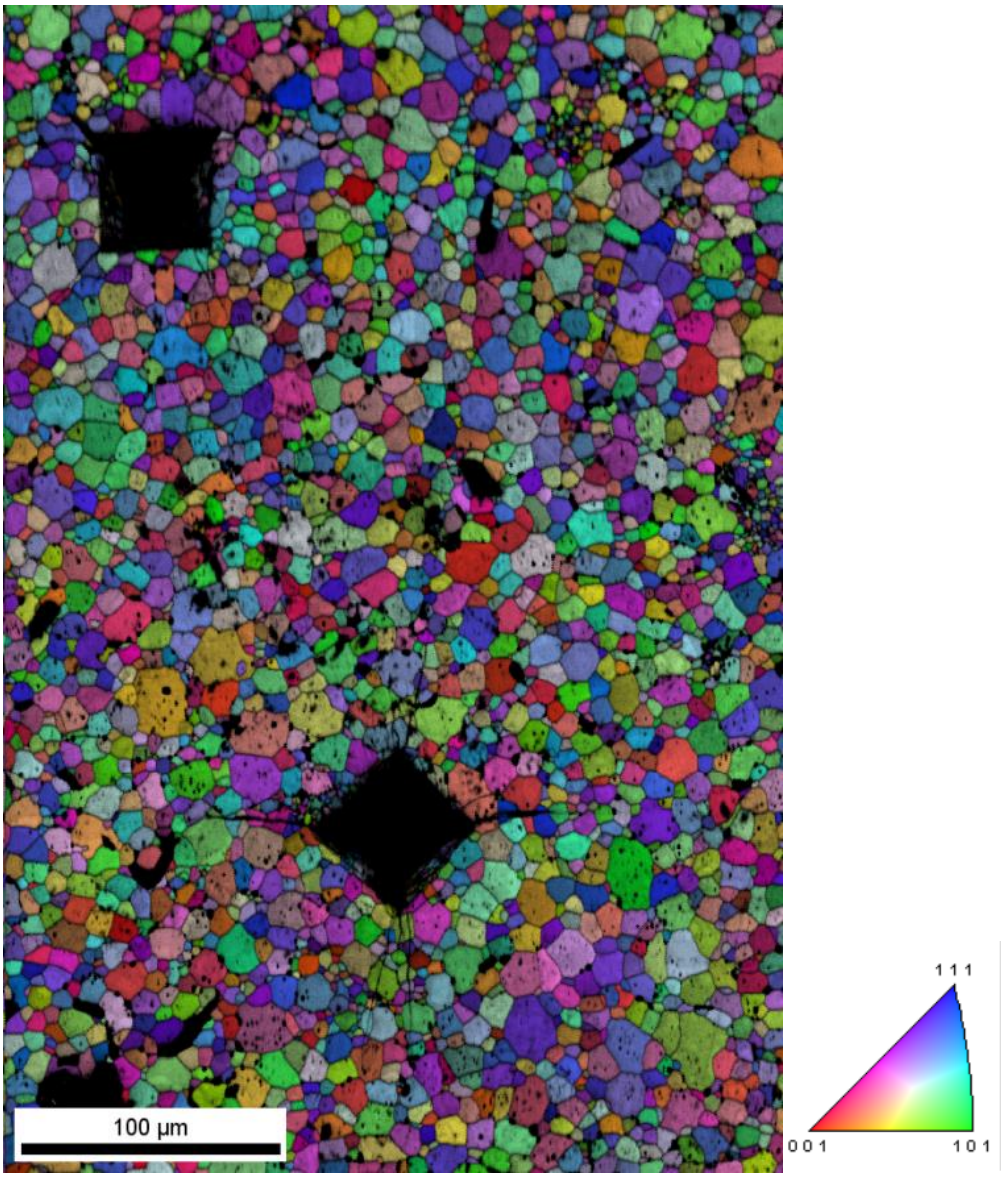

Figure 5.18. EBSD and image quality map (IQ) for slice 1.

The Vickers indents were used for image alignment and a smaller area (60 µm x 100 µm). The area did not include regions of clusters of small grains and pores that were observed in the pellet, as these pores can affect significantly the collected data. The selected area was carefully chosen to have an average grain size and CSL fraction similar to the overall

sample. Nevertheless, the selected region presented some scatter on the CSL distribution for the 3 slices, as it can be seen on Figure 5.19.

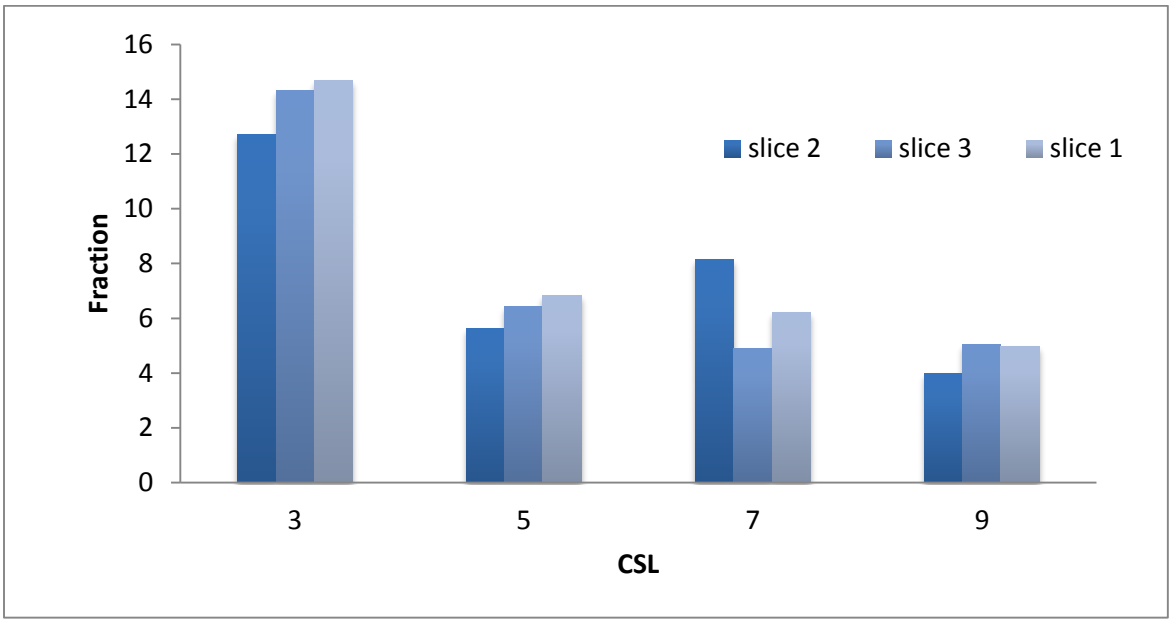

Figure 5.19. Comparison of the fraction of CSL GBs for the 3 slices (sample 2, 95%TD).

The total fraction of CSL GBs for the selected element area was 16.3% for slice 1, 16.6% for slice 2 and 16.6% for slice 3. Although there was not a large variation on the total fraction of CSL GBs, there seems to be a variation on each $\sum$, as the grain size and shape changed across the thickness (Figure 5.20). Similar results can be seen on the misorientation distribution, shown in Figure 5.21.

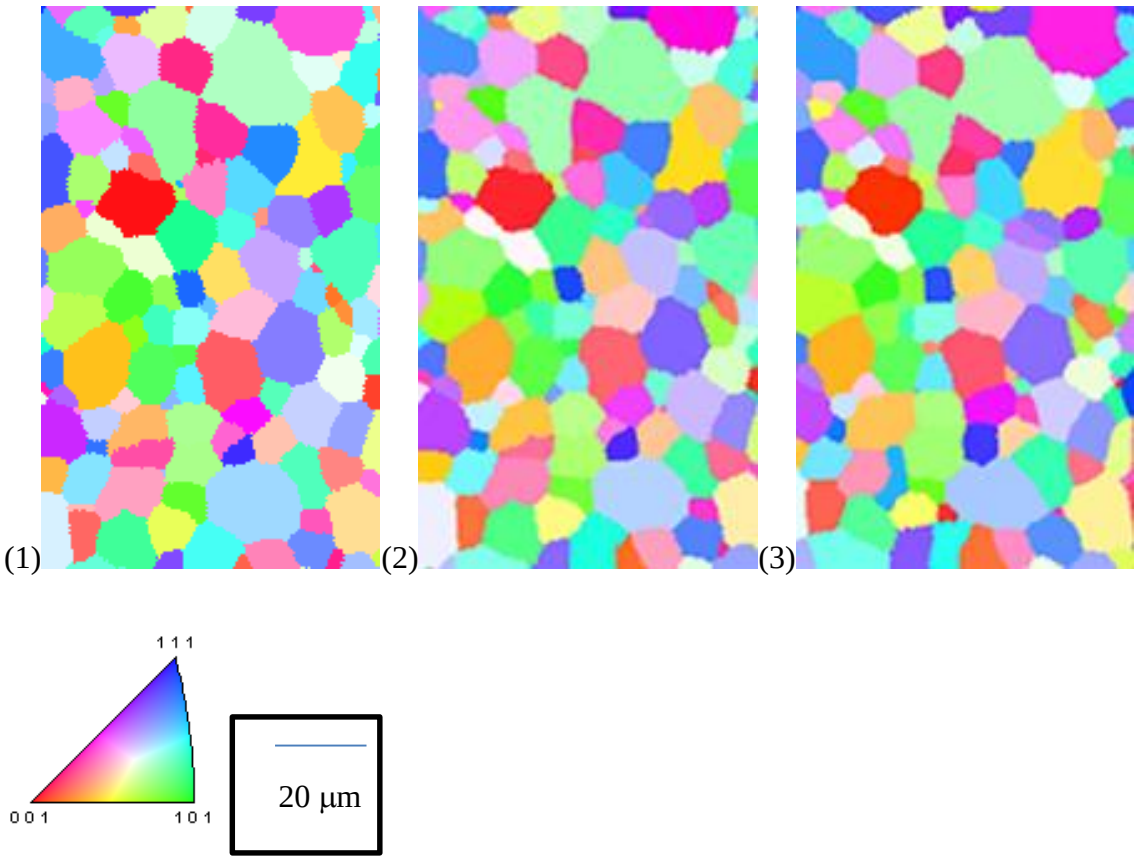

Figure 5.20. Three slices used for serial sectioning. The spacing between the first (a) and second (b) slice is 0.5 μm and between the second and the third (c) is 1.6 μm. The selected area is 60 μm by 100 μm.

The changes in grain size and shape also represent variations on the length and distribution of the GB through the thickness. Figure 5.21 shows the misorientation plots of the two slices, where slight variations on the total number fraction of low and high angle GBs can be seen; this, in turn, can locally affect the mass diffusion properties on the sample [100]. Although the changes in the number fraction of GBs are not significant, GB diffusion can be affected by local variations of the length of the different GBs shown in Figures 5.22. The location, geometry, length and connectivity of the different GBs can affect the mass

transport of the fission products in the pellet. As expected, the majority of the GBs have a high angle misorientation. These GBs are longer in average than mid angle and CSL GBs and most of them are connected (Figure 5.22). However the presence of shorter, disconnected, low diffusivity GBs will affect the overall diffusion behavior of the pellet, as these GBs can act as "percolation bottlenecks" [100]. Moreover, microstructural data from samples fabricated under different conditions, can be used to study how the fabrication parameters can affect the connectivity of GB with misorientation with microstructural-explicit models as the one presented by Lim et al. [102].

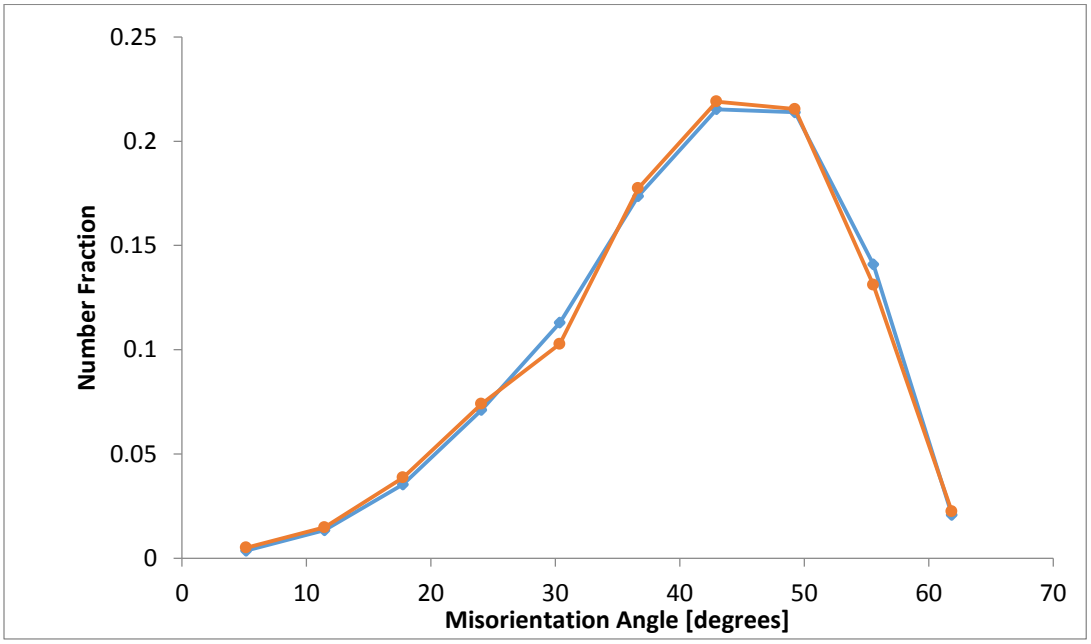

Figure 5.21. Misorientation plots for slices 1 (blue) and 3 (red).

Figures 5.20, 5.21 and 5.22 show local differences on the microstructure and GB connectivity for the three slices. The shape and size of the grains changes and new grains appear. These images were used as input to obtain a 3D image of the microstructure. The

pores were suppressed from the image for ease of manipulation. The 3D reconstruction can be seen on Figure 5.23.

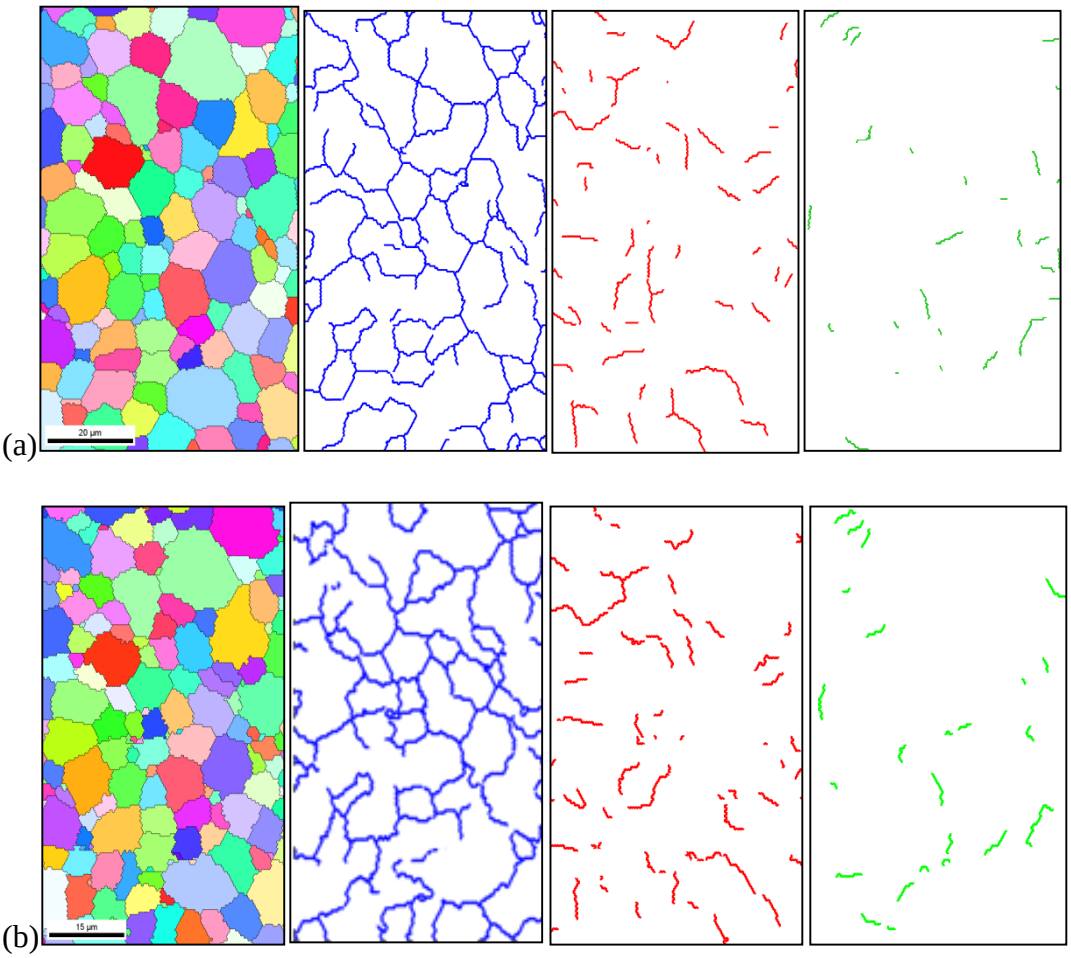

Figure 5.22. EBSD maps, high angle GB (blue), low angle GB (red) and CSL GB (Σ3-11, green) for slice 1 (a) and slice 3 (b)

The reconstructed microstructure can be used as input to develop 3-D finite element (FE) models, based on the actual grain geometry as well as GB misorientation and connectivity, to study mass and heat transport at the nuclear fuel. The model is a part of a broader project not covered in this study but that is based on these results. The results also indicates that is

feasible to obtain 3-D reconstructed models based on EBS maps, SEM and OM images. The methodology used to construct the model was used and improved in section 5.4.2 to reconstruct three different microstructures from serial sectioning using FIB data (EBSD maps and SEM images).

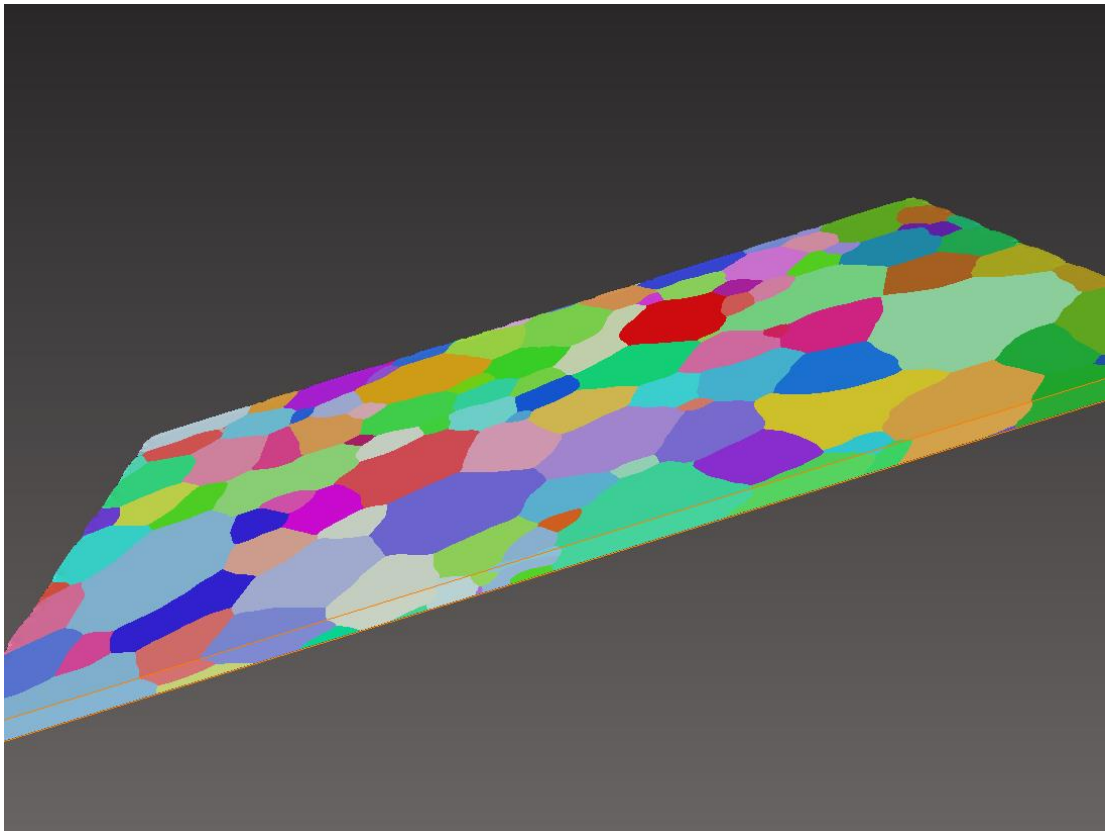

Figure 5.23. 3D reconstruction of the microstructure of the selected area.

5.2.5 What did we learn from sample 2 (95% TD)?

The second sample that we characterized and sample 1 (insulator pellet) presented a similar fraction of CSL boundaries, but a different CSL distribution. These results indicate that the

area selected for study plays a key role on the CSL distribution and on how representative the results can be of the overall microstructure.

The distribution of the porosity and correlated the results with the pore geometry and location were studied. The results show that large pores tend to be lenticular, while smaller pores are more spherical in shape. Also, larger pores tend to locate at TJs while smaller pores are left behind inside grains and GBs.

Finally, a small 3-D reconstruction of the microstructure was done using serial sectioning. Microstructural differences were observed thru the thickness as the new grains appear and some grains disappear. One could speculate that these microstructural changes would affect locally the GB connectivity and therefore the percolation of fission products in the fuel, as Lim et al. results suggest [102].

However, these results cannot determine how the processing conditions can affect the microstructure, especially the CSL distribution, as the two samples so far analyzed were manufactured under fairly different conditions; including the powder composition (see Table 4.1). The results so far indicate that the CSL distribution is sensitive to the manufacturing conditions, but no specific trends can be derived.

The next groups of samples were manufactured under similar conditions except for one; therefore, they can be used to determine if and how a specific processing parameter can affect the microstructure, particularly the CSL distribution.

5.3 Effect of the sintering ramp on the microstructure

Three samples manufactured under similar conditions but with variations on the heating rate of the sintering ramp were studied to determine how this parameter can affect the overall microstructure.

5.3.1 General description of the microstructures

Figure 5.24 shows SEM and optical images for the three studied samples (8, 9 and 10, see Table 4.1). In the case of the samples with the fast (20°C/min, sample #10) and intermediate (10 °C/min sample 8) sintering ramp velocities, the overall surface seem smooth with small round pores, as previously seen for sample 2, and some large lenticular pores due to possible defects during pressing and sintering. However, some cracks and possible grain pullout was observed in sample 9 (sample with slowest sintering ramp), creating a very uneven surface.

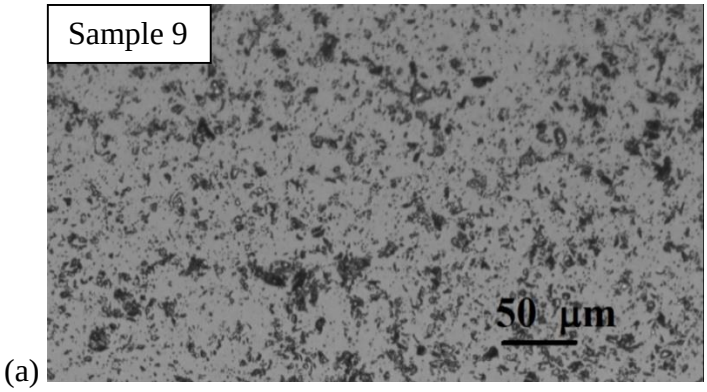

(a)

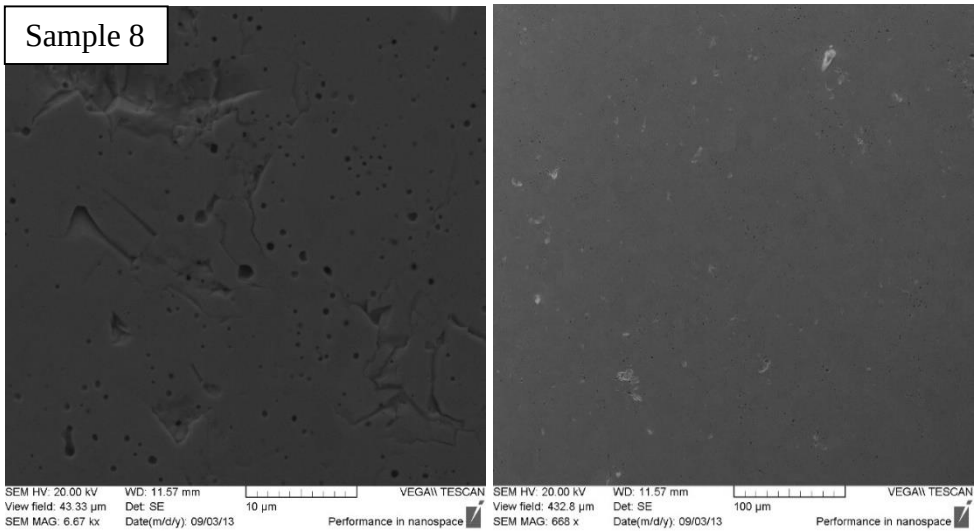

(b)

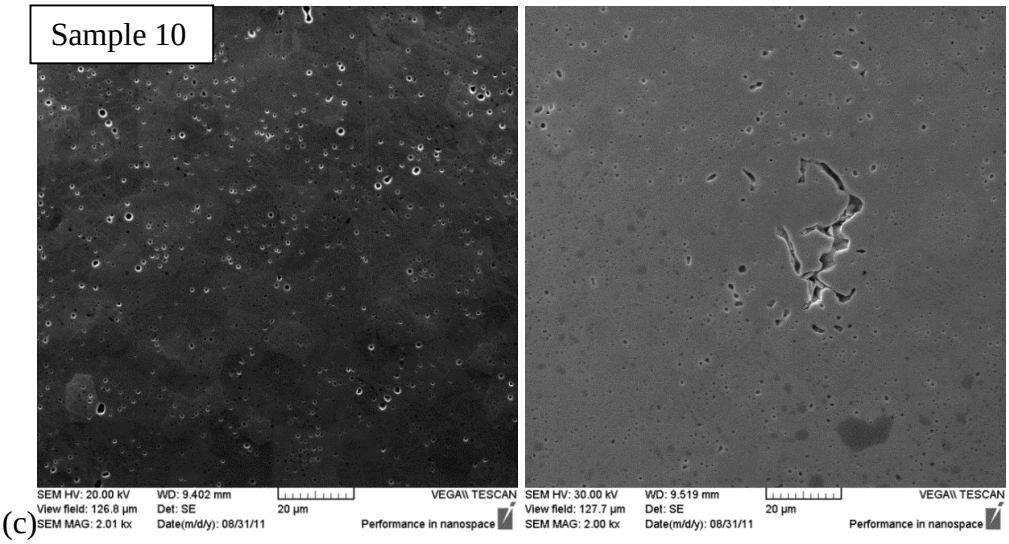

(c)

Figure 5.24. SEM and optical images for the three studied samples: (a) sample 9 (5°C/min), (b) sample 8 (10°C/min) and (c) sample 10 (20°C/min).

Sample 9 was made with the slowest sintering ramp had an uneven surface after polishing. The uneven surface was probably due to grain pullout during polishing caused by the presence of a second phase, presumably U_4O_9.

As seen in Figure 5.25, changes in the initial atmosphere conditions or the initial powder composition can drift the O/M to a region of equilibrium of the UO_2 and U_4O_9 phases. For instance, at 600 K, the equilibrium partial pressure of oxygen for the UO_2 + U_4O_9 region is in the order of 10^{-23} atm, indicating that a precise control of the oxygen content is required during the sintering cycle. Presumably a faster heating cycle will avoid the reach of equilibrium of the two phases during heating and sintering will occur at the UO_{2+x} region.

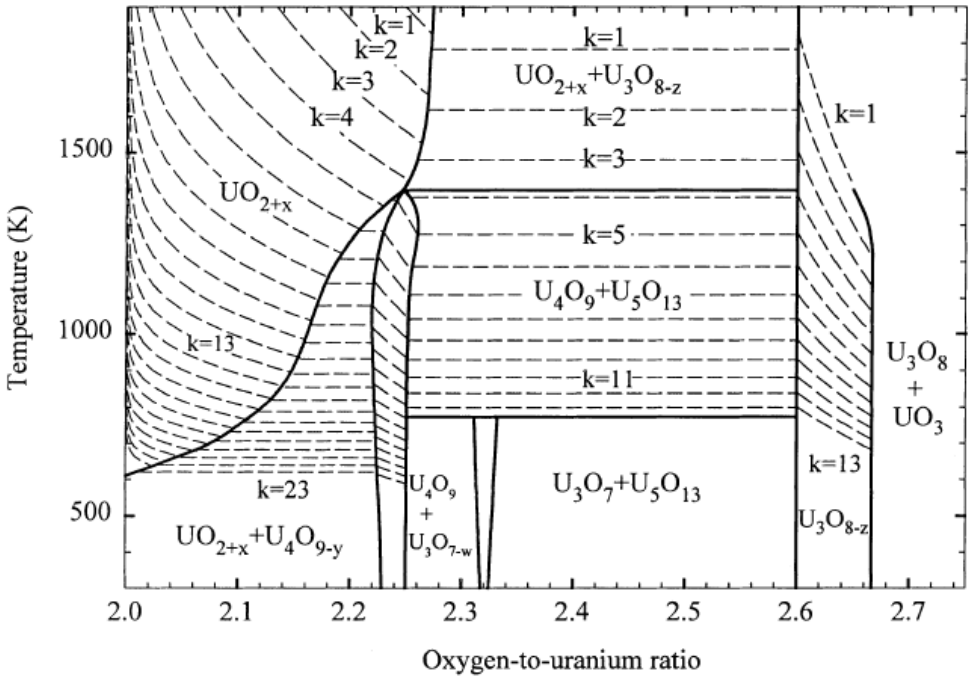

Figure 5.25. Phase diagram of the U-O system with oxygen pressure isobars superimposed. The isobars are indicated by the index k in $p=10^{-k}$, with p in atmospheres [114].

In order to corroborate the hypothesis of the presence of a second phase, EDS data were obtained for different spots of sample 9 and compared to a point scan for sample 10. The results were used to determine if there were variations on the composition and corroborate the presence of a second phase. The results are shown in Figures 5.26, 5.27 and Table 5.2.

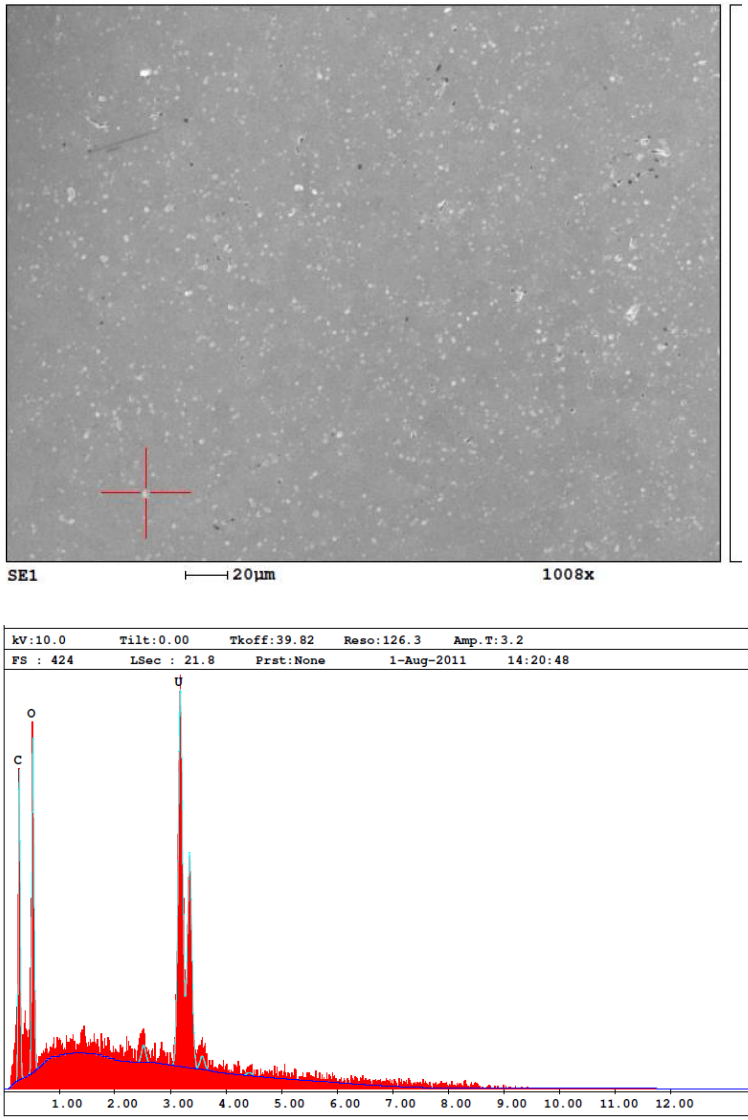

Figure 5.26 EDS spectra for the selected region (indicated by + in the SEM image) of sample 10.

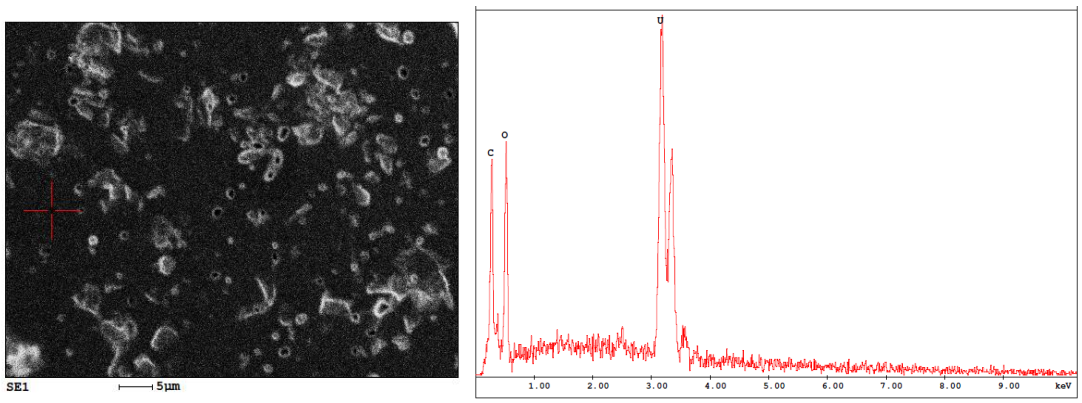

(1)

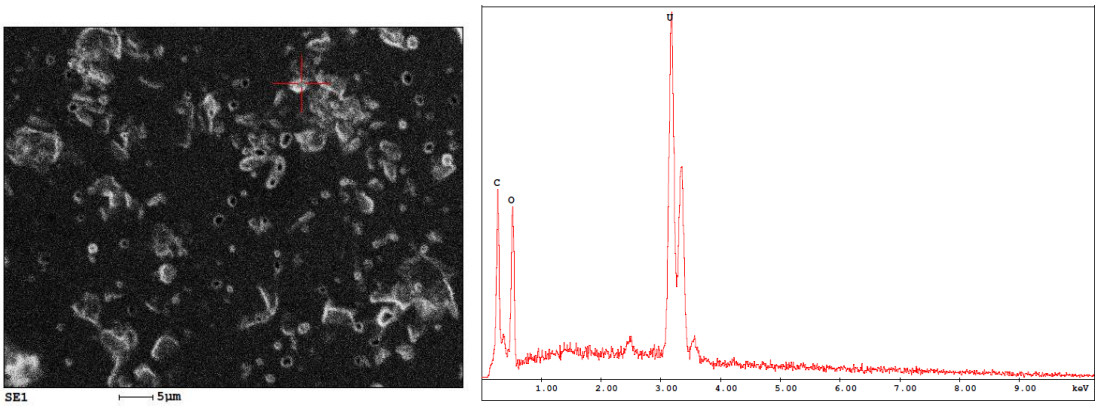

(2)

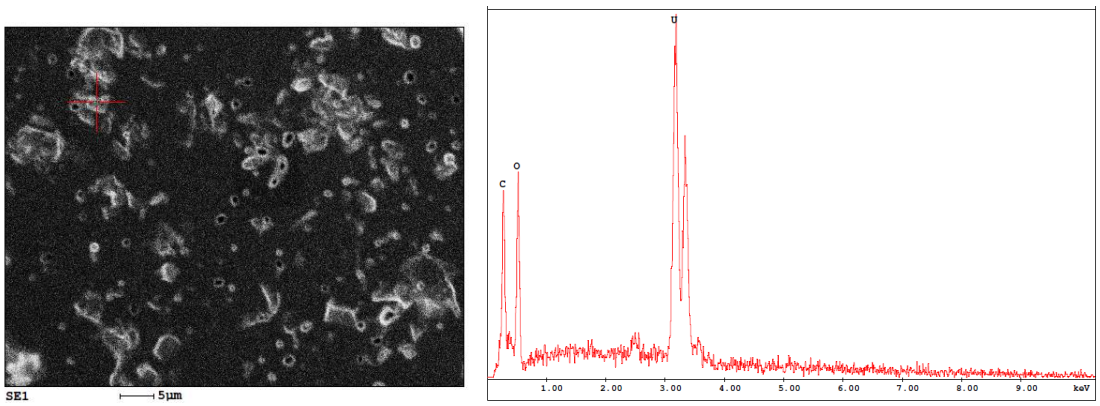

(3)

Figure 5.27. EDS spectra for selected regions (indicated by +) of sample 9.

Table 5.2 EDS quantitative results for samples 9 and 10

Sample	U at.%	O at.%
9 (1)	24	76
9 (2)	23	77
9 (3)	23	77
10	26	74

The carbon peaks in the EDS spectra could be explained as residue of the diamond suspension during polishing, signal from the carbon tape and/or contamination on the SEM chamber. In the case of sample 9, no significant compositional differences were observed in the EDS for the selected areas, as seen in Table 5.2. However, the results were compared with an EDS scan on sample 10 indicated that sample 9 had a slightly larger atomic percent of oxygen atoms, that could be explained by the presence of a second phase. Moreover, the point scans for sample 9 indicates slightly higher oxygen content at the grey regions, which could support the hypothesis of a second phase. The latter could be consistent with the results reported by Murray [115], where low temperature oxidation of UO_2 in the composition range of UO_2-U_4O_9 resulted in a statistical distribution of oxygen throughout the lattice while maintaining the fluorite structure. Moreover, compositions in the range of UO_2 to U_4O_9 are a single phase [115], that could explain why no significant compositional differences where observed in the point scans.

Samples 8 and 10 where further characterized to determine if and how the heating ramp velocity affects the fuel's microstructure.

5.3.2 Characterization of samples 8 and 10

Two of the three analyzed samples where studied using EBSD, as seen in Figure 5.29. Sample 8, had significantly more manufacturing defects than sample 10 as seen in Figures 5.24 and 5.28. As the surface quality on sample 8 was not as good as in sample 10, a smaller EBSD scan was performed (200 μm x 200 μm) to determine if the sample could be scanned. The comparisons of the obtained results are only as a proof of principle, as the selected areas have different sizes.

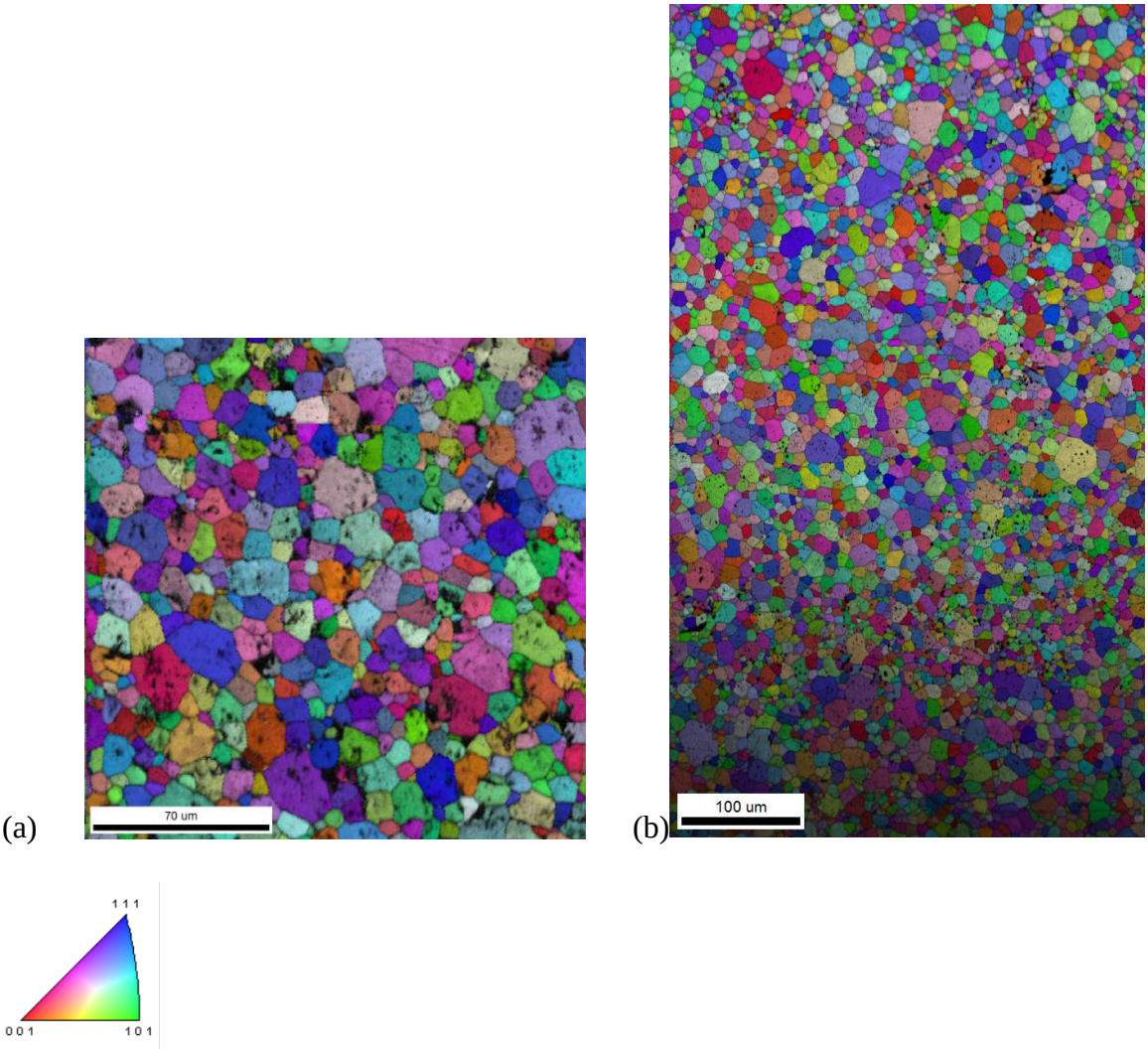

Figure 5.28. IPF and IQ maps of samples 8 (a) and 10 (b).

The general results can be seen in Table 5.3. From the results it can be seen that both samples have similar CSL fractions and distributions, although the fraction of Σ3 GBS seems to increase slightly for sample 10. Additionally, sample 10 has an average grain size slightly smaller than sample 8. However, the results from Figure 5.29 indicate the sample 10 has a larger fraction of large grains, with almost a bimodal distribution in both cases. Furthermore, these larger grains were studied by using a partition of the data for grains larger than 2.5 times the average size; the selected data are shown in Figure 5.30.

Table 5.3 General results for sample 8 and 10. The CSL fraction represent the length fraction of GBS that fits the CSL model using the Brandon criteria. The fraction of ∑s boundaries represent the fraction of CSL boundaries distribution over the CSL population.

Sample	**°C/min**	**Gs**	**dev**	**misorientation**	**CSL**	**Σ3**	**Σ5**	**Σ7**	**Σ9**	**Σ11**
8	10	8.3	4.6	40.7	0.16	0.12	0.06	0.06	0.07	0.06
10	5	7.9	4.4	40.9	0.16	0.15	0.07	0.07	0.06	0.06

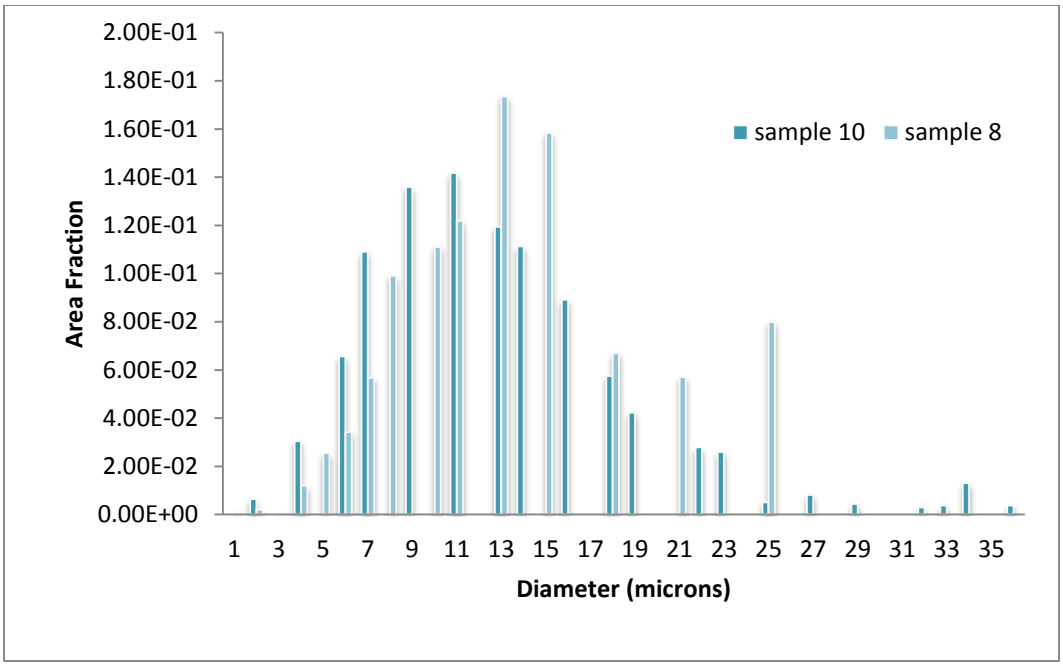

Figure 5.29. Grain size distribution for samples 8 and 10.

(a)

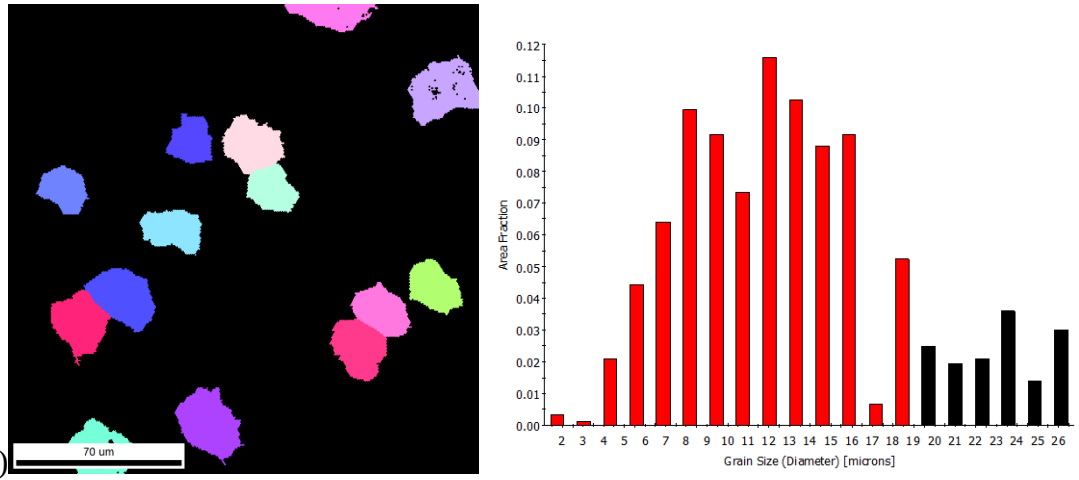

(b)

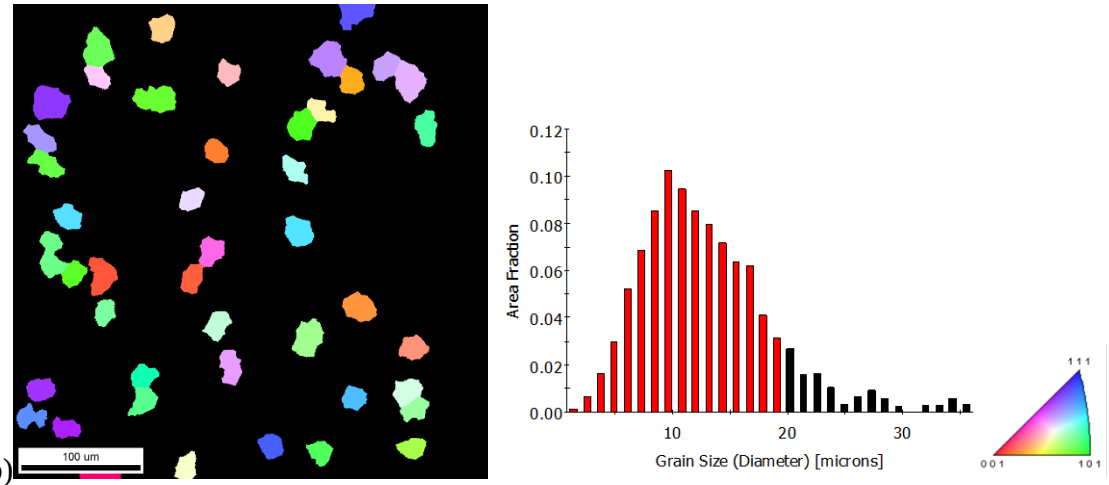

Figure 5.30. Selected grain size and grains for the partition: (a) Sample 8 and (b) Sample 10.

Finally, the overall crystallographic texture for the two samples was compared with the crystallographic texture of the partitions; the results are shown in Figure 5.31.

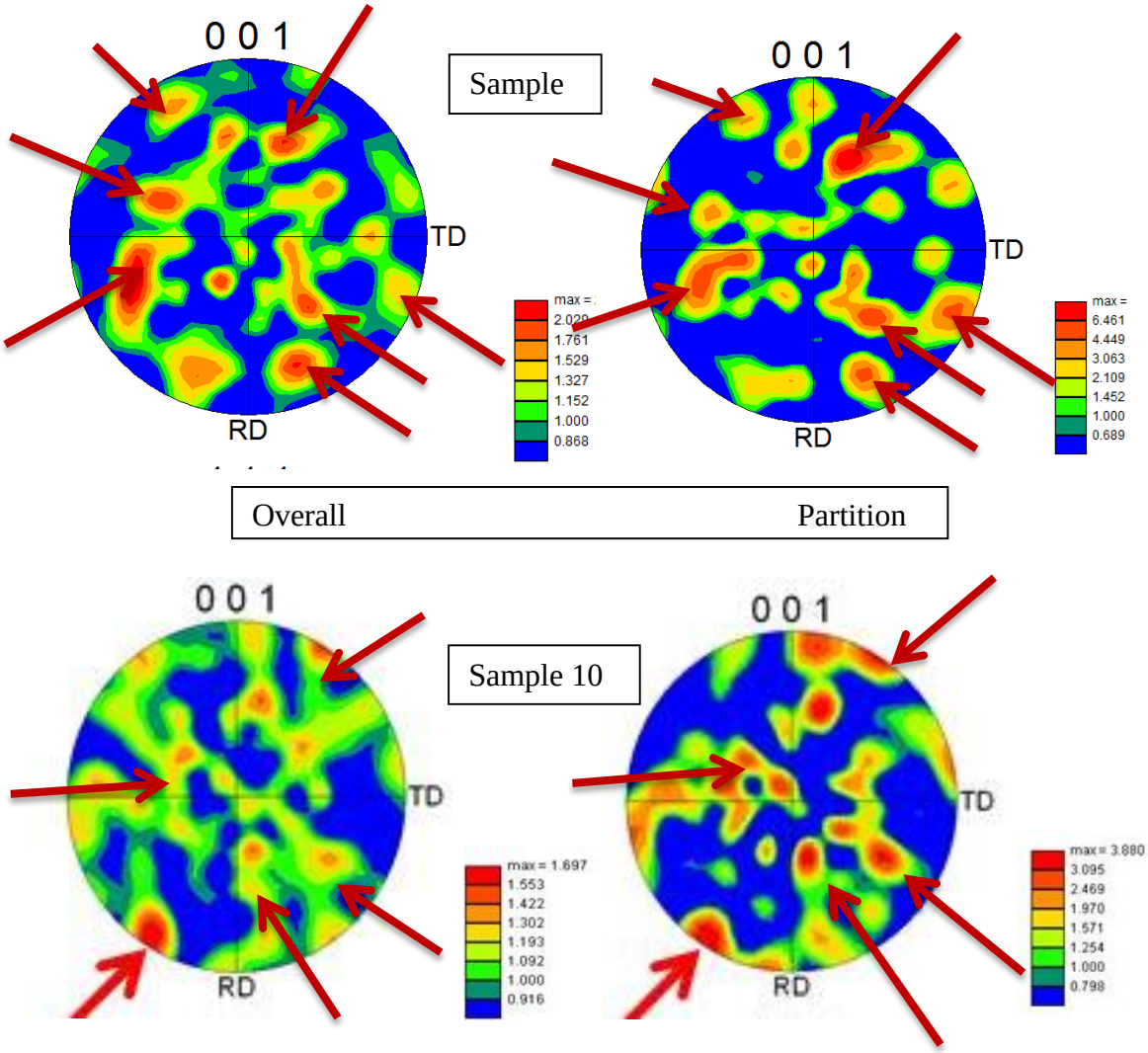

Figure 5.31 Crystallographic texture distribution for samples 8 and 10. RD is defined as the rolling direction and TD is the transverse direction. For this case, both directions are radial directions, as both directions are contained on the plane of the sample (RD is the y axis and TD is the x axis on the sample plane).

The pole figures shown in Figure 5.31 represent a two dimensional projection of the distribution of the different crystallographic orientations for the grains. The three dimensional orientation distribution functions (ODF) give the relative frequency of crystals

having the same orientation described by Euler angles and measured in multiples of the random distribution. Therefore, these maps represent a quantitative tool to determine the level of preferential texture of a sample [106].

The lower the texture intensity is, the less sharp the texture; consequently the grains are oriented randomly. Usually also the larger the dataset, the smaller the texture intensity as there are more data points. The latter can explain the results for sample 8, where the texture peaks at around 8, compared to the overall distribution ~2. However, in both cases it can be seen that the texture seems to be driven by the larger grains, as highlighted in Figure 5.31 by the arrows. Additionally, the results indicate the grains are somewhat preferentially oriented at the radial direction. These results suggest that there might be some preferential crystallographic orientation for grain growth.

5.3.3 Lessons learnt from samples sintered under different sintering ramp velocities

Three samples that were manufactured under the same conditions, but with changes in the heating rate of the sintering ramp. A good control on the sintering atmosphere is required to fix the sample composition. Although the sample's stoichiometry is unknown, the obtained results suggest that a slow heating ramp velocity possibly shift the sample composition to a two phase region. Therefore, a fast heating ramp seems the best way to assure that the samples are sintered at the UO_{2+x} region.

Additionally, larger grains seem to control the crystallographic texture of the sample, suggesting that grains oriented in specific crystallographic directions grow preferentially over randomly oriented grains. However, so far no crystallographic data on the GBs of

these grains has been studied. Why are these grains growing larger as compared with the rest?

Moreover, how prominent is the effect of the larger grains is over the sample's texture? Also, why these grains are growing more: is this related to the GB mobility? If so, which GBs are moving more?

Samples with known stoichiometries were studied to determine how and if the oxygen content affects the microstructure. The results are shown in next section and will try to answer some of these questions.

5.4 Effect of the oxygen content (stoichiometry) on the microstructure

So far, samples with different densities and manufactured using different heating velocities were studied. Results from the characterization of these samples seem to indicate that the CSL distribution varies depending on the sample and the variability can change with the selected area. Manufacturing defects, more specifically pressing defects, can affect locally the microstructure, causing variations on the porosity, grain size and GB misorientation, as well as the CSL fraction and distribution. Also, precautions are needed to control the sintering atmosphere's oxygen content as well as the heating ramp rate as a second phase could appear.

The next set of samples was manufactured with no lubricants. Die lubrication allows better packing of the powder particles during pressing, but leaves residues that usually evaporate, decompose or sublimate during the initial sintering stage. In order to avoid defects such as cracking and bulging, the green pellet needs to be heated very slowly [113], which can affect the sample composition as previously discusssed. If the sintering is done without

lubricants there is no need to take precautions during the initial heating of the sample. However, the sample's green density will be lower as the particles cannot easily flow and accommodate in the mold.

These samples were manufactured under the same conditions, as described in Table 4.1, but with variations on the oxygen content to control the final stoichiometry. The microstructure of samples with different stoichiometries can help us emulate different radial positions on the fuel, as the large temperature gradients in-pile can generate O/M gradients, as described on Chapter 2.

The samples were characterized using both 2-D and 3-D techniques. First, serial sectioning data was obtained using FIB for the three samples (samples 4, 5, 6; O/M=2.0.2.06 and 2.14); the data were used to obtain 3-D models of the microstructure. Then, the samples were then mechanically polished, and larger areas were analyzed to determine variations on microstructural features such as grain size distribution and GB character within the sintered pellets over distances larger than those that could be examined with the FIB data. The results as well as the advantages and disadvantages of each method are discussed next.

5.4.1 General description of the microstructure from FIB

Typical EBSD maps that show both crystallographic orientations and porosity are shown in Figure 5.32. As seen in the figure, there are some differences in the three microstructures. The stoichiometric sample has more curved GBs, whereas $UO_{2.14}$ has straighter GBs. This is an indication that the microstructure of the oxygen rich sample is indeed more "mature" than for the stoichiometric sample. Curved GBs are common in samples that are in the intermediate stages of sintering, as should be the case here. These results are consistent with the literature [96] as the oxygen rich sample has a higher defect density, which makes GBs and pores more mobile and should lead to straighter GBs. In all cases some abnormal grain growth was observed for grains with more than 6 facets; this behavior is usually associated with the final stage of sintering, and it could be a result of local higher density regions or high energy GBs

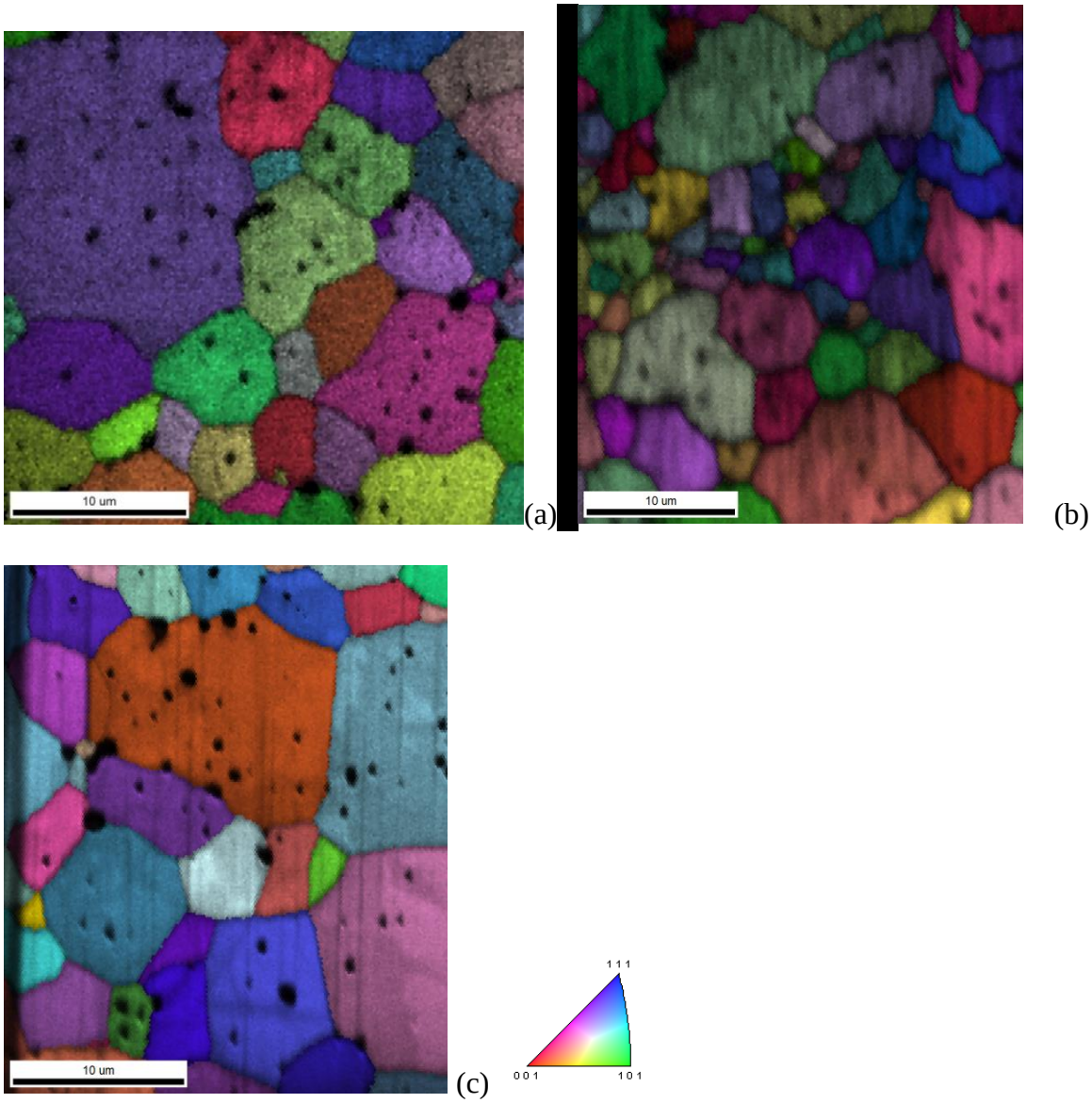

Figure 5.32. Examples of the three microstructures: superimposed image quality maps and inverse pole figures for the (a) $UO_{2.00}$ (sample 4), (b) $UO_{2.06}$ (sample 5) and (c) $UO_{2.14}$ (sample 6). Colors for each grain correspond to their out-of-plane crystallographic orientations (radial direction of the pellets) given by the standard triangle legend.

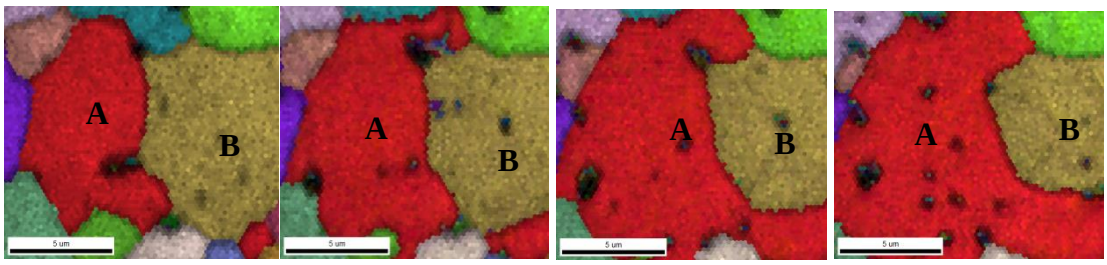

Figure 5.33. Detail of the GB-pore interaction for two grains (A) and (B) in the $UO_{2.00}$ sample. The slices are separated 0.66 μm in the radial direction of the pellet.

The driving force of grain growth is a decrease in free energy that is accomplished by the reduction in the total GB area. The GB migration occurs by atom transport across the GB due a surface curvature and a pressure gradient between grains. In porous materials the grain growth is a result of interaction between GBs and pores, that can cause pore dragging decreasing or impeding the GB motion [112].

In general, the migration of a GB should be accompanied by the migration of its TJs and GB migration will depend ability of TJs to move [117]. However, large pores, located at TJs could impede GB mobility due to GB pinning. In fact, most of the pores are located either inside larger grains or at TJs, as seen both in Figures 5.32 and 5.33. These pores seem to affect the GB motion as the passing GB can either stay behind or find a path to pass the pinning pore and leave it behind. Therefore, the grains with more mobile GBs will contain large pores.

These observations provide some indications of how the GBs move to make the microstructure evolve in time. In this particular case, images through the thickness of the stoichiometric sample (see Figure 5.33), which show a snapshot of what the microstructure was doing at the moment the temperature was reduced and the sintering stopped (or slowed

down significantly), suggest that the GBs move around the pores that are pinning them to make grains grow. Note that GBs between the (A) and (B) grains are pinned at several points through the radial direction.

This GB morphology was observed only in some boundaries and is likely related to GB energy and mobility. When a GB approaches a pore its energy increases and once it reaches the pore its energy decreases; then the boundary energy needs to be increased to pull away from the pore [95]. Therefore, the GB might not have enough energy to pull away from the pore, but because some neighbor GBs are concave, the GB will move towards them and around the pore.

The GBs that are touching or located close to the large pores are curved and the curvature seems to decrease in the areas where there is no interaction with the pores.

The images show how the bowed boundaries are moving around the large pore located at a TJ. Once the GB passes the pore, it seems to straighten out until a new pore is reached. The direction in which the GB will move seems to depend on the GB curvature, as grains tend to grow towards their center of curvature. The latter also seems related to the number of neighbors: small grains, with convex curved GBs and less than 6 facets disappear, and larger grains with more than 6 facets grow. The facets of more stable grains, those with at least 6 neighbors, are in general straight when no pores are present at the GBs or TJs; while GBs in grains with less than 6 neighbors tend to be curved regardless of the presence of pores.

Regarding the grain size, an average value was obtained over the thickness of the samples, using several 2-D slices spaced by at least one grain thickness, along the radial direction, as seen in Figure 5.34, to avoid double counting grains. The stoichiometric sample

(O/M=2.0) had an average grain size of 3.6 ± 3.1 μm, the sample with intermediate oxygen content (O/M=2.06) was 3.4 ± 2.0 μm and the oxygen rich (O/M=2.14) sample 3.9 ± 2.7 μm. Although grain sizes are similar, $UO_{2.14}$ has slightly larger grains, as expected. The main difference seems to be grain shape, as grains in $UO_{2.14}$ are more equiaxial and less curved, as discussed above, which, again, is consistent with the faster kinetics expected in that case. Regarding the sample with intermediate oxygen content, the image in Figure 5.35 shows clearly that there was a larger density of small sized grains, including clusters of small pores and grains. As previously discussed in section 5.4.2, these clusters can significantly affect the distribution of grain size locally. Therefore, a larger dataset might be needed to obtain more representative results.

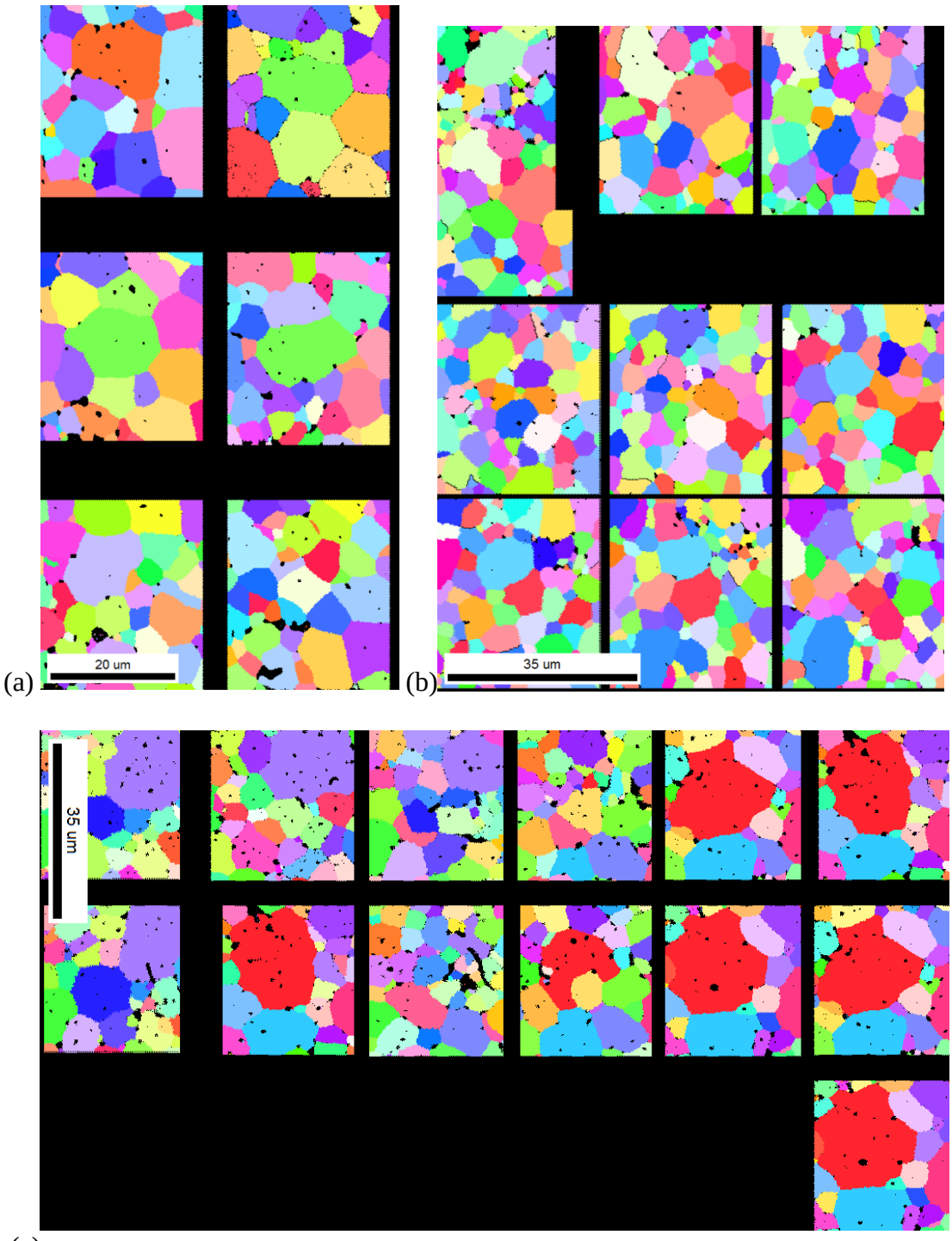

(a) (b)

(c)

Figure 5.34. Selected slices from the FIB serial sectioning set of the studied samples: (a) O/M=2.00, (b) O/M=2.06 and (c) O/M=2.14.

Special GBs that match the Coincidence Site Lattice (CSL) model [98] were analyzed as well, since low energy GBs can be found among them [118]. The distributions of CSL boundaries for the three samples are shown in Figure 5.35.

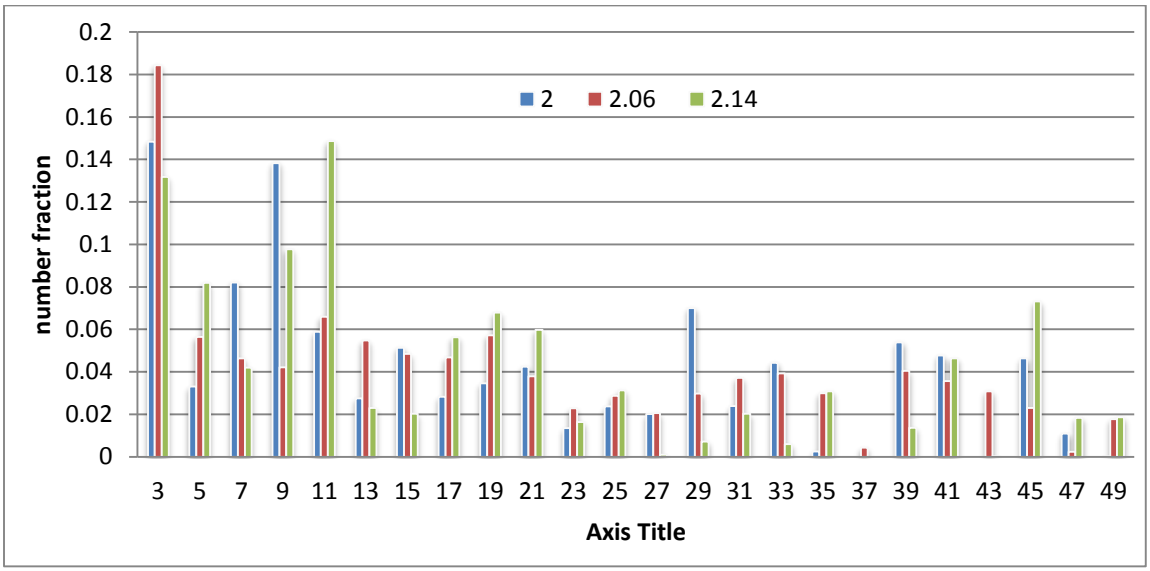

Figure 5.35. Distributions of CSL GBs for the three samples.

The results show that all samples had a similar CSL fraction, ~0.20. However, there are some differences in their CSL distributions. For instance, the stoichiometric sample had a large fraction of Σ3 and Σ9 GBs. This could be related to the low mobility of these GBs and the GB pinning. It seems that lower energy GBs grow (in length) preferentially over high energy GBs to minimize the energy of the system. In the case of $UO_{2.14}$, as the GBs have more mobility, there is still a large amount of Σ3 and Σ9 GBs, but also more Σ5 and Σ11 GBs, so energy can be minimized by grain growth, which reduces interfacial energy. Regarding the distribution of the intermediate stoichiometry sample, no large peaks (except at Σ3) were observed. The distribution could be related to a larger amount of grains and

grain boundaries, creating a more diverse GB population that could be more representative of the overall microstructure. As previously discussed, the analyzed areas might be too small to be representative of the microstructure, as large pores and pore clusters were observed in the samples, and some of the larger grains occupy most of the studied area in some cases (2.0 and 2.14 samples). These defects can locally affect the microstructure and not be representative of the overall microstructure. Therefore, a larger scan of the area that better represents the microstructure is needed. Section 5.4.3 includes scans of larger areas that were studied to determine how representative the FIB area was in comparison to the overall microstructure.

Moreover, the serial sectioning images were used to reconstruct the 3-D microstructure of the samples to evaluate actual grain sizes and shapes and to obtain the GB planes. The results are shown next.

5.4.2 3D Microstructure Reconstruction

The SEM images as well as the EBSD image quality maps were used to align the slices. Once the images were aligned, EBSD orientation maps were used to reconstruct the grains on each sample. Figure 5.36 shows the three different types of images used in the process.

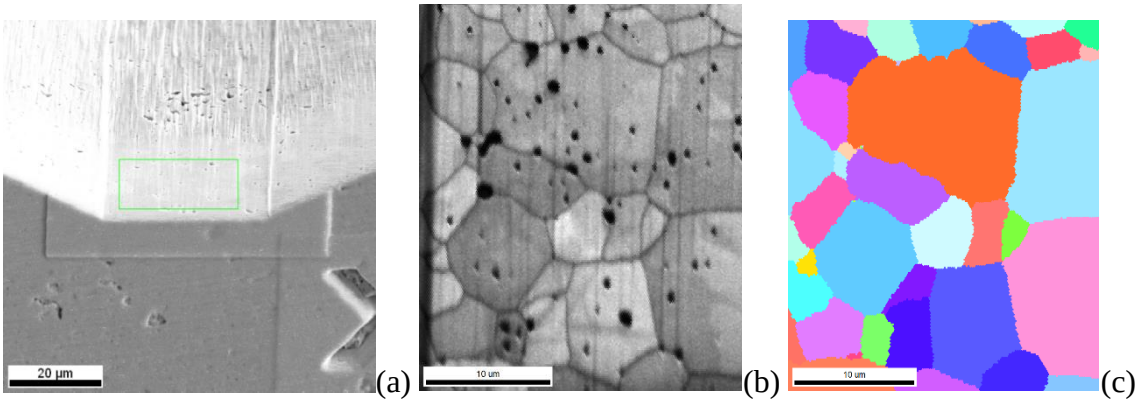

(a) (b) (c)

Figure 5.36. Examples of the different images used for alignment and reconstruction of the microstructure. (a) Secondary electron SEM image, (b) EBSD Image quality map and (c) EBSD orientation map.

The reconstructed microstructures for two samples are shown in Figure 5.37. An interesting feature is that in all cases there is an elongation of the grains in the radial direction of the pellet that is more pronounced in the $UO_{2.00}$ sample. Some selected grains of each microstructure are shown in Figures 6c and 6d, where the elongation can be seen. There are curved GBs for both specimens, but, as mentioned above, the $UO_{2.00}$ sample has a larger population of these grains.

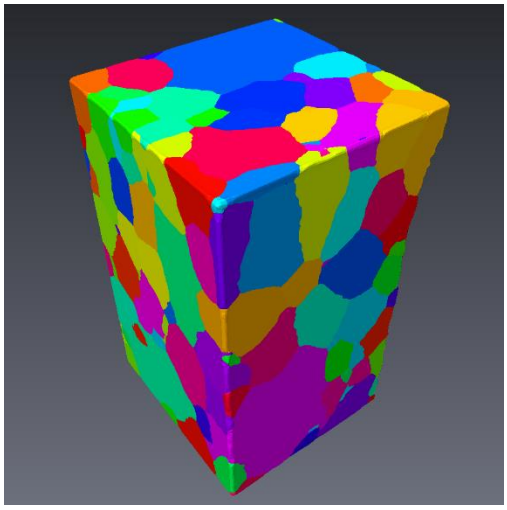
(a)
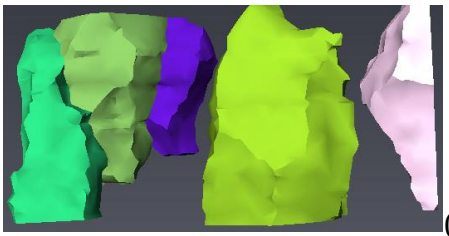
(b)
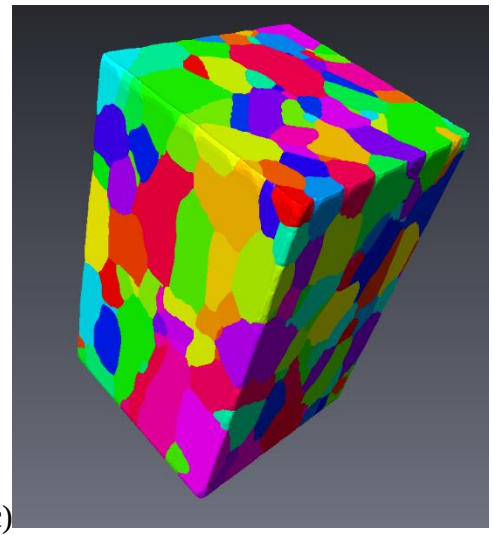
(c)
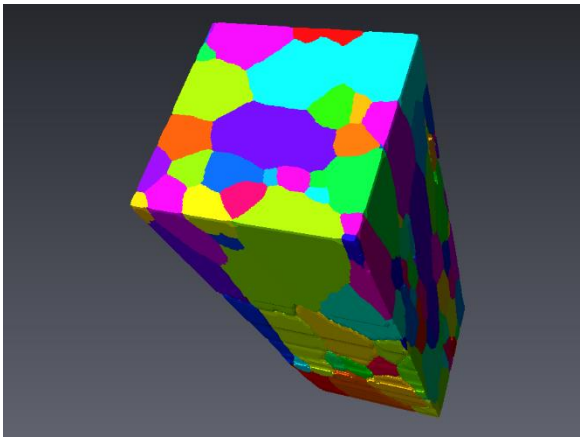
(d)
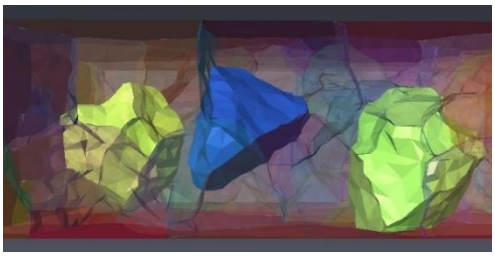
(e)

Figure 5.37. Selected areas of reconstructed microstructure of the two samples: overall view (a) and some grains (b) for $UO_{2.00}$ (sample 4) (c) Overall view for $UO_{2.06}$ (sample 5). (d) Overall view and selected grains (e) for $UO_{2.14}$ (sample 6).

Grain volumes were obtained and grain diameters were calculated, assuming they were spheres. The results are shown in Figure 5.38. The average grain size for all samples was around ~5μm for the samples with O/M 2.0 and 2.14, and around 3 μm for the 2.06 sample. The distribution trend is similar to that obtained in 2-D, where $UO_{2.06}$ has a larger population of smaller grains. Additionally, some extremely large grains (≥ 15 μm) were observed in samples 4 and 6 (O/M=2.0 and 2.14). The sample with O/M 2.06 had almost twice the number of grains than the other two samples, with a large population of smaller grains (>3μm). As previously reported, these samples tend to have clusters of pores and small grains and depending on the selected area of study these clusters can locally alter the microstructure generating results that are not representative of the overall population. On the other hand, selecting an area with a slightly larger population of abnormally large grains can also affect the results of grain size distribution and GB character, and could explain the results for samples 4 (O/M=2.0) and (O/M=2.14). Another possibility is that sample 5 (O/M=2.06) was undergoing through a recrystallization process where new small grains were appearing, increasing he overall population, shown in Figure 5.38. Larger areas that include larger grain and GB populations are required to determine the accuracy of these results.

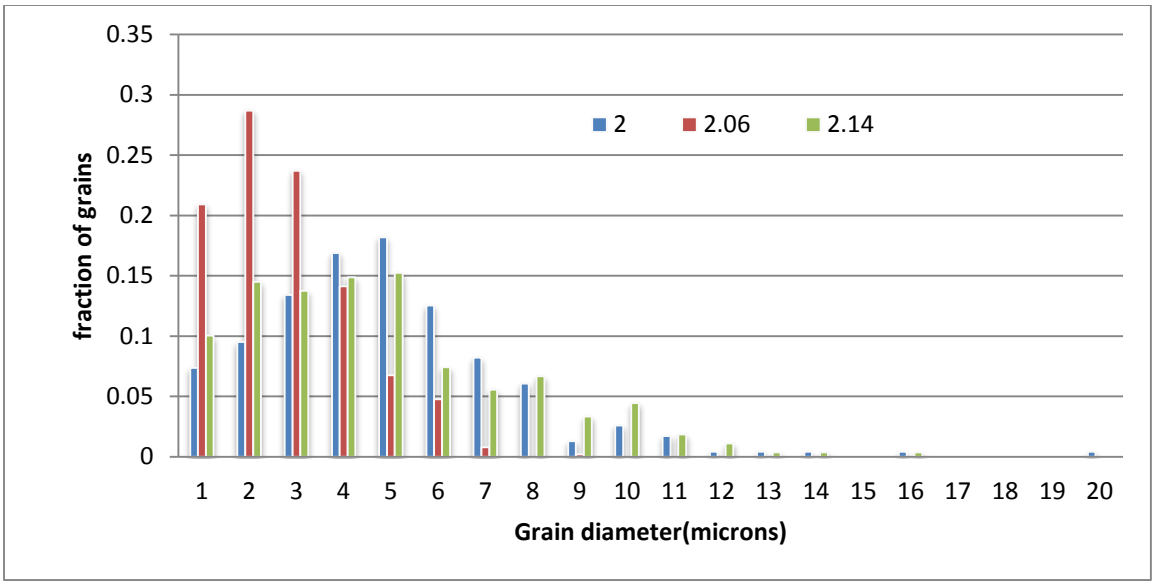

Figure 5.38. Grain size distribution for samples with different O/M values from 3-D measurements.

In most of the cases (samples 4 and 6), the grain diameter was larger than in the 2-D case, as expected, since 2-D measurements underestimate grain size. Also, as seen in Figure 5.37, the grains are elongated in the radial direction, as the 2-D slices are arranged with respect to the Z axis, the grain size is consistent with a smaller diameter. Sample 5 (O/M= 2.06) was the exception on this trend, where the 2-D grain size was larger than the 3-D calculated diameter. The difference could be explained by the results shown in Figure 5.3, where it can be seen that most of the population of the grains have an average size of less than 3μm. The selection of the area to study to determine the average grain size from 2-D slices was selected to be spaced at least one average grain size and could have excluded a large population of the smaller grains for the calculation. Also, as mentioned before, clusters of pores larger than the average grain size can cause GB pinning and delay or

impede grain growth. Therefore the selection of the area of study can affect statistical results such as average grain size and distribution.

Finally, the 3-D model was used to determine the physical normals of the GBs for the samples with O/M 2.0 and 2.14. These normals were then used to find the crystallographic orientations of the boundary planes, as discussed next.

The crystallography of a GB is characterized by five macroscopic degrees of freedom: three independent parameters to describe the misorientation between the grains (a rotation axis and a misorientation angle) and two parameters to describe the orientation of the boundary plane [109]. The 2-D EBSD data can be used to obtain rotation axes and misorientation angles. However, the GB plane orientation requires a 3-D reconstruction, as the boundary is buried through the surface [119]. The study was done for the samples with the lowest and highest oxygen content to determine how and if the O/M affects the GB character.

The boundary plane crystallography can influence GB properties such as energy, mobility, corrosion resistance and segregation [118, 119]. It is important to determine if there are changes in the GB crystallography when more defects are introduced in the lattice, as it would happen in-pile when the fuel becomes oxygen rich. Figures 5.39 and 5.40 show GB texture plots that relate the rotation axis, the misorientation angle, and the distribution of crystallographic GB normals for the two samples. Over 200 GBs were analyzed in each case, the results for some of the low and very high angle boundaries (0^0-30^0 and $>60^0$) are not discussed as there were not enough data points on this range, so the discussion is limited to the most common grain boundaries (30^0-60^0).

The GB normal is related to the GB character (tilt, twist or mixed). The rotation axis for twist GBs is parallel to the GB normal, while for tilt GBs it is perpendicular [120]. These parameters are extremely important, since the crystallographic orientation of the GB plane can have a great influence on the GB properties [119], as the misorientation angle/axis pair is not enough to explain why some GBs have different properties for a given misorientation.

The GB texture plots shown in Figures 5.39a and 5.40a represent the rotation axes, for GBs in UO_2 and $UO_{2.14}$, respectively, while the 5.39b and 5.40b represent the corresponding distributions of GB normals. Results are plotted in 10° intervals for the angle of misorientation. Note that there are several differences and similarities on the results for the two samples.

Both samples have a small peak of <101> rotation axes for misorientations larger than 40^0 and also have a less intense peak at <111>; as seen in Figures 5.39 and 5.404, most of the GBs are located in this range; therefore, these two rotation axes seem to be common for most GBs for the two O/M values. In addition, as shown in Figure 5.36, there are several $\sum 9$ (38.94^0/<110>) GBs that are consistent with the peaks at <110> in the range of 30^0-50^0.

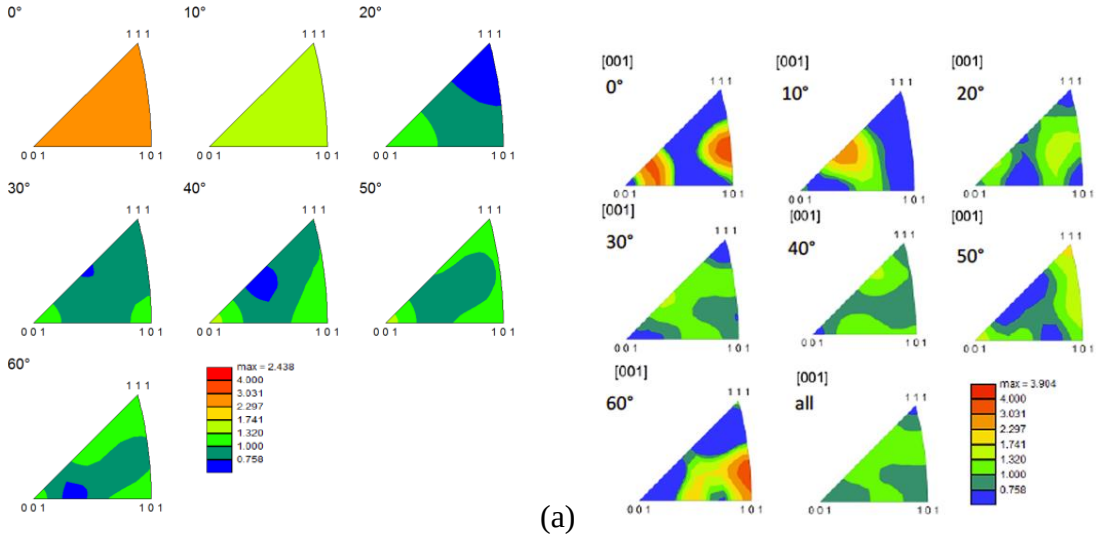

Figure 5.39. (a) Grain boundary texture plot and (b) crystallographic GB normals for $UO_{2.00}$.

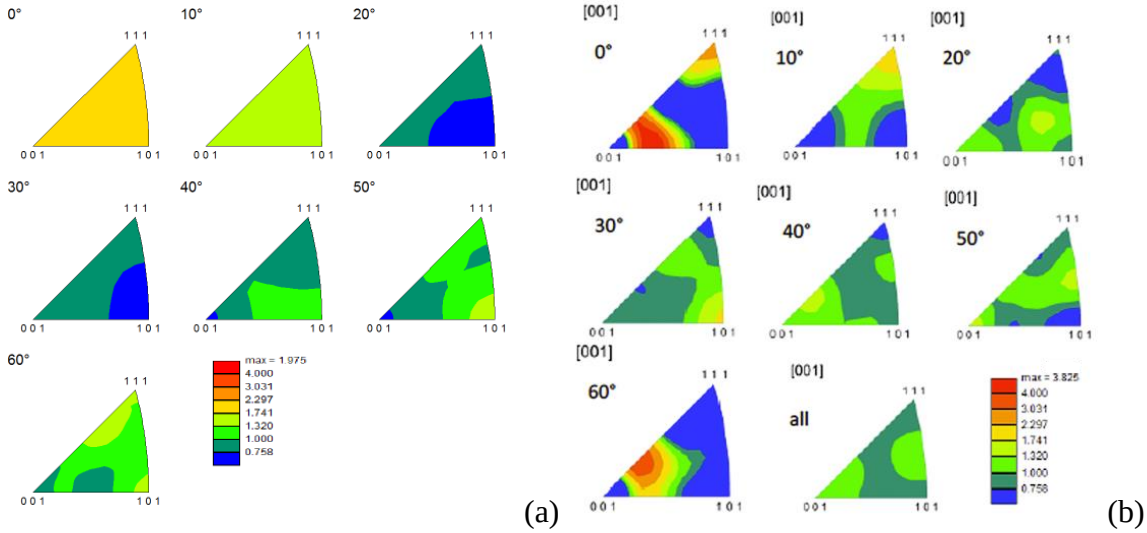

Figure 5.40. (a) Grain boundary texture plot and (b) crystallographic GB normals for $UO_{2.14}$.

In both samples, a large fraction of $\sum 3$ (60^0/<111>) GBs was observed, which is consistent with the results shown in Figures 5.39 and 5.40 in terms of rotation axis and misorientation angle. However, a significant peak at {111} plane, the plane for the ideal twin, for the GB

normal is not present at 60°, but a small peak at {111} can be seen for the stoichiometric sample in the 50-60° interval. The $UO_{2.14}$ specimen does not show such peak, which suggest that the ∑3 GBs in that sample might not of the type with the lowest energy. A large fraction of ∑11 (50.98°/<110>) GBs was also observed in both samples, which is consistent with the results shown in the 40°-60° range.

The main difference in both samples seems to be the <001> peak in the rotation axis distribution at larger misorientation angles. The non-stoichiometric sample lacks GBs at this rotation axis, while the stoichiometric sample has a higher fraction of GBs in this range. This could be the mechanism for energy minimization in UO_2; it has been observed that GBs parallel to low index planes may occur more frequently than predicted by a random probability [118] and rotation axes along a low index direction would tend to favor this for either tilt or twist boundaries.

Regarding the GB normals, the majority of the GBs are located in the range of 30^0-60^0. In the case of the stoichiometric sample, there seems to be an absence of GB normals located at the {001} and {111} in the 30^0-50^0 range; while no GBs are present around [105] and {013} at the 50^0-60^0 range. The most common GB plane for the 30^0-40^0 range is around {113}; that could be consistent with the ∑11 twinning plane. In the 40^0-50^0 range the most common plane seems to be around [105] while the most common GBs for the 50^0-60^0 range are located around {001}, {111} and {221}. The latter could be consistent with tilt ∑3 GBs, as {211} and {111} are twinning planes, and could be a mechanism for energy minimization.

In the case of the non-stoichiometric sample, there seems to be also an absence of GB planes at {111} in the 30^0-50^0 and {101} for 50^0-60^0. The most common GB plane for the

30^0-40^0 range is close to {101}; [30] for 40^0-50^0 and; {001} and {221} for 50^0-60^0. The [121] is a twinning plane for $\sum 9$ GBs, and this could be a mechanism for energy minimization of the GBs. These results can be used to guide simulations of GB energetics related to, e.g., fission gas segregation [122], since they allow to define prototypical GBs defined by their full five degrees of freedom, so that the properties of "typical" GBs can be modeled and studied. In this case, the O/M makes a difference on GB characteristics, which suggests that the GB effects in-pile will evolve as oxygen content increases with burn-up, since a transition towards higher mobility GBs seems to take place, which favors grain growth and overall microstructure evolution.

The results show that it is possible to fully characterize the GBs using the methodology described here. However, more GBs need to be analyzed to obtain more statistically reliable results.

The process to determine the GB normal is extremely slow an tedious, as plane cuts are need to be done for each GB to obtain the physical GB planes. Then the crystallographic data are manually obtained for each GB. The physical GB planes are rotated using the crystallographic rotation matrix to determine the crystallographic normal. Finally the data are separated based on misorientation angle and plotted using the OIM software. The whole process can take weeks to complete depending on the size of the data set and is very sensitive to human error during the collection of the physical normal. Also, as a large number of GBs were curved and/or pinned by pores an a question on the validity of the reported results arises, as small shifts on the plane cuts cut lead to large variations on the orientation of the physical normal.

The samples were mechanically polished and larger areas were scanned to obtain EBSD patterns and compare the results, particularly in terms of the presence of large elongated grains, as there is a possibility that their presence in the FIB data might be an artifact of doing the serial sectioning close to the surface of the sample Also, the data from the 2-D scans were used to obtain GB traces and determine the overall distribution of the GB normals.

5.4.3 2-D Characterization of the samples

After the 2-D and 3-D characterization of the samples were done, several questions surfaced: Are the grains elongated only at the edge of the sample? How representative are the results of the overall microstructure? As the GBs are curved, is there a particular GB type that has higher mobility? The three samples with different O/M values were mechanically polished and characterized to try to answer the above questions.

As described in the experimental procedures, EBSD scans of 400 μm x 400 μm were obtained for the samples with different O/M at three different regions (center, middle and edge) to determine if there were significant variations in microstructure along the radial direction of the pellets. The samples were also characterized using SEM to study porosity and other defects.

All the pellets presented cracks near the edges. Also grain pull-off was observed in all cases as well as pore clusters, larger pores and round pores. Figure 5.41 shows general and detailed views of some of the studied samples.

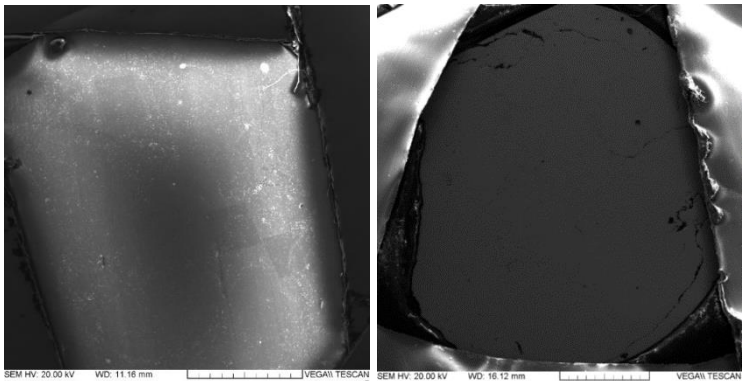

2.06(91X) 2.14(71X)

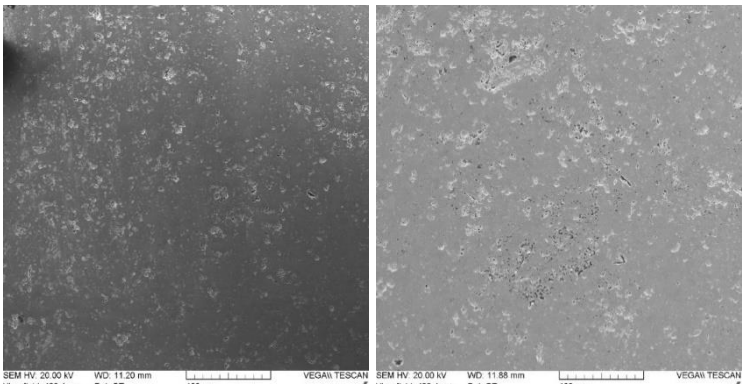

2.06 (667X) 2.14 (667X)

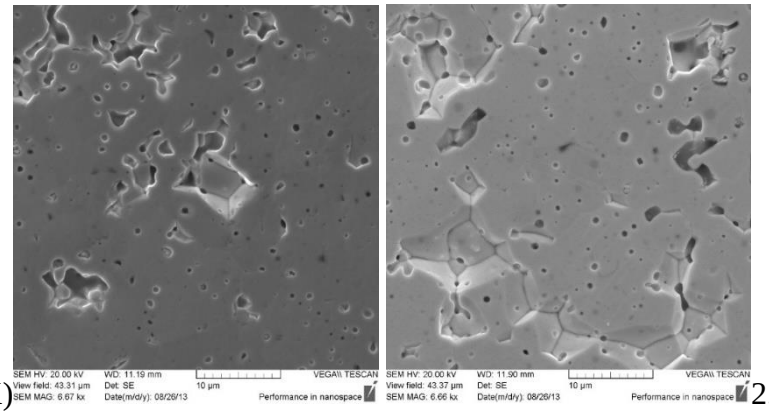

2.06(6.67kX) 2.14(6.66kX)

Figure 5.41. General view and details of defects in the samples 5 (O/M= 2.06) and 6 (O/M=2.14). From the lower magnification images it can be seen that the sample with O/M=2.06 was charging more that the sample with O/M=2.14. Details on possible grain pullout and porosity distribution all over the sample can be seen from the images at medium and high magnification. The images at higher magnification show details of porosity shape

as location, which, includes elongated and irregular large pores as well as round pores located at GBs and triple junctions.

Sample 6 (O/M=2.14) had several large cracks around the periphery and in the radial direction, as seen in Figure 5.41. All the samples had pore clusters, especially closer to the edge. These pores, mostly irregular in shape, could possibly form during the early sintering stages

Another defect observed in all the SEM images was grain pullout. Defects like these could have been created during sample preparation (cut, grinding, and polishing). As a consequence of grain pullout, porosity located at triple junctions and grain boundaries can be observed. These pores were mostly round in shape. Some interconnected porosity was also observed, this type of porosity is consistent with intermediate stages of sintering.

The stoichiometric sample presented charging and distortion issues. Only smaller areas could be studied at particular times and discharging during the scanning on the SEM was constantly observed.

In order to fully characterize the samples, three EBSD scans were performed near the center, middle and edge of each pellet. As previously described, the edge of the samples was full of cracks and pores. Therefore, the scans were performed near the edge of the sample, but not at the edge itself (about 500 μm from the edge). The idea behind these scans was to determine if there was microstructural variability (i.e., grain size, GB misorientation, CSL distribution) along the radial direction of the pellets and to determine if the oxygen content has an effect on the microstructure, as according to the literature, grain growth is enhanced with higher oxygen content. Figure 5.42 shows the selected areas for the three samples.

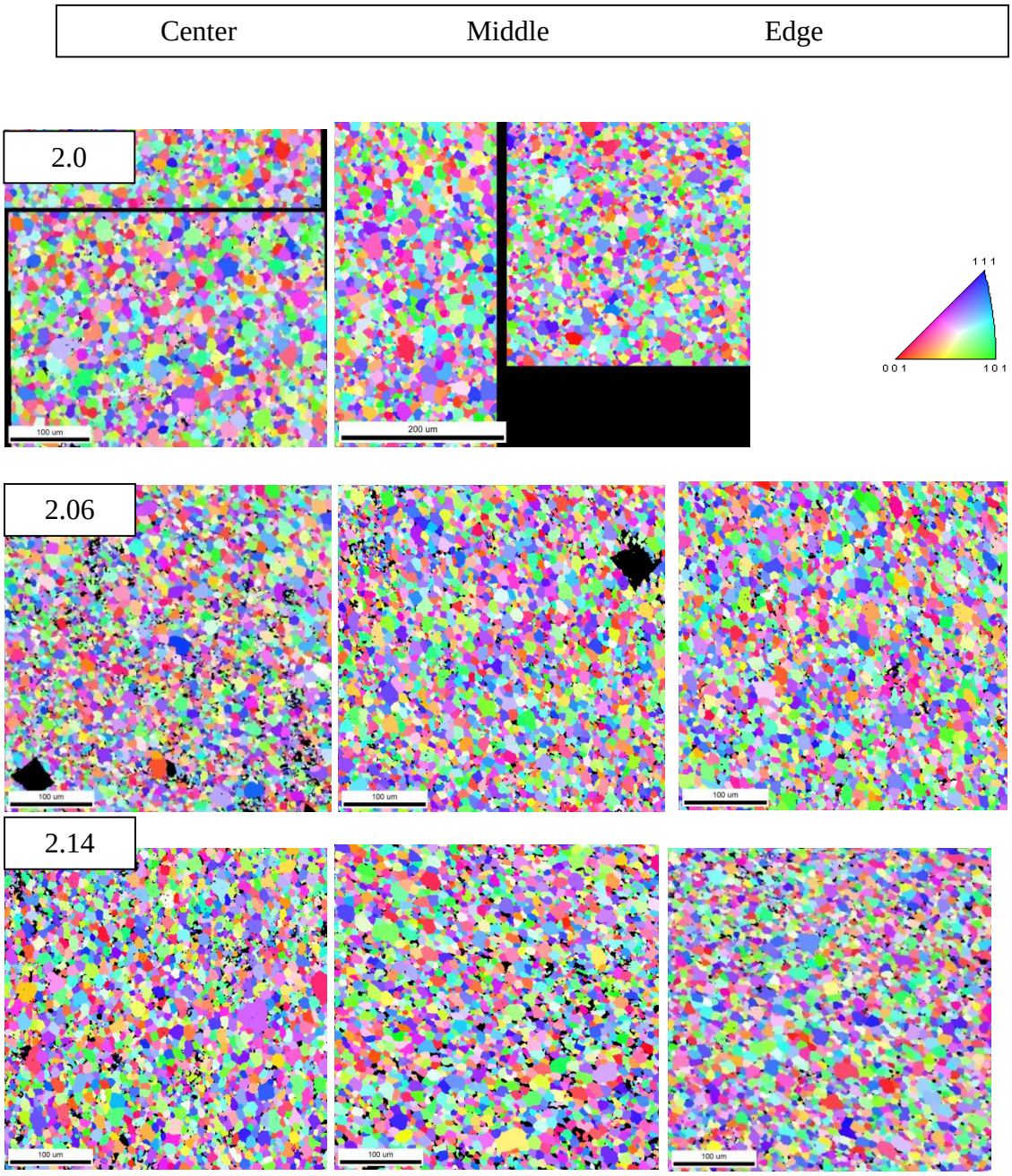

Figure 5.42. IPF maps of the three studies areas (center, middle and edge) for the samples with different O/M.

Regarding of the GB misorientation distribution (Figure 5.43), the average misorientation peaks at 41° for all samples and is consistent with the results reported in previous sections. No large variations were found at the three studied areas, indicating that there is little or no

significant texture variations along the radial direction in each sample or among the samples.

Regarding the grain size distribution, Figure 5.44 shows the results for the studied samples. Even though, on average, the grain size for these samples has no large variations, the distribution of the grain size has some significant differences. The sample with the highest oxygen content has a larger tail on the distribution with clearly larger grains in size. This result is consistent with the literature, as an increase of the O/M increases the GB mobility, allowing grain growth [106]. The results for a more detailed study of these large grains, based on the partitions discussed at section 5.3.2, will be discussed in section 5.4.3. These results will help to determine why those particular grains are growing more than the average grain and if possible predict which grains or GBs will be more energetically more favorable to enhance grain growth.

Additionally, the presence of large pores and pore clusters affects the GB mobility as GBs can be physically confined by surrounded pores. This could explain the local differences on the grain size for the different selected areas for each sample. Large populations of pore clusters were observed at the center of sample 2.06, which could explain the larger area fraction of small grains on its distribution.

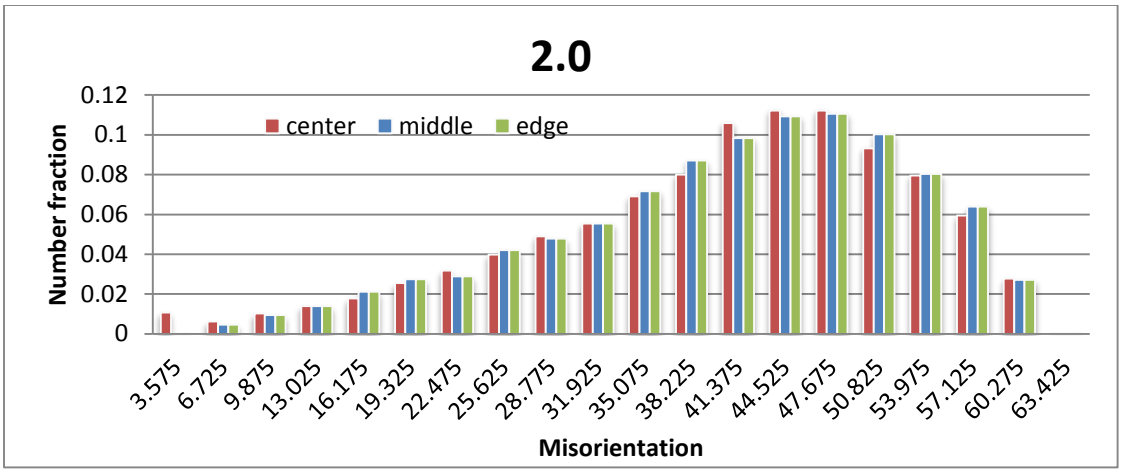

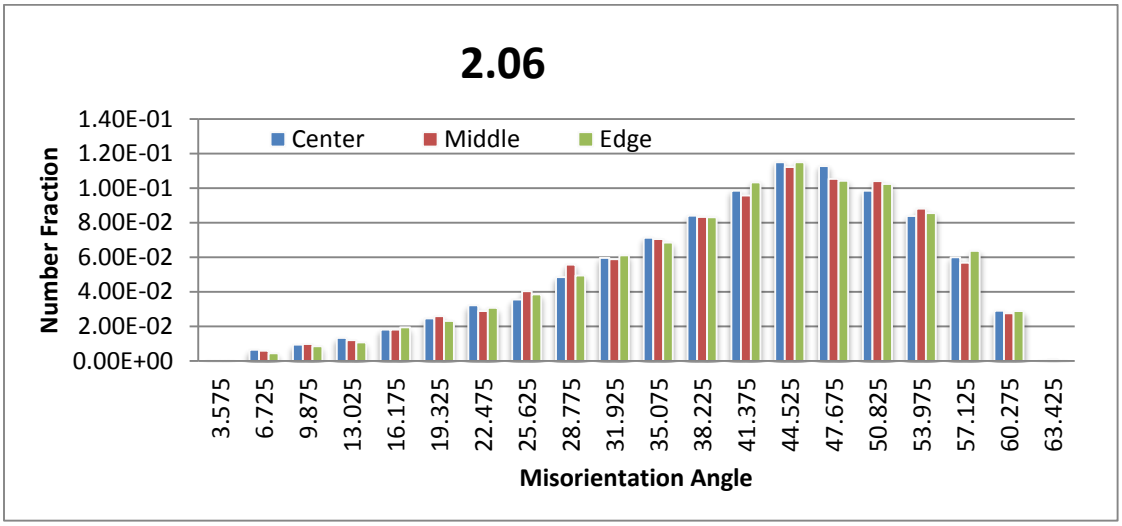

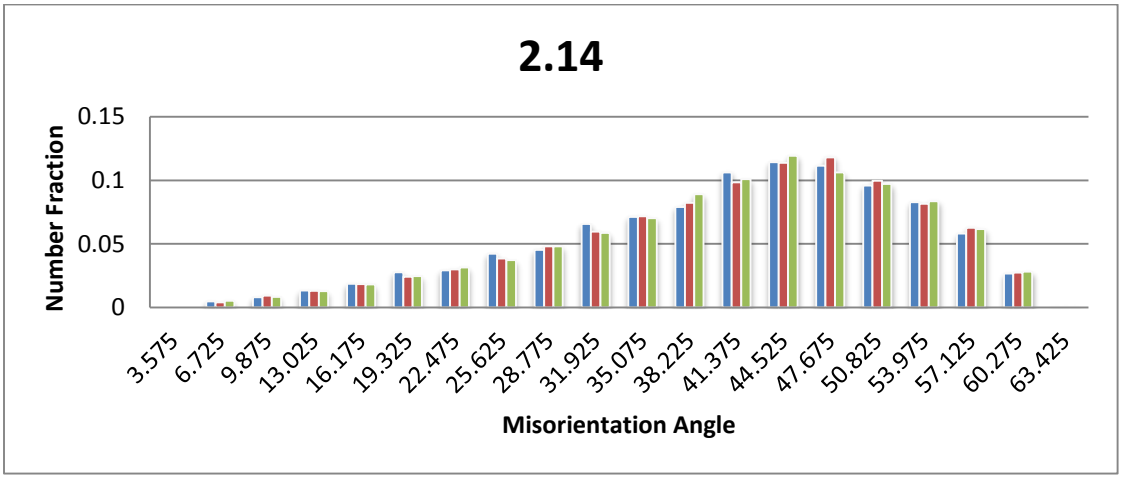

Figure 5.43. Misorientation distribution of the samples with different O/M values (2.0, 2.06 and 2.14).

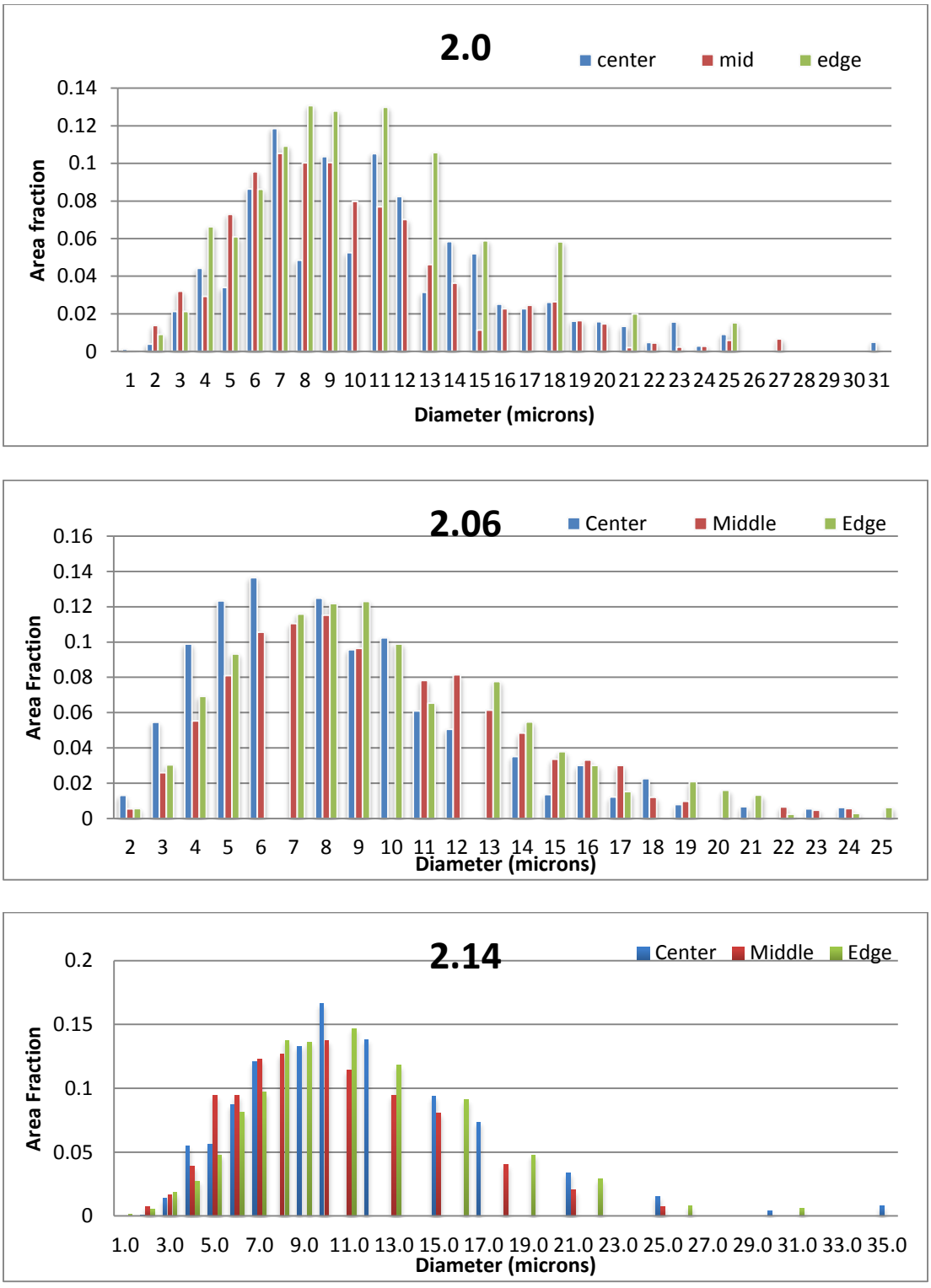

Figure 5.44. Distribution of grain size of the samples with different O/M values (2.0, 2.06 and 2.14).

The CSL distribution for these samples is shown in Figure 5.45. The CSL fractions were calculated as the fraction length of a particular CSL boundary over the CSL population, to determine if the proportion of CSL boundaries are maintained or changes depending on the O/M or location of the analyzed area (regardless of the total CSL fraction). No large variations within the different studied areas were observed. In all cases the CSL fraction was very similar and the distribution for the first five Σ boundaries had no significant changes in all cases. Moreover, the Σ3 GBs were the most abundant in all cases, with twice the number fraction of the next Σ boundary in abundance. In general, no significance differences were observed on the studied microstructural parameters with respect to the location within the samples. These results suggest that the microstructure has no significant changes along the radial direction of the pellets.

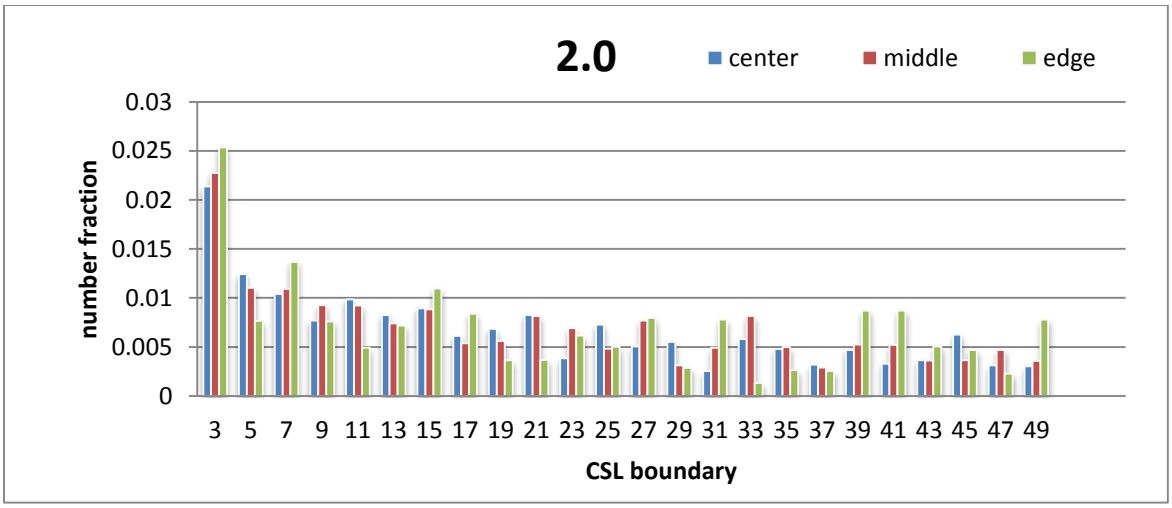

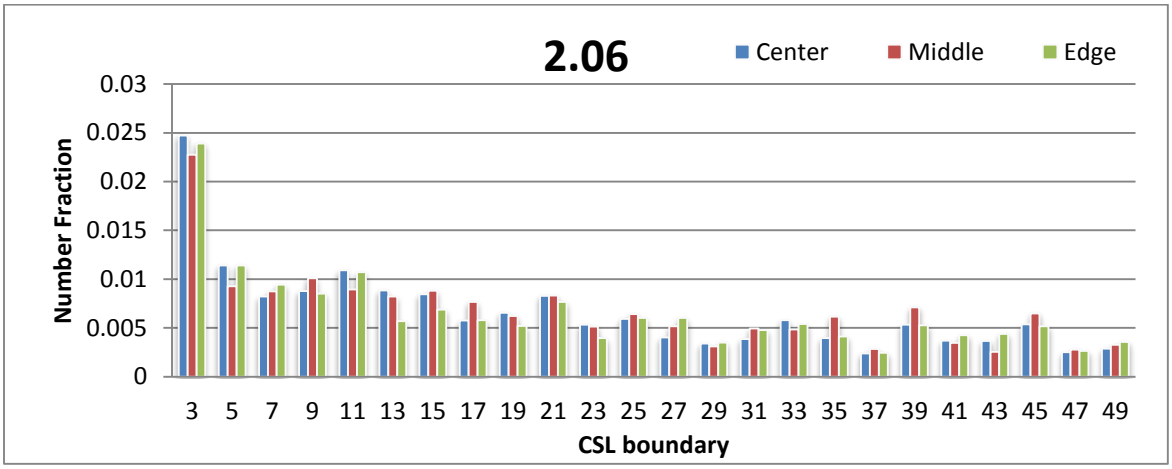

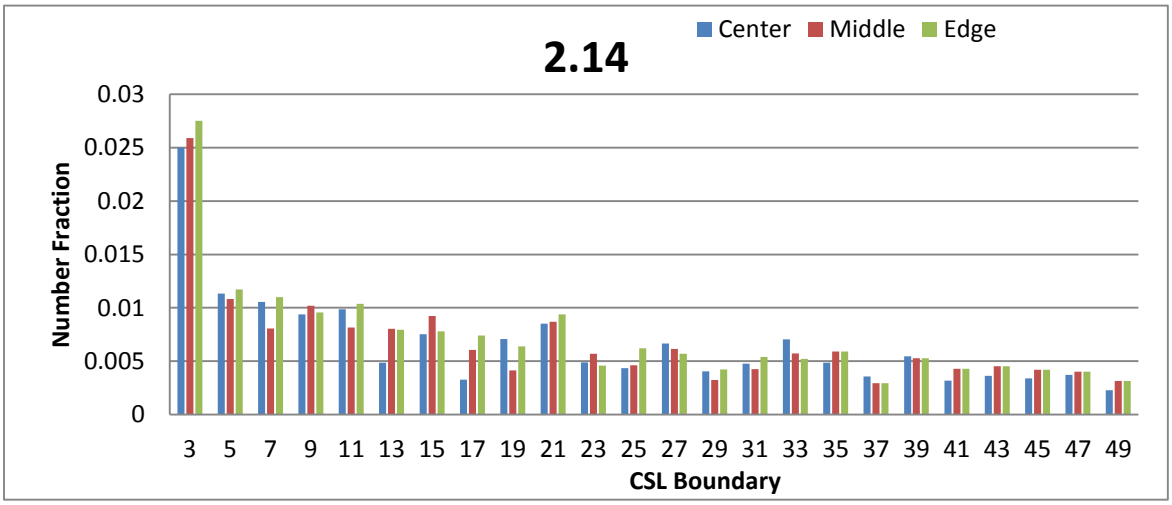

Figure 5.45. Distribution of the CSL distribution of the samples with different O/M values (2.0, 2.06 and 2.14).

Finally, the distribution of the GB normals for the larger 2-D scans was calculated based on a GB trace analysis. In this case the datasets were larger than in the 3-D model, which allow generating more statistically relevant information. The normals were calculated for each region and as a merged dataset that included all the studied regions for each sample. The calculations were based on the methodology proposed by Saylor et al. [133] and required a large dataset (more than 10,000 GBs). This requirement restrict the capability to determine the distribution based on GB misorientation, as larger datasets are required. The overall distribution for all the misorientations is shown in Figure 5.46.

In the case of the large scans, it can be seen that the predominant normal plane, regardless of the O/M or the location of the studied area is {111}, which, as previously discussed, is a twinning plane for the fluorite structure. The results are consistent with the literature that indicates that the GB plane distributions are anisotropic and that there is a preference for low-index/low energy GB planes for fixed misorientations. Moreover, there seems to be an inverse correlation between GB plane distributions and GB energy distributions. It has been reported that low-energy GBs represent a larger fraction of the GB population in both area and frequency. Furthermore, the distribution can be sensitive to impurities [Rohrer, 2011].

However, these results contrast with the results obtained from the 3-D reconstruction, where there was a lack of GB planes at {111} for the two studied samples. Additionally, there seems to be a low concentration of GB planes at {001} in conflict with the 3-D results for the 2.14 sample. One of our initial concerns for the 3-D results was the size of the areas studied and how representative it was for the overall microstructure. After further inspection, defects such as ring cap and cracks at the edge of the samples were detected.

The selected area for FIB was located in all cases at the edge of the sample, where these manufacturing defects were observed. This in turn could locally increase the variations on the microstructure.

Additionally, as previously discussed, the shape and geometry of the GBs makes extremely difficult the determination of the GB normals. Moreover it can be seen from Figure 5.45 that even though there are no large variations on the distribution of the GB normal for the studied samples the plots for the near edge datasets have less GBs near {101}. Therefore, at least regarding the GB normal, larger areas are needed to determine its distribution. Furthermore, in order to determine how representative the FIB data were of the overall microstructure, the data obtained by serial sectioning and mechanical polishing will be compared next.

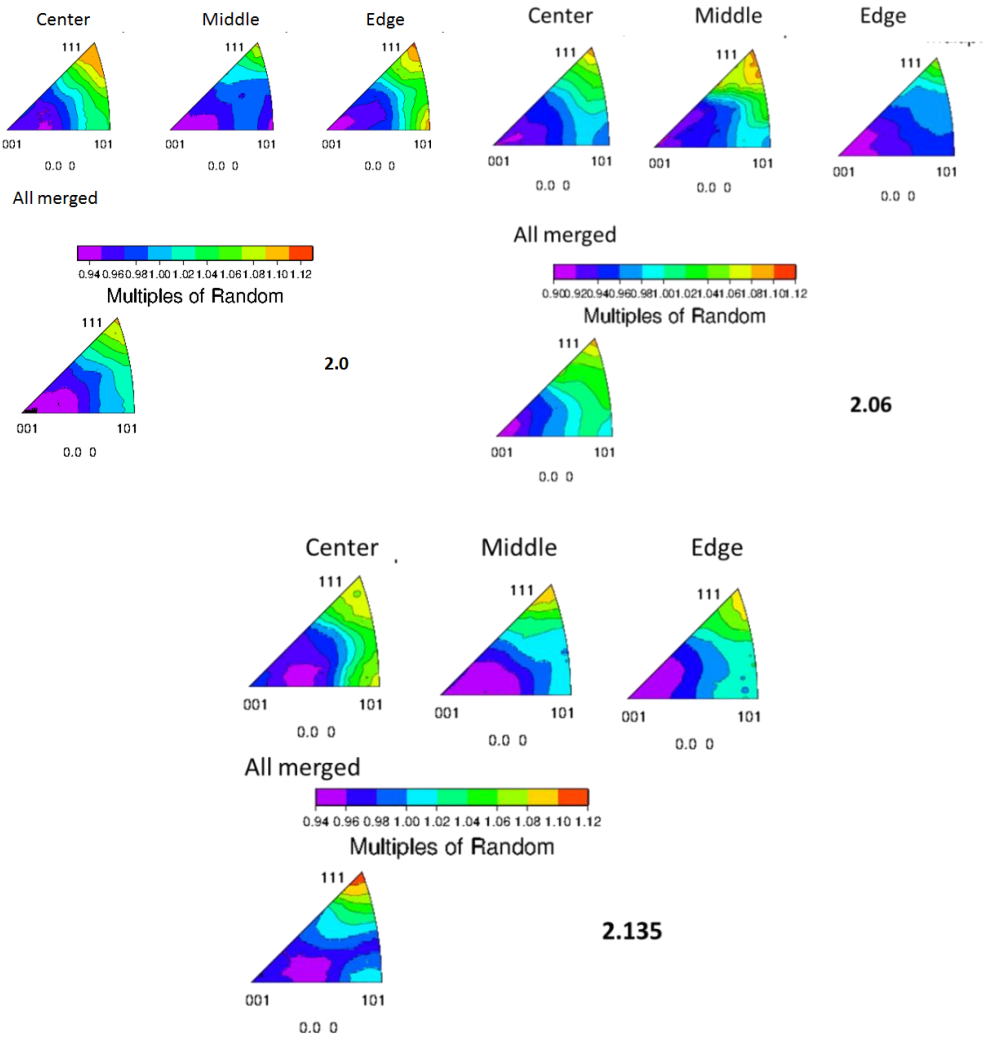

Figure 5.46. Grain boundary normal calculated from trace analysis for the studied samples (3, 4 and 5).

Moreover, Table 5.4 shows the results for grain size, GB misorientation, CSL fraction and some selected CSLs for all the studied areas and samples.

As expected there are significant changes on the grain size between the FIB 2-D slices and the mechanically polished area; as the 3-D reconstruction show that the grains are elongated in the radial direction. The 2-D large scans were done on top of the sample and

the 2-D FIB results are from longitudinal sections of the sample. There seems to be a small grain size increase on the grain size as the O/M increases, as expected. More than the average grain size, differences on the distribution were observed in Figure 5.43, as the sample with the highest O/M had a longer tail in the distribution, with grains up to 35 µm in diameter.

Table 5.4. Microstructural features calculated from different datasets for samples 4, 5 and 6. The fraction of the CSLs boundaries represent a normalized fraction with respect to the total CSL length fraction.

O/M	location	grain size (µm)	STD Dev (µm)	misorientation	CSL	Σ3	Σ5	Σ7	Σ9	Σ11
2.0	edge	5.7	3.3	40.6	0.17	0.13	0.07	0.07	0.05	0.05
2.0	mid	5.8	3.3	40.9	0.17	0.15	0.05	0.08	0.05	0.03
2.0	center	6.5	3.7	41.4	0.16	0.13	0.08	0.06	0.05	0.17
2.0	avg	6	1.2	41.0	0.7	0.14	0.07	0.07	0.05	0.08
2.0 fib		3.6	3.1	41.2	0.19	0.15	0.03	0.08	0.14	0.06
2.0 3-D		5.0	3	-						
2.06	edge	6.1	3.3	41.2	0.16	0.15	0.07	0.06	0.05	0.07
2.06	mid	5.9	3.3	40.9	0.16	0.14	0.06	0.05	0.06	0.06
2.06	center	5.1	2.9	41.0	0.16	0.15	0.07	0.05	0.06	0.07
2.06	avg	5.7	0.5	41.0	0.16	0.15	0.07	0.05	0.06	0.07
2.06 fib		3.4	2.0	40.9	0.17	0.18	0.06	0.05	0.04	0.07
2.06 3-D		3.6	1.4	-						
2.14	edge	6.4	3.6	41.0	0.18	0.16	0.07	0.06	0.06	0.06
2.14	mid	5.9	3.2	41.1	0.16	0.16	0.07	0.05	0.06	0.05
2.14	center	6.7	3.5	40.8	0.16	0.16	0.07	0.07	0.06	0.06
2.14	avg	6.3	0.4	41.0	0.17	0.16	0.07	0.06	0.06	0.06
2.14 fib		3.9	2.7	42	0.20	0.13	0.08	0.04	0.10	0.15
2.14 3-D		4.7	2.9	-						

In order to determine how representative the FIB area was over the whole microstructure, a study based on the results of Section 5.2 was performed. The original 400 μm x 400 μm center scan for the sample with O/M 2.06 was divided into smaller areas to study local variations on the microstructure with respect to the original scan. The smaller scans had areas of: 200 μm x 400 μm, 200 μm x 200 μm, 100 μm x 100 μm and a couple of scans of 50 μm x 50 μm (see Figure 5.46). The results are shown in table 5.5.

Table 5.5. Calculated statistics for different areas based on the center scan for the sample 2.06

size	location	gs	stdev	misorient	stdev	csl fractio	stdev	3	stdev	5	stdev	7	stdev	9	stdev	11	stdev
400x400	center	5.1		41		0.16		0.15		0.07		0.05		0.06		0.07	
400x200	top	5.4	0.2	40.9	0.1	0.16	0.000	0.16	0.01	0.06	0.01	0.05	0	0.06	0.00	0.08	0.01
400x200	bottom	4.8	0.2	41.1	0.1	0.16	0.000	0.15	0.00	0.08	0.01	0.05	0	0.05	0.01	0.06	0.01
200x200	top left	5.1	0.0	41.3	0.2	0.16	0.001	0.14	0.01	0.05	0.01	0.05	0.00	0.06	0.00	0.08	0.01
200x200	top right	5.6	0.4	40.8	0.1	0.17	0.004	0.18	0.02	0.07	0.00	0.06	0.01	0.06	0.00	0.08	0.01
200x200	b left	4.8	0.2	40.9	0.1	0.16	0.003	0.14	0.01	0.10	0.02	0.06	0.01	0.05	0.01	0.06	0.01
200x200	b right	4.8	0.2	41.0	0.0	0.16	0.001	0.17	0.01	0.07	0.00	0.04	0.01	0.05	0.01	0.06	0.01
100x100	blbr	4.2	0.6	40.8	0.1	0.16	0.000	0.17	0.01	0.09	0.01	0.06	0.01	0.09	0.02	0.04	0.02
100x100	brbr	4.2	0.6	41.7	0.5	0.15	0.007	0.17	0.01	0.03	0.03	0.02	0.02	0.06	0.00	0.07	0.00
100x100	brtl	4.7	0.3	40.2	0.6	0.16	0.000	0.18	0.02	0.08	0.01	0.03	0.01	0.04	0.01	0.09	0.01
100x100	brtr	4.9	0.1	41.7	0.5	0.16	0.000	0.16	0.01	0.1	0.02	0.07	0.01	0.01	0.04	0.01	0.04
100x100	bltl	4.4	0.5	40.4	0.4	0.14	0.014	0.17	0.01	0.07	0.00	0.04	0.01	0.03	0.02	0.11	0.03
100x100	bltr	4.8	0.2	40.1	0.6	0.16	0.000	0.16	0.01	0.1	0.02	0.07	0.01	0.07	0.01	0.09	0.01
100x100	brbl	4.8	0.2	40.4	0.4	0.17	0.007	0.15	0.00	0.12	0.04	0.02	0.02	0.04	0.01	0.06	0.01
100x100	blbl	4.4	0.5	40.8	0.1	0.18	0.014	0.14	0.01	0.08	0.01	0.04	0.01	0.04	0.01	0.03	0.03
100x100	tlbl	4.4	0.5	40.4	0.4	0.16	0.000	0.08	0.05	0.11	0.03	0.07	0.01	0.05	0.01	0.05	0.01
100x100	tlbr	4.8	0.2	40.8	0.1	0.14	0.014	0.17	0.01	0.05	0.01	0.07	0.01	0.04	0.01	0.03	0.03
100x100	tltl	5.4	0.2	40.7	0.2	0.17	0.007	0.15	0.00	0.05	0.01	0.02	0.02	0.1	0.03	0.1	0.02
100x100	tltr	6.1	0.7	40	0.7	0.18	0.014	0.13	0.01	0.08	0.01	0.08	0.02	0.05	0.01	0.06	0.01
100x100	trbl	5.2	0.1	40.8	0.1	0.14	0.014	0.17	0.01	0.08	0.01	0.06	0.01	0.06	0.00	0.04	0.02
100x100	trbr	5.2	0.1	40.9	0.1	0.17	0.007	0.17	0.01	0.06	0.01	0.04	0.01	0.07	0.01	0.17	0.07
100x100	trtl	5.3	0.1	41.6	0.4	0.17	0.007	0.23	0.06	0.05	0.01	0.05	0.00	0.06	0.00	0.07	0.00
100x100	trtr	6.1	0.7	40	0.7	0.18	0.014	0.13	0.01	0.08	0.01	0.08	0.02	0.05	0.01	0.06	0.01
50x50	tltltl	5.0	0.1	41.9	0.6	0.14	0.014	0.17	0.01	0.04	0.02	0.02	0.02	0.06	0.00	0.06	0.01
50x50	tltltr	5.3	0.1	41.3	0.2	0.19	0.021	0.1	0.04	0.05	0.01	0	0.04	0.1	0.03	0.02	0.04

50µm x 50µm 100µm x 100µm 200µm x 200µm

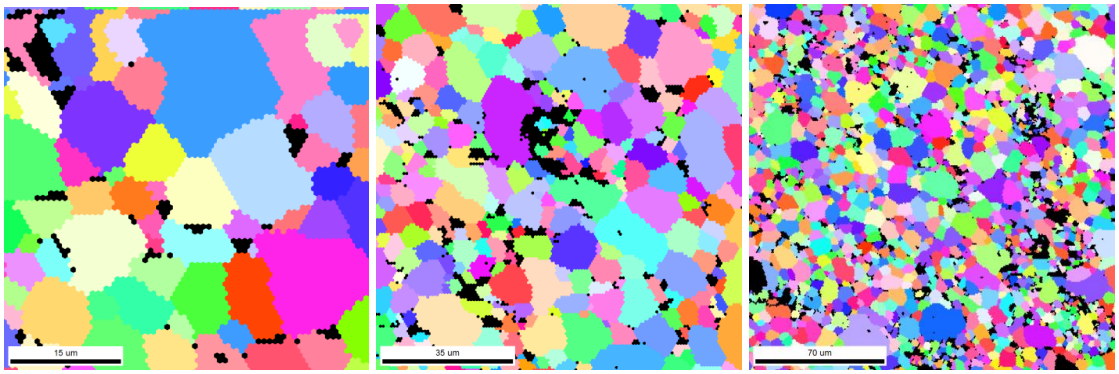

200µm x 400µm

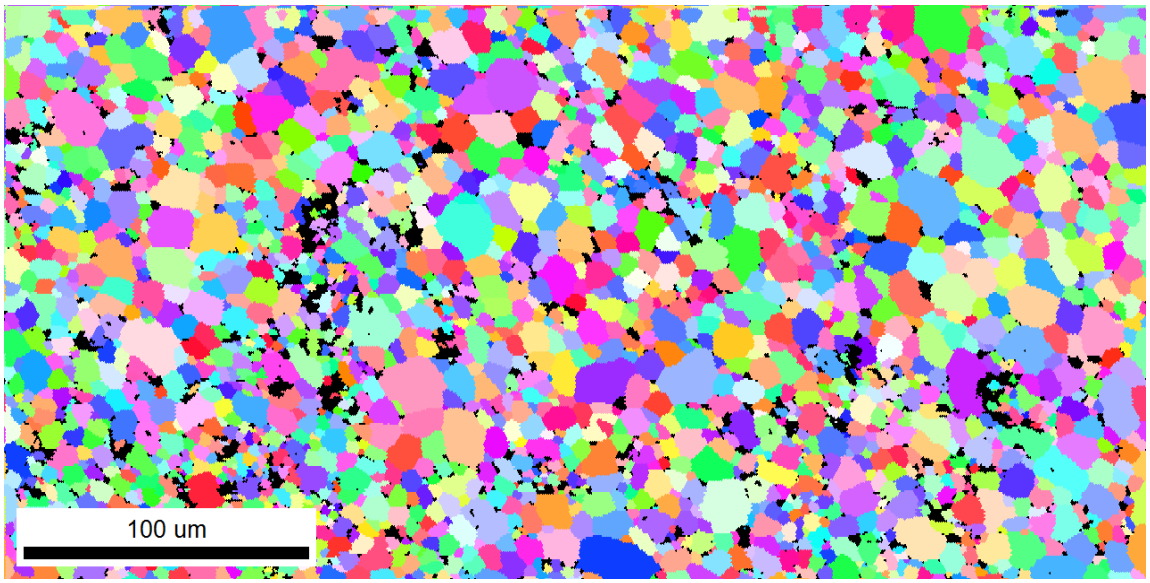

Figure 5.47. Some of the studied areas to determine grain size, CSL and misorientation distributions for sample 5 (O/M=2.06).

The results show that there is small scatter in the data regarding the average GB misorientation. However, in the case of the grain size, the 100 µm x 100 µm area has up to ~14% deviation with respect to the average grain size of the original 400 µm x 400 µm area. The large variability on the grain size can be visualized in Figure 5.47 where clusters

of pores and small grains are distributed along the studied area. Smaller areas can be either free of these clusters or can contain multiple clusters, increasing or decreasing significantly the average grain size. The same analysis can be applied to the CSL distribution, where also variations in the CSL fraction and distribution were observed. Moreover, in general as the Σ number increases the population of that particular type of GB decreases, increasing the variability for a particular CSL GB. The latter could explain for instance the large variability on the normalized fraction of ∑11 GBs for sample 4 (O/M=2.0).As expected in none of the studied regions the average grain size was equivalent to the FIB 2-D sections. These results are consistent with the 3-D models where elongated grains were observed. The latter observation explains the differences on the grain size distribution for the 2-D data from the FIB slices (radial direction, smaller diameter) and the mechanically polished slices (longitudinal direction, larger diameter).

Regarding the rest of the microstructural parameters, from Table 5.4 it can be seen that the selected data from the FIB slices is in general representative of the overall microstructure as has very similar average misorientation angles, CSL fractions and CSL distributions, with respect to the overall distributions.

In all cases, large grains were observed. This observation raised a question: Was something special in all these large grains that allowed them grow more than most of the grains? In the next section we will study the crystallography of these grains and more importantly the crystallography of their GBs; as these GBs seem to be more mobile than the rest.

5.4.4 Partitioned data for samples 4, 5 and 6

As previously discussed, some abnormally large grains were observed in the samples. A partition that only included grains with sizes larger than 2.5 times the average size was obtained for all samples with different O/M values. Figures 5.48 - 5.50 show IPF maps with the selected grains.

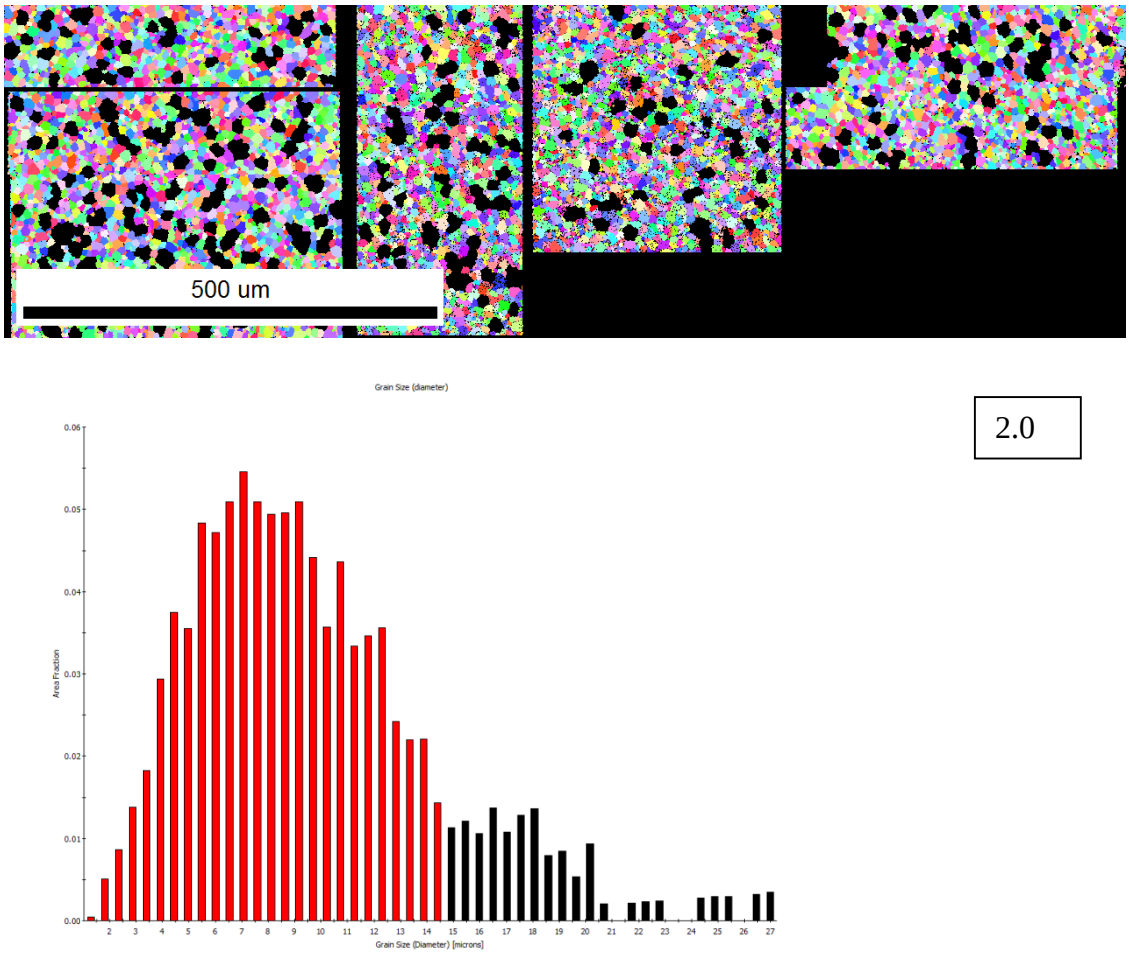

Figure 5.48. Selected grains (in black) for the partition of sample with O/M=2.0

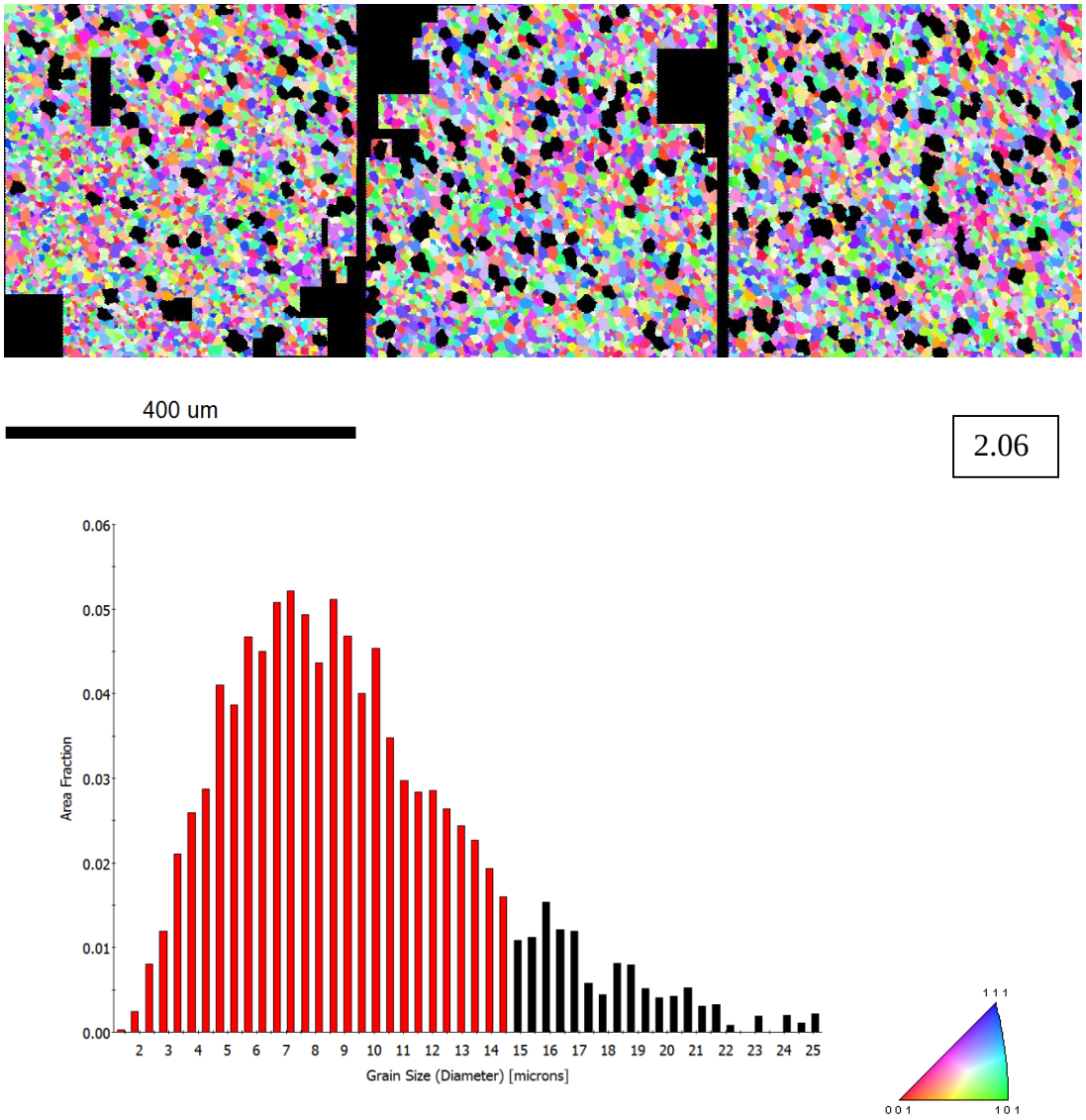

Figure 5.49. Selected grains (in black) for the partition of sample with O/M=2.06.

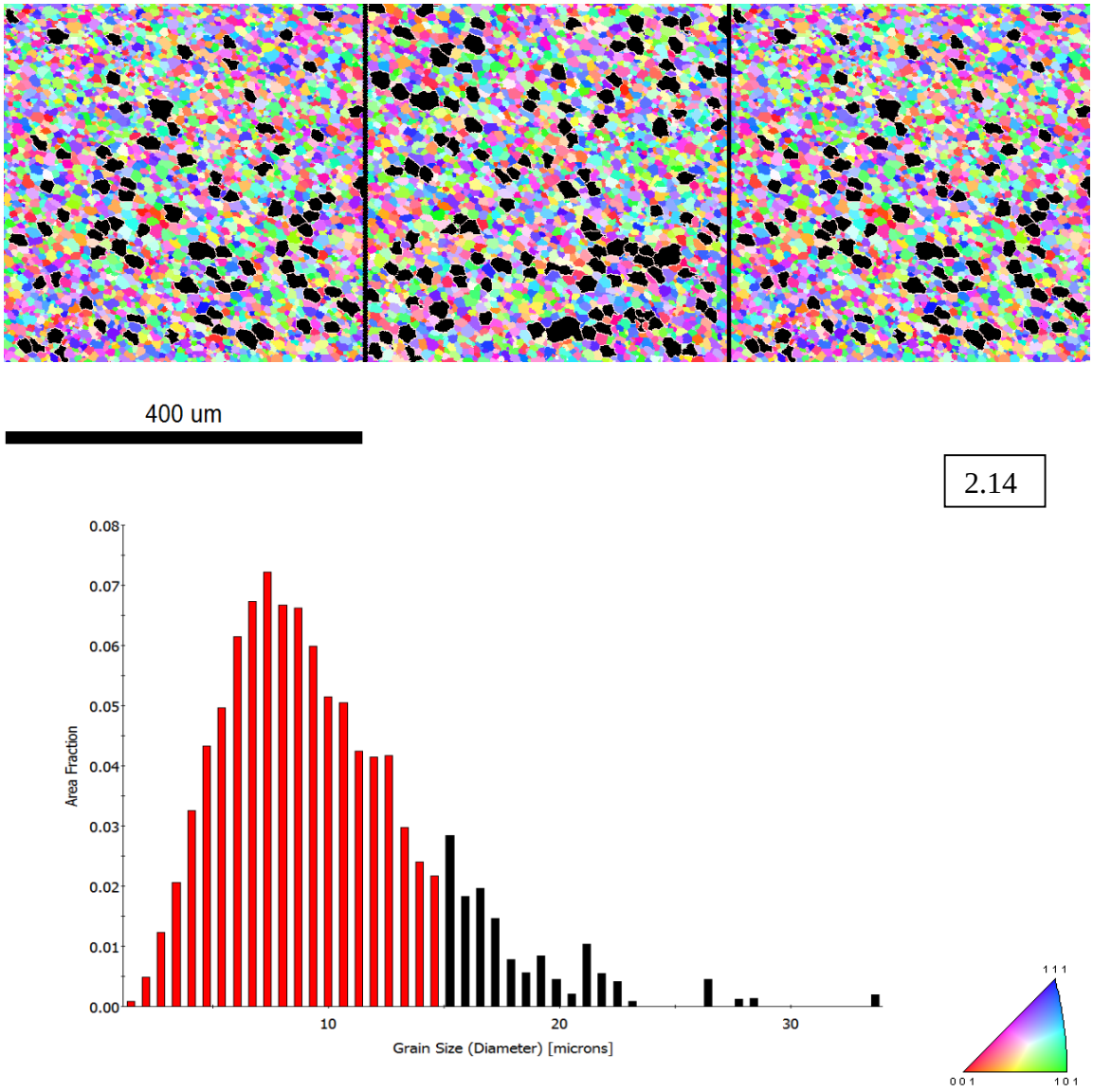

Figure 5.50. Selected grains (in black) for the partition of sample with O/M=2.14.

An interesting result was that for the 2.06 sample only 10% of the grains are in the partition, while 18% of the grains are in the partition for the 2.14 sample, while the fraction of large grains at the O/M 2.0 was around 17%. These observations could reinforce the previously mentioned hypothesis of recrystallization for the sample with O/M 2.06.

Moreover, crystallographic information was obtained for all the GBs of the partitioned data set. Over 2000 GBs were analyzed to determine the number of neighbors for each grain, the GB texture and the CSL distribution. The idea was to determine the characteristics of the large grains and try to find insight into the reasons why they grow larger than the rest from these data.

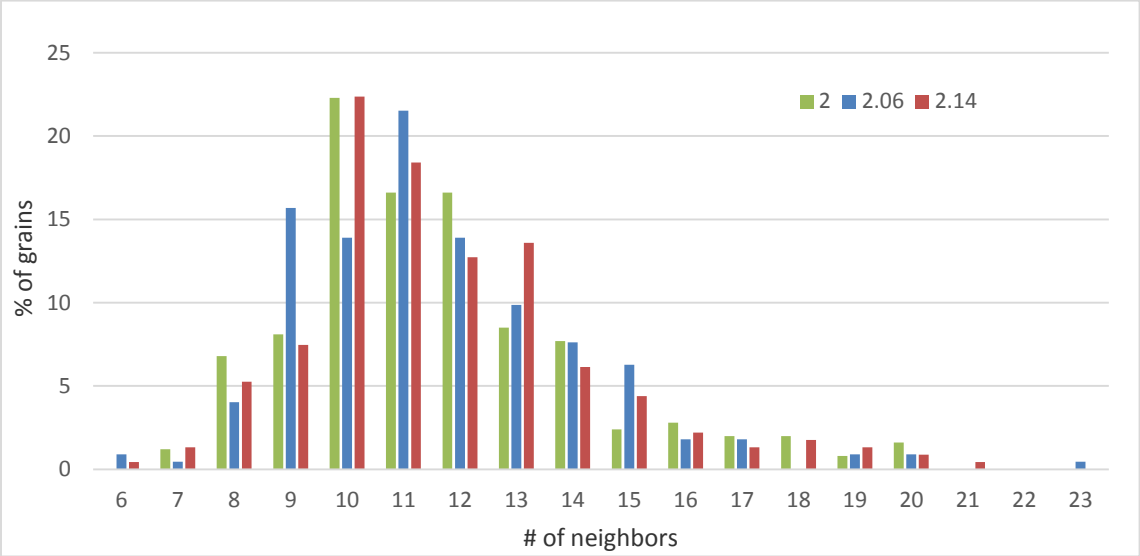

Figure 5.50. Frequency distribution of the number of neighboring grains for the large grain partition.

Table 5.6. Number of neighbors for the large grains in the partitioned data for samples 4, 5 and 6.

O/M	Mode	Mean	St. Dev.
2.0	10.7	11.6	2.5
2.06	10.6	11.6	2.5
2.14	10.8	11.7	2.7

Regarding the number of neighbors, it can be seen from Figure 5.51 and Table 5.6, that there are similar trends in all cases. Moreover, from Table 5.6 it can be seen that the values of the mode and mean number of grains are about the same for all cases. As the previously discussed in the 3-D section, grains with more than 6 neighbors tend to keep growing while grains with less than 6 neighbors will disappear. All the grains in the partitioned data had at least 6 neighbors. Therefore, these large grains with up to 23 neighbors will preferably grow over smaller grains.

As most of the traditional ceramics, the pellets were made of a powder that was compressed and one can assume that the initial stages of the microstructure development, the GB distribution is isotropic. However, it has been shown, in computer simulations, that anisotropic GB distributions can be developed from initially isotropic distributions due to energy anisotropy. Furthermore, recent models suggest that the GB distribution evolves to a steady state with anisotropic GB population distribution that is inversely related to the energy [33].

A similar result was observed for the CSL distribution, Figure 5.52, where slightly larger fractions of more stable $\sum 3$ GBs were found for the sample with higher oxygen content. The sample with intermediate oxygen content has a larger fraction of $\sum 9$ GBs, similar to sample 1 where a less "mature" microstructure was observed. The stoichiometric sample had a larger fraction of lower Σs such as $\Sigma 15$, $\Sigma 21$ and $\Sigma 49$, these results could be again related to the "maturity" of the microstructure, the GB mobility and GB energy.

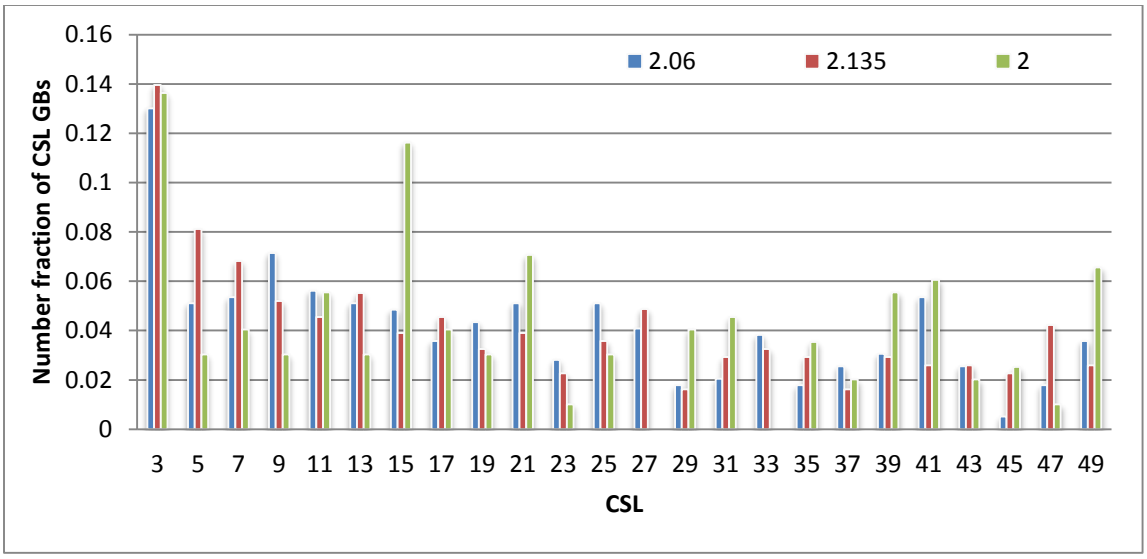

Figure 5.52. CSL distribution for the partitioned large grains in samples with different O/M.

Again, as in section 5.3, we wanted to study the larger grains to determine if there were any crystallographic characteristics that allow these grains to grow over the average size. Texture plots of the overall microstructure and the partitions were obtained, as shown in Figure 5.52.

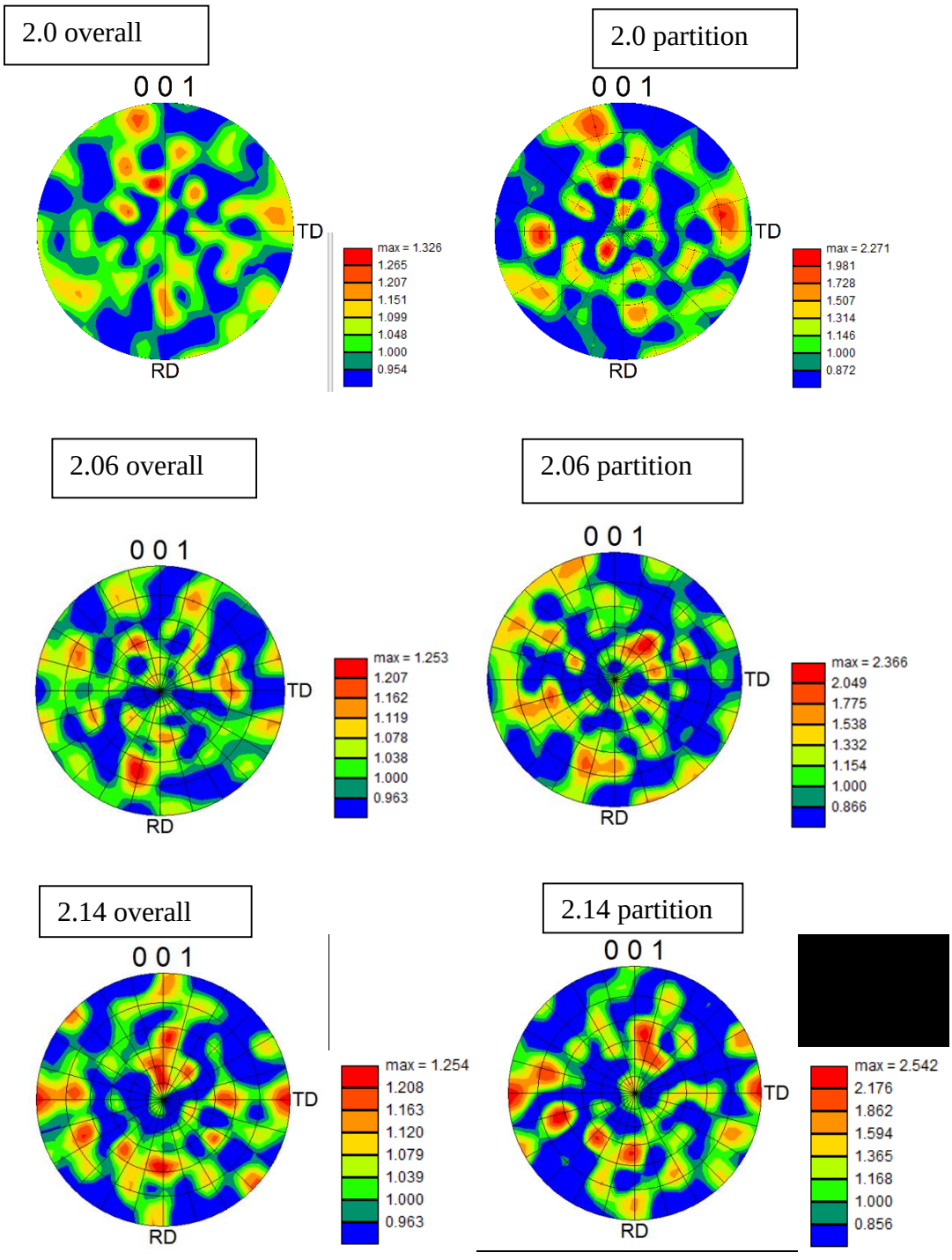

Figure 5.53. Crystallographic texture of the samples with different O/M: (2.0, 2.06 and 2.135).

The results from Figure 5.53 indicate that there is not a strong texture in the samples, not even in the partitions. There is a small tendency for grains to orient at the radial direction (in this case TD and RD). Again, some of the peaks for the overall sample coincide with the partitioned data, suggesting that the large grains somewhat dominate the texture. However, there is still a question unanswered: why these grains are growing more than the rest?

As 2-D EBSD data was available, a closer look of the crystallography of the GBs of these large grains was taken to determine if there is something on the GB character that lead them to abnormally grow. Figures 5.54-56 show the results for the texture plots of these GBs as well as the overall results for each sample.

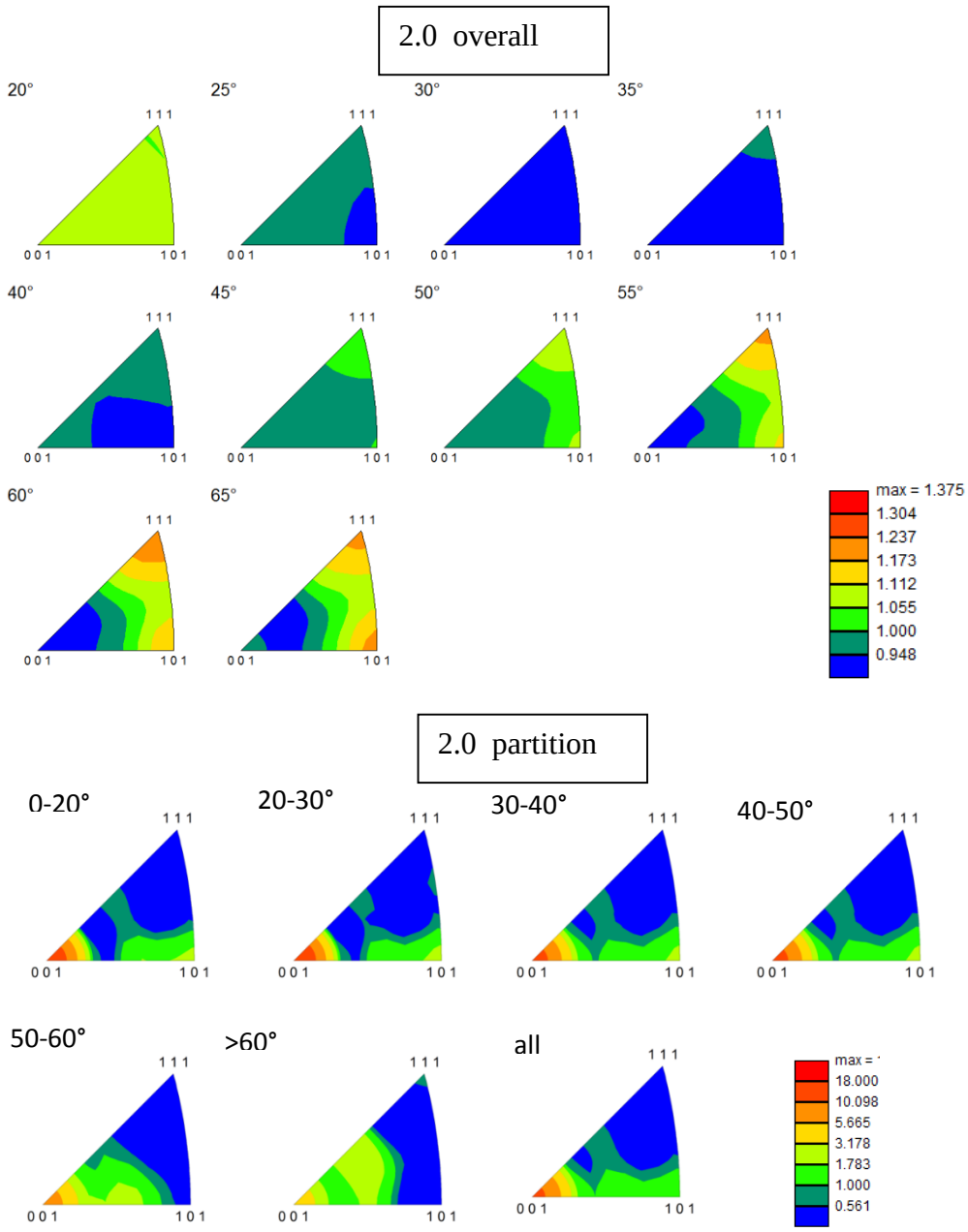

Figure 5.54. GB texture plots for the 2.0 sample.

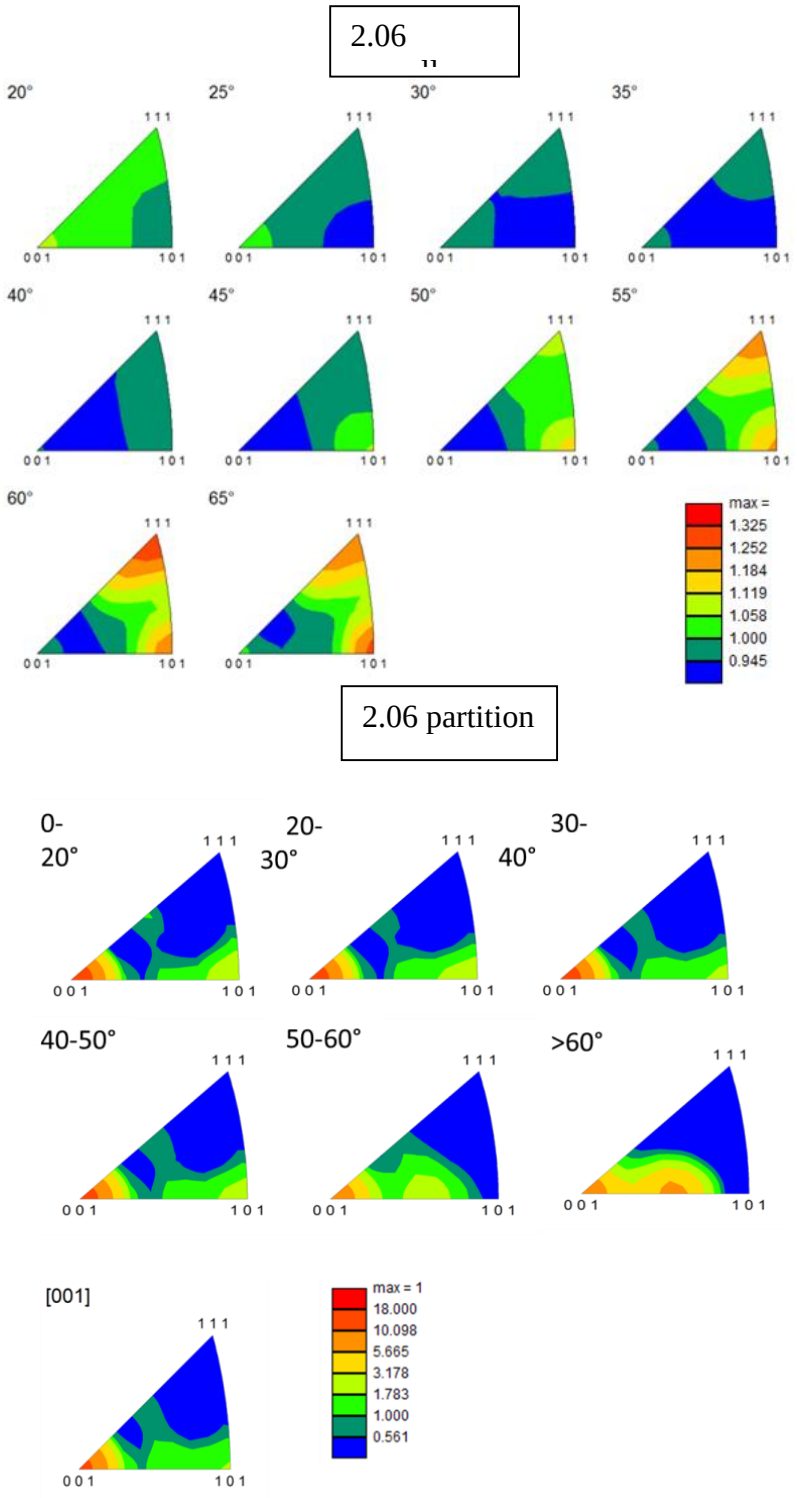

Figure 5.54. GB texture plots for the 2.06 sample.

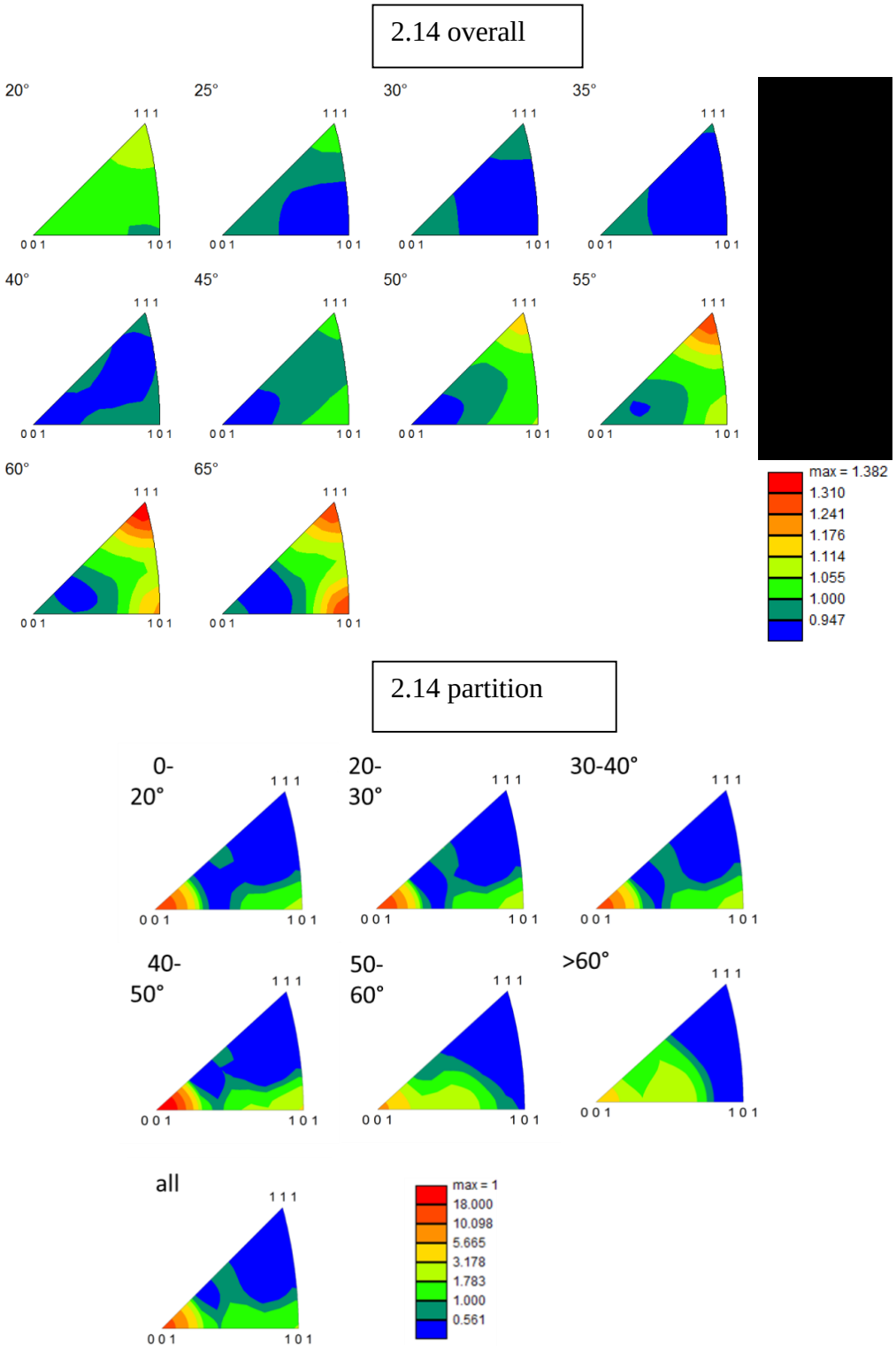

Figure 5.56. GB texture plots for the 2.14 sample.

The thermodynamic driving force for sintering is a reduction of the interfacial free energy by replacing the solid-vapor interfaces for solid-solid interfaces. The latter is mainly achieved by coarsening and densification. The total interfacial area is reduced by coarsening, while high energy interfaces are replaced by low energy interfaces during densification. During solid-state sintering, local mass transport is driven by the chemical potential difference between two grains. The chemical potential difference is related mainly to the curvature of the GB and GBs will move towards its center of curvature until they become flat, or smaller grains disappear [127].

Figures 5.54-56 show that the trends for the GB texture regardless of the O/M are quite similar. For the overall distribution in the samples, most of the high-angle GBs have a rotation axis of <111> and <101>. However, the partitioned data shows that most of the GBs around large grains have the <001> rotation axis with some oriented along <101>. Only few GBs had located <111> rotation axes, suggesting that the GBs near this rotation axisare not growing. The results suggest that GBs with a rotation axis of [001] are more common in larger grains, and could dominate the grain growth during the later stages of sintering. The literature indicates that surface energy, GB energy, GB mobility and the mobility of the pores can be sensitive to the O/M [125]. However, the results presented here indicate that the GB type associated to large grains seems to be independent of the oxygen content.

Regarding on a hypothesis to explain the preferential misorientation of these GBs one could propose several ideas:

These GBs seem to be able to pass pores and leave them behind, as shown in Figure 5.34. Pores exert a dragging force over the GBs slowing down the GB mobility[34], if these GBs

can move around the pores or easily detach from the pores, the pore-free GBs can migrate faster than the GBs with pores, facilitating grain growth.

Simulations by Holm et al.[126] for anisotropic grain growth indicate that GB energy is more important than mobility in determining the steady state misorientation distribution functions (MDF), and that the MDF is not kinetically constrained by mobility. These GBs could be have lower energy than other random GBs and could potentially lengthen at the expense of higher energy GBs, generating abnormal grain growth.

Moreover, molecular dynamics (MD) calculations of GB energy vs. misorientation angle done by Carmack and Zhang [134] are shown in Figure 5.57. These calculations indicate that <100> twist GB have the lowest GB energy, while <110> have the lowest GB energy. These results are consistent with the hypothesis that lower energy GBs are stable and grow, while higher energy GBs tend to disappear to minimize the system energy.

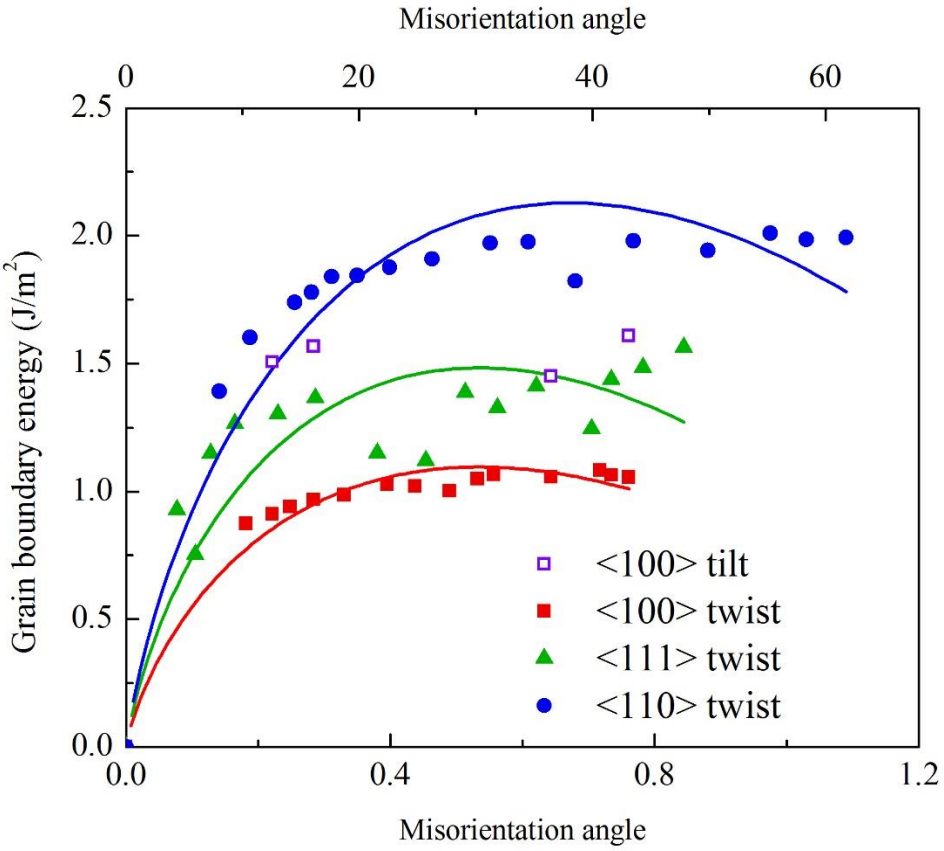

$$\gamma_{gb} = E_0\,\theta(A_0 - \ln\theta), \text{ where } E_0 = \mu b/4\pi(1-\nu);\;\; A_0 = 1 + \ln(b/2\pi r_0)$$

Figure 5.57. Grain boundary energy vs misorientation angle for GBs with different rotation axis. [134]

The abnormal grain growth could also be related to the diffusivity of the uranium atoms. The diffusion of uranium atoms is about 5 orders of magnitude lower than the oxygen diffusivity, the diffusivity of the uranium atoms will control the grain growth rate [127, 128]. Moreover, uranium vacancy is the predominant metal defect in stoichiometric and hyper-stoichiometric urania [127]. The <001> direction can be the best candidate for the U

atoms to move to a neighboring vacancy or to the octahedral site, as seen in Figure 5.58. It has been reported that it is more energetically favorable for U defects to associate with oxygen defects, such as $1U_V^{4+}+2O_V^{2-}$ [130] among multiple possibilities of combinations of oxygen and uranium defects. These defect clusters have enough mobility to contribute significantly to mass transport in the material [127]. In order to maintain charge electroneutrality some of these defects tend to locate at specific planes and sites in the fluorite lattice [131] that could restrict the available sites and directions for the cluster to move. An increase of the concentration of these defects could locally enhance the GB mobility.

(a) 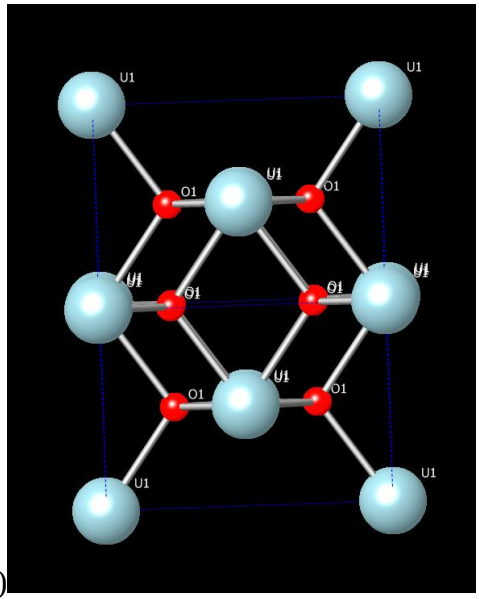

(b) 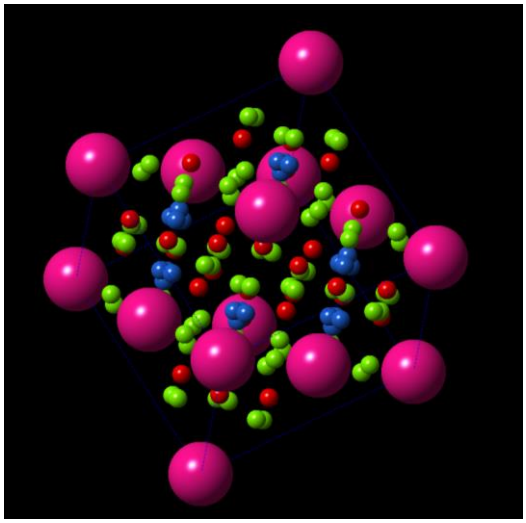

Figure 5.58. (a) Crystal structure of UO_2: Oxygen atoms are in red and uranium atoms are light blue. (b) All possible interstitial sites proposed by Willis for the 2:2:2 defects [132]: Pink atoms are uranium, red atoms are the oxygen atoms at the regular lattice positions, blue and green atoms are the O' and O'' interstitial positions.

Observations from Muggelberg et at. indicate that for the (001) urania surface, the atomic periodicity correspond to a half monolayer of oxygen atoms arranged in out of phase domain along the [110] and directions. Moreover, certain uranium atoms move closer together to form dimers and move together slightly in the <001> direction leaving empty rows [133]. Can a similar structure be present at certain GBs? If so the empty rows could be paths for the uranium atoms or defect clusters to move and enhance the mass transport at these GBs.

One could speculate that GBs with the <001> rotation axis could preferentially segregate impurities and or defects that lower its energy and could potentially increase its mobility to favor grain growth. Figure 5.59 shows a Σ5(310)/[001] tilt GB of UO_2, from the figure it can be seen that there are potentially some openings in the GB structure along the <001> that could accommodate some point defects, aiding GB diffusivity.

Furthermore, a few molecular dynamics simulations have been done to study GB migration in [001] twist and [001] twin GBs, both in Σ and random high angle GBs, for FCC metals [43-45]. Results show that as the local GB symmetry decreases the string-like cooperative atomic motions and that the atomistic mechanism are sensitive to GB orientation and local symmetry [134].

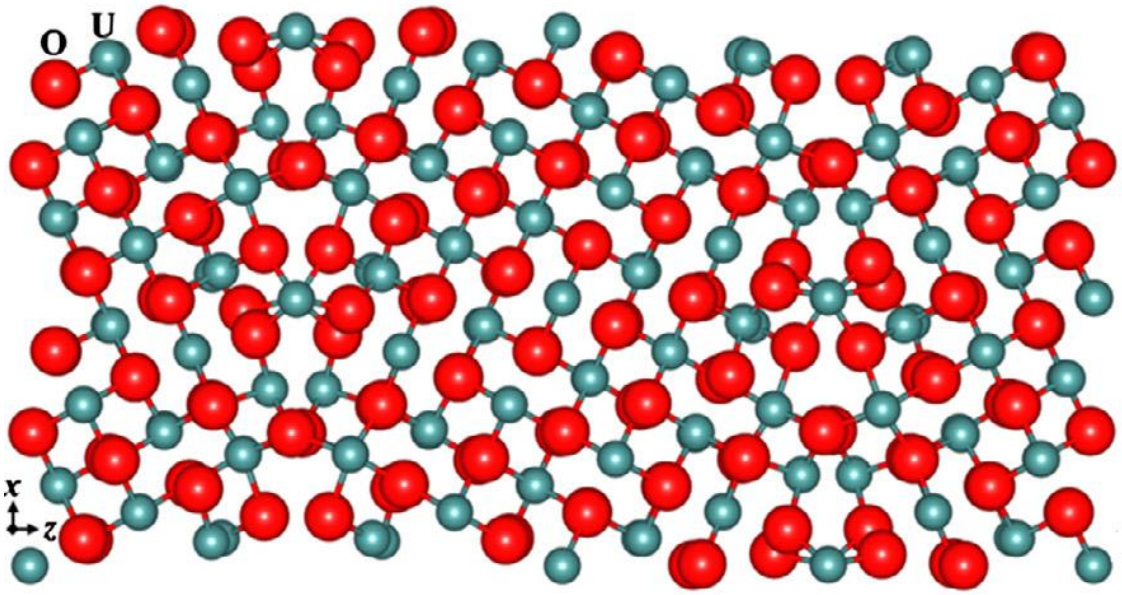

Figure 5.59. Σ5(310)/[001] tilt GB of UO_2 (U is the small blue-gray atom and O is the large red atom. [65]

However there is not enough information available in the literature or in our results that could directly explain why these particular GBs are more frequent in larger grains than other GBs with different rotation axis. In the next section, a sample will be subjected to interrupted heating and will be scanned to obtain EBSD scans to further study GB mobility.

5.5 Heat treatment

Sample 38 was heat treated as described in Chapter 4, to obtain more information to relate grain growth and crystallography. Figure 5.60 shows EBSD maps of the before and after microstructures of the sample.

(a)

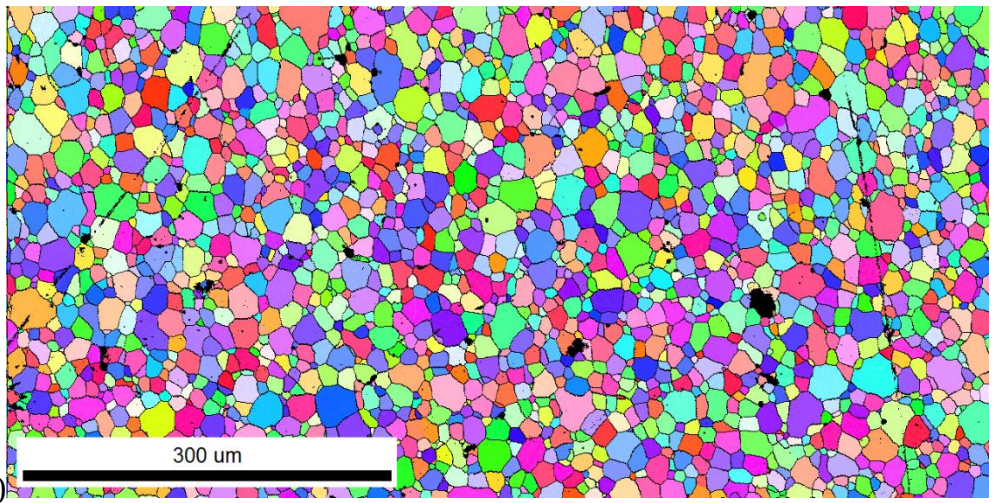

(b)

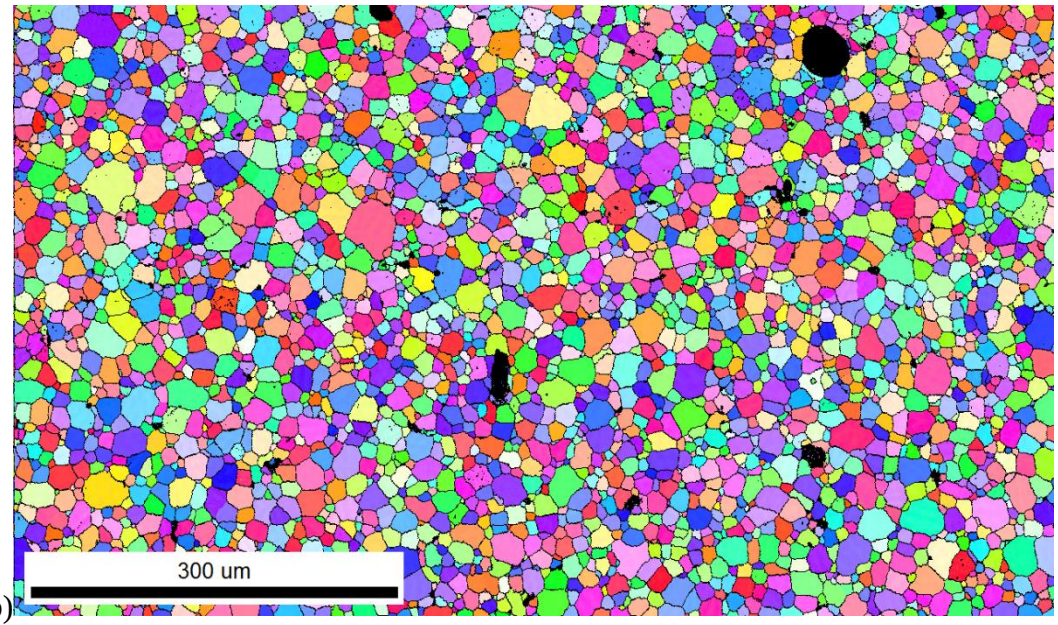

Figure 5.60. EBSD maps (a) before (800 μm by 400μm) and (b) after the heat treatment (850μm by 500μm) at 300x (sample 38).

It can be seen that grain growth occurred during the heat treatment. An example of a smaller area where some of the grains and grain boundaries moved is shown in Figure 5.61.

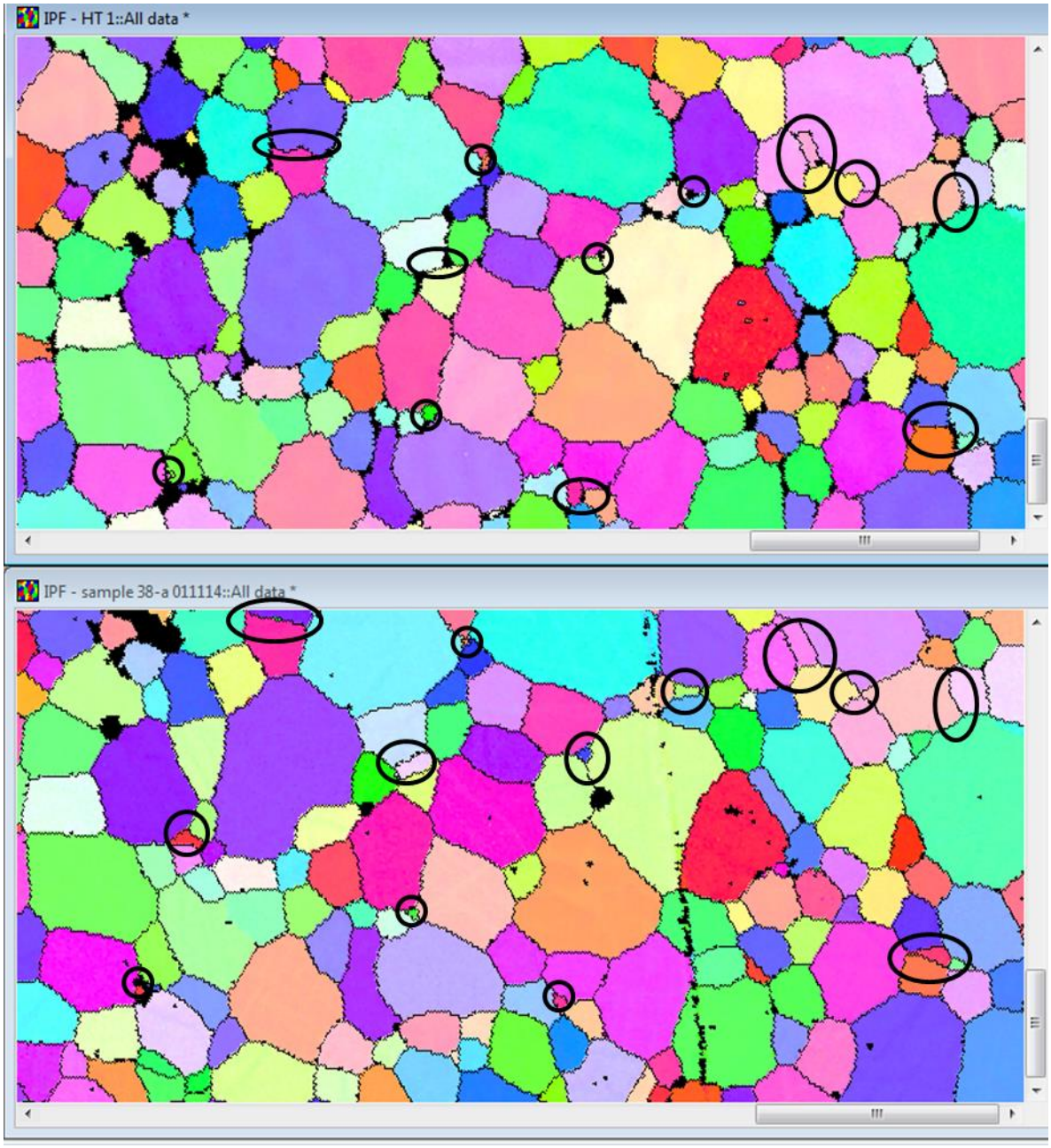

Figure 5.61 Detail of microstructural changes in the sample after the heat treatment. The bottom image is and EBSD map of the initial microstructure and the top image is the after EBSD map (sample 38).

One of the main objectives of this experiment was to study how the GB move during grain growth. The EBSD data was used to obtain grain orientation spread maps and Kernel average misorientation maps of the before and after microstructures.

The grain orientation spread maps compares the average deviation between the orientation of each point in the grain and the average orientation for the grain. Figure 5.62 shows the maps for the before and after microstructures. Grains with a blue color have no spread and all the points in a grain have the same orientation. Grains colored with red have the largest spread. It can be seen from the figure that for the overall microstructure, the map changes from blue to green. This observation indicates that in general the disorder in the lattice is increasing as locally the orientation is changing within the grain. Moreover, large grains tend to have a lower spread (blue) than smaller grains (green, yellow, orange and red); corroborating our previous results that larger grains tend to be more stable.

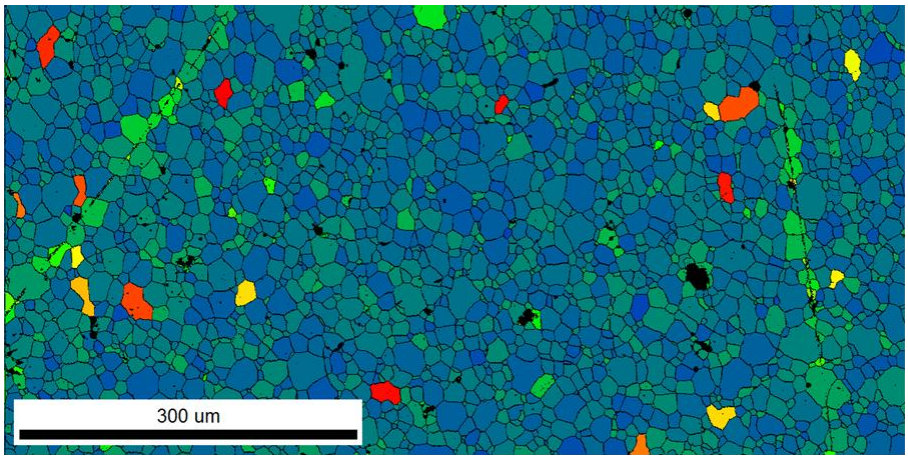

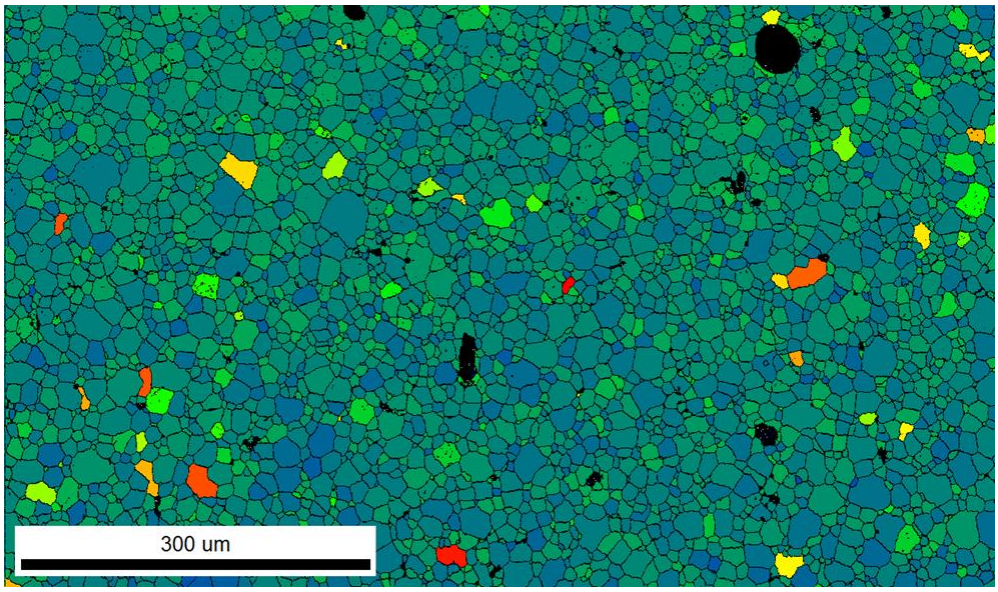

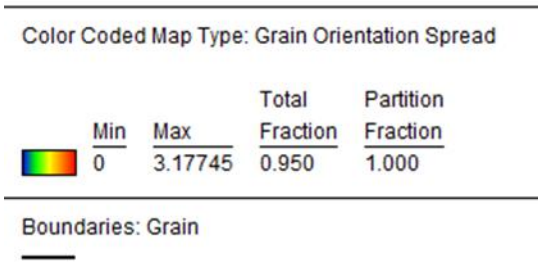

Figure 5.62. Grain orientation spread maps for before and after the heat treatment (sample 38).

The Kernel average misorientation maps show the distribution of local misorientations based on Kernel average misorientation between neighboring points. A center point is assigned with an average misorientation of its nearest neighbors and then the points are compared with the center point to determine local orientation variations. Figure 5.62 shows the Kernel average misorientation maps for the before and after microstructures. In the maps GB are highlighted in black. A blue color, again indicates that there is little or no difference between the orientations of the neighboring points, while red indicates a misorientation of 5°, in this case a grain is defined by neighboring points with misorientation less than 5°. The results from these maps are remarkable, circled in red are highlighted yellow lines that were grain boundaries and after the heat treatment lowered locally the misorientation to less than 5°, at least near the GBs promoting grain growth. As seen in the previous maps, the local disorder inside the grains increased for the after microstructure. Large grains seem to be affected less as smaller grains are rotating to match a closer orientation to the larger grains and promote grain growth. Examples of some of these grains are shown in Figure 5.64.

(a)

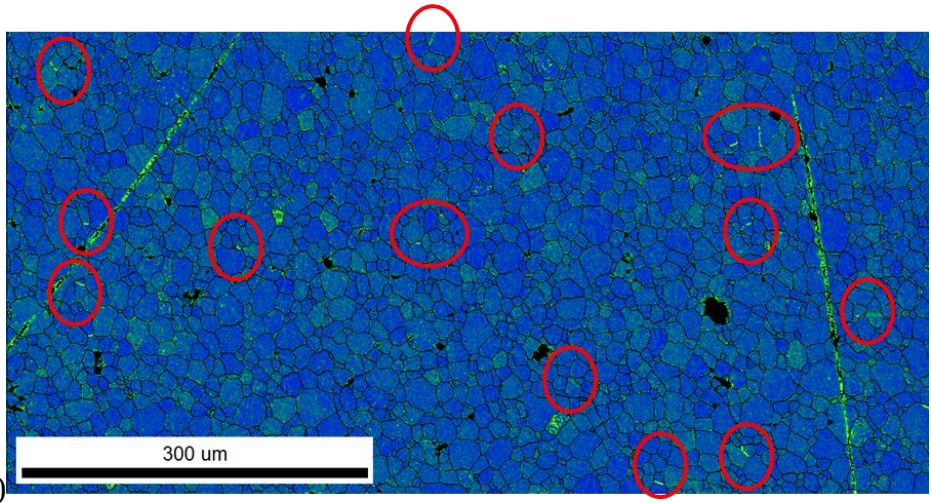

(b)

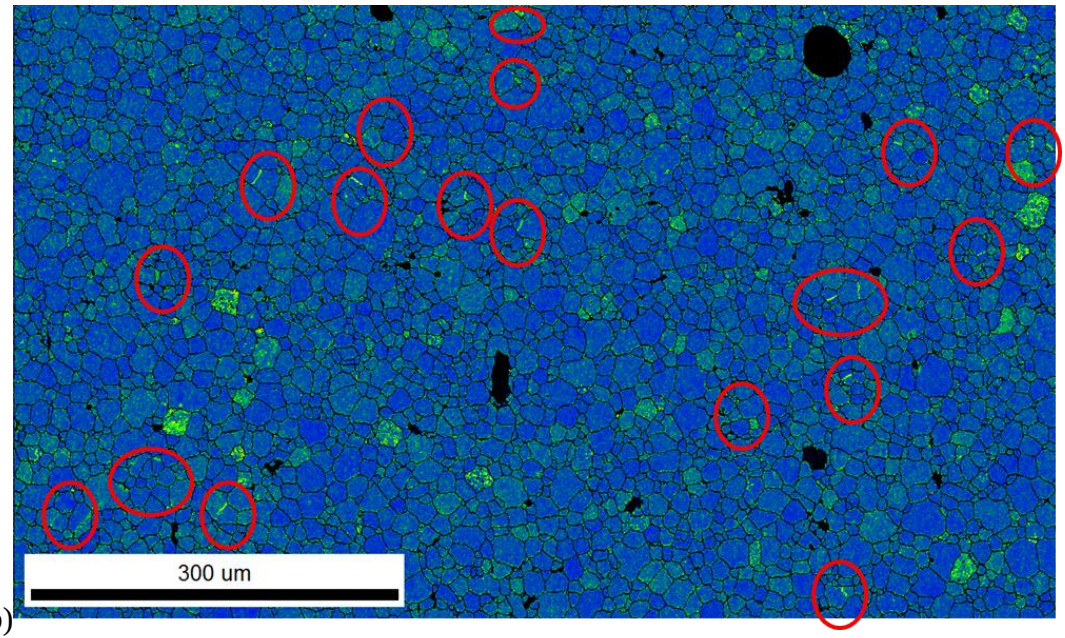

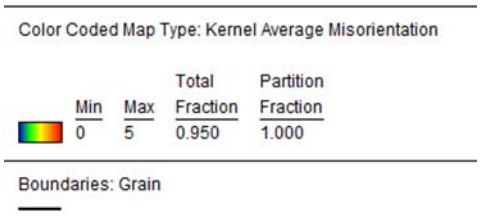

Figure 5.63. Kernel average misorientation maps: (a) before and (b) after the heat treatment for sample 38.

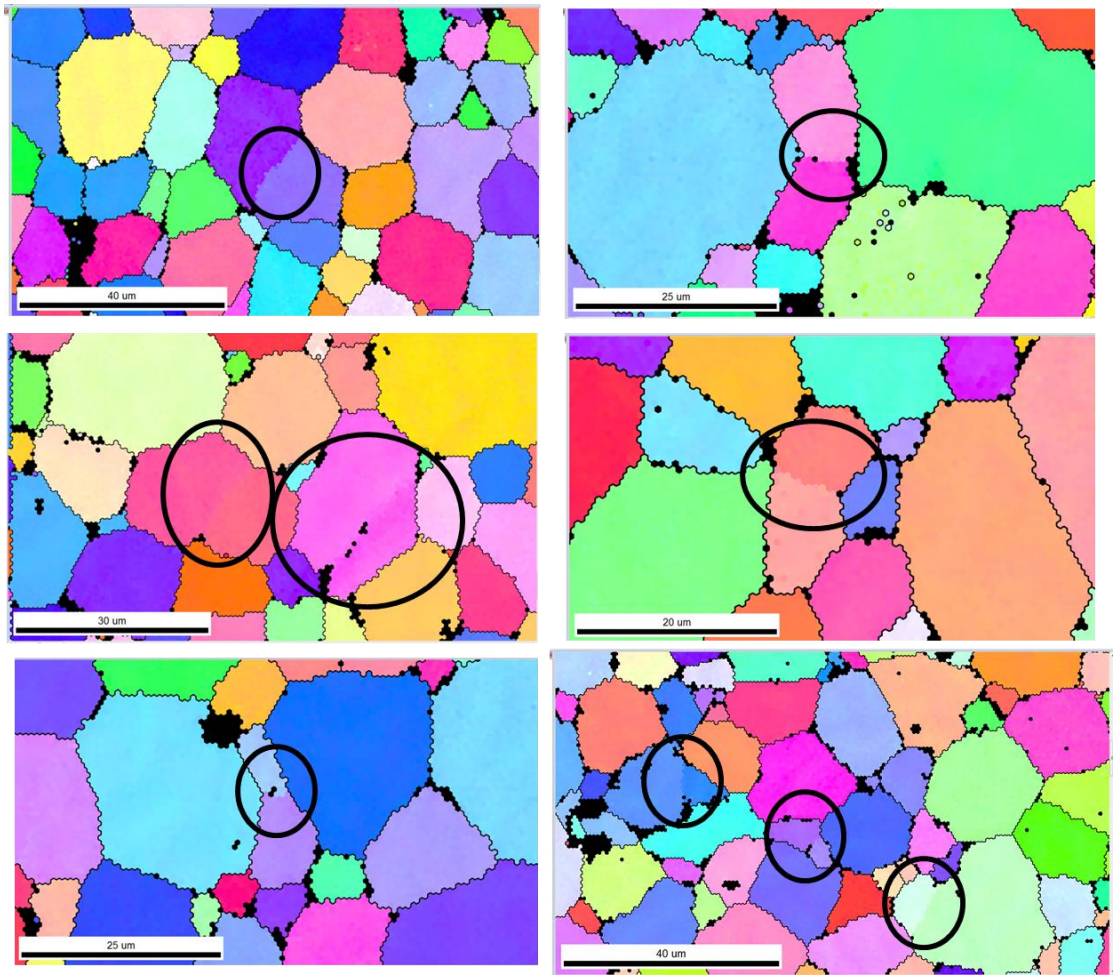

Figure 5.64. IPF maps of selected grains in sample 38 after heat treatment. The GB are highlighted in black and the grains that presented grain growth are circled.

From these results we propose that grain growth can occur by a "rotation front" mechanism, where neighboring atoms rotate to try to match the orientation of a neighboring grain. As previously stated the uranium atoms have very slow diffusivity that could slow and limit the grain growth. Therefore, it seems that GB diffusivity/motion alone is not the only mechanism for grain growth in this case. The lattice rotation could potentially be aided by

point defects, defect clusters and dislocations, but more data needs to be collected in order to precisely determine how this “rotation front” expands in the grain lattice.

Clusters of grains with similar orientations were observed not only on the heat treated sample but in all the studied samples, and could represent the early stages of the mechanism. Moreover, this clusters seem to preferentially have orientations near to the vertices of the inverse pole figure, and it could be consistent with results presented in the literature that states that grains tend to evolve to low index orientations.

As seen in Figure 5.65, GB lengthening was observed in between large grains (red circle) as well as the “rotation front”. The IPF map on the top is the after microstructure, it can be seen that a pore that was located in between the two old grains was absorbed and that the “old boundary” in between the two grains that form the large grain became straighter.

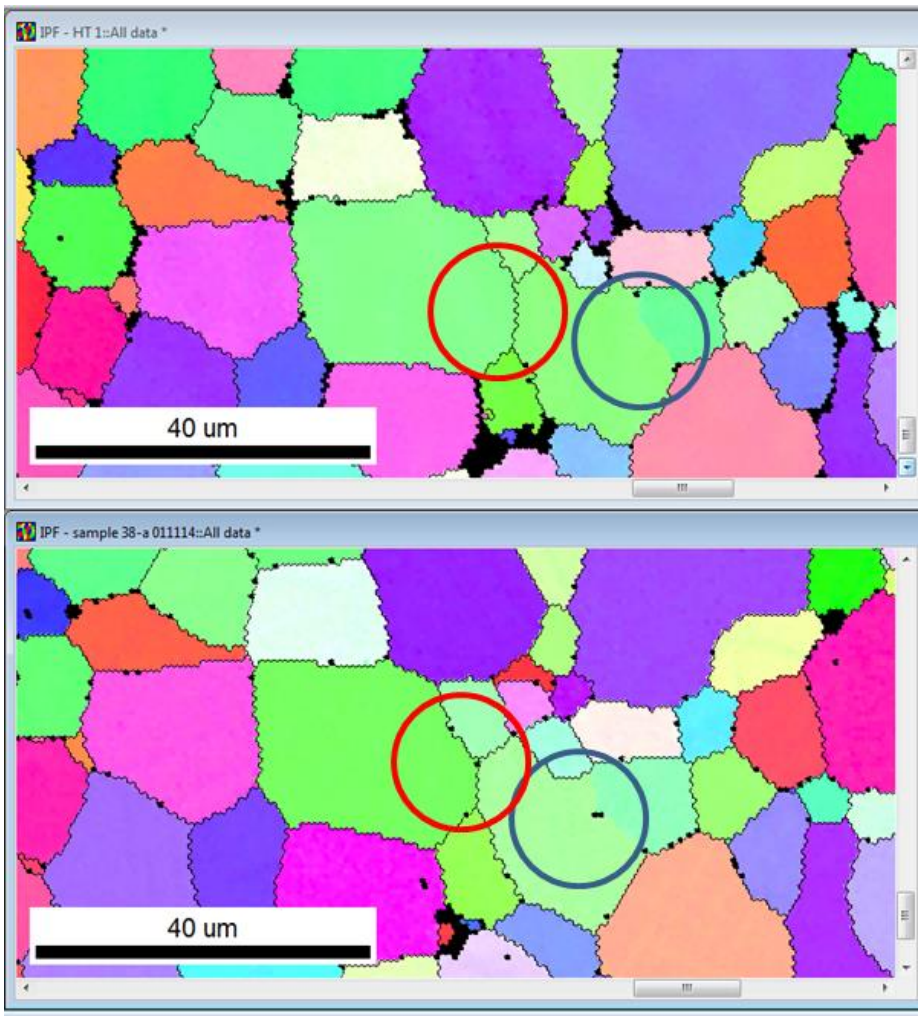

Figure 5.65. IPF maps of the after (top) and before (bottom) microstructure of sample 38. Grain boundaries are highlighted in black, the red circle shows the grain growth by GB lengthening and the blue circle shows grain growth by "rotation front".

This grain growth mechanism, to the best of the author knowledge has not been reported. However, Monte Carlo simulations of grain growth for nanocrystalline urania by Govers [135], suggest that rather than randomly oriented grains, the microstructure evolves to larger grains with lower angle GBs as seen in Figure 5.66.

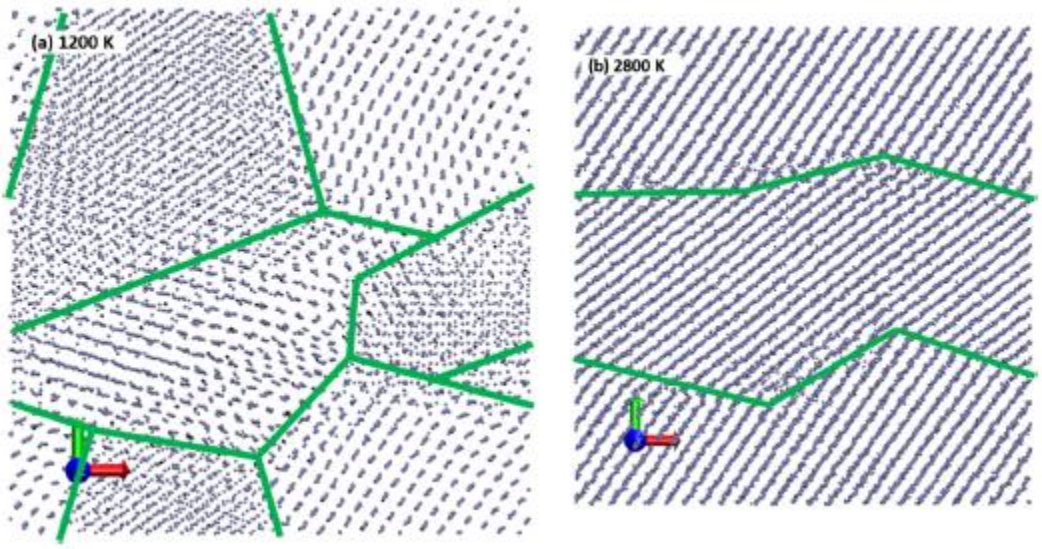

Figure 5.66. Microstructure of the small system after 1000 ps at 1200K (left) and 2800K (right). Only U atoms are shown. [135]

The results presented in this work indicate that crystallographic data of the grains and GB are necessary to understand how the microstructure of the fuel will evolve, not only inside the reactor but also during sintering.

CHAPTER 6

CONCLUSIONS

- It was found that the CSL distribution seems to be sensitive to the manufacturing conditions. The CSL distribution of the insulator pellet (86% TD, sample 1) was compared to a cubic zirconia sample and to a depleted UO_2 sample with higher density (95% TD, sample 2) and the results shown significant variations on the CSL distribution, including a larger fraction of Σ9 GBs for the insulator pellet (sample 1). These results were attributed to a possible less "mature" microstructure in the insulator pellet, since its low density implies that sintering of this sample was not taken to its final stage, as well as the possibility that area selected for study in the insulator sample was not statistically representative of its overall microstructure.
- The CSL distribution can be used to determine the minimum representative area of the microstructure as this measurement is very sensitive to variations of microstructural features such as porosity, grain size and GB distribution (misorientation, geometry, location). Although CSL fractions of GBs were similar for all the studied samples, the CSL distribution changed depending on the processing conditions as well as the "maturity" of the microstructure. This, in turn, suggests that, depending on the processing conditions (powder composition and size, temperature, time, sintering atmosphere, etc.), some grain boundaries could potentially grow preferentially over others to minimize the energy of the system.
- The pore shape seems to be related to the pore size, as the pore size increases the pore shape changes from rounded to elliptical. A relationship between pore size and location within the microstructure was established: small pores tend to locate inside

the grains and GBs, whereas large pores tend to locate at TJs. There is a similar fraction and distribution of pores at mid angle and CSL boundaries, while most of the pores are located at high angle GBs, especially larger pores. There is a negligible fraction of pores in low angle GBs. This again can be related to a mechanism for energy minimization as pores migrate to higher energy GBs to lower their energy.

- The pore size distribution at TJs consisted of mostly small pores, followed by nearly equal fractions of medium and large pores. The majority of TJs that contain pores has at least 2 high angle GBs. These results suggest that pores at TJs tend to be more stable and pores located at GBs and inside the grains will migrate and coarse the pores located at TJs. Furthermore, larger pores are located at TJs with at least two high angle GBs, suggesting that pores tend migrate to high energy sites to minimize the total energy.
- A preliminary 3-D model based on the EBSD data from serial sectioning was obtained. The serial sectioning data can be used to determine microstructural changes through the sample's thickness. The later was possible by developing a fairly precise polishing method where 0.5 μm were removed in every step.
- The heating rate of the sintering ramp seems to have a strong effect on the evolution of the microstructure. Slow sintering ramps could potentially shift the microstructure from a one phase (UO_{2+x}) to a two phase microstructure (UO_{2+x} and U_4O_{9-y} or U_3O_{8-z}) during the initial sintering process, significantly affecting the final product.

- Larger grains, at least 2.5 times the average size, seem to have a fairly strong crystallographic texture distribution and dominate the overall texture of the samples manufactured under different sintering ramps. The same study was done for the samples manufactured with different stoichiometry and similar results were observed. These observations seem to indicate that larger grains, manufactured under different conditions, dominate the crystallographic texture of the uranium dioxide sampled. These results suggest that the mechanism that controls grain growth seems to be independent of both processing conditions and stoichiometry.
- Regarding he samples with different O/M, results from serial sectioning indicate that the oxygen content in UO_{2+x} has an effect on the evolution of the fuel's microstructure during sintering. The O/M=2.14 sample had more equiaxial grains with more straight grain boundaries while the O/M=2.0 sample had more curved GBs. Out of the three studied stoichiometries, the sample with O/M=2.06 had a larger grain population. Abnormally large with curved GBs and > 6 neighbors (2-D) were observed in all three O/M values.
- Moreover, although, on average, the grain size for the samples with different O/M has no large variations, the distribution of the grain size has some significant differences. The sample with the highest oxygen content has a larger tail on the distribution with clearly larger grains in size. This result is consistent with the literature, as an increase of the O/M promoted grain growth.
- As small pores and grain clusters were observed in the samples with different O/M, a larger area was scanned for the three samples and 2-D EBSD data was obtained and compared to the serial sectioning data. The results indicate that larger areas can

significantly decrease the variability on the measured CSL fraction and distribution for the three samples. However, as the Σ GB increases (larger than Σ11), the population of these GB decreases, increasing their variability.

- Regarding the GB normals calculated from 3-D reconstruction of the samples with O/M=2.0 and 2.14; there seems to be an absence of {111} GB planes in the 30^0-50^0, regardless of the oxygen content. However, the most common GB planes were different in each case, the majority of GB planes in the 30^0-40^0 range for the stoichiometric samples are around {112} and {113}; while for the non-stoichiometric sample are {011} and {113}. These could give insights on what planes are more favorable on the material, as most of the GBs have a misorientation around 42^0 and both samples seem to have in common the {113} plane. That plane is also a twinning plane for ∑11 (50.48^0/<110>) GBs, and a rather large fraction of these GBs were observed in $UO_{2.14}$.
- However, the results obtained from planar sections suggest that the predominant normal plane, regardless of the O/M or the location of the studied area is {111}, which, as previously discussed, is a twinning plane for the fluorite structure. The difference between the two sets of results could be associated with the size of the analyzed data set. The distribution from the 2-D planar sections required a large data set (>10^4 GBs), while the 3-D data set was manually collected from a small data set that only included ~200GBs and might be not large enough to be representative of the overall distribution.
- A partition that included only grains 2.5 times the average grain size for the samples with different stoichiometry was analyzed. All the studied grains had at least 6

neighbors with up to 24 neighbors, with an average of 12 neighbors in all cases regardless of the O/M. Moreover, as reported for the samples fabricated under different heating rates for the sintering ramp, the crystallographic texture distribution seems to be strongly driven by these larger grains.

- Regarding the crystallography of the GBs surrounding these large grains, it seems that the preferential misorientation axis, regardless of the oxygen content, is {001}. These results might be related to GB energy and structure. Among the possible hypothesis to explain these results is that enhanced diffusion of point defects and defect clusters that could enhance the GB diffusion in boundaries with a {001} rotation axis. The latter could be related to the particular structure of these GBs and or the presence of different complexions generated by the segregation of impurities of the powder to these GBs.
- Grain growth seem to occur at least by two mechanisms at the final sintering stage. Grain boundary lengthening was observed between large stable grains. A second mechanism, referred in this work as "rotation front", was also observed. In this case, grains rotate to match the orientation of a neighboring grain to eventually merge to the neighboring grain.

The work presented here clearly indicates that even when typical microstructural parameters such as density and grain size are similar between samples, as is the case here, differences can still be present in other microstructural parameters, such as grain boundary character and GB-pore interactions, both of which affect the sintering kinetics. In this case, observations on the trends for these two parameters were consistent with the small

differences in final densities obtained under otherwise identical sintering conditions and demonstrate that more detailed microstructure characterization can be important to improve our quantitative and qualitative understanding of microstructural effects on sintering of oxide fuels. However, regardless of the manufacturing conditions, some specific GBs seem to dominate the grain growth and, therefore, could potentially drive the microstructure evolution of the fuel.

CHAPTER 7

FUTURE WORK

There is not much information available in the literature on how the processing conditions and parameters can affect the microstructure of the fuel pellet in terms of its crystallography. To fully understand the results presented here a deeper characterization of the GBs that belong to the large grains is needed as it seem that these GBs drive the grain growth.

The main limitation of the study material is its radioactivity, as cutting, gridding and polishing has to be done in self-contained environments, which complicates the sample preparation technique and limits the availability of facilities to characterize the samples. Part of the work described in this dissertation was to develop techniques to handle, cut and polish samples for characterization (as described in Appendices A, B and C). Here are a few ideas on what can be done next to complement the results obtained in this study:

- Ideally, the polished samples can be taken to SEM-FIB equipped with an EBSD detector. The samples can be scanned to determine its crystallography, including GB misorientation and rotation axis. If some of the GBs are long enough, the region around, including the GB can be cut, polished and separated using the FIB for Transmission Electron Microscopy (TEM) and atom probe analysis. Samples with different crystallography including CSL GB (at least $\Sigma 3$, $\Sigma 5$, $\Sigma 11$) and high angle GBs with {001} rotation axis, as well as random high angle GBs should be included. The study should help to determine GB structure and composition, to establish if in fact there is a higher concentration of impurities and/or defects that

enhance grain growth for GBs with {001} rotation axis in comparison to the rest of the random high angle GBs. The latter can be done by performing heat treatments that can be potentially done over the samples to increase grain size and obtain large enough GBs. The GBs from these large grains, can be harvested from polycrystalline materials using FIB. Heat treatments could also potentially be applied in-situ in the TEM to study effects of GB kinetics on grain growth, for the selected GBs.

- These results can be complemented with atom probe, to determine oxygen and uranium atoms concentration at these GBs. As previously mentioned this analysis can only be done at selected facilities such as Idaho National Laboratory and Oak Ridge National Laboratory. The availability of time to use the facilities is scarce and highly competitive and a proposal needs to be written to the Nuclear Reactor Users Facilities.
- Additionally, to obtain more details on the microstructure, as well as to collect more 3-D data, high energy x-ray diffraction data could be collected for these samples. The 3-D data can be used to obtain larger datasets to determine grain size and shape as well as GB curvature. Samples with different fabrication conditions such as O/M (same samples used in this study), sintering temperature and variations on density (for instance interrupted sintering cycle) can be used. The 3-D can help to deeper the understanding on the mechanism of grain growth. Samples from an interrupted sintering cycle can be used to track grains and study grain growth. Data can potentially be used to fully characterize GBs of large grains and study its GB texture, to determine if in fact there is a potential preferential rotation axis (texture)

for the abnormally large grains. An interrupted heat treatment, similar to the one described in this work could be used to characterize the samples, using high energy x-ray diffraction and study in 3-D the grain growth.

- Determine a more systematic method to collect GB normal data from serial sectioning data and reconstructed microstructures in a way that can be related to the GB crystallography.
- Also, study how other parameters such as sintering temperature, powder composition, doping, sintering atmosphere, can affect the GB crystallography as well as the porosity distribution, shape and location. Moreover, study other stoichiometry values in between the ones presented in this work, to increase the available datasets and deepen the understanding of how the oxygen content affects the GB character.
- Obtain molecular dynamics models of the {001} GBs (both CSL and high angle) to determine its energy and why these GBs seem to be responsible for grain growth.
- Obtain Monte Carlo simulations of the sintering process to study the "rotation front" mechanism and determine exactly how grains merge to form larger grains.
- The crystallographic data obtained from serial sectioning in this study can be used as inputs for finite element models (FE). The models can be used to determine how and if these different microstructure affect heat and mass transport of the fuel.

REFERENCES

1. DOE. *Fuel Cycle Research and Development Program*. 2012; Available from: http://www.nuclear.energy.gov/fuelcycle/neFuelCycle.html.
2. Agency, I.A.E., *Nuclear Fuel Cycle Information System*, in *A directory of Nuclear Fuel Cycle Facilities*. 2009, IAEA: Vienna, Austria.
3. Agency, N.E., *Nuclear Energy Outlook*, L. Echevarri, Editor. 2008.
4. Olander, D., *Nuclear fuels" Present and future.* Journal of Nuclear Materials, 2009. **389**(1): p. 1-22.
5. Radford, K.C. and J.M. Pope, *Controlled porosity reactor fuel.* Journal of Nuclear Materials, 1977. **64**(3): p. 289-299.
6. Radford, K.C. and J.M. Pope, *UO2 fuel pellet microstructure modification through impurity additions.* Journal of Nuclear Materials, 1983. **116**:p. 305-313.
7. Radford, K.C., *Effect of fabrication parameters and microstructure on the mechanical strength of UO2 fuel pellets.* Journal of Nuclear Materials, 1979. **84**: p. 222-236.
8. Harada, Y., *UO2 sintering in controlled oxygen atmospheres of three-stage process.* Journal of Nuclear Materials, 1997. **245**: p. 217-223.
9. Assmann, H., W. Dörr, and M. Peehs, *Control of UO2 microstructure by oxidative sintering.* Journal of Nuclear Materials, 1986. **140**(1): p. 1-6.
10. Paraschiv, M.C., A. Paraschiv, and V.V. Grecu, *On the nuclear oxide fuel densification, swelling and thermal re-sintering.* Journal of Nuclear Materials, 2002. **302**(2–3): p. 109-124.
11. Dillon, S.J. and G.S. Rohrer, *Characterization of the Grain-Boundary Character and Energy Distributions of Yttria Using Automated Serial Sectioning and EBSD in the FIB.* Journal of the American Ceramic Society, 2009. **92**(7): p. 1580-1585.
12. Idriss, H., *Surface reactions of uranium oxide powder, thin films and single crystals.* Surface Science Reports. **65**(3): p. 67-109.
13. Lee, C.B., et al., *A new mechanistic and engineering fission gas release model for a uranium dioxide fuel.* Journal of Nuclear Science and Technology, 2008. **45**(1): p. 60-71.
14. Wolf, D., *Structure and energy of grain boundaries*, in *Handbook of Materials Modeling*, S. Yip, Editor. 2005, Springer. p. 1953-1983.
15. Agency, O.N.E., *Fission Gas Behaviour in Water Reactor Fuels*. OECD Publishing.
16. Stehle, H., H. Assmann, and F. Wunderlich, *Uranium dioxide properties for LWR fuel rods.* Nuclear Engineering and Design, 1975. **33**(2): p. 230-260.
17. Baichi, M., et al., *Thermodynamics of the O–U system: III – Critical assessment of phase diagram data in the U–UO2+x composition range.* Journal of Nuclear Materials, 2006. **349**(1–2): p. 57-82.
18. Skomurski, F.N., et al., *Charge distribution and oxygen diffusion in hyperstoichiometric uranium dioxide UO2+x.* Journal of Nuclear Materials, 2013. **434**(1–3): p. 422-433.

19. Govers, K., et al., *Molecular dynamics simulation of helium and oxygen diffusion in UO2 x.* Journal of Nuclear Materials, 2009. **395**(1-3): p. 131-139.
20. Amato, I., Colombo, R.L. and Protti, A.M., *Influence of Stoichiometry on the Rate of Grain Growth.* Journal of the American Ceramic Society, 1963. **46**(8): p. 407.
21. Guenau, C., Baichi, M., Labroche, D., Chatilllon, C., Sundman, B., *Thermodynamic assesment of the uranium-oxygen system.* Journal of Nuclear Materials, 2002. (304): p. 161-175.
22. Naito, K., Tsuji, T., Matsui, T., *Defect structrure and related properties of UO2 and doped UO2*, in *NATO: Advanced Research Workshop on Non-Stoichiometric Compounds*, J.a.W. Nowotny, W., Editor. 1989, Kluwer Academic Publishers: Rottarch-Egern, Germany. p. 27-44.
23. Banerjee, S. and T.R. Govindan Kutty, *10 - Nuclear Fuels*, in *Functional Materials*, S. Banerjee and A. Tyagi, Editors. 2012, Elsevier: London. p. 387-466.
24. Stehle, H. and H. Assmann, *The dependence of in-reactor UO2 densification on temperature and microstructure.* Journal of Nuclear Materials, 1974. **52**(2): p. 303-308.
25. Schuster, E., et al., *Escape of fission products from defective fuel rods of light water reactors.* Nuclear Engineering and Design, 1981. **64**(1): p. 81-85.
26. Assmann, H. and H. Stehle, *Thermal and in-reactor densification of UO2: Mechanisms and experimental results.* Nuclear Engineering and Design, 1978. **48**(1): p. 49-67.
27. Stuart, W.I. and R.B. Adams, *Effect of sintering atmosphere on the density of uranium dioxide pellets.* Journal of Nuclear Materials, 1975. **58**(2): p. 201-204.
28. Kingery, W.D., *Introduction to Ceramics*. Second Edition ed. 1960: John Wiley and Sons.
29. Hsueh, C.H. and A.G. Evans, *Microstructure evolution during sintering: The role of evaporation/condensation.* Acta Metallurgica, 1983. **31**(1): p. 189-198.
30. German, R.M., *Coarsening in Sintering: Grain Shape Distribution, Grain Size Distribution, and Grain Growth Kinetics in Solid-Pore Systems.* Critical Reviews in Solid State and Materials Sciences, 2010. **35**(4): p. 263-305.
31. Coble, R.L., *Sintering Crystalline Solids. I. Intermediate and Final State Diffusion Models.* J. Appl. Phys., 1961. **32**(5): p. 787-792.
32. Bernard, D., et al., *First direct 3D visualisation of microstructural evolutions during sintering through X-ray computed microtomography.* Acta Materialia, 2005. **53**(1): p. 121-128.
33. Fang, T.-T. and H.I. Palmour, *Evolution of Pore Morphology in Sintering Powder Compacts.* Ceramics International, 1990. **16**: p. 1-10.
34. Joung, C.Y., et al., *Fabrication method for UO2 pellets with large grains or a single grain by sintering in air.* Journal of Nuclear Materials, 2008. **375**(2): p. 209-212.

35. Ali, M.E.-S. and R. Lorenzelli, *Kinetics of initial stage of sintering of UO2 and UO2 with Nd2O3 addition.* Journal of Nuclear Materials, 1979. **87**(1): p. 90-96.
36. Fuhrman, N., Hower, L.D. and Holden, R.B., *Low Temperature Sintering of Uranium Dioxide.* Journal of the American Ceramic Society, 1963. **46**(3): p. 114-121.
37. Han, J.K., W.K. Park, and H.S. Kim, *The sintering behavior of the hyperstoichiometric uranium dioxide in oxidative atmosphere.* Journal of the Korean Nuclear Society, 1984. **15**(3).
38. Williams, J., et al., *Sintering of uranium oxides of composition UO2 to U3O8 in various atmospheres.* Journal of Nuclear Materials, 1959. **1**(1): p. 28-38.
39. ARENBERG, C.A. and P. JAHN, *Steam Sintering of Uranium Dioxide.* Journal of the American Ceramic Society, 1958. **41**(5): p. 179-183.
40. Bernard-Granger, G. and C. Guizard, *New relationships between relative density and grain size during solid-state sintering of ceramic powders.* Acta Materialia, 2008. **56**(20): p. 6273-6282.
41. Liu, Y. and B.R. Patterson, *Grain growth inhibition by porosity.* Acta Metallurgica et Materialia, 1993. **41**(9): p. 2651-2656.
42. Svoboda, J., Riedel, H., *Pore-Boundary Interactions and Evolution Equations for the Porosity and The Grain Size During Sintering.* Acta metal. mater., 1992. **40**(11): p. 2829-2840.
43. Kok, K.D., *Nuclear Engineering Handbook*. 2009: CRC Press.
44. Maca, K., V. Pouchly, and P. Zalud, *Two-Step Sintering of oxide ceramics with various crystal structures.* Journal of the European Ceramic Society. **30**(2): p. 583-589.
45. Kutty, T.R.G., et al., *Densification behaviour of UO2 in six different atmospheres.* Journal of Nuclear Materials, 2002. **305**(2-3): p. 159-168.
46. Knorr, D.B., R.M. Cannon, and R.L. Coble, *Overview no. 84: An analysis of diffusion and diffusional creep in stoichiometric and hyperstoichiometric uranium dioxide.* Acta Metallurgica, 1989. **37**(8): p. 2103-2123.
47. Lay, K.W. and B.E. Carter, *Role of the O/U ratio on the sintering of UO2.* Journal of Nuclear Materials, 1969. **30**(1–2): p. 74-87.
48. Lahiri, D., et al., *Study on sintering kinetics and activation energy of UO2 pellets using three different methods.* Journal of Nuclear Materials, 2006. **357**(1–3): p. 88-96.
49. Amato, I., R.L. Colombo, and A.P. Balzari, *Grain growth in pure and titania-doped uranium dioxide.* Journal of Nuclear Materials, 1966. **18**(3): p. 252-260.
50. Dehaudt, P., L. Bourgeois, and H. Chevrel, *Activation energy of UO_2 and UO_{2+X} sintering.* Journal of Nuclear Materials, 2001. **299**: p. 250-259.
51. Stehle, H. and H. Assmann, *In-reactor UO2 densification.* Journal of Nuclear Materials, 1976. **61**(3): p. 326-329.
52. Yuda, R. and K. Une, *Effect of sintering atmosphere on the densification of UO2-Gd2O3 compacts.* Journal of Nuclear Materials, 1991. **178**(2-3): p. 195-203.

53. Hastings, I.J., *Effect of Initial Grain Size on Fission Gas Release from Irradiated UO2 fuel.* Communications of the American Ceramic Society, 1983(September): p. C-150 - C-151.
54. Childs, B.G., *Fission product effects in uranium dioxide.* Journal of Nuclear Materials, 1963. **9**(3): p. 217-244.
55. Olander, D.R., et al., *Light Water Reactor Fuel Design and Performance*, in *Encyclopedia of Materials: Science and Technology (Second Edition)*. 2001, Elsevier: Oxford. p. 4490-4504.
56. Veshchunov, M.S., *New models for UO2 fuel structure evolution under irradiation in fast reactors.* Journal of Nuclear Materials. **415**(1): p. 96-103.
57. Chockalingam, K., P.C. Millett, and M.R. Tonks, *Effects of intergranular gas bubbles on thermal conductivity.* Journal of Nuclear Materials, 2012. **430**(1–3): p. 166-170.
58. Millett, P.C. and M. Tonks, *Meso-scale modeling of the influence of intergranular gas bubbles on effective thermal conductivity.* Journal of Nuclear Materials, 2011. **412**(3): p. 281-286.
59. Williamson, R.L., et al., *Multidimensional multiphysics simulation of nuclear fuel behavior.* Journal of Nuclear Materials, 2012. **423**(1–3): p. 149-163.
60. Spino, J. and P. Peerani, *Oxygen stoichiometry shift of irradiated LWR-fuels at high burn-ups: Review of data and alternative interpretation of recently published results.* Journal of Nuclear Materials, 2008. **375**(1): p. 8-25.
61. Jo, W.a.H., N-M., *Interfaces and Microstructures in Materials*, in *Ceramics Science and Technology Properties*, R.a.C. Riedel, I-W., Editor. 2010, Weiley-VCH Verlach GmbH & Co: Weinheim.
62. Déchamps, M., F. Baribier, and A. Marrouche, *Grain-boundaries: Criteria of specialness and deviation from CSL misorientation.* Acta Metallurgica, 1987. **35**(1): p. 101-107.
63. Baluffi, R.W., *Grain Boundary Structure and Segregation*, in *ASM Materials Science Seminar*. 1978, ASM. p. 193-237.
64. Fisher, C.A.J., Matsubara, H., *The influence of grain boundary misorientation on ionic conductivity in YSZ.* Journal of the European Ceramic Society, 1999. **19**: p. 703-707.
65. Nerikar, P.V. et al, *Grain Boundaries in Uranium Dioxide: Scanning Electron Microscopy Experiments and Atomistic Simulations.* J. Am. Ceram. Soc., 2011. **94**(6): p. 1893-1900.
66. Chen, Y. and C.A. Schuh, *Diffusion on grain boundary networks: Percolation theory and effective medium approximations.* Acta mater., 2006. **54**(4709).
67. Mishin, Y., Herzig, Chr., Bernardini, J., Gust., W., *Grain boundary diffusion: fundamentals to recent developments.* International Materials Reviews, 1997. **42**(4): p. 155-178.
68. Lim, H., Rudman, K., Krishnan, K. McDonald, R., Dickerson, P., Byler, D., Peralta, P., Stanek, C., McClellan, K., *Microstructurally Explicit Simulation of Intergranular Mass Transport in Oxide Nuclear Fuels.* J. Nuc. Technology, 2013. **To be published**.

69. Rudman, K., Dickerson, P., Byler, D., McDonald, R., Lim, H., Peralta, P., Stanek, C., McClellan, K., *3-D Characterization of Sintered UO_{2+x}: Effects of Oxygen Content on Microstructure and its Evolution.* J. Nuc. Technology, 2013. **To be published**.
70. Matzke, H. and A. Turos, *Ion implantation studies of UO2 and UN.* Journal of Nuclear Materials, 1992. **188**(0): p. 285-292.
71. Rondinella, V., Wiss, T., *The high burn-up structure in nuclear fuel.* Materials Today, 2010. **13**(12): p. 24-32.
72. Bal Raj, S., *Chapter 5 - Fission Product Release and Transport*, in *Nuclear Safety in Light Water Reactors*. Academic Press: Boston. p. 425-517.
73. Olander, D.R. and P. Van Uffelen, *On the role of grain boundary diffusion in fission gas release.* Journal of Nuclear Materials, 2001. **288**: p. 137-147.
74. Millet, P., M. Tonks, and B. Riner, *Mesoscale Modeling of Nuclear Fuel Microstrures*. 06/18/2012: ATR User's Week: Idaho National Laboratory.
75. Chubb, W., *The mobility of gas bubbles in uranium dioxide.* Journal of Nuclear Materials, 1980. **91**(1): p. 240.
76. Chubb, W., V.W. Storhok, and D.L. Keller, *Observations relating to the mechanisms of swelling and gas release in uranium dioxide at high temperatures.* Journal of Nuclear Materials, 1972. **44**(2): p. 136-152.
77. Lösönen, P., *On the behaviour of intragranular fission gas in UO2 fuel.* Journal of Nuclear Materials, 2000. **280**(1): p. 56-72.
78. Ozrin, V.D., *A model for evolution of oxygen potential and stoichiometry deviation in irradiated UO2 fuel.* Journal of Nuclear Materials. **419**: p. 371-377.
79. Soo Kim, Y., *A thermodynamic evaluation of the U–O system from UO2 to U3O8.* Journal of Nuclear Materials, 2000. **279**(2–3): p. 173-180.
80. Brandon, D.G., *STRUCTURE OF HIGH-ANGLE GRAIN BOUNDARIES.* Acta Metallurgica, 1966. **14**(11): p. 1479-&.
81. Ishii, T., K. Naito, and K. Oshima, *Electrical conductivity and defect structures in non-stoichiometric uo2+x.* Journal of Nuclear Materials, 1970. **36**(3): p. 288-296.
82. Randle, V., *Sigma-Boundary Statistics by Length and Number.* Interface Science, 2002. **10**(4): p. 271-277.
83. Mackenzie, J.K., *Second Paper on Statistics Associated with the Random Disorientation of Cubes.* Biometrika, 1958. **45**(1-2): p. 229-240.
84. Vonlanthen, P. and B. Grobety, *Grain Boundary Distribution in Alumina and Zirconia Ceramics.* Ceram. Int., 2008. **34**: p. 1459-72.
85. Mykura, H., *Checklist of Cubic Coincidence Site Lattice Relations. Grain-Boundary Structure and Kinetics*. 1979: Metals Park, American Society for Metals.
86. Wolf, D., *Handbook of materials modeling*, ed. S. Yip. Vol. 2. 2005, New York: Springer.
87. Brandon, D.G., *The structure of high-angle grain boundaries.* Acta Metallurgica, 1966. **14**(11): p. 1479-1484.

88. Randle, V., *Application of electron backscatter diffraction to grain boundary characterisation.* International Materials Reviews, 2004. **49**: p. 1-11.
89. Randle, V., H. Davies, and I. Cross, *Grain boundary misorientation distributions.* Current Opinion in Solid State and Materials Science, 2001. **5**(1): p. 3-8.
90. Radford, K.C., *Effect of fabrication parameters and microstructure on the mechanical strength of UO2 fuel pellets.* Journal of Nuclear Materials, 1979. **84**(1-2): p. 222-236.
91. Radford, K.C. and J.M. Pope, *UO2 fuel pellet microstructure modification through impurity additions.* Journal of Nuclear Materials, 1983. **116**(2-3): p. 305-313.
92. King, A. and S. Shekhar, *What does it mean to be special? The significance and application of the Brandon criterion.* Journal of Materials Science, 2006. **41**(23): p. 7675-7682.
93. G. S. Rohrer, V.R., *Measurements of the five-parameter grain boundary distribution for planar sections*, in *Electron Backscatter Diffraction in Materials Science*, M.K. A. J. Schwartz, B.L. Adamsm D.P. Field, Editor. 2009, Springer: New York.
94. A. P. Sutton, R.W.B., *Interfaces in Crystalline Materials*. Monographs on the physics and chemistry of materials. 1995, New York: Oxford Science Publications.
95. Randle, V., *Sigma-Boundary Statistics by Length and Number.* Interface Science, 2002. **10**(4): p. 271-277.
96. Mackenzie, J.K., *Second Paper on Statistics Associated with the Random Disorientation of Cubes.* Biometrika, 1958. **45**(1-2): p. 229-240.
97. Vonlanthen, P. and B. Grobety, *Grain Boundary Distribution in Alumina and Zirconia Ceramics.* Ceram. Int., 2008. **34**: p. 1459-72.
98. Kingery, W.D., *Introduction to Ceramics*. Second Edition ed. 1960: John Wiley and Sons.
99. Mykura, H., *Checklist of Cubic Coincidence Site Lattice Relations. Grain-Boundary Structure and Kinetics*. 1979: Metals Park, American Society for Metals.
100. Wolf, D., *Handbook of materials modeling*, ed. S. Yip. Vol. 2. 2005, New York: Springer.
101. Brandon, D.G., *The structure of high-angle grain boundaries.* Acta Metallurgica, 1966. **14**(11): p. 1479-1484.
102. Randle, V., *Application of electron backscatter diffraction to grain boundary characterisation.* International Materials Reviews, 2004. **49**: p. 1-11.
103. Chen, Y. and C.A. Schuh, *Diffusion on grain boundary networks: Percolation theory and effective medium approximations.* Acta mater., 2006. **54**(4709).
104. Randle, V., H. Davies, and I. Cross, *Grain boundary misorientation distributions.* Current Opinion in Solid State and Materials Science, 2001. **5**(1): p. 3-8.
105. Lim, H., Rudman, K., Krishnan, K. McDonald, R., Dickerson, P., Byler, D., Peralta, P., Stanek, C., McClellan, K., *Microstructurally Explicit Simulation of*

Intergranular Mass Transport in Oxide Nuclear Fuels. J. Nuc. Technology, 2013. **To be published**.
106. Radford, K.C., *Effect of fabrication parameters and microstructure on the mechanical strength of UO2 fuel pellets.* Journal of Nuclear Materials, 1979. **84**(1-2): p. 222-236.
107. Radford, K.C. and J.M. Pope, *UO2 fuel pellet microstructure modification through impurity additions.* Journal of Nuclear Materials, 1983. **116**(2-3): p. 305-313.
108. Yuda, R. and K. Une, *Effect of sintering atmosphere on the densification of UO2---Gd2O3 compacts.* Journal of Nuclear Materials, 1991. **178**(2-3): p. 195-203.
109. Assmann, H., W. Dörr, and M. Peehs, *Control of UO2 microstructure by oxidative sintering.* Journal of Nuclear Materials, 1986. **140**(1): p. 1-6.
110. Stehle, H. and H. Assmann, *In-reactor UO2 densification.* Journal of Nuclear Materials, 1976. **61**(3): p. 326-329.
111. Rondinella, V.V. and T. Wiss, *The high burn-up structure in nuclear fuel.* Materials Today. **13**(12): p. 24-32.
112. Hsueh, C.H., A.G. Evans, and R.L. Coble, *Microstructure development during final/intermediate stage sinteringâ€"I. Pore/grain boundary separation.* Acta Metallurgica, 1982. **30**(7): p. 1269-1279.
113. Liu, Y. and B.R. Patterson, *Grain growth inhibition by porosity.* Acta Metallurgica et Materialia, 1993. **41**(9): p. 2651-2656.
114. German, R.M., *Coarsening in Sintering: Grain Shape Distribution, Grain Size Distribution, and Grain Growth Kinetics in Solid-Pore Systems.* Critical Reviews in Solid State and Materials Sciences, 2010. **35**(4): p. 263-305.
115. Veshchunov, M., *Modelling of Grain Growth Kinetics in Porous Ceramic Materials under Normal and Irradiation Conditions.* Materials, 2009. **2**(3): p. 1252-1287.
116. Fang, T.-T. and H.I. Palmour, *Evolution of Pore Morphology in Sintering Powder Compacts.* Ceramics International, 1990. **16**: p. 1-10.
117. Soo Kim, Y., *A thermodynamic evaluation of the U–O system from UO2 to U3O8.* Journal of Nuclear Materials, 2000. **279**(2–3): p. 173-180.
118. Murray, P., *Developments in oxide fuels at Harwell.* Journal of Nuclear Materials, 1981. **100**(1–3): p. 67-71.
119. Rajan, K., *Representations of texture in orientation space*, in *Electron Backscatter Diffraction in Materials Science*, A. Schwartz, M. Kumar, and B. Adams, Editors. 2000, Kluwer Academic/Plenum Publishers: USA. p. 31-50.
120. Jo, W.a.H., N-M., *Interfaces and Microstructures in Materials*, in *Ceramics Science and Technology Properties*, R.a.C. Riedel, I-W., Editor. 2010, Weiley-VCH Verlach GmbH & Co: Weinheim.
121. King, A. and S. Shekhar, *What does it mean to be special? The significance and application of the Brandon criterion.* Journal of Materials Science, 2006. **41**(23): p. 7675-7682.
122. G. S. Rohrer, V.R., *Measurements of the five-parameter grain boundary distribution for planar sections*, in *Electron Backscatter Diffraction in*

Materials Science, M.K. A. J. Schwartz, B.L. Adamsm D.P. Field, Editor. 2009, Springer: New York.
123. A. P. Sutton, R.W.B., *Interfaces in Crystalline Materials*. Monographs on the physics and chemistry of materials. 1995, New York: Oxford Science Publications.
124. Fuhrman, N., Hower, L.D. and Holden, R.B., *Low Temperature Sintering of Uranium Dioxide.* Journal of the American Ceramic Society, 1963. **46**(3): p. 114-121.
125. P.V. Nerikar, K.R., T.G. Desai, D. Byler, C. Unal, K.J. McClellan, S.R. Phillpot, S.B. Sinnott, P. Peralta, B.P. Uberuaga, and C.R. Stanek, *Grain Boundaries in Uranium Dioxide: Scanning Electron Microscopy Experiments and Atomistic Simulations.* J. Am. Ceram. Soc., 2011. **94**(6): p. 1893-1900.
126. Saylor, D., et al., *Measuring the five-parameter grain-boundary distribution from observations of planar sections.* Metallurgical and Materials Transactions A, 2004. **35**(7): p. 1981-1989.
127. Aidhy, D.S., D. Wolf, and A. El-Azab, *Comparison of point-defect clustering in irradiated CeO2 and UO2: A unified view from molecular dynamics simulations and experiments.* Scripta Materialia, 2011. **65**(10): p. 867-870.
128. Desgranges, L., et al., *Characterisation of uranium vacancies in hyper stoichiometric uranium dioxide.* Journal of the European Ceramic Society, 2005. **25**(12): p. 2683-2686.
129. Freyss, M., T. Petit, and J.-P. Crocombette, *Point defects in uranium dioxide: Ab initio pseudopotential approach in the generalized gradient approximation.* Journal of Nuclear Materials, 2005. **347**(1–2): p. 44-51.
130. Ahmed, K., et al., *Phase field simulation of grain growth in porous uranium dioxide.* Journal of Nuclear Materials, 2014. **446**(1–3): p. 90-99.
131. Holm, E.A., G.N. Hassold, and M.A. Miodownik, *On misorientation distribution evolution during anisotropic grain growth.* Acta Materialia, 2001. **49**(15): p. 2981-2991.
132. Saylor, D. M., et al., *Measuring the five-parameter grain-boundary distribution from observations of planar sections*. Metallurgical and Materials Transactions A, 2004 **35**(7): p. 1981-1989
133. Roher, G., *Measuring and inerpreting the structure of grain boundary networks.* Journal of the American Ceramic Society, 2011 **94** (3): p. 633-646
134. Carmack, J. Zhang, Y. *Molecular Dynamics Study of Grain Boundary Properties in UO2.* TMS 2014 San Diego
135. Govers, K. et al., *Molecular dynamics simulations of helium and oxygen diffusion in UO2.* Journal of Nuclear Materials, 2009. **395** (1-3) p. 131-139

APPENDIX A

RADIOACTIVE SAMPLE POLISHING PROCEDURE

There are several options available to polishing samples inside the glovebox. If the sample is mounted in epoxy, the Minimet is ideal for automated polishing, otherwise manual polishing is required. In the case of manual polishing the donut can be used or fingers/tweezers depending on the sample requirements. Finger/tweezer polishing is recommended for samples that are mostly flat and only require final polishing (maybe some grinding using lapping film and is recommended only for advanced users). If grinding is needed, the use a doughnut is highly recommended to obtain flat samples. Details on each procedure and general recommendations will be described in details bellow.

A.1. Polishing method

Use this flowchart to determine the most suitable method of polishing:

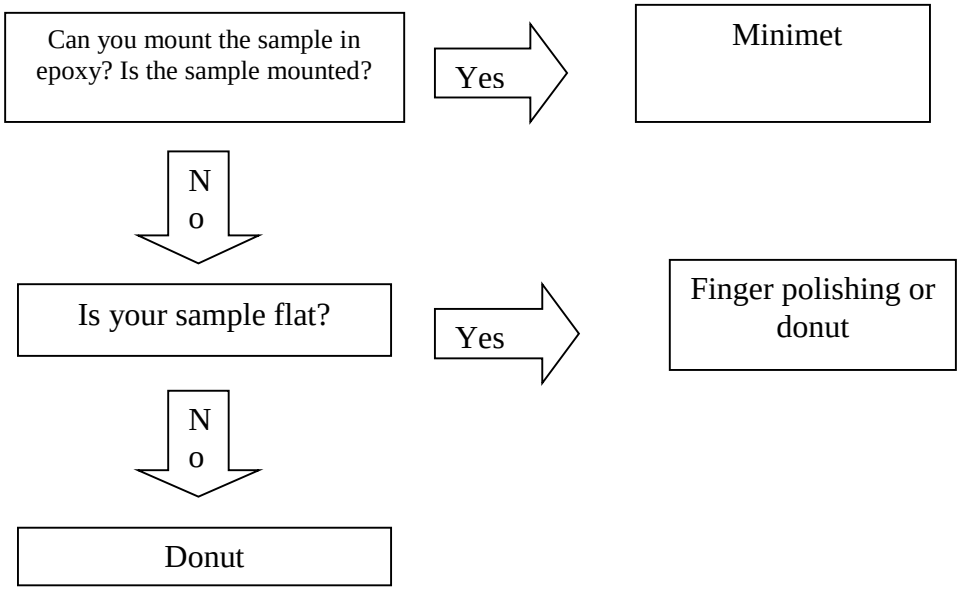

Figure A.1. Flowchart used to determine the most adequate polishing method.

In order to be able to use the Minimet, the sample has to be mounted in epoxy. Follow the instructions to mix and cure the epoxy (see section A.3). The mounted sample needs to be

flat in both ends; grinding or machining with the lathe is frequently used to flatten the back end of the mounted sample. Also, a hole needs to be drilled to fit the Minimet attachement for polishing. There are several Minimet polishers outside the glovebox to practice how to use it.

Coarse grinding (less than 800 gritt) is not recommended in the Minimet as the samples tend to wobble, manual polishing is encouraged at the initial stages if suitable.

Manual polishing can be used to retouch samples or when mounting is not an option, i.e. samples that will be tested at high temperatures. Remember that in order to do EBSD scans the sample needs to be flat at both ends so you might need to polish both sides. In such cases one side will be just grinded up to 800 or 1200 gritt and the other side will be polished all the way to colloidal silica as needed.

Finger/tweezer polishing is recommended for samples only that need final polishing. Otherwise using a donut is recommended in order to maintain flatness.

A.2 Polishing Supplies

Always plan ahead the polishing and sample/waste handling!!!

Figure A.2 shows a typical setup outside the glovebox for handling, cleaning and/or manipulating radioactive samples. Some supplies are required more often than others but everything that you might need has to be accessible at your working space. All liquids and chemicals need to be labeled.

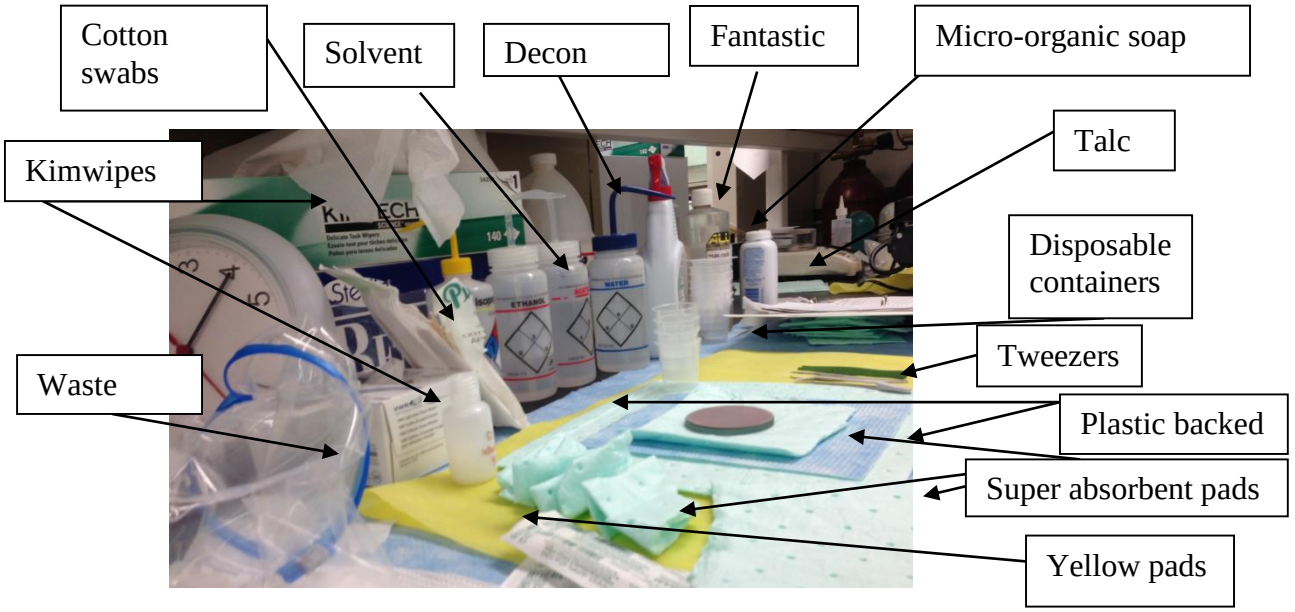

Figure A.2. Example of work area

This is a list of the most common supplies required inside and outside the glovebox:

- Super absorbent pads (green pads): Full pads, quarter pads (at least two per polishing step) and smaller squares and rectangles (5-10 pieces per step). These pads are extremely using to absorb liquids, contain spills, cleaning and decontamination.
- Cotton swabs. Cotton swabs can be used to hold samples in epoxy, hold in place pads, cleaning surfaces, decontamination, as brushes for the decon paint, surveying, etc. Be sure that you keep them handy and you have at least ¼-1/2 bags at all times inside the glovebox.
- Plastic backed spill pads. Use these pads with the plastic side always against your table/working surface. Always use it in conjunction with the super absorbent pads

to cover your working space. Smaller pieces can be used for decontamination and also to place contaminated tweezers and samples.

- Decon Paint. This paint can cover contaminated and "suspicious" surfaces/tools and be peeled off once it dries. Is needed to clean the donut after polishing and any other tools as required. Pour the paint on your surface and use a cotton swab if required to spread the paint. Make sure that you apply a thick coat on your surface as it will be easier to peel off. However, the thicker the layer the longer it will take to dry. Use a plastic backed pad as support (on the plastic side to place your tool/object and then apply the paint.

  NOTE: All the solid objects inside the glovebox that are likely to become contaminated should be made of materials that can be easily decontaminated. The outer surfaces are treated with impervious protective coatings, strippable paints or protective layers of surfactants to make decontamination easy and efficient to the highest extent. Therefore, all the equipment inside the glovebox must be protected with strippable paint.

  Work surfaces designed for handling solutions may be protected with coatings or strippable paints. The strippable film is simply removed upon contamination of the work and discarded. The most common base for strippable paints is a co-polymer of vinyl-acetate or vinyl-chloride. Strippable paints can be used not only as a means of preventive protection, but also as a means of subsequent decontamination. By spreading the paint over the contaminated area and allowing sometime for complete drying, a considerable part of the contaminant is usually removed with the layer of the stripped film [1].

- Kimwipes. Both Large and small can be used to clean and manipulate samples.
- Gloves. Always keep at least one extra pair available at all times both inside and outside the glovebox. Inside the glovebox use XL gloves and add tabs on the bottom for easy removal (use duct tape to create your tabs, separate and label the left and right gloves for easy retrieval inside the glovebox).
- Plastic bags. Ziploc or similar bags with zippers are highly recommended as are easy to manipulate inside the glovebox. Usually we need about 1 gallon bags per two polishing steps. You will need to double bag the waste before placing the trash in the transfer chamber. You can a use larger bag (2.5 gal) to place a couple of waste bags if possible. Keep always at least two bags for your waste at any given time, both inside and outside.
- Fantastic or similar. Use Fantastic for decontamination of most of the surfaces and tools. Do not use Fantastic on your samples, or at any surface that will go in the SEM or in a furnace as it will expel fumes that can contaminate the SEM and Tube furnace as well as it can react with your sample. Use water and other solvents (acetone, methanol, ethanol, isopropanol, etc.) to clean.
- Yellow pads. These pads are treated with a wax that will retain dust particles. Use them always to cover the surface of the trays in the transfer chamber and working space.
- Microorganic soap. Use only outside the glovebox to clean the sample surface from colloidal silica residue. Apply a small amount (see instructions on the bottle) on a pad (that has to be placed on a glass plate inside a plastic bowl) and add water. Use

tweezers to manipulate the sample and clean (as you were polishing). Rinse with water (in the bowl). More details will be provided in the decontamination section.

- Solvents. Keep isopropanol inside the glovebox for final cleaning and to use as necessary. Outside the glovebox for decontamination use: acetone, methanol, ethanol, isopropanol.
- Polishing pads-SiC papers. Keep them in bags labeled. The pads need to be cut most the times to fit the glass plates of the minimet.
- Colloidal silica and suspensions. Keep the amount of water based solutions at the minimum. Colloidal silica-Hydrogen peroxide mixes are more efficient the first two days after mixing. Its potency is highly reduced over time. Colloidal silica-Hydrogen peroxide solutions can be too aggressive to porous/cracked/poorly compacted samples and need to be used with caution.
- Polishing bowls/glass plates. Design for the Minimet. This bowls locally contain contamination during polishing and will be used for automated and manual polishing. Must clean every bowl/plate immediately after use. (AFTER EACH POLISHING STEP)
- Water. De-iodized water is used for polishing and cleaning. Estimate how much water you will need and keep it to a minimum, as the glovebox has controlled atmosphere (humidity and oxygen). Smaller bottles can be used to refill the water bottle located inside the glovebox. Remember to adequately label each container.
- Tweezers. Avoid at all cost sharp tweezers as they can perforate your gloves. Plastic tweezers are ideal for most applications but metal tweezers can be used.

- Diamond suspensions. Several suspensions with different particle size are available inside the glovebox.
- Dosimeter, ring, lab coat, goggles and other PPE as required. The protective gloves must go over the sleeves of the lab coat and must be sealed with duct tape (tape around the gloves, ask for help if you need it) to ensure that there is no exposed skin in case of contamination. Check hands and arms before starting, if you have any exposed cut or injury use band aids/adhesives to cover that area.
- Others as needed.

A.3. Mounting samples in epoxy

- Samples can be mounted in epoxy outside the glovebox if required. The sample can be manipulated and stored in the large transfer chamber.
- Be aware that the mixture of epoxy resin and hardener is non-toxic, but each component by itself is toxic (see MSDS for details) and can generate mixed liquid wastes. Those wastes are not desirable and need special permission to be handled and disposed. Be extremely careful during the preparation of the resin and avoid spill any of the components.
- Appropriate "clean" tools, i.e., tweezers, epoxy resin, hardener, molds, etc., will be gathered and used to set up the mounting procedure before the pellets are taken from their container. These tools will be placed on top of a "clean" large piece of plastic-backed absorbent paper.
- Epoxy resin and hardener will be mixed in appropriate amounts (by volume, as per instructions of the manufacturer) and set aside. Use an appropriate mold release

compound (to make sure that the encapsulated sample can be taken out from the mold easily.

- A pellet will be taken from their container and placed in the plastic mold using tweezers and trying to keep the secondary gloves "clean". Pour epoxy on top of the pellet inside the mold and wait for it to solidify and cure.
- Clean tweezers using lint free wipes (Kim wipes) and appropriate solutions (Fantastic or similar).
- Survey your hands and possible contaminated surfaces and proceed accordingly to your findings. Decontaminate if necessary.
- Discard contaminated wipes, gloves and waste in appropriate waste bag and place it in the appropriate container.
- Once the epoxy is cured you will need to flatten the back surface.
- Move the cured sample into the working space outside the glovebox.
- Carefully remove the mounted sample from the mold, place the mounted sample in a labeled container/bag.
- Clean the mold and glass plate, if used, using fantastic or similar solution and dispose the waste accordingly. Survey the mold to check that is clean if contamination is encountered decontaminate until clean.
- If possible use the lathe to achieve a flat surface. Cover most of the lathe surface with the yellow waxed pads to recover the waste. Use pads, cotton swabs and Fantastic (or similar) to clean the lathe after done. Survey the lathe after cleaning to check for contamination. After cleaning, lubricate the surfaces (use recommended oil/lubricant) to avoid oxidation.

- The lathe can also be used to drill a center hole for the Minimet pin.
- If the lathe cannot be used to flatten the back side, manually grind using SiC papers inside the glovebox. Use the recommendations for polishing described in 1.6 and 1.7.

A.4. Attaching samples to the donut

- The samples can be attached to the center rod using Crystalbond™, outside the glovebox.
- Determine the supplies needed. Usually the list includes: sample, donut, gloves, cotton swabs, acetone, fantastic, kimwipes, tweezers, Crystalbond™, etc.
- Prepare the area where you will work. Use yellow pads and some plastic backed paper to cover your working surface.
- Place yellow a pad in the large transfer chamber as well as plastic backed paper. You will store the mounted sample in the transfer chamber while the Crystalbond™ cools down and fully solidifies (Do not pump down the transfer chamber until the Crystalbond™ is fully cured).
- Use a puck or a metal surface to melt the Crystalbond™.
- Once the Crystalbond™ is molten rapidly wet the center rod with the Crystalbond™ and place the sample on top. Use metal tweezers to move around the sample and add Crystalbond™ if necessary. This technique requires practice and sometimes, several attempts are required to attach the sample, as the Crystalbond™ solidifies fairly quickly.

- Let the center rod cool down and move it to the transfer chamber to let the Crystalbond™ fully solidify.
- Clean surfaces and tools as required.
- Inside the glovebox transfer chamber, proceed to cover the center rod with kimwipes and place it in a labeled bag.
- Survey your hands and all required surfaces and clean as necessary.

A.5. Introducing the sample/supplies inside the glovebox.

Before introducing or removing samples, supplies, waste, etc. from the glovebox ask authorization from P. Peralta. To open the glovebox a key must be used and P. Peralta will be the only person to provide the key. Be sure to wear all the required protective clothing. Use always an extra pair of gloves as described in Appendix C. Also check if the vacuum pump is fully functional (usual pitch, the vacuum pump is connected, vacuum oil level, moist filter), the glovebox light is working, that you have enough waste buckets, nitrogen gas available.

- Plan ahead and have all the materials/tools handy, before manipulating the sample. Keep in mind that after starting only one hand will be used for manipulating the sample (or any surface/tool/equipment that is presumably contaminated) and a "clean" hand is needed for handling everything else that is assumed to be clean. Estimate the approximate amount of waste that can be generated and place a waste bag accordingly. Place the waste bag in a fixed area that can be easily reached by both hands.
- Store the pellets individually in appropriately labeled plastic containers.

- Be sure that all the items that you are introducing into the glovebox are bagged. Do not fully close the bags, as it can introduce air to the system.
- Avoid glass containers and sharps as it can puncture the gloves.
- Bag the liquid separately, include some super absorbing pads in the bag and leave the caps slightly loose in order to evacuate all the air. Be mindful with the colloidal silica as it can dry and crystallize during the vacuum process. If you observe a leak, close the bag and discard with the waste.
- Check the antechamber pressure and be sure that is 0" Hg and that all the evacuation and refill valves are closed. Check also that all the inner doors of the transfer chambers are locked.
- Unlock the transfer chamber lock and open the door once you are ready. You do not need to use gloves at this point as you are not handling any radioactive/contaminated sample.
- Put gloves if necessary and place the supplies inside the transfer chamber. Survey your hands and discard your gloves if you do not find any contamination (if you were manipulating a radioactive sample). If you find contamination proceed to decontaminate, survey your hands and discard your gloves when no contamination is detected.
- Close and lock the transfer chamber door.
- Check that the vacuum pump is on and proceed to evacuate. The evacuation time will depend on the number of selected cycles, for the small transfer chamber:
    a. 1 cycle, evacuate 30 to 40 min.
    b. 2 cycles, evacuate 10 t0 15 min each time.

c. 3 cycles, evacuate 3 to 5 min each time.

d. For the large transfer chamber evacuate at least for an hour, the longer the better, and cycle at least one time to maximize the air extraction.

- Before refilling the transfer chamber check the oxygen and moisture reading, if any of the readings is higher than 250ppm, do not refill or use the glovebox. Proceed to purge the glovebox for at least 30 min (read instruction on the glovebox manual on how to purge the glovebox), let the readings settle, if the readings are still high after 30min, try to purge again for a longer cycle. If the readings are still higher than 250ppm you will need to regenerate the oxygen/moisture trap (Follow the instructions described in the manual). **NOTE:** If purging is necessary, leave the room during purging and do not allow people in the room for at least two hours to fully evacuate. You can get quickly enter the room and stop the purging cycle but avoid staying in the room afterwards.
- Refill the transfer chamber, be gentle and open the valve slowly, especially for the larger transfer chamber. Keep your feet close to the pedal and add nitrogen to the main chamber to compensate the gas loss at the main chamber.
- On the final refill cycle, close the refill valve when the antechamber vacuum gauge stabilizes at the same pressure as the glovebox (about 0”Hg).
- To ease the working conditions, lower the glovebox pressure limits. Go to the control panel touch screen and press the PRESSURE CONTROL touch key. A new screen will appear, set the limits to -2 – 0.5’’ water column pressing the DEC (decrease) and INC (increase) touch keys. The minimum window size is 0.5’’ water column. Use the pedals to manually increase and decrease the glovebox pressure as

necessary. While using the glovebox and specially when changing the pressure conditions keep the vacuum pump on.

- If the readings are less than 250ppm (ideally should be less than 100ppm), put on your gloves add some talc on top and introduce your hands in the glovebox gloves.
- Grab a pair of gloves and put on top of the glovebox gloves. Be sure that you have a clean surface to place your supplies.
- Open the transfer chamber inner door and proceed to take out the supplies/samples from the transfer chamber.
- Place your supplies at their respective locations and proceed to prepare for polishing.

A.6. Pre-polishing steps

- Determine what you will need and double it (you can get triplicates in some cases).
- Prepare your working space. Place mats/pads as necessary at the space that you will use for sample manipulation and decontamination.
- Overestimate the space required for work, that way any spill can be easily cleaned and contained.
- Keep handy tweezers, cotton swabs, kimwipes, extra gloves, super absorbent pads and other supplies as needed.
- Place the papers/polish pads on the glass plates. Use at least two for each step. Place the glass plates in their bowls (match the notch in the class with the tab in the bowl). Place the bowls on top of each other and make a tower, put them in order starting with the first that you will need on top.

- Place the first bowl on the Minimet. Your setup for polishing will required the bowls secured in the Minimet regardless of the technique as is the only way that the bowl will sit flat.
- Check that the Minimet is connected and the back switch is on. Turn on the Minimet on to check that is running as sometimes doesn't. If the Minimet do not start let it rest for a day or two and try again. Often dust particles interfere with the speed controller and the Minime stops working. This is a problem that can be checked and easily fixed outside the glovebox but it get tricky inside the glovebox as it needs to be taken apart.

A.7. Polishing

Grinding and polishing inside the glovebox follows the same steps that you would use outside the glovebox but requires more concentration and effort. Be aware that you have to keep one hand clean at all times.

Again, keep at a reachable distance all the cleaning supplies and tools that you might need as well as the polishing supplies. In some cases you will have to keep open bottles/containers around as you only have one clean hand available. Be mindful on where you place the liquids as you want to avoid spills. Also try to keep the amount of water used as a minimal as possible to control the humidity and oxygen levels inside the glovebox. However, remember that the colloidal silica can dry very fast and leave an undesirable layer on your sample that can be hard to clean so use water as necessary.

Decontaminate between steps. The goal during grinding/polishing is to avoid the generation of radioactive dust/particles therefore wet grinding polishing is a must. Never

let the bowls, polishing pads, grinding papers, sample, etc. dry. Keep the pads moist at all times and once you are done at that step, hold the sample with tweezers on top of the polishing bowl and rinse with water. Use wet and dry cotton swabs to finish cleaning the sample. Dry the sample completely and place it aside in a designated space. Then proceed to spray Fantastic (or similar) into the bowl, let it sit for a few minutes to help the SiC papers/pads soak and loosen the glue on the back. Flip the entire bowl into a green pad (usually a quarter of a full pad is enough) discard the pad. Grab the bowl and its contents with large kimwipes and place it over a clean pad. Spray fantastic again on the bowl and clean it with fantastic at least twice, until clean. Do a final rinse with a little bit of water to get rid of the fantastic residue. Grab the "cleaned" bowl with kimwipes and place it at the designated area. Grab the glass plate and use tweezers to extract the paper/polishing pads, use kimwipes, green pads, and plastic backed pads as necessary. In some cases be mindful that you will need both of your hands. Clean the glass plate on top of a setup with green pads and plastic backed pads. Use fantastic all over the surface and clean using kimwipes, clean at least twice and use water at the end to rinse the residue of fantastic, the glass plate should look transparent and residue-free. Grab the "clean" glass plate and place it at the designated area. Change your gloves; use your "clean" hand to remove the glove from the "dirty hand". For more details on how to change the gloves refer to appendix C.

In general, use coarse SiC grinding papers to expose the sample surface that is embedded in epoxy. Coarse grinding can be also used in manual polishing to flatten the sample. The usual available SiC papers are: 320, 400, 600, 800 and 1200 gritt. As the oxide samples tend to be harder than SiC, diamond suspensions or diamond lapping films are recommended. All the diamond suspensions are propylene-glycol based and need to be

treated as mixed waste; segregation of this particular waste is required. For larger particle size (>3microns) a pad that consist of a metal mesh is suggested. This will be the first step after the SiC papers, add a couple of drops the suspension and some water if necessary. The next step will require a mixture of equal parts of 0.25 or 1 micron diamond suspension and 0.04 microns colloidal silica in a hard silk cloth. For the final steps 0.04 microns colloidal silica and water, on either an imperial cloth pad (looks like a velvet) for more porous/delicate samples or chempads (chemically resistant synthetic fiber cloth) for more sturdy samples. Another final step can be added to sturdy samples (if the sample has cracks, delamination or is very porous avoid this step): a fresh (not older than a couple of days) mixture of 5 parts of colloidal silica (0.02 or 0.04 microns) to 1 part of 30% hydrogen peroxide. This step is more aggressive as the hydrogen peroxide has a higher etching rate and can be very useful for serial sectioning or a faster polishing. The time and amounts of the steps will vary depending on the sample, as a rule the final polishing step takes at least an hour. An example the polishing sequence for a d-UO_2 is shown in Table A.1.

Table A.1. Polishing procedure for d-UO_2 samples.

Step	**Abrasive**	**P. size**	**Working surface**	**Lubricant**	**Load**	**RPM**	**Time**
Grinding	SiC	400	Wet abrasive paper	water	None	Manual	As necessary to expose the sample
Grinding	SiC	600	Wet abrasive paper	water	None	Manual	3 min
Grinding	SiC	800	Wet abrasive paper	water	None	15	5 min
Grinding	SiC	1200	Wet abrasive paper	water	None	20	5 min
Grinding	Diamond	3	Cermesh	Propylene-glycol/water	1	20	5 min
Polishing	Diamond	1	Nylon cloth	Propylene-glycol/ water	1	20	5 min
Polishing	Diamond Colloidal silica	0.25 0.04	Hard silk or nylon cloth	water	1	20	10 min
Polishing	Colloidal silica (C.S.)	0.04 or 0.02	Short-napped fiber cloth or chemically resistant short-napped pad	water	1	25-30	40-60 min
Polishing	5:C. S 1: Hydrogen peroxide	0.02	chemically resistant short-napped pad	water	1	25-30	20-60 min

Clean after each step. Once you are done polishing and cleaning, rinse the sample with water and gently polish it on a clean soft synthetic fiber cloth with water for 2-5 min. Rinse again the sample with water and then with isopropanol. Gently dry the sample with cotton swabs and/or kimwipes and store in a properly labeled container. Place the container in a clean bag and store accordingly. Clean and decontaminate tweezers, bowls, tools and surfaces as necessary. Change your gloves after you are done cleaning and double bag the trash. Grab the waste bag with a large kimwipes and store the trash in the large transfer chamber, make sure that a yellow pad or a large kimwipes is placed on the tray.

Write in the log the amount of material removed during polishing. To make an estimate of the amount of material you need to know the sample's density and diameter. Knowing the sample's diameter and density, assume that the thickness removed is proportional to the media that you used (for instance if you used 0.02 microns colloidal silica assume that you removed 0.02 microns) therefore the amount of removed material is the volume (area x thickness) X density (10.97grs/cm^3 x %TD). Then the activity for d-UO_2 is 14.8 Bq/mg and 1Bq=2.7E-8mCi, knowing the amount of mass removed you can determine the amount of the source used in mCi. The material removed should be in the waste bags; therefore this should match the value filled out in the waste. In the case that no polishing was done, we will assume that 0.1% of that number is the waste generated during cleaning/decontamination and is the amount that will be used in the waste containers that do not contain waste from polishing.

A.8. Removal samples/tools and waste from the glovebox

Before introducing or removing samples, supplies, waste, etc. from the glovebox ask authorization from P. Peralta. To open the glovebox a key must be used and P. Peralta will be the only person to provide the key. Be sure to wear all the required protective clothing. Use always an extra pair of gloves as described in appendix A. Also check if the vacuum pump is fully functional (usual pitch, the vacuum pump is connected, vacuum oil level, moist filter), the glovebox light is working, that you have enough waste buckets, nitrogen gas available.

- Plan ahead and have all the materials/tools handy, before manipulating the sample. Keep in mind that after starting only one hand will be used for manipulating the sample (or any surface/tool/equipment that is presumably contaminated) and a "clean" hand is needed for handling everything else that is assumed to be clean. Estimate the approximate amount of waste that can be generated and place a waste bag accordingly. Place the waste bag in a fixed area that can be easily reached by both hands.
- Use protective gear.
- Prepare your work station. An example of a setup is shown in Figure 2.
- Make sure that the inner door is locked and proceed to open the outer door.
- Always assume contamination therefore always test for contamination. Keep the bags (with tools/samples/waste) inside the transfer chamber and use a wipe or a cotton swab to survey the bag.
- Proceed to remove the bags from the transfer chamber, one at a time, and place it at the designated space. Decontaminate if necessary until clean.

- Place the waste bags in the waste containers. Decontaminate first if necessary (readings higher than background) even if it is trash.
- Lock the airlock.
- Open the bags, and carefully remove the sample or the contents. Wipe with lint free wipes (or appropriate wipe) the sample in order to do wipe test for contamination.
- If the sample (or the container) is contaminated clean using lint free wipes and appropriate solutions (409 or similar for containers and tools, water and soap for sample). Dispose of wipes and container appropriately.
- If the sample was polished the following procedure is needed in order to clean the sample:
    a) Re-polish the sample with water and microorganic soap in a minimet bowl/platen set (use velvety or soft).
    b) Rinse the sample with water (inside the bowl).
    c) Place the sample in a small disposable container and fill it with water.
    d) Place the container with the sample in the ultrasonic cleaner and clean for at least 15 min.
    e) Clean the bowl/plate as previously described.
    f) Take the container out of the ultrasonic cleaner, use small pieces of the green pads to absorb the liquid and remove the sample.
    g) Dispose the container
    h) Place the sample in a new container and add acetone, follow steps d), f) and g).
    i) Keep cleaning with ethanol, methanol and isopropanol and follow step h).

j) Dry the sample using kimwipes and cotton swabs.

k) Place the sample in a properly labeled container.

l) Dispose the waste.

m) Change gloves in between steps or after cleaning if necessary.

- To minimize sample handling in the microscope room, the sample must be placed in the SEM sample holder prior to leaving the lab in ERC 368.
    - Use carbon tape/dot to place the sample in the stub.
    - Use copper tape to cover edges and non-conductive surfaces.
- Write in the log when the sample was removed from the glovebox, the dose observed on the detector and the decontamination process. The sample must be "clean" before leaving the room. If residual contamination is suspected keep cleaning the sample until is "clean".
- Always label the container with the name of the sample, date and other relevant data.
- Before leaving the room, take an extra pair of gloves and disposable bags for caution. Use these bags to dispose wipes, gloves and other suspicious wastes generated in ISTB2 129-A. In case of generation of radiation wastes use these bags, use always double bag in order to contain possible contamination.

A.9. Waste handling

- Plan ahead and have all the materials/tools handy, before manipulating the sample. Keep in mind that after starting only one hand will be used for manipulating the

sample (or any surface/tool/equipment that is presumably contaminated) and a "clean" hand is needed for handling everything else that is assumed to be clean. Estimate the approximate amount of waste that can be generated and place a waste bag accordingly. Place the waste bag in a fixed area that can be easily reached by both hands.

- No radioactive wastes shall be disposed of by conventional methods. This means particularly that solid wastes may not be placed in the standard waste containers to be collected by housekeeping personnel, and that liquid wastes may not be discharged into the sewer [2].
- To insure that solid and liquid wastes are kept separated, the laboratory must be equipped with at least one container for solid dry waste and one for liquid waste. The solid dry waste containers must be obtained from the Radiation Safety Office. They must be kept fitted with a disposable waterproof polyethylene liner.
- Place all the used wipes and other solid wastes inside the designated place in the glovebox. Be sure to use double bags to avoid contamination outside the waste bag. Use the double bag for taking out the waste bag out to the waste container. Always wear an extra pair of gloves to dispose the waste, discard the gloves before closing the waste container. Place a "clean" lint free wipe on the transfer chamber. Place the waste bag over the lint free wipe.
- Waste containers are placed under the glovebox. Always check with wipe test (or use a cotton swab) for contamination in the outer bag. Take out the waste disposal bags (double bagged) and place it in the container, close the container. Use the

logbook to keep track of the amount of radioactive material removed during sample preparation and fill out the forms for each container every time the container is full.

- Request for removal of liquid and dry waste may be made by telephone to the Radiation Safety Office. Telephone: 480-965-6140
- Please note that for liquid waste, special permits are required. Be aware of that before generating any liquid waste. Ask P. Peralta for approval.
- In order to minimize the waste generation and the working time, plan ahead the preparation and sample handling.

A.10. Transporting the sample outside the laboratory (but inside the university)

Within the institutional grounds, all radionuclides must be transported in non-shatterable containers or carrying cases with the cover fastened securely so it will not fall off the case if it is dropped. There should not be any removable radioactive contamination on the surface of the container, but in the event there is contamination it should be below 20dis/min per 100cm^2 for alpha contamination. A route should be chosen to encounter minimal pedestrian traffic [3].

Call P. Peralta before moving the sample out of the lab in ERC-368, be sure that you have clearance to move the sample.

While transportation, the package must be in possession and under the direct control of the person authorized for the transportation. Follow the planned route; do not walk into campus with the sample to non-authorized buildings.

When arriving to the lab located in ISTB2 129A:

- Always check for people at the laboratory and tell them you are in the facilities with the samples. Ask the personnel not authorized to handle radioactive samples to

leave the vicinities of the microscope room and not to enter. A sign will be placed on the door to warn others of the presence of a radioactive material sample and to stay away if not authorized to handle radioactive materials.

- Keep the sample only in the Microscope Room (ISTB2 129A) or in the glovebox.
- Prepare your workspace, including waste bags and decontamination solutions. Remember not to use fantastic on the sample or sample holder, use isopropanol or water and soap if needed.
- Once in the room (ISTB2 129A) open the Microscope door, open the container and place the microscope sample holder in the microscope chamber using the designated tweezers.
- After the sample is placed in the microscope, dispose the gloves in a designated radioactive waste bag.
- When finished, place a new pair of gloves and retrieve the sample, use the special tweezers to retrieve the sample. Place all the wipes and gloves in the radioactive waste bag. Double bag the waste and dispose it properly (the radioactive waste containers are located underneath the glovebox in ISTB2-129).
- Place the sample in its container, and then in a bag or container. Clean with lint free wipes and appropriate solution any tools/ surfaces that were touched by the sample. Dispose accordingly all the waste. Survey the surfaces, tools and sample containers before leaving. If necessary decontaminate until everything is “clean”.
- The sample can be stored in the glovebox located at ISTB2-129 or taken back to the lab ERC-368 and place it in the glovebox). Go directly to the lab. After placing the sample remember to wash hands and arms thoroughly.

A.11. Other considerations

Work that can result in contamination of the table tops and work surfaces should be done in trays with a protective liner. The surfaces will be protected using plastic-backed absorbent paper (i.e. Kimpak), after the paper is used, it should be discarded frequently to prevent radioactive materials from dusting off the surface [2,3].

After polishing the sample, periodic surveys of the immediate areas in which the radioactive materials are being used must be performed. In addition, these areas should be inspected each and every time there is a reason to suspect a contamination incident. Records will be kept on both positive and negative survey results in the authorized user's laboratory logs [2].

While using the glovebox do not try to reach your face, adjust protective glasses or scratch the face. These movements cannot be done inside the glovebox but are reactions that must be avoided because the window can be contaminated.

After you are done, remember to use the sticky pad (located in the floor of the radioactive area) to clean your shoes. Survey hands, arms, clothing, and shoes. If any abnormality is detected, report to P. Peralta and the Radiation Safety Office immediately. Clean thoroughly your hands and forearms with water and soap before leaving the lab. Do not rub eyes, scratch skin, touch face or hair without previously cleaning the hands.

Protective clothing must not be taken out of the local areas in which their use is required unless they are monitored and determined free of contamination. In addition of the above mentioned, other protective clothes can be used such as coveralls and shoe covers [3]. Moreover, under no conditions should protective clothing be worn in eating places.

References

1. Severa, J., Bar, J.: Handbook of radioactive contamination and decontamination. Elsevier (1991) 78-79, 113-115, 117-125, 246-247
2. U.S. Department Health, Education and Welfare: The National Institute of Health Radiation Safety Guide. Radiation Safety Branch Division of Research Services (1979) 11-15
3. Shapiro, J.: Radiation Protection A Guide for Scientists and Physician. Harvard University Press (1990) 33-35, 284-288, 307-308

APPENDIX B

SAMPLE CUTTING

Sample 38, was sliced in two pieces for further heat treatment. A general procedure for cutting was developed and is described below.

1) Ideally the sample needs to be flat on both sides, polishing on both faces is recommended, as seen in Figure B.1.

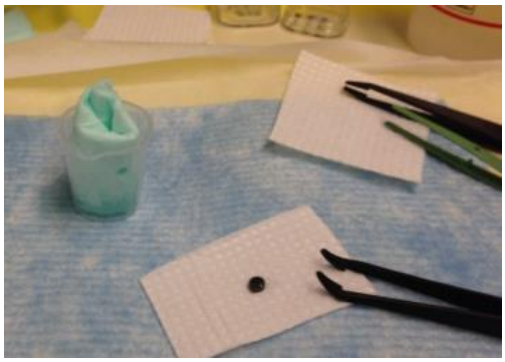

Figure B.1. Example of polished sample ready to be cut.

2) Glue the sample to the mid-edge of a aluminum plate using Crystalbond™:
    - Place the metal plate in the hot plate and heat up to ~150F. Once the plate is warm, rub the Crystalbond™ into the plate until a thin coat is formed (Figure B.2).

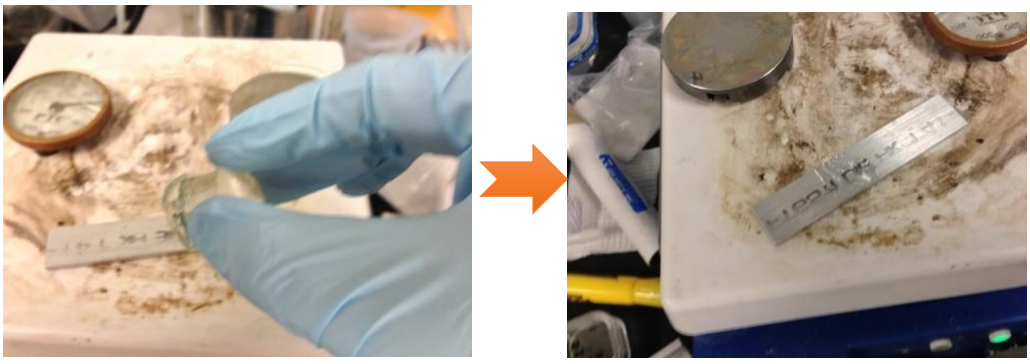

Figure B.2. Example of how to apply of Crystalbond™.

- Place the sample sample on the metal plate and apply a gentle pressure on the top of the sample, using a cotton swap, to secure the sample into the Crystalbond™ (Figure B.3(a)).
- Using thongs carefully remove the mounted sample from the heating plate and cool down. (Figure B.3(b)).

(a)  (b) 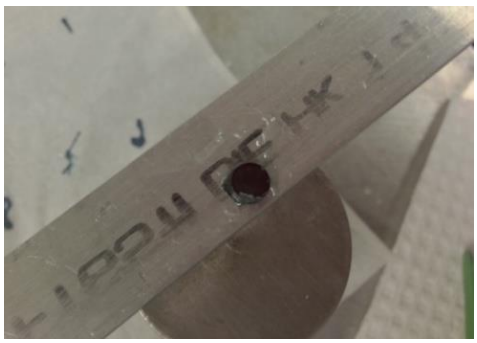

Figure B.3. (a) Sample placed over melted crystal bond and, (b) Sample cooling down.

3) Once the sample cool down, add a coat of water soluble Crystalbond™ (wax like):
   - First using a razor blade, slice the wax into small pieces, as in Figure B.4.

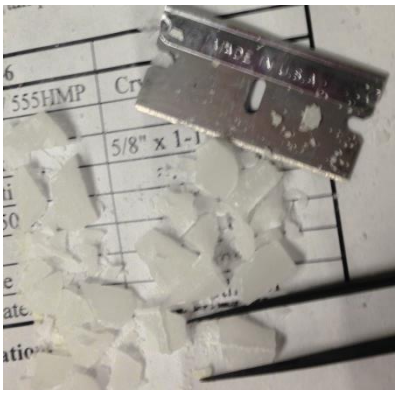

Figure B.4. Sliced pieces of water soluble Crystalbond™ (wax like).

- Place the small pieces over a metal plate, which was previously heated in the heating plate (Figure B.5)

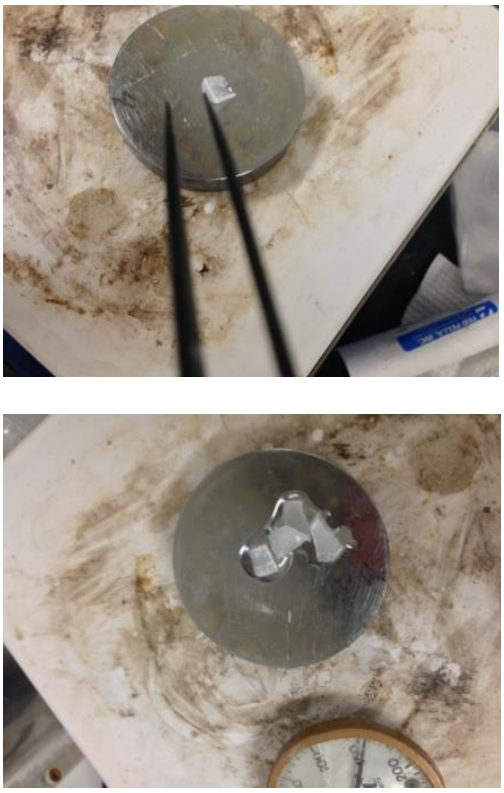

Figure B.5. Melting pieces of water soluble Crystalbond™ (wax like)

- Once the wax melts, carefully pour it over the mounted sample (Figure B.6); use paper towels or plastic backed paper as secondary containment. This step can be repeated several times until the sample is completely cover.

Figure B.6. Pouring molten water-soluble Crystalbond™ (wax like) into the sample.

- Let the wax cool down and solidify.

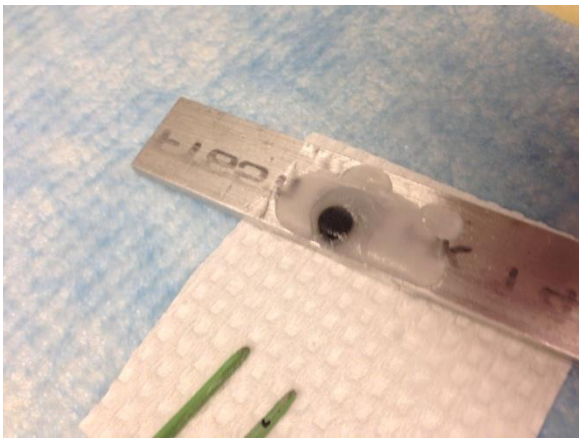

Figure B.7. Mounted sample.

4) Place the mounted sample (shown in Figure B.7) in a sealed platic bag.

5) Determine the supplies that you will need in the glovebox for cutting including: tweezers, cotton swabs, kimwipes, extra gloves, super absorbent pads, waste bags, fantastic, water, yellow pads, plastic backed pads, and other supplies as needed.
    - For cutting is highly recommended to use a dye (for example vegetable dye used for cooking/icing) in the water. The coloring in the water will help to determine leaks, spills and contamination, facilitating the decontamination process. For the 4inch low density diamond cutting wheel about 150ml of water are required for cutting.
    - Among the supplies add at least two packages of gelatin, that will be used later to contain the liquid waste.
    - All the components (or at least the ones that can be) of the low speed cutting machine must be coated with the strippable paint. Special attention in required on the fluid container as it will be in contact with most of the waste during cutting.
    - Include large pads of the plastic backed paper to cover all the surroundings of the cutting machine.
6) Place every tool/material/supply that will not be used during the cutting procedure in a plastic bag and move to one area of the glovebox. This step will include the minimet, the bowls and platens and other supplies (see Figure B.8(a)).
7) Place plastic backed paper pads to cover all the bottom surface of the glovebox, including exposed cable cords and equipment.
8) Place plastic backed pads and green pads on top, especially at the area where the cutting machine will be placed and the decontamination area.

9) Prepare enough plastic bags to manage the waste generated during and after cutting.

(a)  (b) 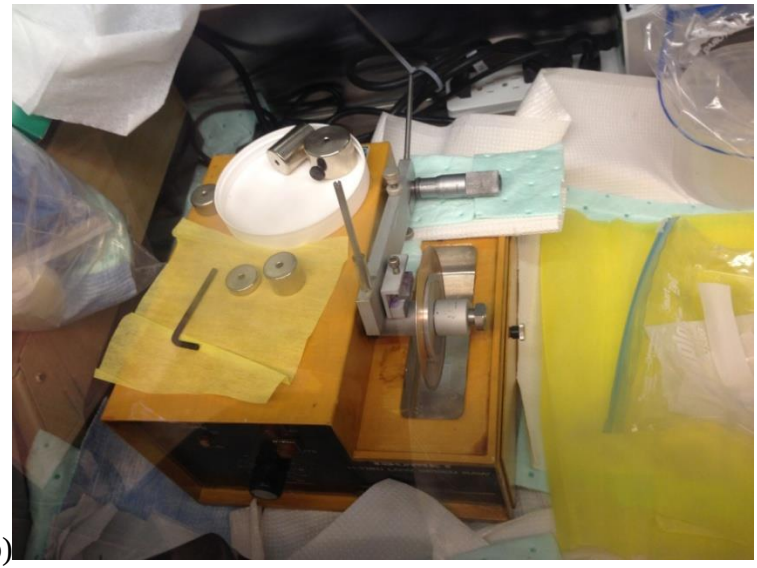

Figure B.8. (a) Side view of the glovebox, note that all the non-necessary supplies are bagged. (b) Top view of the cutting machine.

10) Ensemble the cutting machine, use weights as necessary (see Figure B.8(b)).

11) To open the fluid container turn the knob 90° clockwise and detach. The tray can be removed from its base to clean and can be lift up afterwards for cutting, by lifting at the back end of the base. Place plastic backed paper/green pads on the base if necessary and close.

12) Place plastic backed paper and green pads at the back and sides on the sample holder has the fluid can drip when lifting the arm.

13) Place the blade in position.

14) Turn off the blower; close the blower inlet and outlet valves (Figure B.9). **KEEP IT OFF UNTIL ALL THE DECONTAMINATION PROCEDURES ARE DONE.**

Figure B.9. Blower power switch, blower inlet and output valves locations.

15) Place the colored water in the fluid tray.

16) Place the sample in the sample holder and adjust the position of the sample as necessary.

17) Place the required weights in the back and front.

18) Select the desired speed (as slow as possible, use speed knob to adjust) and start cutting (press start).

19) Cut until the blade reaches the metal substrate and press stop (Figure B.10).

Figure B.10. Mounted sample after cut.

20) Carefully remove the sample from the sample holder and decontaminate with water and cotton swabs. Cover the sample with yellow pads and carefully place it in a plastic bag.

21) Carefully remove the blade (use tweezers and pads to detach). Decontaminate the blade and other components with fantastic and water as necessary. Change gloves between decontamination steps.

22) Quickly add the gelatin to the waste water in the tray and carefully mix using cotton swabs.

23) Clean any possible contaminated areas (the dyed water helps to determine possible leaks and contaminated spots as seen in Figure B.11).

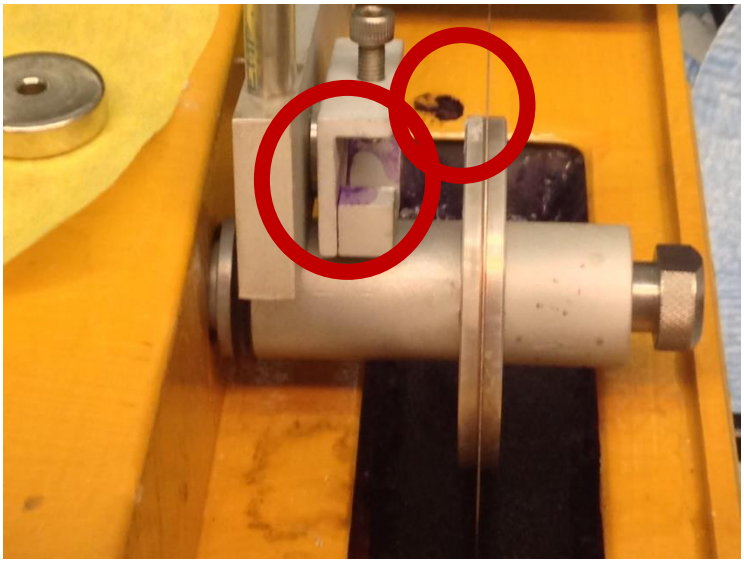

Figure B.11. Spotted contaminated surfaces during/after cutting.

24) Open the side door and without moving the tray check for possible contamination and carefully clean using fantastic and cotton swabs.

25) Place a borosilicate glass beaker in the heating plate and heat about 100ml of water to near boiling point.

26) Place a self-contained smaller plastic beaker in the decontamination area over several green pads.

27) Carefully place the sample in the plastic beaker.

28) Using thongs carefully pour the water in the plastic beaker over the sample (Figure B.12(a).

29) Using cotton swabs, carefully scrub the surface until the wax is removed (Figure B.12(b)).

30) Use green pads to absorb the water. Rinse the sample with water, dry the sample and discard the container.

(a) 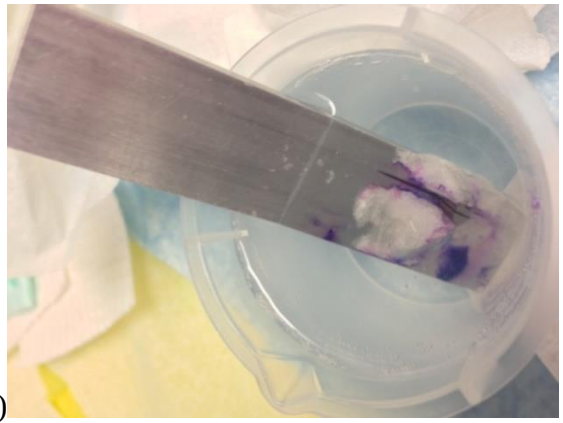 (b) 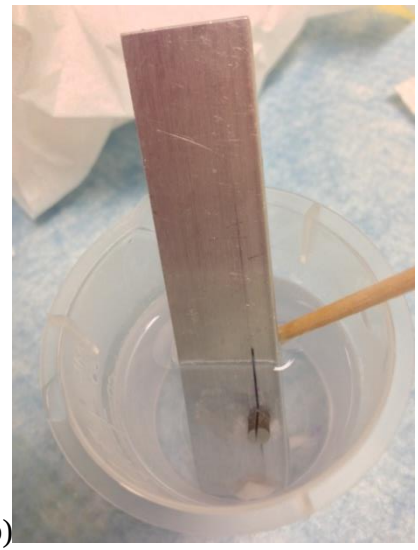

Figure B.12. Dissolving the water soluble Crystalbond™ after cutting: (a) Submerge the sample in hot water and (b) Use a cotton swab to finish removing the wax.

31) Scrub again the sample ensemble using cotton swabs and isopropanol over green pads and yellow pads. Once the sample is clean, wrap the sample in a yellow pad piece and place it on a plastic bag on a side. Decontaminate tools and working area.
32) The gelatin tends to dry fast as the atmosphere in the glovebox is usually dry. Leave the gelatin over night and prepare to clean.
    - If the procedure is done right, the gelatin will attach to the decon paint in the walls of the tray and will come out as a whole.
    - Place a piece of yellow pad on the decontamination area.
    - Open the side door to remove the tray (Figure B.13(a)).
    - Carefully place the tray over the yellow pad or green pad.

- Using sharper tweezers carefully peel out the decon paint from the outer sides of the tray (Figure B.13(b)).
- Use cotton swabs to help to remove the gelatin waste and place it directly into a waste bag covered with yellow pads and close the bag immediately.
- Clean the tray (Figure B.13(c)) with fantastic and green pads as necessary, and then rinse with water. Double bag all the waste.

(a)  (b) 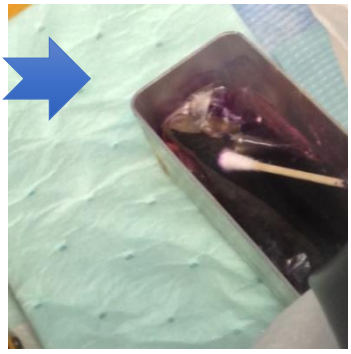 (c) 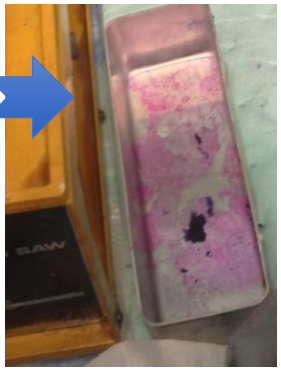

Figure B.13. Secuence of decontamination the fluid tray: (a) open the side door and slide the tray out; (b) remove the tray and peel out the decon paint; (c) Carefully pull out the gelatin and discard and clean the tray.

33) To remove the sample from the metal plate:

- Soak the ensemble in acetone overnight in a plastic disposable container, over green and plastic backed pads.
- Cover the container with paraffin film and label appropriately.
- Once the Crystalbond™ is dissolved: recover the sample, clean the sample with isopropanol and place the pieces in an adequate container (label the container).

34) Once the glovebox is cleaned and decontaminated. Proceed to open the outlet and inlet valves and turn on the recirculation system.

35) Write in the log the amount of material removed during cutting. Estimate the amount removed using the procedure described in A.7.

APPENDIX C

PROTECTIVE GLOVES

Always check for punctures in the gloves inside the glovebox before starting any procedure. If a puncture is detected, tie the two gloves together and inform P. Peralta and the Office of Radiation Safety. Do not continue working with the sample at this point.

To work in the glovebox, a pair of gloves must be placed over the gloves inside the glovebox.

1) Take a new pair of gloves from the box of nitrile (or latex) gloves inside the glovebox before starting any procedure.
2) Place the necessary amount of duct tape over the end of each glove to make a tab that will facilitate the removal of the glove after being used (see Figure C.1). Make sure that the tape is placed outside and inside the glove. Place the tape outside and the fold it and tape in the outside forming a tab.

Figure C.1. Gloves with duct tape. Notice that the tab is big enough to remove afterwards the glove without touching the actual gloves.

3) Place the gloves over the gloves placed inside the glovebox. This way the gloves within the glovebox will be considered “clean”.
4) Every time that the radioactive sample, waste and equipments are handled, use only one hand (always the same hand, this hand will be considered “dirty” or “contaminated”).

5) When removing the gloves (nitrile or latex) always use the “clean” gloves (the one hand that never touched the sample, wastes or machines) to remove the “dirty” gloves (this way you are sure that you are not spreading the contamination) use the hand that has no extra gloves (only glovebox’s glove) to remove the other glove. Pull the gloves using the tab to avoid cross contamination (see Figure C.2).
6) Dispose properly the gloves (they should be with the inside out) in the solid waste container.

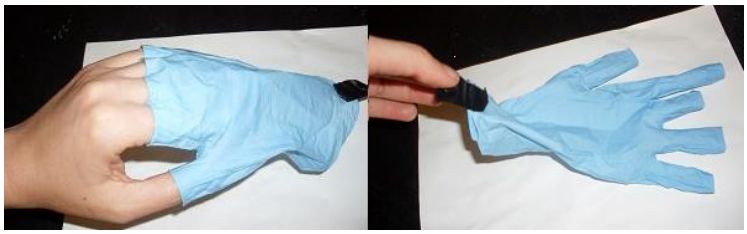

Figure C.2. Removal of the gloves using the tab. Notice that after the removal the glove is inside out.

In order to keep working inside the glovebox, a new pair of gloves must be placed over the glovebox gloves for each procedure.

Change the gloves as often as required, but be aware that one hand must be always kept “clean”. Use the tab to remove the gloves and avoid contamination.

To work outside the glovebox:

Before starting to work in the glovebox always use a pair of gloves (nitrile or latex). These gloves must be placed over the lab coat sleeve and taped around with duct tape.

When manipulating the sample outside the glovebox an extra pair of gloves must be used. These gloves must be placed over the duct taped gloves and can be changed as often as necessary or at least after cleaning the sample. These gloves must have a tab like describe in b for ease the removal and minimize contamination.